Millisecond Dynamics of Biological Systems Investigated with Magnetic Tweezers and Small-Angle X-Ray Scattering

Philipp Ulrich Walker

München 2018

Millisecond Dynamics of Biological Systems Investigated with Magnetic Tweezers and Small-Angle X-Ray Scattering

Philipp Ulrich Walker

Dissertation
an der Fakultät für Physik
der Ludwig–Maximilians–Universität
München

vorgelegt von
Philipp Ulrich Walker
aus München

München, den 12.04.2018

Erstgutachter: Prof. Dr. Jan Lipfert
Zweitgutachter: Prof. Dr. Ralf Jungmann
Tag der mündlichen Prüfung: 12.06.2018

Zusammenfassung

Alle lebenden Organismen bestehen aus Zellen. Diese Zellen wiederum besitzen verschiedenen Komponenten, unter anderem Makromoleküle wie Desoxyribonukleinsäure (DNA) und Proteine. Damit eine Zelle ihre Funktionen ausführen kann, ist das Zusammenspiel dieser beiden Komponenten besonders wichtig. DNA liegt in Zellen im natürlichen Zustand stark aufgewickelt und gebogen vor. Damit die Information von Proteinen abgelesen werden kann, muss die DNA lokal entwunden werden. Um das Zusammenspiel von DNA und Proteinen zu verstehen, ist ein fundiertes Wissen über DNA- und Proteinmechanik vonnöten. Eine Herausforderung hierbei ist die Zeitskala, auf der sich diese Interaktionen abspielen, welche z.B. im Bereich von Mikro- oder Millisekunden liegen kann. Die mechanischen Eigenschaften von DNA können auch in der Nanotechnologie eingesetzt werden. Nanotechnologie im Allgemeinen, aber auch insbesondere in biologischen Anwendungen, ist ein stark wachsendes Feld. Aus DNA können große Komplexe hergestellt werden, so genannte DNA-Origamis, die als Bausteine für biologische Nanotechnologie fungieren. Für erfolgreiche Anwendungen, etwa um Medikamente zu transportieren, ist es nötig, komplexe und dynamische DNA Origamis herzustellen. Um biologische Funktionen zu imitieren, ist eine hohe Geschwindigkeit der Konfigurationsänderungen von DNA-Origamis essentiell.

In dieser Arbeit wurden mit schnellen "magnetischen Pinzetten" (magnetic tweezers, MT) und zeitaufgelöster Kleinwinkel-Röntgenstreuung (Small-angle X-ray scattering, SAXS) verschiedene biologische Systeme untersucht. Hierzu wurde ein MT Instrument aufgebaut, sowie die erforderliche Auswertesoftware geschrieben. Der Aufbau ermöglicht viele Moleküle gleichzeitig zu observieren und eine Teilmenge davon mit (sub-)Millisekunden Zeitauflösung zu messen. Mit der schnellen Zeitauflösung konnte die Schlaufenausbildung (plectoneme) bei Verdrehung von DNA Molekülen untersucht werden. Es wurde eine Kraft- und Salzabhängigkeit festgestellt. Entfaltung der gemessenen DNA Auslenkung mit der Punktspreizfunktion des Versuchsaufbaus resultierte in eine Aufbau-unabhängige 3D Energielandschaft in Abhängigkeit von Rotation und Auslenkung. Hiermit konnte eine Asymmetrie in Auslenkungs- und Rotationsrichtung festgestellt werden. Mit der hoch parallelisierten magnetischen Pinzette und einer während dieser Arbeit neu entwickelten Anbindungsstrategie wurde die kraftabhängige Entfaltung der Proteindomäne "ddFLN4" unter konstanter Kraft charakterisiert. Es konnte gezeigt werden, dass die Überlebenszeit vor einer Entfaltung und einer Zurückfaltung exponentiell von der Kraft abhängt. Die Anbindung des Proteins erfolgt auf einer Seite kovalent und auf der anderen Seite mit einer biologischen Protein-Ligand Bindung (Streptavidin-Biotin), für die eine doppelt exponentiell verlaufende Überlebenswahrscheinlichkeit, bei konstanter Kraft, festgestellt wurde.

Der zweite Teil der Arbeit beschäftigt sich mit der Dimerisierung von zwei Form-komplementären DNA-Origami Monomeren, sowie der salzabhängigen Konformationsänderung eines X-förmigen DNA-Origamis. Hierzu wurden zeitaufgelöste SAXS Versuche durchgeführt. Es konnte beobachtet werden, dass ein großer Unterschied in der Reaktionsgeschwindigkeit vorhanden ist, obwohl in beiden Fällen die DNA-Origami-Bindungen auf dem gleichen Prinzip der Stapelbindung zwischen Nukleobasen beruhen. Die Reaktionszeiten erstrecken sich von Stunden für die Dimerisierung bis hin zum Millisekundenbereich für die Konformationsänderung, was im zweiten Fall auf die vordefinierte Ausrichtung der Bindungsstellen zurückzuführen ist. Das Vermessen der Konformationsänderung nahe dem Diffusionslimit wurde durch ein sehr schnelles, turbulentes, Mischen mit einer flussunterbrechenden Analyse und einem SAXS Messaufbau mit extrem hohen Photonenfluss ermöglicht.

Abstract

Living cells need many components to fulfill their function in nature. Two main components are deoxyribonucleic acid (DNA) and proteins. The DNA stores the genetic information of cells, including the amino acid sequence of proteins. The information stored in the DNA, encoded within the sequence of its bases, is hidden from the outside by the backbone of the DNA. In a cell, DNA is highly compacted into a small volume and highly twisted and bent, making it difficult to access the information. Therefore, proteins have to locally unwind the DNA, which is crucial to read and copy the information. To understand this process, it is important to get a detailed understanding of the mechanics of DNA.
Proteins are the key players in cellular metabolism. They can control biological processes within the cell, but also enable communication with their environment. In nature, proteins can be exposed to and have to bear and deal with external forces. For the force response of these proteins, not only the life time, i.e. how long they can withstand an external force, but also if and how fast they can refold into their natural configuration, is of interest.
Besides its biological relevance, DNA can also be used as a building block for nanotechnology. The potential of this technology is its bio-compatibility. Therefore, it is thought that in the future it can be used as functional machines, e.g. as a transporter for drug delivery, or to adopt and improve functions of other existing (biological) systems. To construct large, complex, and dynamic DNA origamis, a detailed understanding of the mechanics of the DNA and of large DNA complexes is essential.
Biological processes are typically very fast. Protein folding and unfolding events can occur in the micro- and millisecond regime. To mimic biological processes, DNA origamis have to change their configuration within the same order of magnitude. The physicochemical interactions and processes within the DNA, and proteins, as well as DNA-protein interactions, occur on time scales that are difficult to examine.

In this thesis, two different methods were employed to examine fast kinetics of different biological samples. One of them, the so called “magnetic tweezers”, exert a constant force on a superparamagnetic bead. The molecule of interest is tethered between a surface and the bead, so that the force response of individual, single molecules can be examined. A magnetic tweezers setup was built to examine many beads in parallel in real time with an acquisition time of a few milliseconds, while for a limited number of beads an acquisition time of sub-milliseconds is possible. A software package written from scratch is able to analyze the large amount of data produced with this setup. The fast acquisition rate of the setup was used to examine the buckling transition (loop formation) of bare DNA. Applying a deconvolution method, not only the kinetics of the buckling transition could be examined with high spatiotemporal resolution, but also an unbiased and precise description of the 3D energy landscape as a function of rotation and extension could be resolved. From this data, the asymmetry in extension and rotational degree of freedom could be shown. The force and salt dependency of the DNA buckling transition could be analyzed and compared to the already known, much slower, RNA

kinetics. Additionally, the highly multiplexed setup and the software package were used to examine the force response of a protein domain (ddFLN4). For this purpose, a new attachment strategy was developed that utilizes a disordered, flexible polypeptide linker and comprises a covalent bond on one terminus and a biological protein-ligand bond (Streptavidin-Biotin) on the other terminus. The lifetime before an unfolding or refolding event occurs could be examined as a function of force. Furthermore, a shortlived intermediate state could be detected and characterized. The lifetime of the attachment utilizing the Streptavidin-Biotin bond was characterized and found to follow a double exponential model at constant force.
The second method used within the framework of this thesis, the so called "small-angle X-ray scattering" (SAXS), uses X-ray radiation to investigate the molecule of interest. Hereto, the sample is in solution without the need for labeling. The dimerization of two shape-complementary DNA origami monomers, and a large-scale conformational change of another DNA origami was investigated in a time-resolved fashion. Although the origamis are based on the same design principle of base-pair-stacking, a striking difference in the time needed for the transition was observed. The slow kinetics of the dimerization were observed to be in the range of minutes to hours, whereas the conformational change within one origami was observed to be in the millisecond regime and close to the diffusion limit. This result indicates the need for pre-alignment of the interfaces to allow fast transitions.
To sum up, within this thesis challenging fast kinetics of different biological samples were investigated. This was performed under force with magnetics tweezers and label-free conformational transitions were observed with SAXS. One key finding is that new, state-of-the-art instruments are able to investigate fast dynamics of biological systems with a time resolution of milliseconds.

This thesis is separated into two parts, starting with magnetic tweezers and continued with SAXS.
Chapters 1 - 3 give a general introduction into the two techniques (magnetic tweezers and SAXS) used within the framework of this thesis. Furthermore, the biological systems (DNA, proteins, DNA origamis) investigated within this thesis are introduced.
Chapter 4 is a detailed description of the MT setup built within the framework of this thesis, including its performance, resolution, and force calibrations.
Chapter 5 gives an overview of the software package written to analyze the data measured during this thesis.
Chapter 6 investigates the buckling transition of DNA. The fast kinetics were measured as a function of force and salt concentration. With deconvolved extension histograms, a 3D energy landscape of the buckling transition was obtained, showing the asymmetry in extensional and rotational degree of freedom.
Chapter 7 focuses on the folding and unfolding of the protein domain ddFLN4 as a function of force. The force dependency of the lifetime of the whole complex as well as the short-lived intermediate state is investigated. Furthermore, the newly developed attachment strategy is characterized.
Chapter 8 demonstrates slow and fast kinetics of DNA origamis. The slow kinetics of the dimerization of two shape complementary DNA origami monomers (minutes to hours) are presented in contrast to the fast kinetics of a DNA origami device (millisecond regime) that is based on the same mechanism but has a pre-aligned axis for the interfaces. It is shown that with a pre-alignment of the interfaces, base-pair stacking interactions allow a conformational transition on a timescale close to the diffusion limit.

Publications

Publication which are part of this thesis:

1. Linda K. Bruetzel*, Philipp U. Walker*, Thomas Gerling, Hendrik Dietz, Jan Lipfert; **"Time-Resolved Small-Angle X-Ray Scattering Reveals Millisecond Transitions of a DNA Origami Switch"**; *Nano Letters* (DOI: 10.1021/acs.nanolett.8b00592) [1]
   *contributed equally to this work

2. Philipp U. Walker, Willem Vanderlinden, Jan Lipfert; **The Dynamics and Energy Landscape of DNA Plectoneme Nucleation**; *BioRxiv* (DOI: https://doi.org/10.1101/280719) [2] and accepted for publication in *Physical Review E*

Other publications, not part of this thesis:

1. Linda K. Bruetzel, Thomas Gerling, Steffen M. Sedlak, Philipp U. Walker, Wenjun Zheng, Hendrik Dietz, Jan Lipfert; **Conformational changes and exibility of DNA devices observed by small-angle X-ray scattering**; *Nano Letters* 16(8), 4871–4879 (2016); (DOI: /10.1021/acs.nanolett.6b01338) [3]

2. Willem Vanderlinden, Tine Brouns, Philipp U. Walker, Pauline Kolbeck, Lukas Milles, Wolfgang Ott, Philipp Nickels, Zeger Debyser, Jan Lipfert; **Strand Transfer Triggers Allosteric Stabilization of a Retroviral Intasome**; submitted to *Cell*

Contents

Zusammenfassung **vii**

Abstract **ix**

Publications **xi**

I Introduction 1

1 Usage and Versatility of Magnetic Tweezers in Biological Applications 3
1.1 Introduction . . . 3
1.2 Magnetic Tweezers Instruments . . . 3
1.3 Biological Systems in Magnetic Tweezers . . . 7

2 DNA as a Building Block for Complex Structures 15
2.1 Introduction . . . 15
2.2 Self-Assembly DNA Origami . . . 16
2.3 Example of Static State-of-the-Art DNA Origami Structures and Morphologies 17
2.4 Dynamic State-of-the-Art DNA Origami Structures and Morphologies . . . 19

3 Small-Angle X-Ray Scattering for Biological Applications 21
3.1 Introduction . . . 21
3.2 Basic Principles of SAXS . . . 21
3.3 Elastic Photon Scattering . . . 22
3.4 Influences on and Pre-Selection of SAXS Data . . . 24
3.5 Basic and Overall Structural Parameter Analysis . . . 26
3.6 Scattering Profile Simulation and Shape Reconstruction . . . 29
3.7 Synchrotron based SAXS . . . 31
3.8 Monochromator . . . 35
3.9 Example of Biological SAXS Beamlines . . . 36
3.10 Time-Resolved SAXS Experiments . . . 37

II Magnetic Tweezers 39

4 Construction and Characterization of a Magnetic Tweezers Setup 41
4.1 Requirements for a State-of-the-Art Magnetic Tweezers Setup . . . 41
4.2 Hardware and Software of the MT Setup . . . 42
4.3 Performance and Calibration . . . 44

5 Analysis Software "MT GUI" 59
5.1 Practical Structure to Address Challenges Regarding the Analysis of MT Data 59
5.2 "MT GUI" Main GUI . . . 62
5.3 "Further Analysis GUI" . . . 65
5.4 "Summary Analysis GUI" . . . 66
5.5 "Force Calibration GUI" . . . 69
5.6 "Hopping Single GUI" . . . 70
5.7 "Edit Hopping Info File GUI" and "Hopping Fast Load GUI" . . . 72
5.8 "Deconvolution GUI" . . . 74

6 The Dynamics and Energy Landscape of DNA Plectoneme Nucleation 77
6.1 Summary . . . 77
6.2 Introduction . . . 78
6.3 Results and Discussion . . . 78
6.4 Conclusion . . . 82
6.5 Acknowledgements . . . 83
6.6 Supplementary Information . . . 88

7 Introducing a New Attachment Strategy for Protein Unfolding Experiments in Magnetic Tweezers 109
7.1 Introduction . . . 109
7.2 Challenges of New Surface Attachment Strategies . . . 111
7.3 Surface Attachment with Linker (PEG) . . . 112
7.4 Surface Attachment with Linker (ELP) . . . 119
7.5 Attachment Chemistry Characterization and Example Protein Un- and Refolding Events . . . 121
7.6 ddFLN4 Force Response - Preliminary Results . . . 127
7.7 Discussion and Outlook . . . 135
7.8 Material and Methods . . . 137

III Small-Angle X-Ray Scattering 141

8 Time-Resolved Small-Angle X-Ray Scattering Reveals Millisecond Transitions of a DNA Origami Switch 143
8.1 Summary . . . 143
8.2 Time-Resolved Small-Angle X-Ray Scattering Reveals Millisecond Transitions of a DNA Origami Switch . . . 144
8.3 Acknowledgements . . . 146
8.4 Author Contributions . . . 146
8.5 Supporting Information . . . 150

IV Conclusion and Outlook 165

9 Conclusion and Outlook 167

V Appendix 171

10 Appendix: Magnetic Tweezers 173
10.1 List of Setup Components 173
10.2 Computational Performance for Different Tracker Algorithms and Tracker Settings 174
10.3 Setup Resolution for Different Tracker Algorithms and Tracker Settings 176
10.4 Flowcharts of MT GUI 179

Bibliography 185

List of Figures 217

List of Tables 221

Acknowledgments 223

Part I

Introduction

Chapter 1

Usage and Versatility of Magnetic Tweezers in Biological Applications

1.1 Introduction

Force plays an essential role in many biological systems. Motion of whole cells as well as proteins and other biomolecules are driven by pico-newton-scale forces [4, 5]. As a force response, mechanical stability of protein structure can be important especially for proteins bearing mechanical function. This is fundamental e.g. for muscle- and cytoskeletal proteins [6, 7], but also for molecular motors [8–10]. Different approaches have been developed to investigate the influence of force on biological systems down to the single-molecule level, such as magnetic tweezers (MT) [11–14], optical tweezers (OT) [15–17], atomic force microscopy (AFM) [18–20], biomembrane force probe [21], flow induced stretching [11, 21], Acoustic Force Spectroscopy (AFS) [22, 23] and recently DNA origamis [24]. In general, these different approaches as well as other experimental setups cover different force ranges and have different force, temporal and spatial resolution [5].
MT cover a wide range of forces combined with a high spatial and temporal resolution [4, 5]. Therefore, a molecule of interest ("tether") is tethered between a glass surface and a superparamagnetic bead. A gradient of an external magnetic field of the MT setup exerts a force on the bead and results in a force clamp [25]. MT can be used to examine different biological systems, such as ribonucleic acid (RNA) [26], deoxyribonucleic acid (DNA) [13, 14] or proteins [27–30].

1.2 Magnetic Tweezers Instruments

In MT, the molecule of interest is tethered between a superparamagnetic bead and the surface of a flow cell (Fig. 1.1). A pump connected to the flow cell allows to prepare the flow cell, adding the sample and beads as well as exchanging the buffer. Magnets placed above the flow cell exert a force on the bead and consequently a force acts on the molecule. Motors control the distance between the magnets and the flow cell, thus allowing to control the applied force. Furthermore, the magnets can be rotated and torque can be applied to a torsionally constrained

molecule. A monochromatic LED illuminates the sample and beads, and the diffraction rings of the beads are captured by a CMOS camera. The objective between the flow cell and the camera is mounted on a piezo stage and thus the focal plane can be changed. The diffraction pattern of the bead changes with the distance to the focal plane and therefore allows to generate a Look-Up-Table (LUT) to extract height information of the bead (Fig. 1.2) [31]. To this end, reference pictures at known positions are taken before the actual measurements are performed. Hence, in addition to the lateral (x and y) position also the horizontal (z) information can be determined while applying a constant force. In general, electro- or permanent magnets can be used. When using permanent magnets the stiffness of the torque trap differs depending on its configuration, resulting in three different types of MT (Fig 1.3): conventional MT, freely orbiting magnetic tweezers (FOMT) and the magnetic torque tweezers (MTT). For all configurations it is possible to pre-calibrate the force, making a force calibration during the actual measurement unnecessary and consequently preventing uncertainties between different measurements due to calibration errors [4, 25, 32–34].

Recent developments in tracking and camera technology make it possible to track many

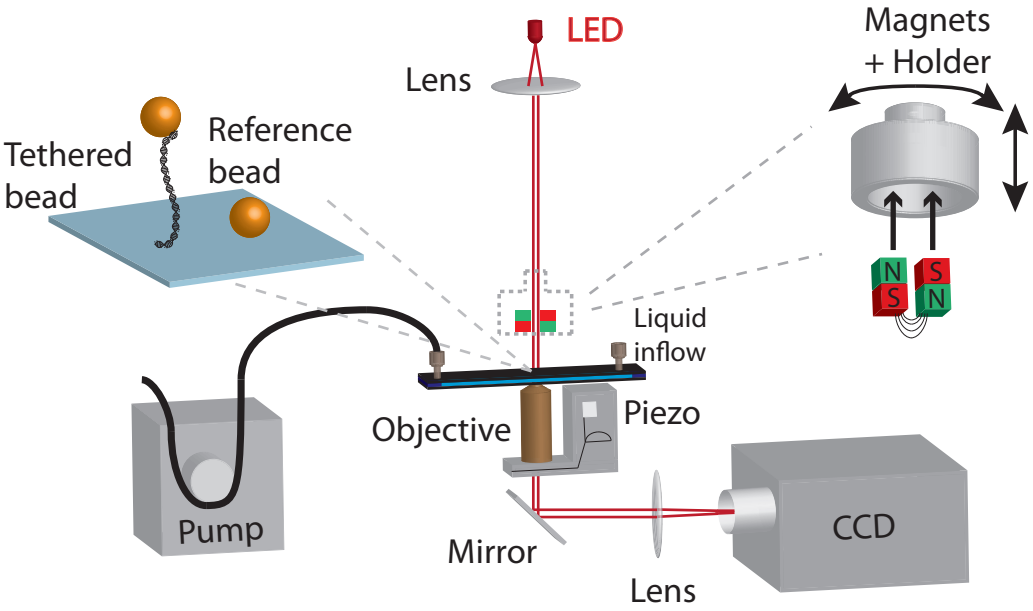

Figure 1.1: Schematic of a conventional magnetic tweezers setup. The system of interest is tethered between the glass surface and a superparamagnetic bead in a flow cell. Magnets placed above the flow cell exert a magnetic force on the bead and elongate the molecule of interest. A linear motor adjusts the distance between the magnets and the sample and hence controls the force. Another motor rotates the magnets which applies a torque to the sample. An LED illuminates the flow cell and the resulting diffraction patterns are captured by an objective and finally by a CMOS camera. The objective is mounted on a piezo controlled stage and the focal plane can be moved for the LUT. A peristaltic pump attached to the flow cell enables the exchange of buffer. A reference bead stuck to the surface can be used to subtract mechanical drift.

($\approx$ 100) beads in parallel in real time without any loss in lateral or temporal resolution [31]. Alternatively it is possible to track less beads with higher frame rates, enabling to measure fast transitions with high temporal resolution [35–37]. Hence, MT are a suitable tool to examine systems of interest with high spatial and temporal resolution under different environmental conditions in pre-calibrated force clamp mode with a large force range, starting from very low

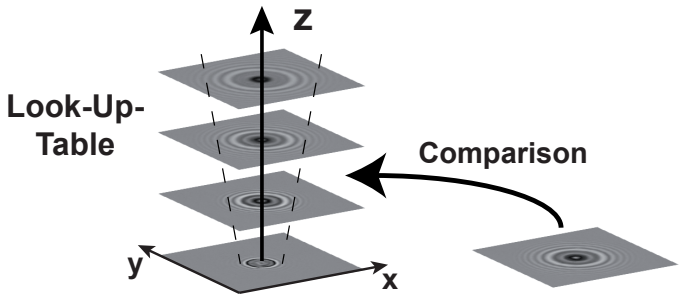

Figure 1.2: Height determination with a LUT. The height information of the bead is extracted from a comparison of the current position with a pre-determined LUT. To this end, the objective and hence the focal plane is moved with the piezo controlled stage and reference pictures are taken before the actual measurements are performed.

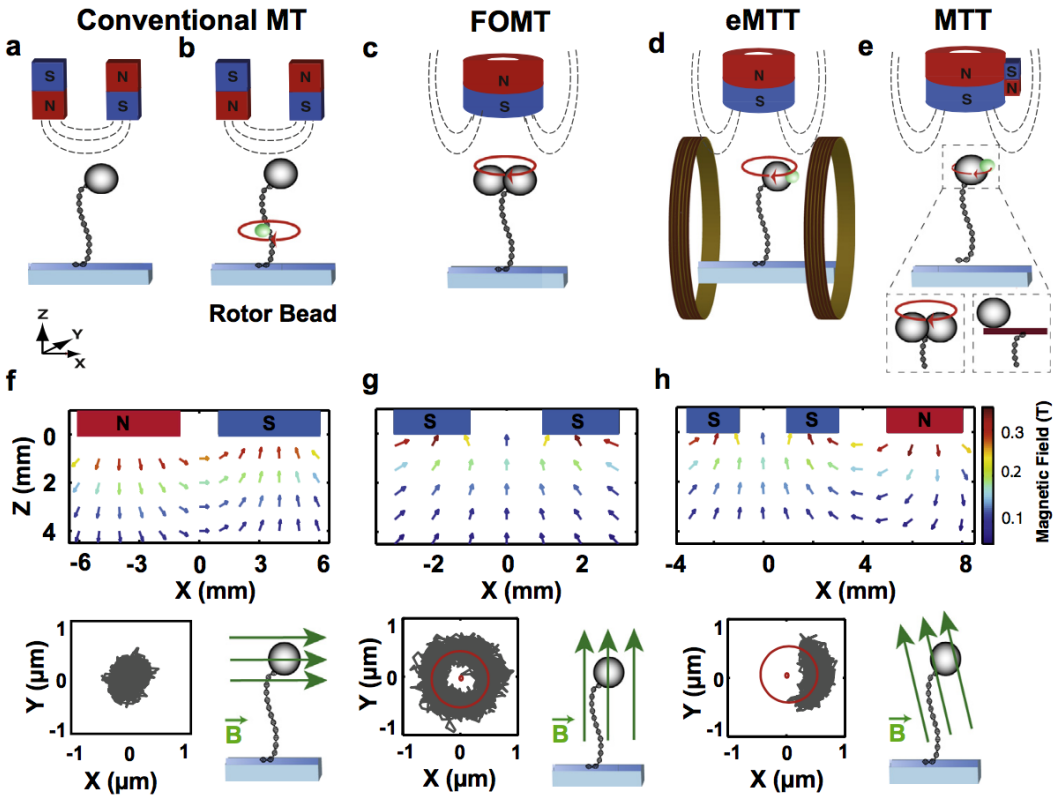

Figure 1.3: Variations of magnetic tweezers (a–e). Conventional MT consist of two cubic, permanent magnets (a, b) that produce a horizontal magnetic field (f) at the location of the magnetic bead, while cylindrical magnets (c–e) create a vertical magnetic field (g). Helmholtz coils around the cylindrical magnets (d), as in electromagnetic torque tweezers (eMTT), or an additional side magnet (e), in magnetic torque tweezers (MTT), slightly tilt the vertical magnetic field (h). The *xy*-fluctuations of the magnetic bead depend strongly on the direction of the magnetic field. The rotation of the bead about the tether axis in (f) is strongly confined and deviates barely from its equilibrium position. This stands in contrast with (g), where the rotation of the bead about the tether axis is completely unconstrained and the bead's fluctuations trace out a doughnut- like shape in the *xy*-plane. In (e) MTT, with a slightly tilted magnetic field (h), the rotation of the bead is weakly confined such that the bead does not trace out a whole circle, but an arc. The field gradients in all MT configurations shown generate (upward) pulling forces on the magnetic beads, thus stretching the molecules of interest. Figure caption adapted from Ref. [14]. Reprint from Ref. [14] with permission from Elsevier.

forces. The direct output is the three-dimensional position of the bead which is attached to the molecule from which further information can be achieved, e.g. the restoring torque of the molecule.

1.2.1 Conventional Magnetic Tweezers

Conventional MT use a pair of cubic permanent magnets to generate a horizontal magnetic field and magnetic field gradient [25] (Fig. 1.3 a, f). The force can be precisely controlled by the distance between the magnets and the flow cell [33, 38] and covers a range from ≈ 0.001 pN to a few hundreds of pN and above [4, 5, 33]. Besides the vertical force, the intrinsic magnetization axis of the beads aligns tightly with the external field [39], strongly dictating the rotation of the bead around the vertical axis. This large rotational trap stiffness correlates precisely the rotational angle of the bead with the magnets. This makes it possible to control and hold the linking number of a torsionally constrained tethered molecule. However, a drawback of the large trap stiffness is that it is difficult to detect any angular changes between the bead and the magnets and hence to measure the restoring torque of the molecule.
A detailed description of a conventional MT setup can be found in chapter 4.

1.2.2 Freely Orbiting Magnetic Tweezers

A freely orbiting magnetic tweezers setup consists of a cylindrical magnet that produces mainly a vertical magnetic field along the tether axis (Fig. 1.3 c, g). As for the conventional MT, the magnetic field gradient exerts a force towards the magnet and can be controlled by the distance between the magnet and the bead. However, in contrast to conventional MT the intrinsic magnetization axis does not align horizontally, but vertically with the magnetic field. Hence, the bead can freely rotate around the vertical axis, in line with the tether axis and consequently the molecule is not torsionally constrained by the magnets. Therefore, the bead rotation can be constrained by the tethered molecule. For a torsionally unconstrained molecule, e.g. a DNA molecule with at least one break in its backbone, the fluctuation in the x-y plane is a circular pattern, while for a torsionally constrained molecule the fluctuation pattern is doughnut- shaped. A doughnut- shaped fluctuation pattern allows to determine angular changes by converting the x-y information into radial and angular coordinates [32].
A competitive method is the rotor bead assay (Fig. 1.3 b). Here, conventional MT are used with an additional, fluorescent, marker bead or gold nanorod attached to the DNA for angular tracking [40–43]. In practice, the rotor bead assay can be more complicated to operate compared to FOMT, in particular separating the force actuation from angular tracking and the need for three attachment points for surface and beads instead of two in FOMT. However, the rotor bead assay has the advantage that a very small particle can be used to track the angular motion, providing a great flexibility and a higher temporal resolution [40].

1.2.3 Magnetic Torque Tweezers

Magnetic torque tweezers combine conventional MT and FOMT by applying a limited angular trap stiffness which can be tuned [44]. The limited trap stiffness enables to measure single molecule torques [45–48]. Its basic concept is very similar to FOMT. A vertical magnetic field is

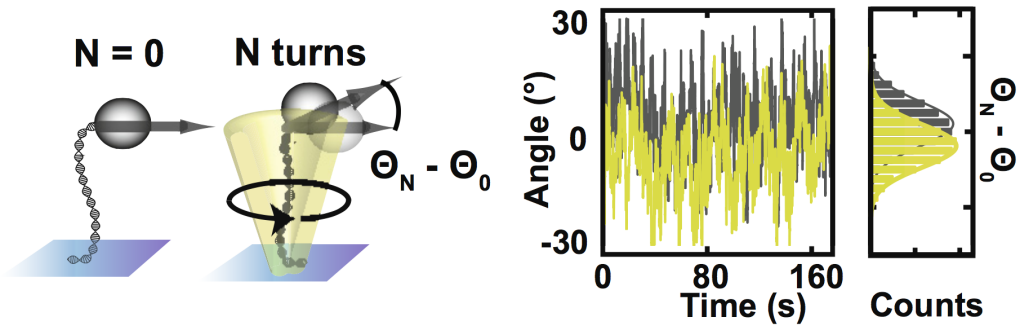

Figure 1.4: Angular tracking in MTT and the torque response of dsDNA. When rotating the magnet and thus the beads, twist is induced in the molecule that can be measured in MTT, based on detecting changes in the rotational angle. Figure caption adapted from Ref [14]. Reprint from Ref. [14] with permission from Elsevier.

generated by a cylindrical magnet and in addition a weak horizontal magnetic field is applied either by Helmholtz coils [49], misalignment of the cylindrical magnet [45, 47] or by a side magnet (Fig. 1.3 d, e, h) [46], leading to a weak angular trap necessary for torque measurements. The weak horizontal field component restricts the fluctuation of the bead, resulting in an arc-shape pattern in the x-y-plane which allows to induce twist and hence to measure the restoring torque of the molecule [44–49].
In MTT the usual measurement coordinate is the angle of the lateral fluctuations. As for FOMT measurements, the x-y fluctuations are transformed into polar coordinates and the difference between the magnet rotations Θ_{rot} and rotation angle of the bead Θ_N can be used to extract information about the restoring torque τ_{mol} in the tethered molecule (Fig. 1.4):

$$\tau_{mol} = -k_\Theta \langle \Theta_N - \Theta_{rot} \rangle \tag{1.1}$$

with k_Θ being the angular trap stiffness:

$$k_\Theta = \frac{k_B T}{Var(\Theta)} \tag{1.2}$$

A common way to measure the angular position is to use the circular arc of the x-y fluctuations (Fig. 1.3 h) [14, 44]. However, several alternative techniques have been established, for example to use and detect inhomogeneities of the beads [26, 47] or to add a fiducial marker bead to the paramagnetic bead (Fig. 1.3 e) [46].

1.3 Biological Systems in Magnetic Tweezers

Magnetic tweezers can be used to investigate different types of samples, including DNA [50, 51], RNA [26] and proteins [28, 30, 52] as well as protein-DNA interaction [46, 53].

1.3.1 DNA

The information and construction plan of an organism is stored in the genome and hence on DNA. The natural DNA consists of four different nucleotides, which contain a phosphate group, a five-carbon sugar and a nitrogenous base (adenine, guanine, thymine, cytosine) (Fig.

1.5a) [54–59]. A triplet of consecutive nucleotides (codons) can specify an amino acid [60, 61] and several amino acids together can (but don't have to) describe a protein [61, 62]. In other words, the arrangement of the nucleotides define the sequence of the amino acids and therefore which protein will be built. However, a large part of the DNA is non-coding and not used as a sequence for proteins.
In its natural configuration, double-stranded DNA (dsDNA) forms a right-handed B-form double helix of ≈ 2 nm diameter with a rise per base pair (bp) of 0.34 nm resulting in 10.5 base pairs for one turn [63, 64]. The double helix structure induces a major and a minor groove, with a width of 2.2 nm and 1.2 nm, respectively [63]. As a consequence, many proteins which bind specific sequences of the dsDNA interact with the sides of the bases in the major groove [65]. Several different models have been developed to describe the mechanical properties of dsDNA. One approach, namely the "worm-like chain"-model (WLC) and its extended variations, describe the DNA as an isotropic elastic rod. Therefore, not only bending but also stretching and twisting of the rod has to be considered and consequently the DNA is characterized by the bending persistence length (L_p), Young's (stretch) modulus (S), torsional persistence length (C) and twist-stretch coupling (D) [66]. However, underlying assumptions limit the elastic rod approximation to not too large forces and torques.
At low forces (< 10 pN), the force extension response of a DNA is in very good agreement with the inextensible WLC model and thus described by purely entropic stretching elasticity [26, 67–69] (Fig. 1.5 b). The persistence length of dsDNA is found to be salt dependent and to decrease with an increase in salt concentration [70, 71]. For ≈ 150 mM monovalent salt L_p is found to be ≈ 45 nm [26, 70–73]. The persistence length is well described by a theoretical approach in the stiff rod limit which splits L_p into an intrinsic and an electrostatic component [74, 75]. At higher

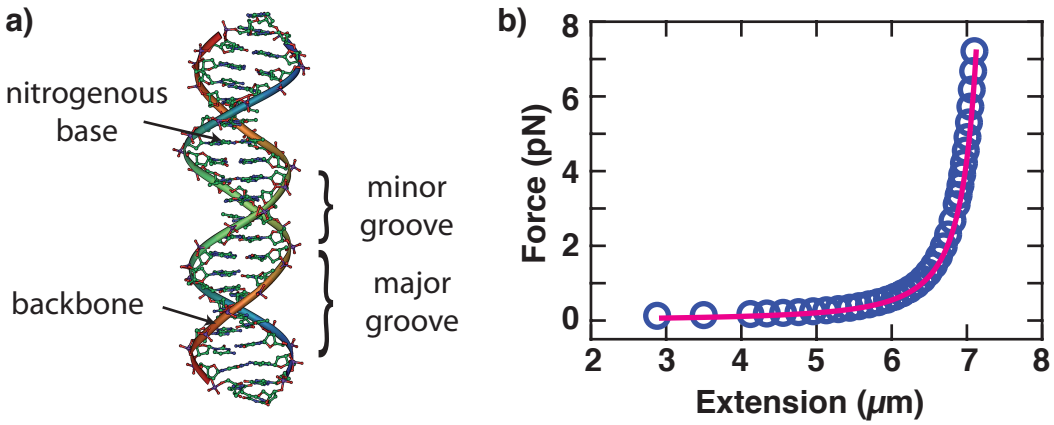

Figure 1.5: Structural model and force-extension response of dsDNA. a) dsDNA consists of four different types of nitrogenous bases enclosed by a backbone. The double helix structure consists of a major and minor groove, with a width of 2.2 and 1.2 nm, respectively. Reprint from Ref. [76] (GNU free document license) b) Force-extension response of DNA. The inextensible WLC model describes the force extension behavior below ≈ 10 pN very well. The persistence length of the shown molecule was determined to be 44 nm in 1x PBS. The force was calibrated as described in chapter 4.3.3.

forces, the inextensible WLC is not capable to accurately describe the force-extension behavior of DNA. However, by introducing the stretch modulus S, the extensible WLC model takes the enthalpic contributions into account and is able to characterize the force-extension data very well [72, 77]. For dsDNA S is found to be ≈ 1000 pN [26, 70, 71, 73, 78]. Above ≈ 50 pN dsDNA

undergoes an overstretching transition that is not described by the extensible WLC model. Besides L_p and S, both describing the bending and elongation properties, the torsional persistence length C (and effective torsional stiffness C_{eff}) is needed to describe physical properties in rotational degree of freedom. One suitable tool to determine C_{eff} is the MTT [44]. Close to the torsional relaxed state of the dsDNA, the torque vs. turns response of the molecule is approximately linear and C_{eff} can be determined directly from the slope: $C_{eff} = L_C/(2\pi N k_B T)\tau_{mol}$ with L_C being the contour length of the DNA and N the number of applied turns. However, C_{eff} increases with increasing force, which is in good approximation described by the Moroz and Nelson model [79]. Based on the coupling of twist and bend fluctuations, Moroz and Nelson are able to describe why C_{eff} is consistently smaller than C and estimates of C can be obtained from rotation-extension curves [79, 80]. However, for low forces ($< \approx 2$ pN) the Moroz and Nelson model significantly overestimates C_{eff} [32, 44, 46, 81]. One approach to account for this deviation is to introduce two different states of the dsDNA helix [82] as also already done for X-ray scattering measurements [83]. Although in better agreement with the experimental data, the use of two sub-states is somewhat arbitrary and further theoretical support is required.
The twist-stretch coupling constant D is the only coupling term between the elastic deformations in the isotropic elastic rod model. D describes the response of the molecule upon overwinding, where positive values correspond to shortening and negative values to lengthening of the molecule. First measurements of the twist-stretch coupling constant for dsDNA revealed a positive value for D [84, 85], whereas later high resolution measurements reported a lengthening of the DNA upon overwinding [86, 87]. In contrast, in similar measurements on ribonucleic acid (RNA) a shortening of the molecule is detected [26]. Many models were able to describe the DNA or RNA measurements, but fail to predict both [26, 84–86, 88–91]. Besides others, these approaches include models such as "HelixMC", which represents the DNA and RNA at the base pair level (successful for DNA, fails for RNA) [26, 89] as well as "oxRNA" and "oxDNA", which represent the RNA and DNA as coarse grains at the single base level and are able to correctly predict RNA data but fail for DNA [90, 91]. Finally, all-atom explicit solvent molecular dynamics simulation were able to correctly describe the RNA as well as DNA twist-stretch behaviour [92]. The simulations revealed that for DNA the reduction in length upon overwinding is caused by an increase in the inclination of bases which reduces the helix radius. However, RNA bases already exhibit a significant inclination in the torsionally relaxed state resulting in less impact on the radius upon overwinding. Therefore the radius of RNA stays approximately constant and consequently the molecule shortens [92]. Nevertheless, the twist-stretch coupling remains a minor effect and can only be detected by high resolution single molecule measurements and described with much effort in simulation [14, 92, 93].

1.3.2 DNA in Magnetic Tweezers

MT can exert force as well as torque on a molecule and therefore enables to investigate the force as well as torque response. Pulling a dsDNA molecule with a force of ≈ 65 pN, the molecule cannot be described with the extensible WLC model anymore, as it undergoes an abrupt lengthening of a factor of ≈ 1.7 for torsionally unconstrained and a gradual extension for torsionally constrained molecule (Fig. 1.6 a) [73, 78, 94–96]. However, the force at which the transition occurs depends on the ionic strength [70, 71, 78], pH [97], sequence of the DNA

(amount of GC base pairs) [98] and temperature [99].
The lengthening and overstretching can be described by two different models. One of them describes the DNA molecule throughout this transition as double stranded with elongated base pairs [78, 100] with a helical twist of ≈ 35 base pairs per turn [41, 101, 102]. The elongated DNA molecule is also called "S-DNA" and hence the transition is known as "BS-transition". The second model describes the transition as a melting of the dsDNA and hence as breaking of the hydrogen bonds upon force, resulting in two single-stranded DNA molecules [70, 95, 97, 99]. However, recent results suggest that the correct model depends on the salt concentration, temperature and dsDNA sequence, hence the S-DNA as well as a strand separation can be applicable [103–105].

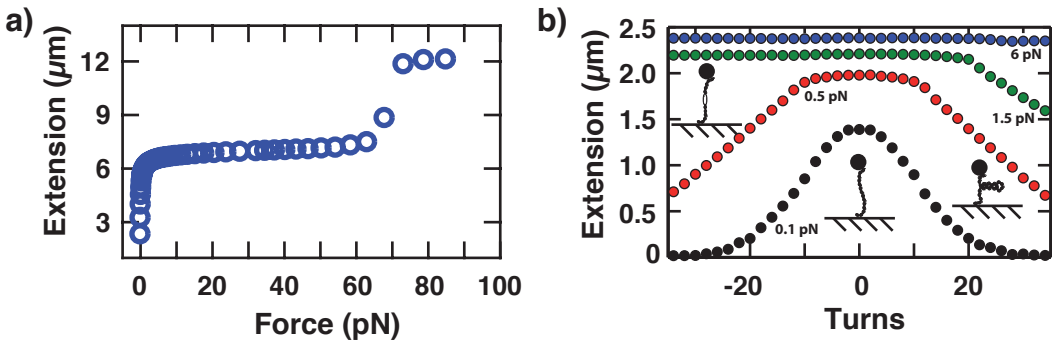

Figure 1.6: BS-transition and rotation curves of dsDNA in MT. a) BS-transition of dsDNA. At ≈ 65 pN the DNA changes from the B-form helix configuration into the overstretched S-form. Data shown for one single ≈ 21 kbp long dsDNA molecule. b) Rotation-extension curves for different forces (0.1 pN: black; 0.5 pN: red; 1.5 pN: green; 6 pN: blue). At low forces, the tether length decreases due to formation of plectonemes with applied turns, resulting in an approximately symmetric curve with zero turns as center. At slightly higher forces local denaturation of the dsDNA causes an asymmetric rotation curve. Above ≈ 6 pN no plectonemes form and the extension of the tether stays approximately constant. Data shown for one ≈ 7kbp long dsDNA molecule. a) and b) measured with the setup including its calibration described in chapter 4.

The response of a dsDNA molecule upon rotation varies depending on the applied force resulting in different types of extension curves as a function of turns controlled by force (Fig. 1.6 b). At low forces (< 1 pN) the extension curve is symmetric and a shortening for overwinding (positive rotations) as well as underwinding (negative rotations) can be observed due to plectonemes (loops/coils) being formed in the dsDNA. The extension of the molecule is observed to decrease linearly with rotation number. Exerting higher forces of ≈ 1 − 5 pN, the rotation curves become asymmetric with nearly no change in extension at negative turns but formation of plectonemes and associated shortening of the molecule for positive rotation of the molecule. Exerting even higher forces, the extension remains approximately constant independent of the number of applied turns and no plectonemes can be observed. Coarse-grained simulation are able to describe the critical torque as well as supercoiling density for the appearance of plectonemes [81, 106].
Although plectonemes can occur as response to both positive and negative twist, the different behavior upon force indicates that both cases have to be considered individually. When dsDNA is underwound while exerting a force < 1 pN, the torsional stress increases approximately linearly until released by plectonemes, which keep the restoring torque in the molecule approximately constant [48, 107, 108]. However, at higher forces the torque increases again

approximately linearly with negative twist until a critical torque of -10 ± 1 pN nm is reached and partial melting of the dsDNA appears [14, 109–111]. At higher negative twist, the restoring torque stays approximately constant, here at the critical buckling torque. Finally, at a supercoiling density of ≈ 1.8 a transition of B-DNA to L-DNA (defined by an overall left handed twist) takes place [112]. However, in general this L-DNA is not identical with the also existing left-handed Z-DNA and depending on force and torque a co-existence of L-, Z-formed and melted DNA exists [43, 113, 114]. L-DNA has with 3 nm an essentially smaller persistence length than B-DNA and consequently is more flexible. In addition, L-DNA is ≈ 1.4 times longer than B-DNA and has an helical twist of ≈ 13 base pairs per turn [112].
When overwinding dsDNA at low forces, at one point the torsional stress is released in plectonemes which keep the restoring torque constant [48, 107, 108, 115]. However, exerting a higher force than ≈ 5 pN, at positive twist the formation of plectonemes is suppressed and instead a conformational change can be observed. As for negative twist, the torque stored in the molecule increases approximately linearly until a critical torque value of ≥ 35 pN nm is reached [41, 46, 116] and the DNA switches from the B-DNA to P-DNA with its bases facing outward [51, 100]. In general, the critical torque of this transition is force dependent and decreases with higher applied force [41, 117]. Below ≈ 20 pN, P-DNA is able to form plectonomes upon overwinding, hence no change in extension is observed. However, at higher forces, an extended P-form is observed, resulting in a lengthening while increasing positive twist. P-DNA differs from B-DNA in many physical properties, such as an elongated contour length by a factor of ≈ 1.5 [41, 51], the small helical twist of 2.6 to 2.7 base pairs per turn [41, 51] and a smaller persistence length of ≈ 19 nm [51].
In the plectonemic regime, hence at least one plectoneme has formed, the linear decrease in extension with the externally defined rotation number of the molecule suggests the formation of one additional coil per turn [81, 106, 107, 118, 119]. Additionally, MT combined with fluorescent imaging made it possible to observe that depending on force and salt, several branches of plectonemes occur in parallel [120]. Theoretical description of supercoiled DNA suggests that in the multiplectoneme regime the restoring torque of the molecule will differ depending on the exact amount of turns.
A detailed investigation focusing on the formation of plectonemes with high speed MT can be found in chapter 6.

1.3.3 Comparison of RNA and DNA in its Mechanical Properties

Besides DNA, another important nucleic acid is the ribonucleic acid. It is essential in many functions of the cell such as gene expression and regulation. Like DNA it is assembled from four different nucleotides, however with guanine, uracil, adenine and cytosine as nitrogenous bases [57, 121]. Despite many similarities with DNA, RNA differs in some chemical and physical properties.
Although the overall physical behavior can be described with similar models as for DNA (e.g. WLC model), different properties must be considered. Unlike dsDNA, dsRNA forms naturally an A-form helix with a smaller inclination of 0.28 nm/bp resulting in 13 base pairs per turn of the helix [122]. The diameter of the dsRNA is with ≈ 2.4 nm larger than for DNA.
The inextensible WLC model reveals an L_p of ≈ 57 nm at ≈ 150 mM monovalent salt concentration, describing the dsRNA as stiffer compared to dsDNA [26, 73]. However, according to

the extensible WLC model dsRNA exhibits a smaller stretch modulus of ≈ 350 pN [26, 73]. The response of torsional stress described by the torsional persistence length follows qualitatively the Moroz and Nelson model [79] and again as for DNA is in better agreement with the model described by Schurr [82]. As discussed in section 1.3.1 the dsRNA shortens with overwinding and hence has a negative twist-stretch coupling constant D in contrast to DNA (see section 1.3.1 for details).
Nevertheless, although there are significant differences the physical properties are in the same order of magnitude and differ only slightly. Furthermore, dsRNA behaves in MT qualitatively similar to dsDNA, hence is able to form plectonemes as well as P-form and L-form configurations upon external rotation [26]. Furthermore, dsRNA can be described by the WLC model with an adapted persistence length and at high force a transition into an S-form can be observed [26]. However, plectoneme formation of dsDNA and dsRNA at otherwise identical conditions is approximately 100 times faster for DNA [26]. These fast transitions occur at the limit of the time resolution of MT setups and can only be precisely detected with high speed MT (see chapter 6).

1.3.4 Proteins in Magnetic Tweezers

Proteins are macromolecules composed of amino acids connected by peptide bonds [123–125]. They are essential for all functions of a cells and in general their three dimensional structure is important for the their specific function [125]. Therefore, protein structure is separated into four different aspects, namely the primary, secondary, tertiary and quaternary structure (Fig. 1.7). The primary structure is the amino acid sequence and describes the protein without a direct description of spatial properties. The secondary structure are local, geometrical structures of the protein, mainly α-helices, β-sheets as well as different kinds of turns. These structures are stabilized by hydrogen bonds between the polypeptide backbones. The energetically allowed angles between the peptide backbones and hence the allowed structures for the secondary structure can be visualized by the Ramachandran diagram [126, 127]. The tertiary structure describes the global shape of one protein. It can be stabilized by different kinds of interactions, such as covalent disulfide bonds as well as non-covalent interactions such as hydrogen bonds, hydrophobic interactions and Van der Waals force. Commonly a formed tertiary structure is referred to as a “folded” protein. Besides these single protein structures, the quaternary structure describes a complex of several units. These structures can consist of the same as well as different types of proteins [125].
To set up its function, proteins have to fold in their native configuration at the end of the transcription and translation process. Regarding the large number of possible conformations of a polypeptide chain (in the order of $\approx 3^{300}$), the Levinthal paradox estimates the time to fold into a protein’s final configuration in the order of the age of the universe [129]. However, measurements determined the folding time of a protein to be in the order of milliseconds [130, 131]. Single-molecule force spectroscopy can reveal the underlying energy landscape of protein folding and unfolding and thus contribute to an explanation to the large difference of the time scale. Measurements have shown that small proteins can often be described by a two-state model, which has no pronounced minima in the energy landscape and hence no metastable intermediate. However, especially in the energy landscape of large proteins, local minima and consequently intermediates can occur [132, 133]. Intermediate state are generally

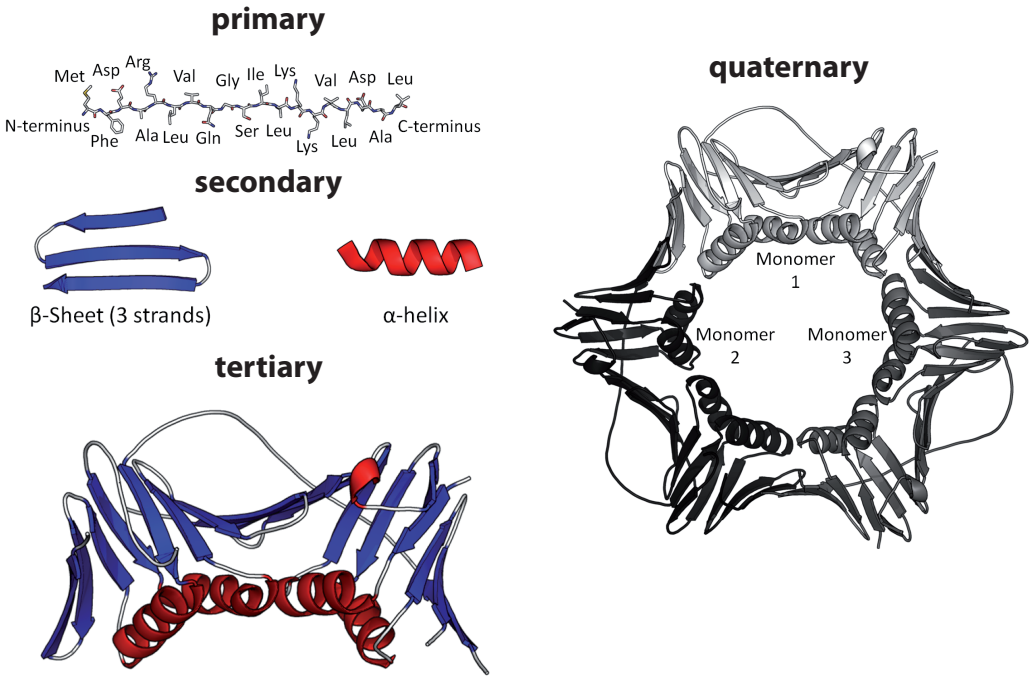

Figure 1.7: Local and global protein structure. The primary structure is the sequence of the protein without geometrical information. The secondary structure consists of local structures. The tertiary structure describes the globel shape of one single protein. The quaternary structure is the shape of a complex of several protein units. Reprint from Ref. [128] (Creative Commons Attribution 4.0 International license).

short-lived and therefore difficult to detect [134–136]. Hence, experiments that should measure protein folding or unfolding in real time need a fast time resolution to capture folding events of whole proteins and even faster to detect intermediate states. Time resolution gets even more important if the force dependency of protein folding and unfolding is taken into account, which for example reduces the life times of intermediates significantly [137, 138].
Structural conformation is important for all proteins, however a subset of proteins have to handle or withstand external forces. In many cases, force-sensing proteins are essential for biological processes, e.g. assembly of cytoskeleton or regulation of muscle gene expression [139–141]. One of these proteins is the large protein "titin", which exists in muscles [142]. Protein domains of titin can reversibly unfold under external force and refold at low or no applied force, and therefore protect the rest of the system [143, 144]. One domain, titin's 27th immunoglobulin (Ig), has been extensively studied by different single molecule force spectroscopy approaches, including AFM, OT and MT [52, 145–147]. It is one of the rare protein domains which have been directly probed as a tether in MT flow cells. A closely related protein is the filamin rod "ddFLN" of Dictyostelium discoideum [7, 148]. The force response of this actin cross-linking rod is believed to be important for its biological function. The fourth of the six protein domains (*ddFLN4*) is more sensitive to force and can refold faster after force induced unfolding than the remaining *ddFLN* protein domains [149]. Studies of unfolding of the protein domain employing constant speed AFM force spectroscopy revealed an intermediate state, which comprises ≈ 60 of the 100 amino acids of the protein domain (Fig. 1.8) [7, 149]. It

is believed that the intermediate state lowers the energy barrier and enables the fast transitions of *ddFLN4*.

Another protein sensitive to force is the multi-domain plasma glycoprotein "von Willebrand

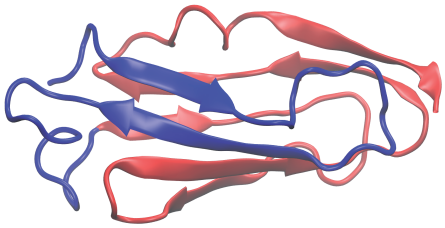

Figure 1.8: Structure of *ddFLN4*. Constant speed AFM single-molecule experiments revealed the existence of a folding and unfolding intermediate state, which is attributed to a stable, ≈ 60 amino acids core segment (red) of *ddFLN4*. The second, smaller segment (≈ 40 amino acids, blue) comprises two β strands. Visualization of PDB file "1KSR" [150].

factor" (VWF). It is naturally present in blood and plays an important role for hemostasis and blood coagulation [151]. To this end, VWF undergoes a forced induced conformational change from a collapsed to a stretched conformation [152–155]. Different measurements of the force response of VWF under different physiologically relevant condition were performed, however lacking measurements at the difficult to achieve low force regime [152, 156, 157].

MT can be used to investigate the interaction of proteins with DNA [32, 53, 158–162]. To this end, a DNA molecule is tethered between the bead and the surface and deviations in the fluctuation as well as length of the DNA tether can be observed upon interaction with specific binding proteins. However, using proteins directly as a tether is difficult to achieve. Issues are mainly caused by unspecific surface interaction of the protein as well as of the beads to the surface, but furthermore specific binding interactions can be blocked, supposedly by the small distance between the bead and the surface. Nevertheless, recent developments made it possible to use proteins directly as tethers between the surface and the bead [27, 52, 141, 163]. This approach can be used to investigate the mechanical properties of proteins with the force range of MT, hence especially at low to medium forces, as well as under force clamp condition with a high spatial and temporal resolution. The design of the MT flow cells enables buffer exchange and hence the exactly same molecules can be investigated under different environments. Furthermore, recent developments towards high speed MT allow to examine short-lived intermediate states. Consequently, MT are able to determine extension values, such as the step sizes but also life times of individual unfolding events as well as their subsequent properties under force clamp condition.

A new approach to tether proteins between the bead and the surface, which utilizes a flexible polypeptide linker, as well as example protein unfolding traces combined with precise length and rate analyzes can be found in chapter 7.

Chapter 2

DNA as a Building Block for Complex Structures

2.1 Introduction

The beginning of "nanotechnology" is difficult to specify, but this field made a big leap forward somewhere in the 1980s [164, 165]. The word "nanotechnology" is not uniquely defined, however common descriptions characterize it as a manipulation of objects with a size below $\approx$ 100 nm in at least one dimension. Different approaches to assemble such small objects are known, mainly divided into bottom-up and top-down methods. While for the latter no direct control at the atomic level is present [166], bottom-up approaches control directly the nanostructure [167]. This can be achieved by different approaches, for example by depositing one atom after the other or by self-assembly methods where the final construct assembles itself from building blocks without external influence [168]. Furthermore, nanotechnology is not limited to a specific field and includes all kinds of different objects from e.g. semiconductor physics, surface science, organic chemistry or biological engineering. The natural size of many biological compounds is in the order of a few nanometers, such as the diameter of DNA [63, 64]. One of the first ideas for using DNA as a building block for nanotechnology was to use DNA molecules as a 3D lattice to arrange proteins in predefined orientations, enabling to gain high resolution X-ray crystallography data [169]. The first attempts of manually defined DNA shapes resulted in symmetric shapes [170, 171]. However, in 2006 a new method, the so called "DNA-origami" was introduced, which is a flexible and customizable procedure to design different nanoscale structures [172]. It allows complex shapes including 2D as well as 3D morphologies with high applicability and compatibility [173–177].

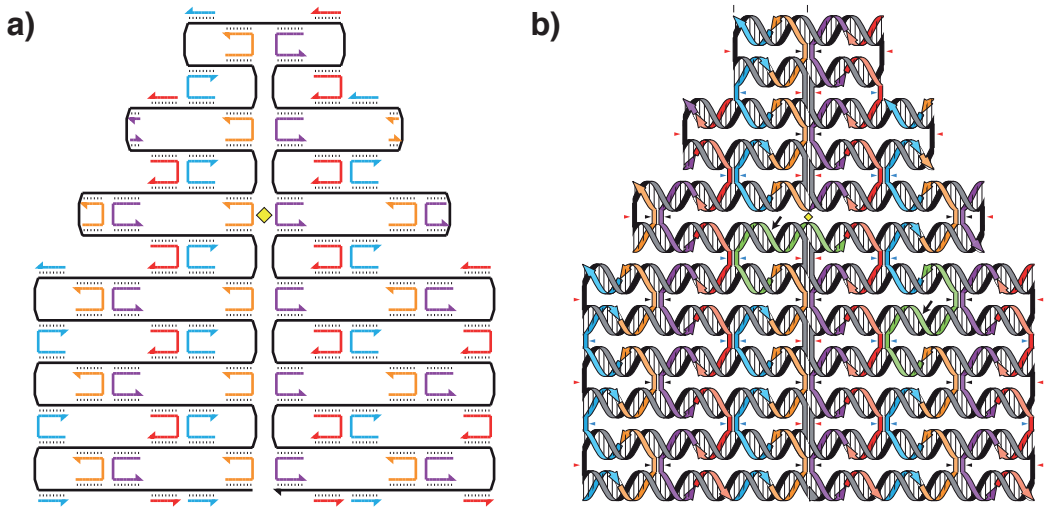

Figure 2.1: Schematic of a self-assembling DNA origami structure. a) Without any external input, one staple strand (short ssDNA oligomer, colored lines) binds to two spatially separated parts of the scaffold strand (long ssDNA, black line) and therefore holding these parts close together. The large number of different staple strands form a 2D or 3D shape of the overall DNA complex. b) Similar to a) with strands drawn as helices. Reprint from Ref. [172] with permission from Springer Nature.

2.2 Self-Assembly DNA Origami

Common self-assembly DNA origamis consist of one long (few kbp) ssDNA scaffold strand as well as many short (e.g. 10 - 60 bp) ssDNA staple strands [178]. Binding of one staple strand to two initially spatially separated parts of the scaffold strand forces the DNA to shrink into a well defined structure (Fig. 2.1). Depending on the selection of staple strands, the same scaffold strand can fold into and form many different shapes. Immobile four-arm branched Holliday junctions allow to link double helical domains [179, 180].
The high specificity of DNA pairing (i.e. base pair binding) enables to produce the DNA origami in one step [181]. Furthermore, as the name "self-assembly" already indicates, apart from the addition of all staple strands as well as a temperature decrease from a high to low annealing temperature, no further external input is needed to form the DNA origamis [181–183]. However, the negative charge of DNA has to be shielded by salt in the buffer to enable successful forming of the origamis and preventing them from falling apart [184].
State-of-the-art DNA origamis can form many different, complex, and asymmetric shapes, reaching sizes of more than 100 nm and a molecular mass in the gigadalton regime [172, 176, 185, 186]. Furthermore, several shape complementary DNA origamis can form even larger DNA origami complexes [176, 187]. Its potential has been already shown in super-resolution microscopy [188], nuclear magnetic resonance spectroscopy (NMR) -based structure analysis of proteins [189], biosensing [190], as a framework for organizing nanomaterials [191, 192], force sensor [24, 174], and more.
DNA origami nanotechnology is a growing field, however also facing some major challenges. Industrial applications, such as drug delivery, would need a large amount of DNA, connected with high costs. Furthermore, to not fall apart, DNA origamis need an unnaturally high amount of salt which is not naturally given in biological environments [193]. However, this problem can be already partly addressed with enveloping PEG-lipid bilayers [194] and oligolysine [193].

A more general approach facing problems of state-of-the-art DNA origamis and increasing its flexibility and application spectrum is to change its basic building principle, e.g. using proteins instead of staple strands to bind different, spatially separated, regions of one long DNA strand [195].
A more physical challenge is to monitor DNA origamis in solution without biases from crystallization or surface effects. Small-angle X-ray scattering (SAXS) is a tool which is able to monitor static DNA origamis in solution and therefore can obtain information about its shape [3], but furthermore time resolved SAXS is able to monitor conformational changes with high temporal resolution (see chapter 3 and 8).

2.3 Example of Static State-of-the-Art DNA Origami Structures and Morphologies

The first DNA origami structures in 2006 formed 2D shapes and were kind of a proof of principle without a direct attributed function (Fig. 2.2 a) [172]. However, further developments led to the first functional DNA origamis, organizing macromolecules in pre-defined geometries [196]. Today, DNA origamis are not limited to 2D structures, but can assemble into a well defined 3D conformation [24, 176, 187, 197, 198]. One common method to build 3D DNA origamis relies on a honeycomb-like structure (Fig. 2.2 b,c) where one single honeycomb can be connected to the next honeycomb and therefore build a robust framework for large structures [176, 197, 199]. Furthermore, a divergence in the number of base pairs of the two connected honeycombs can form well defined global twists [199], increasing the possibilities of 3D DNA origami. Shape-complementary patterns of double helical protrusions and recessions can be used to connect multiple single DNA origamis and form a complex, large, DNA origami based on base-pair stacking [175, 176, 187] (Fig. 2.2 d).

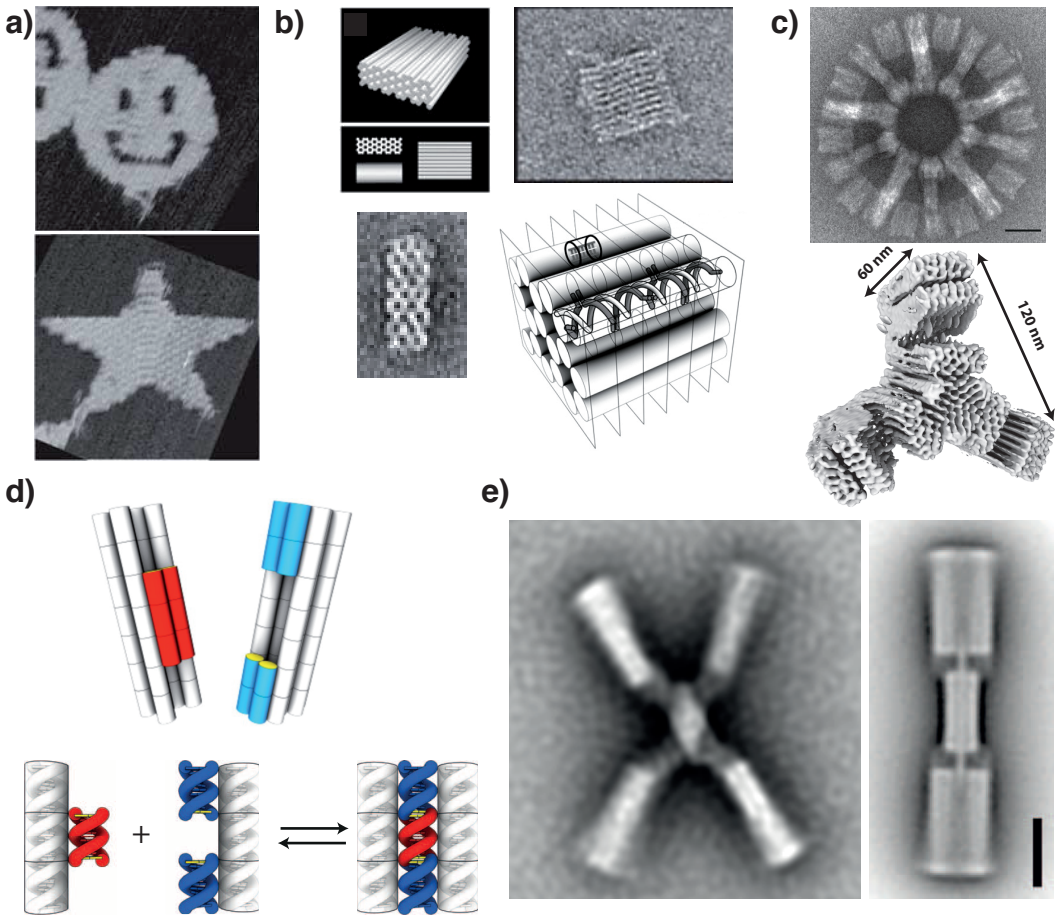

Figure 2.2: Examples of DNA origamis. a) First DNA origamis without a direct application. Reprint from [172] with permission from Springer Nature. b) Honeycomb structure to assemble large 2D and 3D DNA origamis (left top: theoretical structure, right top and left bottom: TEM images, right bottom: Sketch of honeycomb structure). Figure bottom right reprint from Ref [199] with permission from American Association for the Advancement of Science, the others reprints from Ref. [185] with permission from Springer Nature. c) Negative-stained TEM image of a 1.2 GDa polyhedra DNA origami (upper) and cryogenic electron microscopy (Cryo EM) density map of a 3D 61MDa large DNA origami building block. Reprint from Ref. [176] with permission from Springer Nature. d) Sketch of blunt-ended protrusion (red) and recession (blue) principle for building large, multidomain DNA origamis based on base-pair stacking. Reprint from Ref. [182] (upper) with permission from Wiley-VCH GmbH & Co and Ref. [175] (lower) with permission from the American Association for the Advancement of Science. e) Dynamic switchable DNA origami in open (left) and closed (right) configuration (scale bar 20 nm). Reprint from Ref. [175] with permission from the American Association for the Advancement of Science.

2.4 Dynamic State-of-the-Art DNA Origami Structures and Morphologies

As described above, DNA origamis can be produced in many, nearly arbitrary conformation. However, for future applications dynamic DNA origamis might be of interest, e.g. for DNA origami based drug delivery forming a DNA box which can open at the right spot [200]. Thereto, different methods to create dynamical controlled DNA origamis have been developed, which all have in common that they induce a configuration change of the DNA origami triggered by external stimuli.

Addition of ssDNA can trigger a change in the origami shape (by the machanisme of toehold-mediated strand displacement) [201–203] and was used to realize a 3D box which can open one lid [204]. Other design concepts rely on changes in the pH, temperature, ionic strength or external light irradiation. One common approach is the so called "i-motif" [205], which is sensitive to changes in the pH [206] as well as the poly(dG-dC) sequence, which is sensitive to salt concentration and enforces a BZ-transition of the DNA [207], both resulting in a configuration transformation of the DNA origami due to changes in their environment. Furthermore, light irradiation can trigger a transition of the DNA origami structure [208]. DNA origamis labeled with gold-nanoparticles can respond to irradiation and undergo a conformational change [191, 209].

Nevertheless, a new strategy based on base-pair stacking (Fig. 2.2 d) enables not only to build large complex DNA origamis, but also the dynamically control of 2D and 3D shaped DNA origamis [175]. The base-pair stacking interactions are temperature and salt dependent and therefore the protrusion and recession regions of a DNA origami can be bound or unbound [3, 175]. One example is a DNA origami switch (Fig. 2.2 e) which can be in an open or closed configuration, depending on the temperature and salt concentration.

All approaches have in common that they cause a conformational change of the DNA origami, but the time scale of the transition differs significantly. The toehold-mediated strand displacement forces the origami to change its conformation within minutes [201], while the other externally triggered approaches are able to force the change in the shape of the origami within seconds [210, 211]. For base-pair stacking based DNA origamis a detailed description including time resolved small-angle X-ray scattering measurements of a conformational change as well as a dimerization process can be found in chapter 8.

Chapter 3

Small-Angle X-Ray Scattering for Biological Applications

3.1 Introduction

As already described in section 1.3.4, the structure of proteins and other systems is essential for the function of these objects. To gain deeper insights into biological mechanisms it is important to gain detailed information about the structure of biological macromolecules. Furthermore, an accurate understanding of these mechanisms is important to design synthetic objects which can copy, take over, or even improve the function of natural macromolecules. Different approaches exist to gain structural information about biological systems, including indirect methods such as force spectroscopy and direct methods auch as different types of imaging. High resolution structural information with an accuracy of up to a few Ångstroms ($\mathring{A}$) can be obtained for example by nuclear magnetic resonance, X-ray crystallography or cryo-electron microscopy [212, 213]. Furthermore, atomic force microscopy imaging can achieve a resolution of ≈ 1 nm [214]. However, many techniques lack the ability to measure in liquid or otherwise natural environment or are limited by the size of the object.
An alternative approach is small-angle X-ray scattering (SAXS). This solution based method enables to measure biological macromolecules in a broad range of different solutions and buffer conditions while at the same time it is not limited to surface interactions and has no need for crystallization or similar, thus minimizing general biases which can influence measurement results [215]. Furthermore, SAXS is not size-limited and even covers the size range of biological samples up to several giga Dalton. However, since reconstructed SAXS data can in general only achieve a limited spatial resolution, SAXS is often used as a complementary technique to other high resolution methods [216].

3.2 Basic Principles of SAXS

SAXS relies on elastic scattering of photons of an X-ray beam interacting with electrons of the atomic shell of molecules [217]. The pattern of deflected photons is recorded with a camera and saved for further analysis (Fig. 3.1). The molecules are homogeneously diluted and randomly

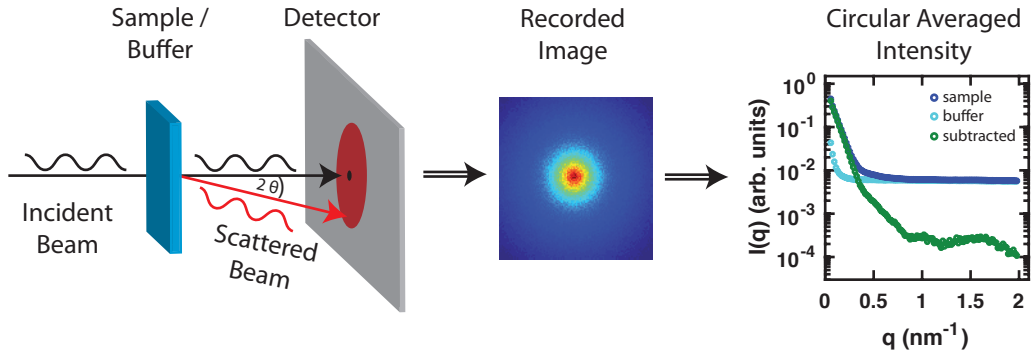

Figure 3.1: Schematic of SAXS experiments. The incident X-ray beam with a wavelength of ≈ 0.5 - 1.5 $\mathring{A}$ scatters elastically with the randomly orientated molecules diluted in buffer. The scattered photons are recorded by a camera and circular averaged, leading to an one dimensional intensity profile as a function of the absolute value of the scattering vector. Measurements are performed for the molecule of interest as well as buffer without the dissolved sample to subtract the buffer profile from the sample profile.

oriented in the buffer. Consequently, the overall scattering profile is radial symmetric and can be circular averaged. Therefore, not one single molecule in one configuration and orientation, but all molecules in all configurations and orientations are averaged. The final output is the scattering intensity as a function of the scattering angle and therefore related to the scattering vector $\vec{q}$. The scattering angle is typically in the range of 0.01°- 2°, where smaller angles are blocked by a beam stop to protect the detector from the direct radiation beam. However, the one-dimensional scattering profile contains information about the three-dimensional structure of the molecules. The monochromatic, collimated X-ray beam can be generated by a laboratory-based setup or by a synchrotron facility. The latter can typically achieve higher flux and therefore a better signal-to-noise ratio [218, 219]. Furthermore, a high flux is needed for fast time resolved SAXS (trSAXS) to enable short measurement times.
To remove the influence of the buffer in the resulting intensity curves as a function of the scattering vector, only buffer without any sample is measured and subtracted from the sample measurement:

$$I(q) = I(q)_{sample} - I(q)_{buffer} \tag{3.1}$$

with $I(q)_{sample}$ the scattering curve of the sample and $I(q)_{buffer}$ the corresponding scattering intensities of the buffer.

3.3 Elastic Photon Scattering

SAXS experiments are based on elastic Rayleigh scattering of photons [220]. The incident X-ray beam with an energy of ≈ 5 – 30 keV [221] stimulates vibration of the electrons of the molecule and thus emission of waves by the electrons with the frequency of the incident beam. The scattered intensity $I_{scattered}$ of one electron at every commonly defined angle 2Θ with the observer placed at $\vec{R}$ can be described by the Thomson formula [222, 223]:

$$I_{scattered}(2\Theta) = \frac{r_e^2}{R^2} \cdot \left(\frac{1 + cos^2(2 \cdot \Theta)}{2}\right) \cdot I_0 \tag{3.2}$$

with r_e^2 the scattering length of a single electron (or classical electron radius) and I_0 the incident beam intensity. The polarization of the photons is described by the expression in brackets, which is approximately 1 for the angular range of SAXS [223]. Therefore, an incident X-ray beam with the wave vector $\vec{k_0}$ is scattered by the electrons of the atom shells of the molecule, changing its direction described by the scattering vector $\vec{q}$ and resulting in the new wave vector $\vec{k'}$ (Fig. 3.2):

$$\mathbf{q} = \mathbf{k'} - \mathbf{k_0} \tag{3.3}$$

with $|\mathbf{k_0}| = |\mathbf{k'}|$ [220]. As already done in formula 3.2, in SAXS experiments it is common to refer to the final scattering angle 2Θ, which corresponds to the angle between $\vec{k_0}$ and $\vec{k'}$.
The scattering vector $\vec{q}$ describes the directional momentum transfer of the photons [215] with the magnitude $q = 4 \cdot \pi/\lambda \cdot sin(\Theta)$ and typically defined and referred in the reciprocal space.

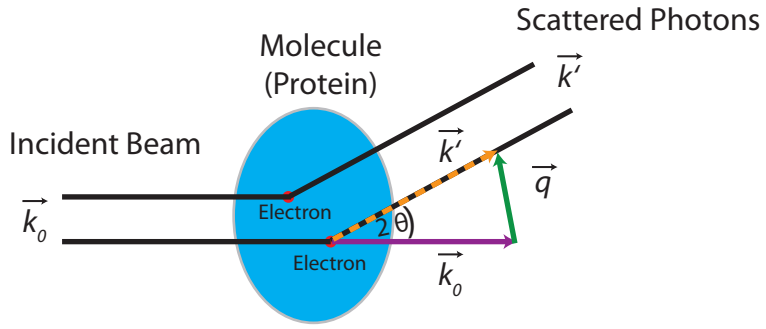

Figure 3.2: Elastic Rayleigh scattering in SAXS experiments. The incident beam scatters elastically at the electrons of the molecule (for clarity only 2 electrons shown). The vibrating electrons emit waves of the frequency of the X-ray beam and described by the Thomson formula with constructive interference for a scattering angle of 2Θ. The momentum transfer between the incident beam and the scattered photons is described by the scattering vector $\vec{q}$ and is the final signal for SAXS experiments. Figure inspired by Ref. [224]

The scattering profile of the whole molecule can be described by the summation of all scattering waves of all electrons. However, the phase has to be taken into account. Therefore, the amplitude $A_j(\mathbf{q})$ of a single particle located at $\vec{r_j}$ is given by:

$$A_j(\mathbf{q}) = f \cdot exp(i \cdot \mathbf{q} \cdot \mathbf{r_j}) \tag{3.4}$$

with f the scattering form factor, hence in general $f = f_e$ for electrons and $f = f_q$ for atoms with f_q the atomic form factor. The exponential takes care of the phase of the photons. For a macromolecule the electrons can be described by a continuous distribution of electrons [220]. Defining the scattering length density $\rho(\mathbf{r})$ corresponding to the electron density $\rho_e(\mathbf{r})$ and f_e:

$$\rho(\mathbf{r}) = f_e \cdot \rho_e(\mathbf{r}) \tag{3.5}$$

the scattering amplitude $A(\mathbf{q})$ can be written as:

$$A(\mathbf{q}) = \sum_j f \cdot exp(i \cdot \mathbf{q} \cdot \mathbf{r_j}) = \int_V \Delta\rho(\mathbf{r}) \cdot exp(i \cdot \mathbf{q} \cdot \mathbf{r}) dV \tag{3.6}$$

with $\Delta\rho(\mathbf{r})$ the excess scattering length density $\Delta\rho(\mathbf{r}) = \rho_{molecule}(\mathbf{r}) - \rho_{solvent}(\mathbf{r})$ [225]. The specific contrast of SAXS experiments is therefore defined by the solvent and molecule and can

be approximately estimated by $\rho_{solvent} \approx 0.33 e^-/\mathring{A}^3$ and $\rho_{molecule} \approx 0.44$ to $0.55\ e^-/\mathring{A}^3$ [215, 226] but can be further reduced by salt, sucrose or similar admixture [224, 227]. A detector for SAXS experiments cannot detect amplitudes but only intensities [217] and therefore the measured intensity is:

$$I(q) = \left\langle |A(\mathbf{q}) \cdot A^*(\mathbf{q})| \right\rangle_\Omega = 4\pi \int_0^\infty r^2 \cdot \gamma(r) \cdot \frac{sin(q \cdot r)}{q \cdot r} \cdot dr \tag{3.7}$$

with the spherically averaged autocorrelation function [217]:

$$\gamma(r) = \left\langle \int \Delta\rho(u) \cdot \Delta\rho(u + r) \cdot du \right\rangle_\omega \tag{3.8}$$

As mentioned above, the molecules can be independent in every orientation during the measurement and therefore $\langle\rangle_\Omega$ represents the averaging over all orientations.
It should be noted that the intensity drops off rapidly for high q values resulting in only a small difference between the sample and the buffer signal and thus into a decrease of the signal-to-noise ratio for an increase of q values (Fig. 3.1).

3.4 Influences on and Pre-Selection of SAXS Data

The signal of SAXS experiments can be influenced by several different reasons which are normally undesired and disturb unbiased measurement results. The total intensity depends on the concentration of the molecules, but also radiation damage has to be taken into account. Both effects can lead to inter particle interaction which can be misinterpreted resulting in incorrect conclusions.

3.4.1 Radiation Damage

Radiation damage in SAXS experiments be caused by direct bond breaking within the molecule while interacting with the X-ray beam, or more prominent due to formation of free radicals (e.g. HO_2^-) in the buffer by photolysis [228]. The free radicals can attach to the biological sample, such as proteins and DNA molecules [229]. However, the impact on DNA is in general less crucial than for proteins [230]. Radiation damage can induce irreversible aggregation of the molecules and hence an increase in the intensity especially for small values of $\vec{q}$, but also unfolding of the protein or fragmentation of the sample. A change in the signal for an expected to be otherwise stable sample is a sign for radiation damage (Fig. 3.3 a), however difficult to distinguish from actual biological transitions in trSAXS experiments.
The probability of radiation damage is related to the absorbed dose of the sample [231]:

$$D = \frac{\Phi \cdot t \cdot A_{abs} \cdot E_{ph}}{\rho \cdot l} \tag{3.9}$$

with Φ the photon flux density of the incident beam, t the time the sample is exposed to the radiation, A_{abs} the fraction of absorbed energy, E_{ph} the energy of a single photon, ρ the sample density and l the length penetrated by the X-ray beam. As mentioned above, the impact of radiation depends on the sample. Regarding typical settings of the X-ray beam of a synchrotron, thus a photon energy of $10 - 12$ keV, an X-ray flux of $\approx 10^{12}$ ph s^{-1} and a beam

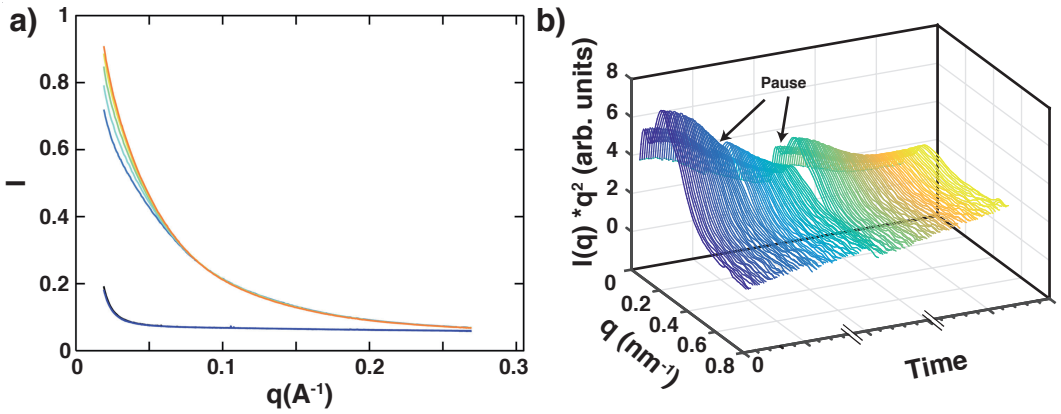

Figure 3.3: Radiation Damage of biological samples in intensity profiles. a) Radiation damage of a static 24-bp DNA duplex at five subsequent 1.0 s exposed time frames and corresponding buffer profiles (bottom curves, black and dark blue). A change at low q values is clearly visible. Figure adapted from Ref. [230] with permission from Springer Nature. b) Radiation damage in Kratky representation of a DNA origami switch construct. The sample was repeatedly exposed within a few seconds followed by a long pause and another phase of repeated exposure as marked in the figure. A decrease in intensity for the DNA origami construct can be observed.

size of $\approx 0.5 \times 0.5\ mm^2$, the dose limit before radiation damage becomes dominant varies from several hundred to several kilo Gray [231].
However, two effects reduce the accuracy of formula 3.9 and have to be taken into account for a precise dose calculation. During the finite measurement time, macromolecules can diffuse into as well as out of the exposed area. Therefore, the effective exposed area increases and hence the effective dose of the sample will be reduced. Furthermore, the beam shape is not a square with the same intensity at every point, but better approximated by a gaussian profile, exerting a higher dose at the center and less at the edges of the exposed area [231]. These effects have to be considered while calculating the exact dose for the measurement [228, 229, 231, 232]. One way to identify the maximum dose without radiation damage is to consecutively expose the sample and compare the single scattering curves for divergence.
An increase of the dead time between different frames can reduce radiation damage but is only feasible to a limited extent for fast trSAXS measurements (Fig. 3.3 b). Another approach to reduce radiation damage is to reduce free radicals by addition of radical scavengers to the buffer. However, side effects, such as a reduction of the signal-to-noise ratio or effects on the sample have to be considered carefully [230, 233, 234]. Furthermore, a flow-through capillary, which keeps the sample in flow while only a small part at fixed position is illuminated, reduces radiation damage of the measurement. Finally, radiation damage also depends on the concentration of the sample and can be reduced finding the optimal concentration. Nevertheless, software tools to evaluate radiation damage are commonly used and can automatically detect radiation damage [232, 235].

3.4.2 Influence of Concentration

To obtain a good signal-to-noise ratio, SAXS experiments with biological samples need a high concentration in the order of ≈ 5 mg/ml. However, a high concentration can cause inter-particle interaction or sample aggregation. Due to the higher molecular weight of aggregates, latter can

be observed by an increase of the intensity at low q values. A too low sample concentration results in a bad signal-to-noise ratio especially at high q values. Therefore, it can be useful to measure a dilution series of different sample concentrations and assemble different q ranges from different sample concentrations. However, in many cases it is sufficient to determine an optimal concentration where the signal-to-noise ratio is sufficiently good in every q range and no aggregation or inter-particle interactions are observed.
Different approaches have been established to detect aggregation and inter-particle interaction. The increase in signal at low q values due to aggregation or attractive inter-particle interactions can be detected by a Guinier analysis (section 3.5.1). In contrast, repulsive inter-particle interaction results in a decrease at low q value and can be identified by the structure factor [224]. Combination of theory and experiments, such as a extrapolation of a dilution series, can be used to compensate these effects [236–238]. Alternatively, different environments can reduce inter-particle interaction, such as the pH or salt concentration of the buffer changing the electrostatic behavior of the sample or screening potential of electrostatic interactions of the buffer, respectively.
The absolute values of SAXS scattering profiles are in general dependent on the concentration of the sample and can be normalized by the forward scattering intensity *I(0)* (see section 3.5.1).

3.5 Basic and Overall Structural Parameter Analysis

SAXS can deliver information about the overall structure of a macromolecule, including the molecular weight, radius of gyration, electron density distribution as well as maximum intramolecular distance [239]. These parameters can be used to gain more information about the system, detect (also time resolved) conformational changes, but also as a check if the scattering curves are consistent with known parameters and therefore as a test for quality and systematic errors of the measurement.

3.5.1 Guinier Analysis for Structural Information

The lowest q values, i.e. the forward scattering, give information about the mass distribution and are associated with the radius of gyration R_g. "It is defined as the root-mean-squared distance of all elemental scattering volumes from their centre of mass weighted by their scattering densities" [236]. Therefore, macromolecules with the same total volume can have different R_g values, so that the radius of gyration can provide information about conformational changes during consecutive measurements. It can be obtained by a Guinier-approximation [240] within a range of $q \cdot R_g < 1.3$ [223]. Its derivation is based on a power series expansion of *sin(qr)/qr* of equation 3.7:

$$\frac{sin(q \cdot r)}{q \cdot r} = 1 - \frac{(q \cdot r)^2}{3!} + \frac{(q \cdot r)^4}{5!} - O((q \cdot r)^6) \tag{3.10}$$

This equation can be further simplified and rewritten as [217, 240]:

$$I(q) = I(0) \cdot \left(1 - \frac{q^2 \cdot R_g^2}{3} + O(q^4)\right) \tag{3.11}$$

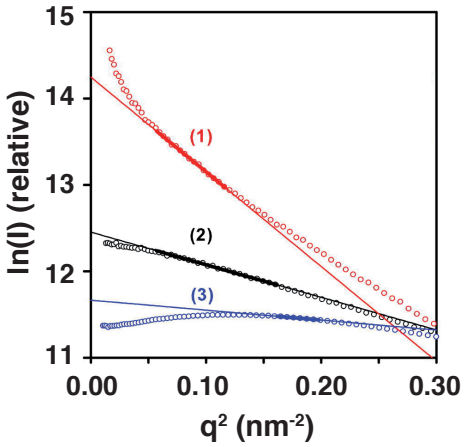

Figure 3.4: Guinier approximation for small q values. The slope of a linear fit of the natural logarithm of I as a function of q^2 yields the radius of gyration as well as the molecular weight. Furthermore, a deviation of the fit indicates aggregation (1), good data (2) and inter-particle repulsion (3). Reprint from Ref. [242] with permission from Elsevier.

and finally transformed into [224]:

$$I(q) \approx I(0) \cdot exp\left(-\frac{q^2 \cdot R_g^2}{3}\right) \tag{3.12}$$

The exponential function can be directly fitted to the intensity profile. However, in practice it can be useful to perform a linear fit to the natural logarithm of the scatting profile as a function of q^2. Nevertheless, in both cases the permitted range of $q \cdot R_g < 1.3$ should not be exceeded. From the fit, the forward scattering at zero angle can be extrapolated. The goodness of the fit is related to the amount of aggregation and/or inter-particle interaction. Aggregation can be seen by a deviation to higher, repulsion by a deviation to lower intensity values compared to the Guinier fit at the lowest q values (Fig. 3.4).
Moreover, the molecular weight of a monodisperse sample can be determined by:

$$I(0) = \kappa \cdot c \cdot (\Delta\rho)^2 \cdot (MW)^2 \tag{3.13}$$

with κ a setup specific proportionality constant which has to be determined by another experiment (e.g. using a molecule with known molecular weight), c the concentration of the sample and MW the (unknown) molecular weight [241].

3.5.2 Representation of SAXS Data in Reciprocal Space

Scattering profiles can be represented in different ways, commonly as $I(q)$, $I(q) \cdot q$ (Holtzer representation) and $I(q) \cdot q^2$ (Fig. 3.5 a). The last one, as a linear function of q, is known as the Kratky representation [243, 244]. For a folded protein, the Kratky representation exhibits a peak followed by a decay induced by an intensity drop of q^{-4} towards higher q values. However, an unfolded or randomly coiled molecule has a slower intensity decay of q^{-2} resulting in a plateau in the lower q-range followed by a linear increase in Kratky representation (Fig. 3.5 b) [244, 245].

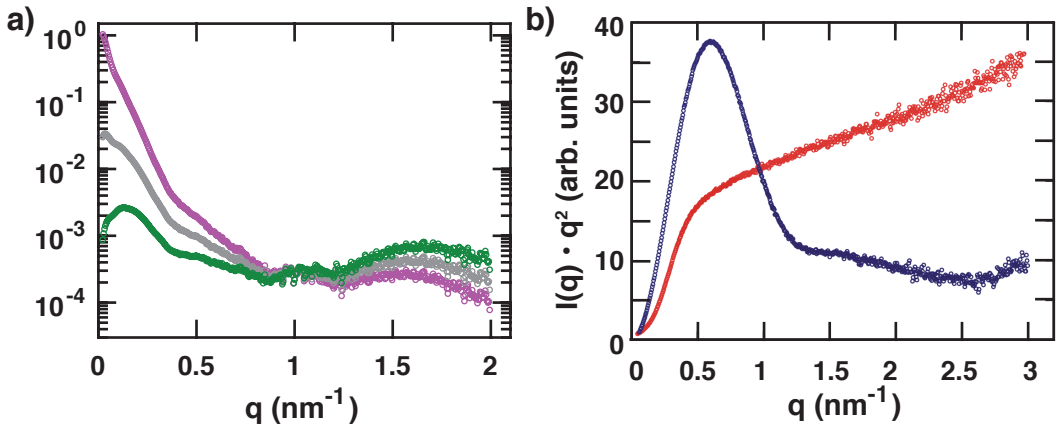

Figure 3.5: a) Different representations of the same scattering data. Purple *I(q)*, gray $I(q)\cdot q$ (Holtzer representation), green $I(q) \cdot q^2$ (Kratky representation). b) Kratky plot of a folded protein (blue) and elongated polypeptide (red). For a compact protein a bell shaped part of the scattering curve is followed by a decay at higher q values, whereas an elongated polypeptide does not exhibit a bell shape and increases linearly at and for higher q values. Figure b) reprint from Ref. [246].

3.5.3 Representation of SAXS Data in Real Space

The raw scattering signal for SAXS experiments is the scattering vector $\vec{q}$ and hence the data are represented in reciprocal space. However, with mathematical operations it is possible to transform the data into real space. As basic principle a Fourier transformation of the q dependent scattering intensities is used to obtain the pair distance distribution function *P(r)* in real space [224]. It represents the distance distribution between particles of the macromolecule weighted by their excess electron density (Fig. 3.6) [217, 224]:

$$P(r) = \frac{r^2}{2 \cdot \pi^2} \int_0^\infty I(q) \frac{sin(q \cdot r)}{q \cdot r} \cdot q^2 \cdot dq \tag{3.14}$$

However, this theoretical approach is unfeasible by the achievable, limited q range of SAXS measurements [217]. Alternatively, several approaches based on indirect Fourier transformation were developed to obtain scattering profiles in real space [247–249]. The indirect inverse Fourier transformation uses r instead of q as integration variable and therefore is capable to avoid the infinity of the integral limiting it to the maximum distance between two particle D_{max} [247]:

$$I(q) = 4 \cdot \pi \int_0^{D_{max}} P(r) \cdot \frac{sin(q \cdot r)}{q \cdot r} \cdot dr \tag{3.15}$$

with

$$P(r) = \sum_{n=0}^{N} c_n \cdot \phi_n(r) \tag{3.16}$$

Hence, *P(r)* is approximated by a limited number (N) of functions $\phi_n(r)$ and coefficients c_n in the range of $0 \leq r \leq D_{max}$. The different coefficients c_n are obtained by a fit of equation 3.15 to experimental data.

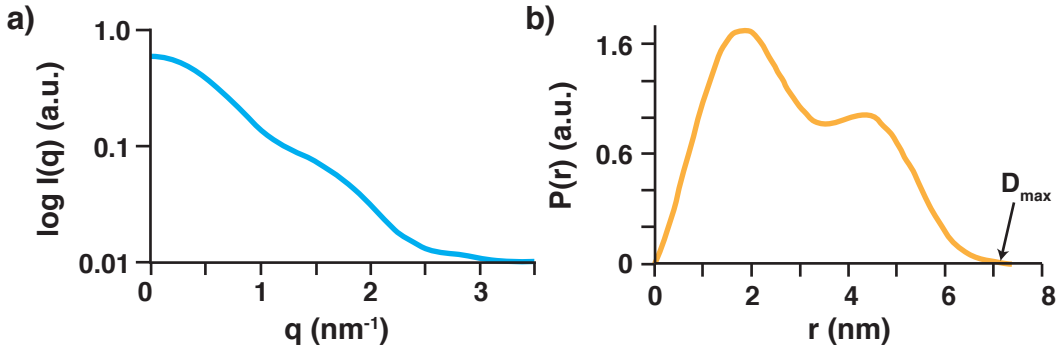

Figure 3.6: Comparison of reciprocal and real space representation. a) Scattering data in reciprocal space. b) Same data projected into real space via indirect inverse Fourier transformation. Reprint from Ref. [250] with permission from Springer Nature.

3.6 Scattering Profile Simulation and Shape Reconstruction

SAXS scattering profiles can be predicted from atomistic structures by different mathematical approaches. Therefore, the scattering curve of the measured macromolecule can be compared with the theoretically predicted one and deviations can be analyzed. Furthermore, shape reconstruction can be used to determine the shape of the molecule from SAXS experiments. Nevertheless, high resolution data from other methods are commonly necessary to extract one single solution for the SAXS reconstruction, while at the same time verifying the high resolution data.

3.6.1 Computation of Theoretical Scattering Profiles

To evaluate SAXS measurements, it can be useful to predict the scattering profiles. This can help to assign conformational states or similar, for example to distinguish between folded and unfolded proteins, but also known atomistic models of macromolecules can be verified by SAXS. Computational approaches to predict the scattering rely on the atomistic models saved in Protein Data Bank (PDB) files or similar formats. To determine a precise intensity profile, it is not sufficient to only calculate the scattering of the molecule of interest, but also of the solvent [224]. Common approaches calculate the scattering profile of the particle in vacuum as well as the scattering intensity of the excluded volume, assimilable to a buffer subtraction. Furthermore, special attention has to be payed to the hydration shell around the macromolecule [251]. Here the water molecules are more ordered and packed with higher density, commonly for proteins in the range of 1.05 - 1.20 times compared to the rest of the solvent [215, 252], and even more for highly charged particles, such as DNA [253]. Consequently, the scattering intensity of the area close to the molecule of interest differs from the rest of the solvent. Depending on the macromolecule the hydration shell can have a non-uniform electron density [253, 254]. Furthermore, an ion atmosphere around charged macromolecules has an impact on the scattering signal and is difficult to exactly predict because of its dynamics and range regulated by the ion species [255, 256].
Different software packages are available to calculate the scattering profiles varying in their

mathematical approaches [251, 257]. One of them is based on spherical harmonics expansion using spherical Bessel functions, the atomic form factor and spherical harmonics of different orders to calculate the I(q) vs. q scattering plot [251]. This computationally fast approach is however of limited use for complex structures, such as macromolecules with internal cavities [258], e.g. complex 3D DNA origami structures. One alternative approach is based on the Debye formula leading to a precise result at the expense of computational speed [257].
However, for direct comparison with experimental data, both approaches need to be fitted to the measurement intensity profile while minimizing the reduced chi-squared (X^2) with a scale factor.

3.6.2 Shape and Morphology Reconstruction

One dimensional scattering curves can be used to reconstruct the three dimensional shape of the macromolecule. Two different basic approaches exist, one without any further input (*ab initio* [215, 259]) while the other one relies on external input (*hybrid approach*). Modern versions of *ab initio* shape reconstruction use closely packed finite-volume elements, such as dummy beads, that fill the simulated area. Every single volume element can be attributed to either the solvent or the macromolecule [260–264]. An optimization algorithm determines the best overlap of the theoretical scattering profile of the dummy finite-volume elements with the experimental intensity curve. However, in general not only one single solution fits the experimental data, resulting in a pool of possible 3D shapes of the molecule (Fig. 3.7) [265, 266]. Furthermore, these volume elements do not directly represent the atomistic structure, but only the overall structure of the molecule.
The *hybrid approach* of shape reconstruction does not only use the one dimensional SAXS scattering profile, but also known structures determined previously with different methods. For many large and/or flexible proteins as well as partly unfolded proteins, high resolution data are difficult to obtain and often limited to (small) specific regions of the whole molecule. SAXS experiments can help to combine these known structures. Several approaches have been developed to combine scattering curves with known atomistic models, such as normal mode analysis, elastic network models and rigid-body modeling [215, 266–268].
For both *ab initio* and *hybrid approaches* different software is available [261, 263, 269].

Figure 3.7: *Ab initio* 3D shape reconstruction of "Thermus flavus 5 S rRNA". a) Five independent reconstructions of the same SAXS scattering curve. The final results of every individual reconstructions are not exactly similar and therefore do not (perfectly) overlap. b) Superposition of ten individual reconstructions. Reprint from Ref. [265] with permission from the American Society for Biochemistry and Molecular Biology.

3.6.3 Biological Relevance of SAXS Scattering Profile Prediction, 3D Shape Reconstruction and Combination with High Resolution Techniques

One challenge of many high resolution techniques, such as electron microscopy, NMR and X-ray crystallography, is to determine an atomistic structure in physiologically environments, hence in its natural conformation. Furthermore, especially flexible or intrinsically disordered domains of proteins can be unnaturally shifted into one configuration by freezing or crystallization. In contrast, SAXS determines low resolution structure in solution and therefore is able to validate atomistic models of structural configurations [215, 270, 271]. Hence, SAXS extends high resolution methods by combining existing atomistic models with additional low resolution data, which can include details about flexible parts of a macromolecule and therefore contains more information about its biological function [243, 271]. Furthermore, dynamic structures, e.g. a switchable DNA origami, can benefit from a combination of these different approaches. For example a theoretical atomistic model can be compared to another atomistic model reconstructed from high resolution data and its morphology in solution can be verified by SAXS measurements. Furthermore, SAXS allows to reconstruct an ensemble of different configurations in solution [3], e.g. with a mathematical decomposition of the scattering data in its characteristic functions (Single-Value-Decomposition [272, 273]), but even beyond, transitions in solution can be monitored in a time resolved manner (see chapter 8).

3.7 Synchrotron based SAXS

SAXS experiments require a high flux and brilliance of X-ray photons (see also section 3.7.1). The currently most common source for such X-rays are synchrotron storage rings, where electrons are forced on curved trajectories and therefore emit X-ray radiation [220, 274]. Modern synchrotrons belong to the third generation of synchrotron light sources and differ from the first and second generation by a significantly higher brilliance. However, free electron lasers (FEL) are assigned to be the fourth generation of X-ray sources and already introduced and entering service. Nevertheless, FEL are until now not commonly used for biological SAXS experiments and still wait to become a standard for different measurement types [220, 275] (Fig. 3.8).

The exact implementation of a synchrotron source is very complicated, however in brief: Electrons are first accelerated by a linear accelerator (LINAC) and brought to even higher energies of several giga electron volts by a booster ring (Fig. 3.9) [276]. Afterwards, the relativistic electrons are injected into an evacuated storage tube where bending magnets keep the electrons in a closed, overall circular ring which also contains straight sections [220]. As for all charged particles, a change in its trajectory results in photon emission and therefore the particle looses energy. This energy difference is compensated by radio frequency supplies. Besides the bending magnets, other magnet configurations such as the so called “undulator” (labeled in Fig. 3.9 with the more general name “insertion device”) can perform a curved acceleration of the electrons resulting in X-ray photons, as further discussed in section 3.7.2. The emitted, straightforward traveling photons leave the electron storage ring, are focused by several optic devices and finally arrive at the experimental hutch to interact with the sample. Among others, the optical part include lenses, mirrors and a monochromator (section 3.8) and

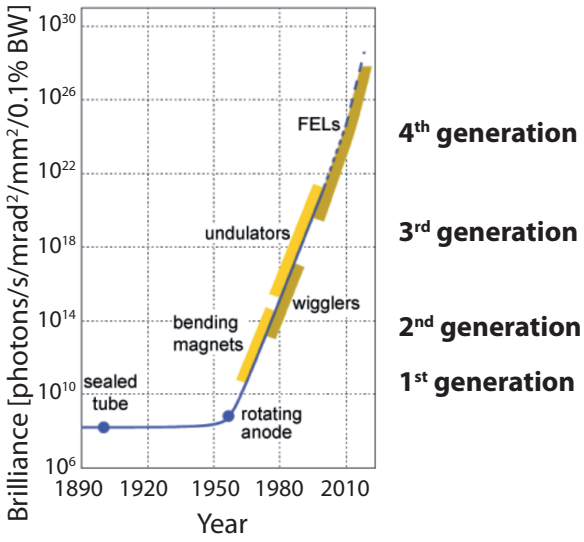

Figure 3.8: Different generation of synchrotron sources. Most common synchrotrons used for SAXS experiments are 3^{rd} generation synchrotrons. Reprint from Ref. [276] with permission from John Wiley and Sons.

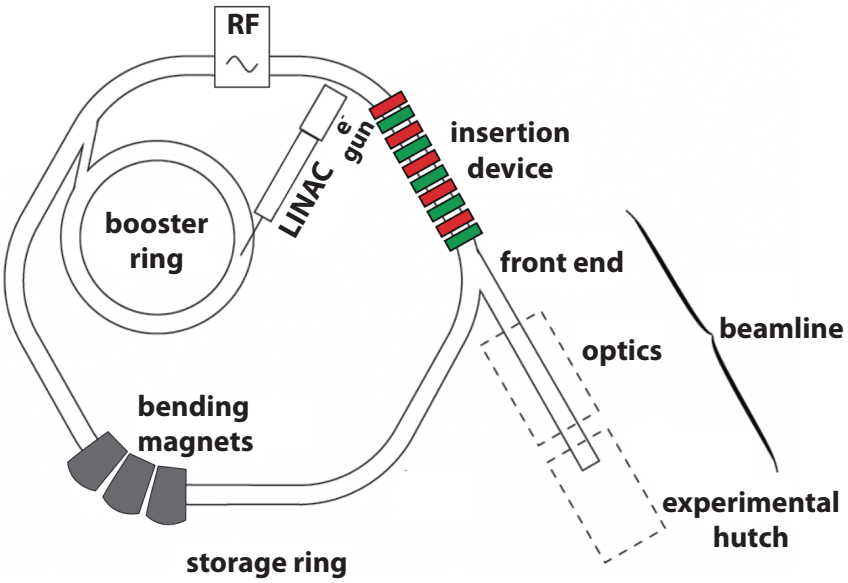

Figure 3.9: Illustration of the main parts of a synchrotron. The electrons are linearly accelerated in the LINAC device and afterwards brought to even higher energies in the booster ring. Electrons with the right energy are injected into the storage ring where bending magnets keep them on a closed orbit. Curved acceleration by bending magnets or magnets of an insertion device force the charged particles to emit radiation. Optics close to the synchrotron focus and fine tune the X-ray beam and deliver the photons to the sample in the experimental hutch. Reprint from Ref. [276] with permission from John Wiley and Sons.

is able to deliver a high intensity X-ray beam, which can be controlled to a certain extent in energy, beam-size, bandwidth and flux. However, mainly the energy and number of electrons in the storage ring set limits of the tunable range [276].

3.7.1 Quality of the X-Ray Photon Source (Brilliance)

The quality and potential of an X-ray source depends on many different physical properties such as the amount of photons per second as well as the final diameter the X-ray beam can be focused [277]. Furthermore, bending magnets as well as undulators have a natural divergence in their emission direction [220]:

$$\Theta = \frac{m_0 \cdot c^2}{E_e} = \gamma^{-1} \tag{3.17}$$

with the opening angle of the emission cone Θ, m_0 the electron rest mass, c the speed of light and E_e the (relativistic) energy of the electrons, summarized in the Lorentz factor γ. Another property which influences the quality of the X-ray beam is the bandwidth of the emission spectrum.
These aspects are summarized in the "brilliance" which is a single value describing the quality of an X-ray source [276]:

$$Brilliance = \frac{photons/second}{(mrad)^2 \cdot (mm^2\ source\ area) \cdot (0.1\%\ bandwidth)} \tag{3.18}$$

Hence it is easy to compare different synchrotron facilities as well as other X-ray sources. In general, a higher value for the brilliance is favored.

3.7.2 Magnet Configuration

Synchrotron facilities can have different magnet configurations to produce the X-ray beam. These magnet configurations include bending magnets, wigglers and undulators (Fig. 3.10). In general, these different configurations of magnets are able to achieve different maximum values of brilliance. Regarding chapter 8, measurements were only performed with bending magnets and an undulator, hence only these two configuration are discussed in detail.

Bending Magnets

Bending magnets are naturally installed in synchrotrons to keep the relativistic electrons in a closed orbit. However, the curved acceleration of the electrons by the magnets cause radiation in form of X-ray photons [276]. The X-ray beam is emitted tangentially to the electron trajectory and consists of a continuous energy spectrum (Fig. 3.11 a). It can be described by the characteristic energy E_C which divides the radiation power in two halves, one consisting of only higher, the other one of only lower energies compared to E_C (Fig. 3.11 a). The characteristic energy depends on the synchrotron properties and can be calculated by [276]:

$$E_C[keV] = 0.665 \cdot E^2[GeV] \cdot B[T] \tag{3.19}$$

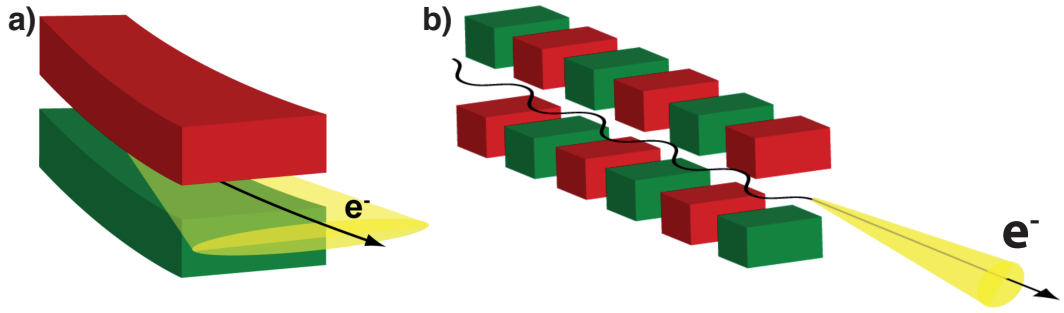

Figure 3.10: Different magnet configurations used at a synchrotron. a) Bending magnets deliver a broad energy spectrum with a relatively high divergence in its emission cone. b) In an underlator the electrons oscillate because of the many alternating magnets, producing a highly monochromatic beam with a small angle of divergence. Reprint from Ref. [276] with permission from John Wiley and Sons.

with the energy E of the electrons in the storage ring and B the magnetic field of the bending magnet.
Bending magnet radiation is linearly polarized when observed in the electron storage plane and elliptically polarized otherwise [278].

Insertion Devices

Insertion devices implemented into the straight sections of the electron storage ring allow for a second method to obtain an X-ray beam. In general, two different design concepts, wigglers and undulators, are common. However, here only the undulator will be discussed. In undulators consecutive magnets are placed in a row with alternating orientations and therefore complementary magnetic fields force the electrons on an oscillating trajectory. The electrons emit photons while passing every single magnet. Particular wavelengths as well as its harmonics n are able to constructively interfere, leading to a more discrete energy spectrum (Fig. 3.11 b) with the energies [276, 279]:

$$E_n[keV] = 0.95 \cdot \frac{n \cdot E^2[GeV]}{(1 + \frac{K^2}{2}) \cdot \lambda_u[cm]} \tag{3.20}$$

with the total particle energy E, the period of oscillation λ_u and a dimensionless parameter K which reflects the properties of the undulator including the maximum magnetic field B_{max} [220]:

$$K = \frac{e \cdot B_{max}}{m_0 \cdot c \cdot k_u} \tag{3.21}$$

where

$$k_u = \frac{2 \cdot \pi}{\lambda_u} \tag{3.22}$$

Here, the direction of observation is assumed to be on axis, otherwise a correction factor of $(\gamma \cdot \Theta)^2$ with the observation angle Θ has to be included in equation 3.20 [220]. The relatively small magnetic fields in undulators result in a value for K smaller than 1 [220, 224].
Undulators have the advantage of a higher flux and brilliance compared to bending magnets (Fig. 3.11 c). The interference of the photons produces a highly (but not perfectly) monochromatic

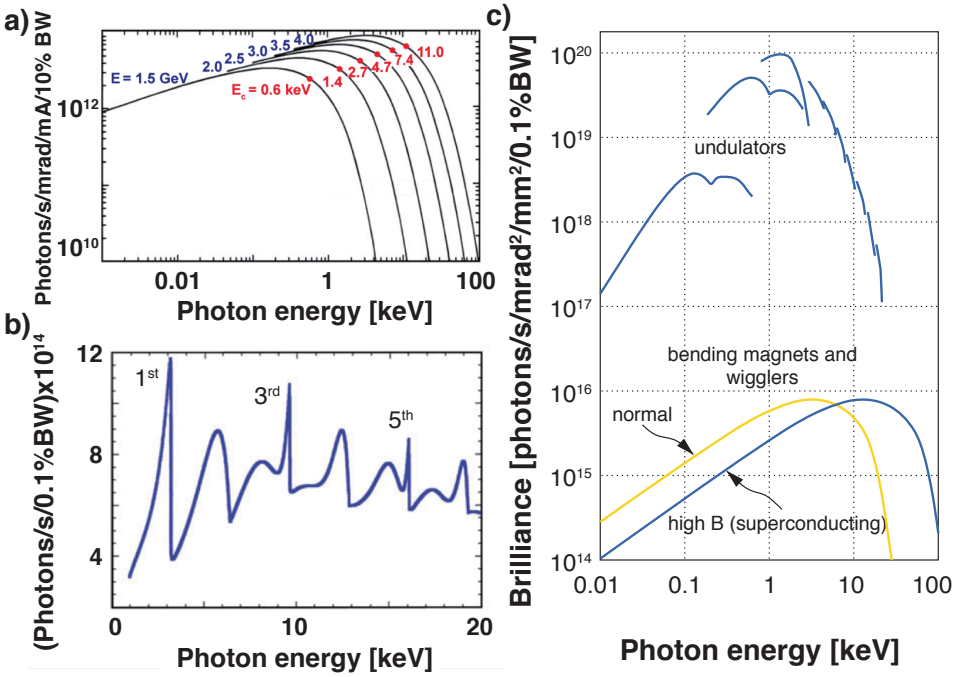

Figure 3.11: Different emission spectra of bending magnets and undulators. a) Energy spectra of bending magnets at different electron energies (blue) and their characteristic energy (red). For every energy the spectra is broad ranged. b) Photon energy of an undulator at the Advanced Photon Source of Illinois at 7 GeV and 100 mA. The undulator is optimized for the 1^{st}, 3^{rd} and 5^{th} radiation harmonics. c) Brilliance of different kinds of magnet configurations used in modern synchrotron facilities. a) and b) reprinted from Ref. [278] with permission from Springer Nature, c) from Ref. [276] with permission from John Wiley and Sons.

radiation. The angle of the radiation cone scales with the number N of periods in the undulator by a factor of $1/\sqrt{N}$ [220]. Furthermore, the polarization of an undulator can be controlled by shifting the relative magnet pole's position, resulting in either linear or circular polarization.

3.8 Monochromator

Undulators produce a quite monochromatic X-ray beam, however for bending magnets and undulators a monochromator is used to generate a more monochromatic beam. Since SAXS measures the intensity of every scattering vector q, which itself depends on the wavelength λ of the photons according to $q = 4 \cdot \pi \cdot sin(\Theta/\lambda)$, a broadened X-ray beam causes a smearing of the scattering curve. Monochromators made of crystals are able to achieve a highly monochromatic X-ray beam [280] based on Bragg's law [281]:

$$m \cdot \lambda = 2 \cdot d \cdot sin(\Theta) \tag{3.23}$$

with m a positive integer, d the distance between lattice planes and Θ the angle of incidence (Fig. 3.12 a). Commonly two crystals separated by a defined distance D are used (Fig. 3.12 b) to achieve a resolution of $\Delta E/E \leq 10^{-10}$ [276, 280]. Rotation of the crystal device changes the angle of incidence and therefore the wavelength(s) which fulfill the Bragg condition [276].

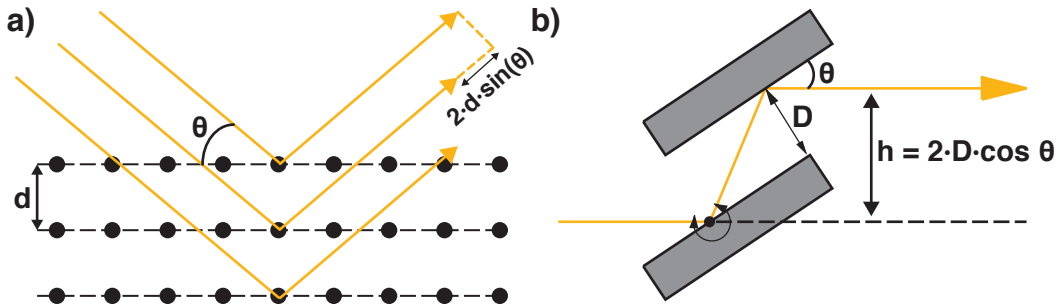

Figure 3.12: Monochromator based on Bragg's law. a) For the same angle of incidence and emergent angle only wavelengths with a phase difference of $n \cdot d \cdot sin(\Theta)$ interfere constructively and therefore produce sharp peaks of wavelengths. b) Commonly used two-crystal-monochromator to obtain a sharp peak of the favored wavelength for SAXS measurements. Figure inspired by [280] and further modified by Thomas Zettl (Ref. [282]).

3.9 Example of Biological SAXS Beamlines

In chapter 8 measurements were performed at two different synchrotron facilities, the ESRF in Grenoble (France) and the DESY in Hamburg (Germany). Beamline "BM29" [283] at the ESRF uses a bending magnet, while beamline "ID02" [284] at the ESRF and "P12" [285] at the DESY generate photons with undulators. The wavelength at all three beamlines is in the order of Ångstroms. The current of the corresponding synchrotron facilities is ≈ 100 mA. At all three beamlines, for static measurements a sample volume of ≈ 30 μl is necessary. However, time resolved measurements at the ID02 need a sample volume in the order of 100 μl. All three beamlines are able to change the temperature of the sample by simple heating of the stage controlled by a software. BM29 and P12 have the possibility to use an automatic sample loader, allowing to prepare many different samples and measuring one after the other without any need of the experimentalist to enter the measurement room ("hutch"). Furthermore, the software detects automatically when the sample is in the right spot to exposure and is able to measure at one position or slowly move the sample to measure at different positions, thus reducing radiation damage. Table 3.1 gives an overview with more details about these three beamlines. In addition, more details about the specific properties of the beamlines can be found in Ref. [283] and [285] for beamline BM29 and P12, respectively, and in Ref. [284, 286, 287] for beamline ID02, as well as their corresponding websites.

Table 3.1: Properties of selected beamlines (P12, BM29, ID02) at two synchrotron facilities (DESY and ESRF). If possible, data for P12, BM29 and ID02 taken from Ref. [285], [283] and [286], respectively. Missing data were filled with information from their corresponding websites. In some cases newer information from the website is used. To achieve all properties, temporary reconstruction (e.g. different sample-detector distance) might be required. Values in brackets are standard / default values for that beamline. Note: The flux is dependent on the current of the synchrotron and therefore only given for default values.

Property	P12	BM29	ID02
Energy (keV)	4.0 - 20.0 (10.0)	7.0 - 15.0 (12.5)	8 - 17 keV (12.4)
Maximum flux (Photons/s)	$\approx 10^{13}$	$\approx 10^{13}$	$\approx 10^{13}$
Beam size (mm × mm)	0.2 × 0.12	(0.5 × 0.5 to 0.7 × 0.7)	min: 0.05 × 0.02 (0.3 × 0.8)
q-range (nm^{-1})	0.006 - 16 (0.02 - 4.5)	0.02 - 6	0.001 - 50
Typical exposure time (s)	$\approx$ 1 (min: 0.03)	$\approx$ 1	$\approx$ 1 (min < 0.001)

3.10 Time-Resolved SAXS Experiments

SAXS is widely used to measure static samples that do not change their configuration over time, mainly due to the low contrast of biological samples as well as their fast kinetics [284]. However, the high flux and brilliance of modern synchrotron facilities as well as the fast readout times of state-of-the-art detectors allow short acquisition times combined with short dead times between the consecutive frames. Therefore, transitions in the range of milliseconds can be observed in a time resolved fashion [284]. In general, conformational changes can occur due to any external influences, such as a change in temperature, addition of binding partner(s) or environmental changes such as the pH or salt concentration. Depending on the system of interest, the limiting factor for the time resolution is not necessarily defined by the X-ray beam but the time it needs to externally trigger and influence the sample and hence the dead time before the first frame [284, 288, 289]. Pump-probe based methods can achieve measurements in the picosecond range, while applications relying on mechanical mixing of two solutions are in general slower. Continuous-flow and stopped-flow mixer are used at SAXS beamlines to mechanically mix two fluids rapidly. While continuous-flow mixer have a shorter dead time before the first measurement point ($< ms$) and the ability to perform many measurements at the same time point, a higher amount of sample is needed [289]. However, very often biological samples are expensive or difficult to obtain, limiting the maximum amount. Microfluidics reducing the total amount of liquid and hence sample suffer from a longer dead time due to the absence of turbulent flow [290–293]. A stopped-flow mixer can be used to minimize the sample volume while having a dead time of typically a few milliseconds [284].
Stopped-flow mixing relies on the turbulent mixing of two liquids [294, 295]. Two pneumatic driven pumps forward the two fluids into a turbulent mixer, where the liquid is mixed for $\approx 10 - 100\ \mu s$ [284] and further transported to the observation chamber (Fig. 3.13). This transportation after mixing causes the main dead time of a few milliseconds before the first frame can be recorded. However, a positive side effect of this transfer including its time delay is a higher quality of mixing due to diffusion and consequently a more homogeneous mixture. In general, the quality of the mixture of a stopped-flow device can be characterized by fluorescence or if possible by a SAXS pattern of a well characterized sample. The mixing quality depends on

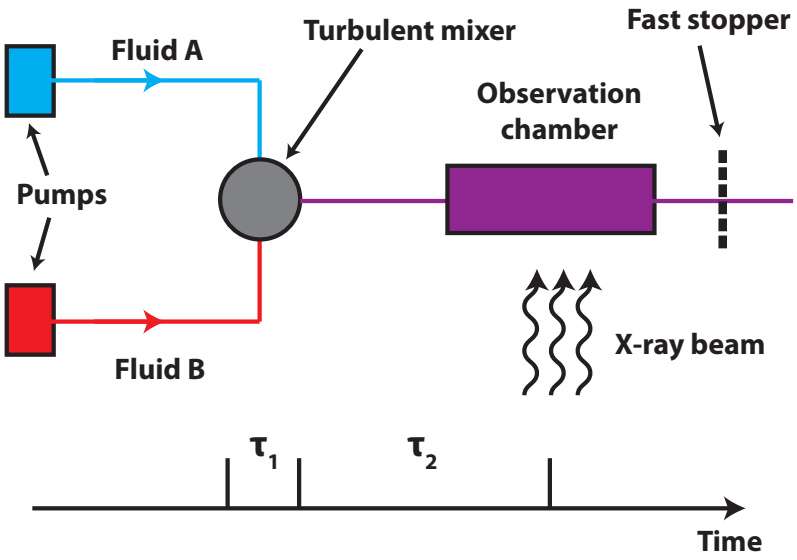

Figure 3.13: Schematic of a stopped-flow mixing device used in trSAXS measurements. Two fluids, commonly only one containing the sample, the other one a binding partner or different environment, are pumped into a turbulent mixer and further transferred into the observation chamber where an X-ray beam with high intensity is used for time resolved measurements. A fast stopper at the end of the system enables a fast stopping of the mixed fluid with a minimum of perturbation. The total dead time between mixing and the first frame of the measurement consists of the mixing time τ_1 and the transfer and diffusive mixing time τ_2. Figure inspired by Ref. [284]

the velocity of the fluids. Decreasing the velocity increases the quality of the mixture, however also increasing the dead time [284]. When the mixture arrives in the observation chamber, the pumps stop and a fast stopper at the end of the chamber stops the fluid movement with a minimum of perturbation.
Time resolved SAXS has been performed for a few biological sample, such as the folding of *Cytochrome C* upon a pH jump [284] as well as RNA folding due to abrupt increase of magnesium concentration [296]. In chapter 8 a stopped-flow mixer was used to perform time resolved SAXS measurements to detect and describe the fast dynamics of DNA origamis including their dependence on pre-specified orientations and alignments.

Part II

Magnetic Tweezers

Chapter 4

Construction and Characterization of a Magnetic Tweezers Setup

A state-of-the-art MT setup was built to perform the measurements presented in chapter 6 and 7. In this chapter, the design, mechanical components and computational capability are described, the spatial resolution is determined, and a precise force calibration is performed. The setup is robust against mechanical influences and simultaneously capable to measure many (> 100) beads in parallel with a bead size dependent nanometer or sub-nanometer spatial resolution. Furthermore, a reduced field-of-view (FOV) enables to track beads in the kHz regime, therefore allowing to measure fast transitions. The spatial resolution is specified by simple standard deviation as well as the Allan deviation for different bead sizes and acquisition frequencies. Moreover, in this chapter a force calibration for MyOne (diameter 1 μm) as well as M270 (diameter 2.8 μm) beads is presented, giving a very precise calibration to serve as a force look-up-table as a function of the distance between the magnets and the flow cell. The use of drift correction, high acquisition frequencies and the Allan variance minimize external as well as internal influences of the measurement conditions, such as a limited time resolution. A test of the homogeneity of the force within one single FOV was performed with individual beads measured at different spots of this FOV. These measurements did not reveal any significant changes in the force at a constant magnet distance and therefore indicate a homogeneous force over the whole FOV.
All MT data presented in this thesis were measured with this setup and the presented calibrations (Fig. 4.1).

4.1 Requirements for a State-of-the-Art Magnetic Tweezers Setup

Recent developments in single-molecule techniques resulted in high-resolution instruments, with position determination of nanometer-scale, sub-second temporal resolution and precise force calibrations [5]. In line, MT have experienced great progress making it a tool for state-of-the-art measurements [35, 37, 297–299]. These improvements make it possible to monitor and

investigate biophysical properties of *in vitro* enzymatic reactions [300, 301], resolve real-time dynamics of DNA interacting proteins [302, 303], molecular motors [304–307] and accompany theoretical models [297]. For many measurement conditions a near-basepair resolution is possible or even a standard, allowing for a precise description of the underlying mechanochemistry [306, 307]. Ongoing developments especially in the camera technology and tracking algorithm result in high multiplexed MT setups with increased temporal and spatial resolution. Most recent MT setups are capable to measure with kHz time- and sub-nanometer spatial resolution [35, 37, 299].
The main goal of the instrument described in this chapter was to track many beads in parallel in real time with a high accuracy in the lateral (x and y) as well as in the vertical (z) dimension, thus obtaining a precise 3D position of the bead. To fulfill these requirements, special attention was directed to aberration effects and homogeneous light illumination as well as reduction of vibrations. The high tracking resolution is available for different camera frequencies associated with different time resolutions of the instrument. Furthermore, the setup is designed to fulfill many practical properties such as an homogeneous force field and a wide range of adjustable forces. To withstand the impact of daily use of different users, further attention was directed to robustness against mechanical influence, flexibility, and a possibility to easily readjust and repair the setup. The setup is characterized by its 3D position tracking resolution and a precise force calibration.

4.2 Hardware and Software of the MT Setup

A general introduction to MT is given in chapter 1, whereas here specific construction details and components are presented. A complete part list of the instrument can be found in the appendix 10.1. A custom-made flow cell holder holds in place and secures the flow cell and connects its outlet to a peristaltic pump. A light-emitting diode (LED) illuminates the sample. The diffraction rings of the defocused beads are captured by an oil-immersion objective and focused with a lens on a complementary metal-oxide-semiconductor (CMOS) camera chip which is placed in the focus of the lens. A piezo is able to control the vertical position of the oil objective in order to build a LUT (Fig. 1.2). A pair of vertically aligned permanent magnets above the flow cell can be moved in vertical direction by a linear stepping motor, thus the distance between the magnets and the flow cell can be controlled. Furthermore, the magnets can be rotated by a rotation motor. Therefore, the force can be controlled and torque applied. The simple LED lens-illumination-system, consisting of one LED and one lens, does not generate perfectly parallel light, and hence the distance between the LED and the magnets (more precisely between the LED and the gap between the magnets) can change the light intensity. To reduce this intensity variation, the LED is mounted on the same arm as the magnets and consequently moves with the magnets, so that the distance between the LED and the magnets remains constant. The illumination path is aligned such that the change in intensity detected by the camera is minimized while moving or turning the magnets.
Images captured by the camera are transferred in *full camera link mode* to a frame grabber card and processed with an open source software [31] with small modifications (including e.g. improvement and optimization for tracking at high acquisition frequencies). This allows to measure the lateral as well as the vertical position of the beads in real time. In the standard configuration of the setup, the x-y position is determined with the quadrant-interpolation

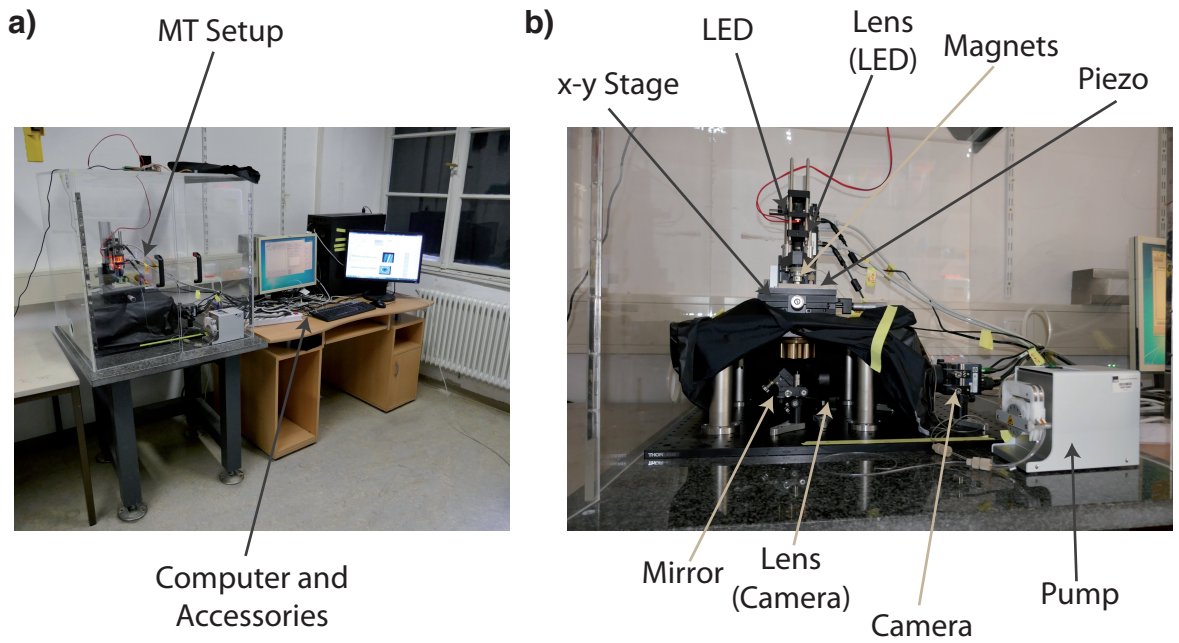

Figure 4.1: Picture of the MT setup. An LED illuminates the flow cell containing the sample. A pair of magnets exert a force on the bead attached to the system of interest. The diffraction pattern of the defocused beads are focused on a CMOS camera and analyzed with an open source Labview code on the computer.

(QI) tracker [308], taking not only the x and y, but also the radial profile into account. The z position is determined based on a LUT as described in chapter 1 (Fig. 1.2) [308]. Besides the QI-tracker, a Cross-Correlation and a simple Center-of-Mass tracker is available. Furthermore, the number of pixel which should be considered by the QI-tracker can be reduced to reduce computational effort. However, the height information of the bead is always calculated by the same interpolation algorithm. The software is able to calculate the positions of the beads on the CPU as well as the GPU of the computer.
The 24.5×18.4 mm^2 large camera chip, containing 12 mega pixels (MP) (4096 px $\times$ 3072 px), is well suited to capture a large FOV of a flow cell. It allows to monitor the whole FOV, with a size in the setups standard configuration of $\approx 440 \times 330$ μm^2, at 58 Hz [309] and even higher frame rates with a reduced FOV, e.g. 1920 px $\times$ 280 px ($\approx$ 4 % of original size) at 1000 Hz or 1792 px $\times$ 100 px at 2500 Hz. A simple high-power LED enables a homogeneous illumination for all possible FOV sizes and allows a brightness up to the limit of the camera for an exposure time down to 1 ms (1000 Hz). At an exposure time of 0.4 ms (2500 Hz) and highest possible intensity of the LED, for common motor positions the brightness detected by the camera is roughly 20-30 % lower than usual. Other light sources, e.g. a fiber-coupled LED, a superluminescent diode or a laser, would allow even better intensities [36, 37], which however was not necessary for the current and planned projects. Furthermore, a better coherence of the light, such as for a superluminescent diode or a laser, generates speckles and consequently results in a noisier image which has to be post-processed [36].
Besides the tethered beads of interest, commonly a reference bead stuck to the surface is measured in parallel and subtracted from the other beads. This makes MT setups robust against drift and low frequency noise. Furthermore, the limited camera frequency cuts off the high frequency noise. Nevertheless, to reduce vibrations, the base of the setup is designed to be

symmetric. Furthermore it is built in the basement on an oil damped table to reduce external influences. A surrounding box protects the instrument from acoustic noise and air currents, and in practice, from (sudden) significant temperature changes do to air movement.
Aberration effects originate mainly from the camera lens, which makes the alignment of this lens very important. To minimize aberration effects, the setup operates in its standard configuration with a 40x oil objective combined with an achromatic doublet camera lens of 250 mm. The advantage of this configuration compared to e.g. an 60x objective with a 160 mm lens (thus approximately the same magnification) is the smaller impact of a misalignment of the lens. Hence the most sensible setup part, the alignment of the objective, the mirror, the lens and the camera can be adjusted without a huge effort, making it possible to run the setup continuously without long service downtimes.
The setup is also calibrated with a 200 mm lens, resulting in a larger FOV at the expense of resolution. Consequently, the setup is built to be robust against external effects while retaining its performance, resolution and flexibility.

4.3 Performance and Calibration

Several tests and calibrations were performed to characterize the setup. The main focus for these tests was laid on the maximal number of beads that can be tracked in parallel in real time, the resolution of the position tracking and setup noise as well as a precise force calibration.

4.3.1 Computational Performance

The setup is designed to track many beads in real time in parallel. In general, different lens and objective combinations change the magnification of the setup and hence the area and number of pixels (region of interest = ROI) necessary to analyze a bead. For a larger magnification, more pixels have to be analyzed, resulting in a higher computational effort. Also, increasing the magnification reduces the total FOV and less beads are visible. Regardless of the magnification, the computational effort can be significantly changed by the number of pixels the QI-tracker uses for its radial alignment, the number of iterations the QI-tracker performs or simply the use of only the Cross-Correlation tracker without the QI-tracker [31]. Table 4.1 gives an overview about the maximal number of beads which can be tracked in real time on the CPU or GPU, respectively. The standard configuration of the setup hardware is a 40x objective combined with a 250 mm lens, while the default tracker settings are 3 iterations while using most of the pixels (“QI Angular sample density = 0.7, “QI radial sample density” = 2, see Cnossen et. al.[31] for details). The setup is initialized to use the CPU for the calculation of the bead position. Assuming a ROI of 80 px × 80 px for MyOne beads (diameter 1 µm) and 110 px × 110 px for M270 beads (diameter 2.8 µm), the setup is able to track 140 and 60 beads with 58 Hz in its default software and hardware configuration, respectively. At 1000 Hz, the same configuration enables to track at least 3 beads for both ROI sizes and at 2500 Hz at least 2 beads can be tracked in real time. Due to the reduced FOV at 1000 and 2500 Hz, a higher number of beads cannot be measured, regardless of the computational limits. For all tested settings, the GPU increases the number of beads that can be tracked in real time, e.g. for the default configuration at 58 Hz approximately by a factor of ≈ 1.5.
Consequently, in its standard configuration, the setup is able to track as many beads as needed

in common experiments. The determined values are consistent with Cnossen et. al.[31], as expected, since the same tracking algorithm and only slightly different computer hardware is used.

Table 4.1: Maximum number of beads that can be tracked in real time at 58 Hz for most common tracker settings. If more beads are tracked than denoted in the table, the camera frequency will be reduced automatically to enable a precise position determination of all beads for all captured frames. "Lens" is the lens in front of the camera, "ROI" the region of interest in pixels for every bead, "Algorithm" the tracking algorithm (QI / 1D Cross-Correlation (Cross-C)), "Iteration" the number of iterations of the QI-tracker, "ang" and "rad" the amount of pixels covered in angular and radial direction of the QI-tracker (see Ref. [31] for details), CPU and GPU the amount of beads which can be tracked in real time without frequency reduction on the CPU or GPU, respectively. Tests performed with a 40x objective, 100 nm steps for the LUT, and the light was constant at a mean camera response value of 120 over the whole FOV. Cross-Correlation tracker was set to: length = 30, width = 64, Iteration = 3. For pixel calibration see table 4.2. Full list with more tracker settings presented in appendix 10.2.

Lens	ROI	Algorithm	Iteration	ang	rad	CPU	GPU
250	110	QI	3	0.7	2	60	85
250	110	QI	2	0.7	2	70	110
250	110	QI	1	0.7	2	105	180
250	110	QI	3	0.5	1	105	185
250	110	$Cross-C$	–	–	–	195	> 500
250	80	QI	3	0.7	2	140	210
250	80	QI	2	0.7	2	170	260
250	80	QI	1	0.7	2	225	400
250	80	QI	3	0.5	1	240	400
250	80	$Cross-C$	–	–	–	360	> 500
200	100	QI	3	0.7	2	110	170
200	100	QI	2	0.7	2	130	230
200	100	QI	1	0.7	2	165	330
200	100	$Cross-C$	–	–	–	230	> 500
200	70	QI	3	0.7	2	160	260
200	70	QI	2	0.7	2	200	370
200	70	QI	1	0.7	2	280	> 500
200	70	$Cross-C$	–	–	–	410	> 500

4.3.2 Resolution of 3D Position Determination

To specify the resolution of the setup the variance of the position of beads attached to the glass surface was measured. Therefore, 1 µm as well as 3 µm polystyrene beads were baked onto the surface and tracked with different tracker settings (see Materials and Methods, section 4.3.4 for details). The same ROI and light intensities as for normal measurements were used. Nevertheless, a larger ROI as well as higher light intensity can increase the tracker performance [31, 37]. Furthermore, both lenses as described in section 4.2 were used in combination with a 40x objective. A larger magnification, e.g. accessible with a 60x objective, can increase the resolution [310]. It should be noted again, that only the lateral tracker algorithm or its settings can be modified. However, the height information of the bead is only indirectly affected by the determination of the center of the bead. An inaccurate description of the center of the bead results in a not radial symmetric diffraction profile of the bead, thus the for the LUT calculated 1D profile of the diffraction pattern is incorrect which finally results in an imprecise

determination of the height of the bead.
To quantify the resolution, two different methods for the analysis were used. The standard deviation calculated over the whole trace is a good estimate of the setup resolution, but will increase with measurement time due to drift. Therefore, the Allan deviation (AD) was used to determine the spatiotemporal resolution. It yields the spatial resolution of a measurement of duration τ, and is defined as one-half of the average difference in position between consecutive intervals of length τ averaged over all intervals [37, 310, 311]. Hence, it specifies the signal stability over a given time scale and determines the drift as well as uncorrelated noise [312]. A reference bead was subtracted before the standard deviation or the AD were calculated.
Throughout all tracker configurations presented in table 4.2, the standard deviation of the tracking noise in lateral dimension is by a factor of roughly 2-3 better than in vertical dimension. Regarding the z fluctuations, within one setup configuration, the errors of the standard deviation of the tracker noise overlap, hence, the tracker settings do not significantly change the setup resolution. Consequently, in the following comparison, only the mean values of the presented tracker settings are considered, i.e. in vertical dimension 1.5 ± 0.1 nm and 3.28 ± 0.02 nm for a 250 mm lens with 3 µm and 1 µm beads, respectively, as well as, 1.6 ± 0.1 nm and 4.64 ± 0.04 nm for a 200 mm lens again with 3 µm and 1 µm beads, respectively. Errors are standard error of the mean.
For the 3 µm beads, the tracking accuracy in z is approximately the same for the 250 mm and 200 mm lens, while for a decrease in the magnification, a decrease in the resolution is observed for the 1 µm beads. Throughout both setup configurations, the tracker accuracy is significantly better for the larger beads, which is in agreement with similar setups [37, 299]. This behaviour can be explained by the larger and more pronounced diffraction patterns for larger bead sizes, containing higher intensity differences and more pixels with information about the bead position [37].
Residual drift not eliminated by the subtraction of a reference bead can increase the standard deviation of the tracker noise. A second approach to characterize the tracking accuracy of the setup is the Allan deviation [37, 310, 311]. The measurement trace is separated into many time segments of duration τ and the AD for this particular τ is calculated. This is repeated for different values of τ. A smaller AD value corresponds to a better resolution. Starting from very small time units (e.g. a few times the camera acquisition time) and increasing τ, the AD drops to smaller values with $\frac{1}{\sqrt{\tau}}$ [37, 299]. This behaviour is explained by the similarity of the AD to the standard error of the mean of the bead positions, which decreases with the square root of the number of independent measurements at the shot noise limit. In other words, the position accuracy increases due to more frames which are averaged until a minimum has been reached. Longer τ values increase the AD because of drift (Fig. 4.2). The τ corresponding to the minimum of the AD is the best measurement duration to have optimal resolution.
The main information extracted from MT experiments is the z position of the bead. Hence, only the vertical dimension is considered for a detailed analysis. Considering the absolute values of the AD within one setup configuration and one bead size, every tracker setting leads to approximately the same AD in vertical dimension. For the setup configuration with the 250 mm camera lens, the minimum of the AD for both bead sizes is roughly the same ($\approx$ 0.1 nm). However, for larger beads the minimum is already achieved for smaller values of τ. Consequently, for $\tau < 5$ s, before drift dominates the AD, the tracking of the 3 µm beads is more accurate (e.g. 0.41 nm vs. 0.16 nm at τ = 1 s for 1 and 3 µm, respectively, with 3xQI

Table 4.2: Standard deviation of different tracker settings and bead sizes for most common tracker settings. "std lat." is the mean value of the standard deviation in x and y in nm, "std z" in z in nm, "nm/Px" the calibrated pixel size in nm (calibrated with a calibration grid), rest as denoted in table 4.1. Throughout all tracker settings, the standard deviation in lateral position is smaller than for the vertical one. While the standard deviation decreases with an increase of the bead size, different tracker settings results in only minor changes. The decrease of the tracker accuracy with a decrease of the magnification is more pronounced for the 1 µm beads. All measurements last 10 min, were performed with a 40x objective and a light intensity response of 120 at the camera. Full list with all tracker settings presented in appendix 10.3. Errors are standard deviation of all tracked beads.

Bead	Lens	nm/Px	ROI	Algorithm	Iteration	ang	rad	std lat.	std z
3	250	107.72	110	*QI*	3	0.7	2	0.5 ± 0.3	2.0 ± 1.2
3	250	107.72	110	*QI*	2	0.7	2	0.5 ± 0.3	1.4 ± 0.6
3	250	107.72	110	*QI*	1	0.7	2	0.8 ± 0.6	1.3 ± 0.6
3	250	107.72	110	*QI*	3	0.5	1	0.4 ± 0.2	1.3 ± 0.6
3	250	107.72	110	*Cross-C*	–	–	–	1.2 ± 0.5	1.3 ± 0.5
1	250	107.72	80	*QI*	3	0.7	2	1.2 ± 0.4	3.2 ± 0.3
1	250	107.72	80	*QI*	2	0.7	2	1.5 ± 0.4	3.3 ± 0.1
1	250	107.72	80	*QI*	1	0.7	2	2.2 ± 0.3	3.3 ± 0.1
1	250	107.72	80	*QI*	3	0.5	1	1.2 ± 0.3	3.3 ± 0.2
1	250	107.72	80	*Cross-C*	–	–	–	1.4 ± 0.1	3.3 ± 0.1
3	200	131.65	100	*QI*	3	0.7	2	0.7 ± 0.3	1.8 ± 0.3
3	200	131.65	100	*QI*	2	0.7	2	0.6 ± 0.2	1.5 ± 1.1
3	200	131.65	100	*QI*	1	0.7	2	1.0 ± 0.3	1.6 ± 0.2
3	200	131.65	100	*QI*	3	0.5	1	0.6 ± 0.2	1.5 ± 0.2
3	200	131.65	100	*Cross-C*	–	–	–	1.6 ± 0.2	1.5 ± 0.3
1	200	131.65	70	*QI*	3	0.7	2	1.9 ± 0.5	4.6 ± 0.4
1	200	131.65	70	*QI*	2	0.7	2	2.3 ± 0.5	4.5 ± 0.1
1	200	131.65	70	*QI*	1	0.7	2	3.1 ± 0.4	4.7 ± 0.2
1	200	131.65	70	*QI*	3	0.5	1	1.8 ± 0.5	4.7 ± 0.2
1	200	131.65	70	*Cross-C*	–	–	–	1.7 ± 0.1	4.7 ± 0.2

and a 250 mm camera lens), which is in agreement with predictions from basic Mie theory for scattering of light [37]. The setup configuration with the 200 mm camera lens exhibits qualitatively the same result. Nevertheless, for both bead sizes the minimum of the AD is reached at ≈ 10 s and the 3 µm beads reveal a reduced AD by a factor of ≈ 2. While the AD of the 3 µm beads does not change significantly for both setup configurations, the tracking resolution of the 1 µm beads decreases with lower magnification. A more detailed analysis of the lateral tracking resolution determined with the AD is presented in appendix 10.3. Briefly, the AD in the lateral dimension differs between the different tracker settings, but does not significantly change with the number of pixels used for the QI-tracker (Fig. 10.2). The smaller impact of the tracker settings for the z dimension is in agreement with Ref. [310]. It can be attributed to the overall good lateral position tracking and the only small impact of a slightly wrong x-y position for the calculation of the vertical position with the help of a LUT. For all QI-tracker settings the AD is lower in the lateral dimension, for the Cross-Correlation tracker the resolution in lateral as well as in vertical direction is approximately the same. Fig. 4.3 illustrates a direct comparison of the 3xQI tracker in lateral and vertical dimension.
The setup is designed to track with different camera frequencies. A shorter acquisition time combined with a higher camera frequency make it possible to calculate the AD for smaller values of τ and, in addition, for one fixed value of τ more frames and hence more tracked

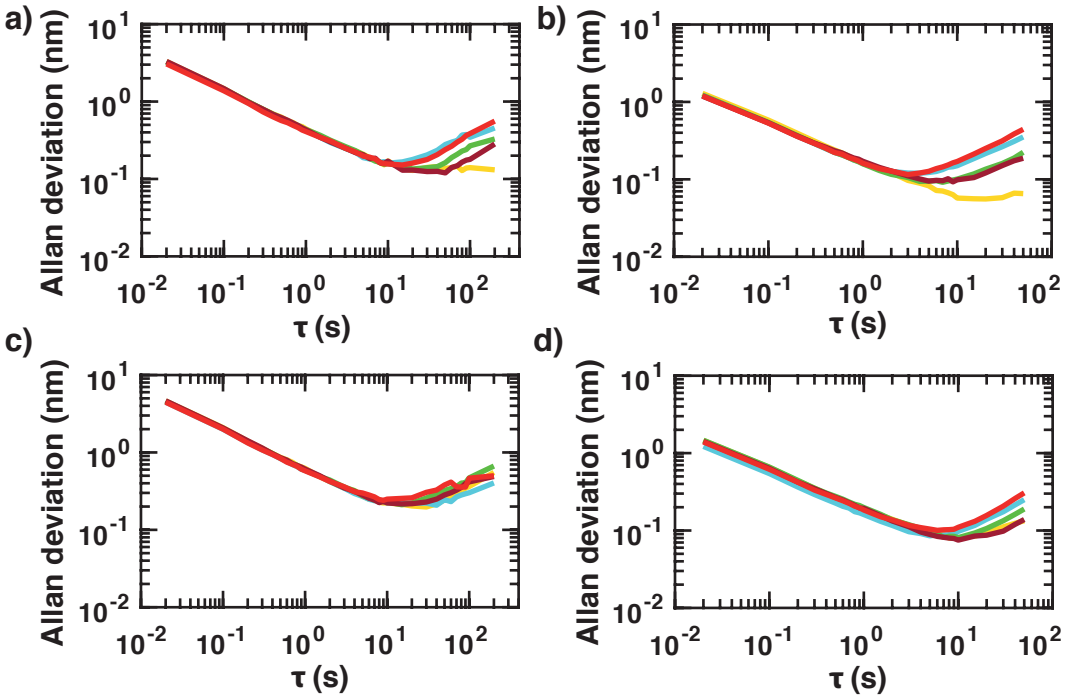

Figure 4.2: Allan deviation in z of different tracker types and settings of polystyrene beads baked to the glass surface. For the same setup configuration and same bead size, the AD of the Cross-Correlation tracker and of different QI-tracker setting deviate only slightly. The tracking performance for 3 µm beads is consistently better than for 1 µm beads. For 1 µm beads the accuracy reduces slightly for the 200 mm camera lens, while for 3 µm beads the accuracy stays approximately constant. a) 1 µm bead with 250 mm lens, b) 3 µm bead with 250 mm lens, c) 1 µm bead with 200 mm camera lens, d) 3 µm bead with 200 mm lens. Red: 3xQI (ang = 0.7, rad = 2), blue: 2xQI (ang = 0.7, rad = 2), green: 1xQI (ang = 0.7, rad = 2), dark red: 3xQI with less pixel (ang = 0.5, rad = 1), yellow: Cross- Correlation tracker (length = 30 px, width = 64 px, iteration = 3). All measurements last 10 min at 58 Hz. Mean values of at least 15 beads. More tracker configurations are presented in appendix 10.1.

positions are analyzed and averaged. Therefore, the AD reduces with higher frequencies before drift dominates the analysis (Fig. 4.3). The difference of the AD below $\tau \approx 3$ s is in excellent agreement with the expected scaling of $\frac{1}{\sqrt{N}}$ resulting in $\sqrt{\frac{1000Hz}{58Hz}}$ = 4.1-fold decrease.
Besides the accuracy of the tracker without magnets (or at one fixed magnet position), a potential change in the vertical position due to tracking issues upon movement of the magnets is of interest (e.g. caused by a light intensity change). Therefore, the obtained position change in the vertical dimension of baked polystyrene beads was analyzed for a movement of the magnets from 1 mm to 10 mm distance between the magnets and the flow cell. The same flow cell as for the tracker noise measurement was used with 3 µm polystyrene beads baked onto the surface. The standard deviation of the measured height change of all beads is 7.1 nm and can be further reduced to 4.8 nm by subtracting a calibration FOV. To this end, another FOV was analyzed in the same manner and the offset of the closest bead of the calibration FOV is subtracted from the current FOV (see Materials and Methods, section 4.3.4 for details).
In conclusion, in both lens configurations the setup is capable to track 1 µm as well as 3 µm beads with a very high resolution and a reduction of long term drift to a minimum while tracking many beads in parallel. An increase in magnification, e.g. by the use of a 60x or 100x objective, is expected to further increase the tracking resolution. Regarding the already good

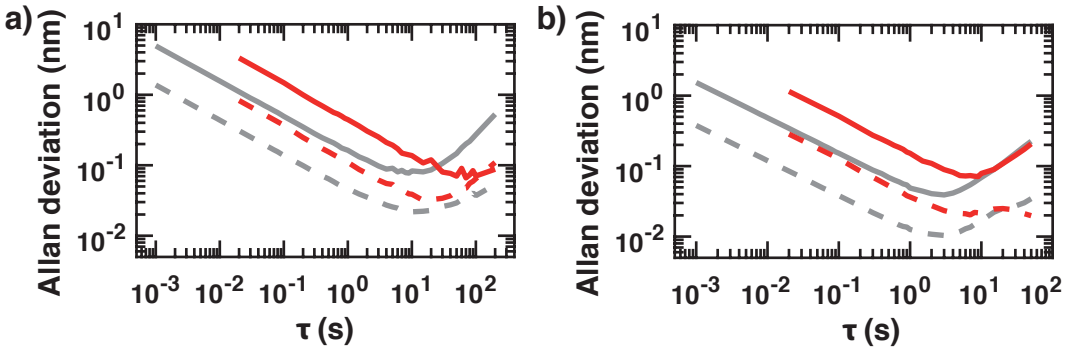

Figure 4.3: Allan Deviation of 58 Hz and 1000 Hz in x and z for polystyrene beads baked to the glass surface. For both bead sizes the AD of the faster tracking is reduced corresponding to a better position accuracy before drift dominates the measurement. Independent of the bead size, the x tracking accuracy is better than for z. a) 1 µm, b) 3 µm bead diameter. Red: 3xQI 58 Hz, gray: 3xQI 1000 Hz, solid line: z, dashed line: x. Measurements last for 30 min, same pair of beads for 58 Hz and 1000 Hz, camera lens = 250 mm.

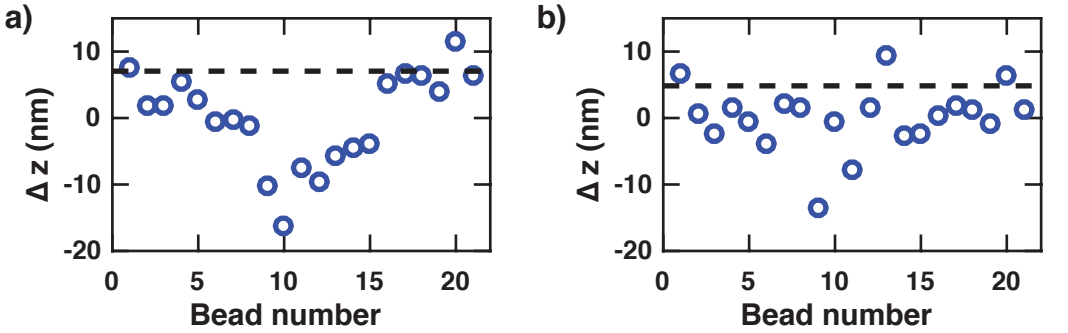

Figure 4.4: Error of height determination after magnet movement for polystyrene beads baked to the glass surface. The magnets are moved from 1 mm to 10 mm distance and the height difference of the 3 µm polystyrene beads is determined after reference bead subtraction. The mean value is set to zero, blue circles are the distances of every bead at both magnet positions, dashed black line the standard deviation of the position change of all beads. A subtraction of a calibration FOV can reduce the standard deviation. a) Without, b) with calibration FOV correction. Setup tracked with 58 Hz in the setup configuration with a 250 mm lens.

resolution for 3 µm beads, a change in the magnification might only be of interest for small beads, but even in this case not necessary for most of the measurement types. Usually, the thermal fluctuation of the tether-bead system dominates the setup noise [37]. Nevertheless, for measurements with small beads that provide a smaller correlation time, the tracker noise should be taken into account at high forces (> 10 pN). However, this force range is not accessible MyOne beads in the standard magnet configuration of the setup for (see section 4.3.3). A higher camera frequency can improve the resolution of beads baked onto the surface, but has less impact on measurements with biological tethers due to the limit defined by the thermal noise. Further improvement can be achieved by increasing the light intensity [31, 37]. The bead material does not change the tracking accuracy [31, 37] and hence the results can be directly transferred to superparamagnetic beads with approximately the same diameter. The spatiotemporal resolution is comparable with similar state-of-the-art MT setups [37, 299]. The error in the vertical position after magnet movement is negligible compared to a typical DNA length used in MT (≈ 3 µm) but has to be considered for very short tethers, e.g. proteins. A higher bead density in the reference FOV will most likely further reduce the offset scattering

and can be taken into account for a more precise total length of the tether determination.

4.3.3 Force Calibration

MT provide a constant force for a fixed distance between the FC and the magnets. In general, the force can be calculated from the gradient of the magnetic field [4, 25]:

$$\mathbf{F} = \frac{1}{2} \cdot \vec{\nabla}(\mathbf{m}(\mathbf{B}) \cdot \mathbf{B}) \tag{4.1}$$

with the bead's magnetization $\vec{m}(\vec{B})$ and the magnetic field $\vec{B}$. However, computational challenges as well as a lack of precise values for the magnetization of a specific type of beads make it difficult to compute the exact magnetic field and therefore the force [25, 33]. An alternative, effective, and easy experimentally accessible approach to determine the force of a MT setup is to analyze the Brownian motion of DNA-tethered beads [25, 33, 38, 313]. Thereto, the x-y and the extension fluctuations of the tether about their equilibrium positions are analyzed. A combination of a Taylor expansion of the energy of the bead-DNA system to the second order and the equipartition theorem results in an expression for the applied force. This expression is dependent on the tether length and the lateral variance due to the Brownian motion and is described by:

$$F = \frac{k_B T < z >}{< \delta x^2 >} \tag{4.2}$$

where k_B is the Boltzmann constant, T the temperature, $< z >$ the DNA extension, and $< \delta x^2 >$ the variance of the lateral bead position. The elongation of the tether and the fluctuation of the beads at different distances between the magnets and the flow cell lead to a look-up-table for the force as a function of the magnet positions. A fit to the measured calibration values leads to the final force calibration of the MT setup.
The bead trajectories are determined from consecutive camera images taken at a fixed sampling frequency. This results in two potential problems, which have to be considered: Each camera image provides a mean position of the bead within the exposure time and consequently high frequency fluctuations average out. Furthermore, frequencies larger than approximately half of the shutter frequency (Nyquist frequency) are affected by aliasing and hence shifted to lower frequencies [33, 38, 313–315]. Thus, the finite shutter time of the camera influences the measured variance, and an increase of the shutter time will reduce the variance and therefore result in an overestimation of the force [33]. Several methods to address this issue are known, such as increasing the camera frequency [33], a blur motion correction [314], calculating the power spectral density (PSD) combined with correction for acquisition artifacts and low-frequency drift [313, 314, 316], as well as using the Allan variance [310].
In general, the applied force can be changed by hardware changes such as the gap between the two magnets [25], or dynamically controlled by the distance between the magnets and the flow cell (in the following referred to as "magnet distance"). The setup is calibrated for MyOne as well as M270 beads with a 1 mm gap and a pair of vertically aligned $(5\ \text{mm})^3$ cubic magnets [25]. To take care of the characteristic time of the system, different measurement times were used at different forces and bead sizes, resulting in a statistical accuracy for every single force of 5 % and 10 % for MyOne and M270 beads, respectively (see Materials and Methods; section 4.3.4 for details). Every single force plateau was analyzed with the Allan variance resulting in a

robust, unbiased, force calibration [33].
To determine correct, not biased, forces and to minimize the influence of aliasing, it is required that the corner frequency does not exceed 80 % of the Nyquist frequency [313–315]. Regarding the standard configuration of the setup, this is $0.8 \cdot \frac{58Hz}{2} = 23Hz$. For MyOne beads, from a PSD analysis, the corner frequency for every magnet position is determined, resulting in values < 15 Hz over the whole force range (Fig. 4.5 a). For every magnet position, the force is calculated by the Allan variance and the standard deviation between the beads as well as the relative error are determined (Fig. 4.5 b). Over the whole force range, the relative error stays approximately constant (≈ 15%) indicating to originate from a variance between the bead properties and not from the force calibration. This assumption is further confirmed by the fact that a measurement at high forces with a higher acquisition frequency of 400 Hz leads to the same forces with very little deviation (Fig. 4.5 c). Finally, the data of the 58 Hz measurement were fitted with a double exponential model, leading to:

$$F = 8.977 \cdot e^{-0.782 \cdot z} + 0.094 \cdot e^{-0.041 \cdot z} - 0.033 \tag{4.3}$$

where F is the force in pN and z the distance of the magnets to the flow cell in mm.

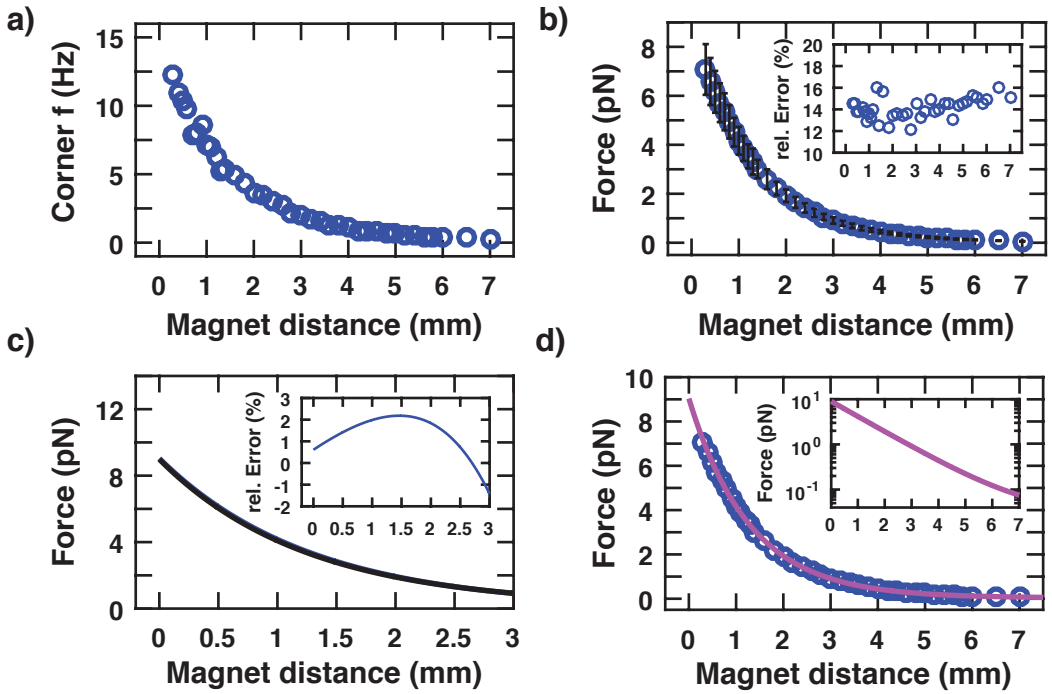

Figure 4.5: Force calibration of MyOne beads. a) Corner frequency f_C determined at an acquisition frequency of 58 Hz for different magnet positions. For all distances between the magnets and the flow cell, f_C is below half of the Nyquist frequency. b) Forces, absolute errors and relative errors at various magnet positions. At smaller magnet distances the force increases. Over the whole force range the relative error remains constant and represents mainly the variation between the bead properties. Given errors are standard deviation between different beads. Data recorded at 58 Hz. c) Forces determined with 58 Hz (blue) and 400 Hz (black) as well as the relative deviation with regard to the 400 Hz (insert). Over the whole considered magnet distances (< 3 mm) the fits of both force calibrations are in good agreement with little deviation. d) Final force calibration for MyOne beads. Over the whole magnet position range, all measurement points recorded at 58 Hz (blue circle) are fitted with a double exponential fit (magenta solid line). For details of fit, the range, and final formula see text. $\chi_r^2 = 0.1$.

In principle, the M270 beads are analyzed the same way, although due to the higher achievable

forces [26, 33], more attention has to be drawn to the blurring and aliasing effects. For magnet distances smaller than ≈ 1 mm and an acquisition frequency of 58 Hz, the corner frequency increases above 80 % of the Nyquist frequency (Fig. 4.6 a). Consequently, these magnet plateaus are not suitable for a force calibration with 58 Hz. In line, the absolute as well as the relative

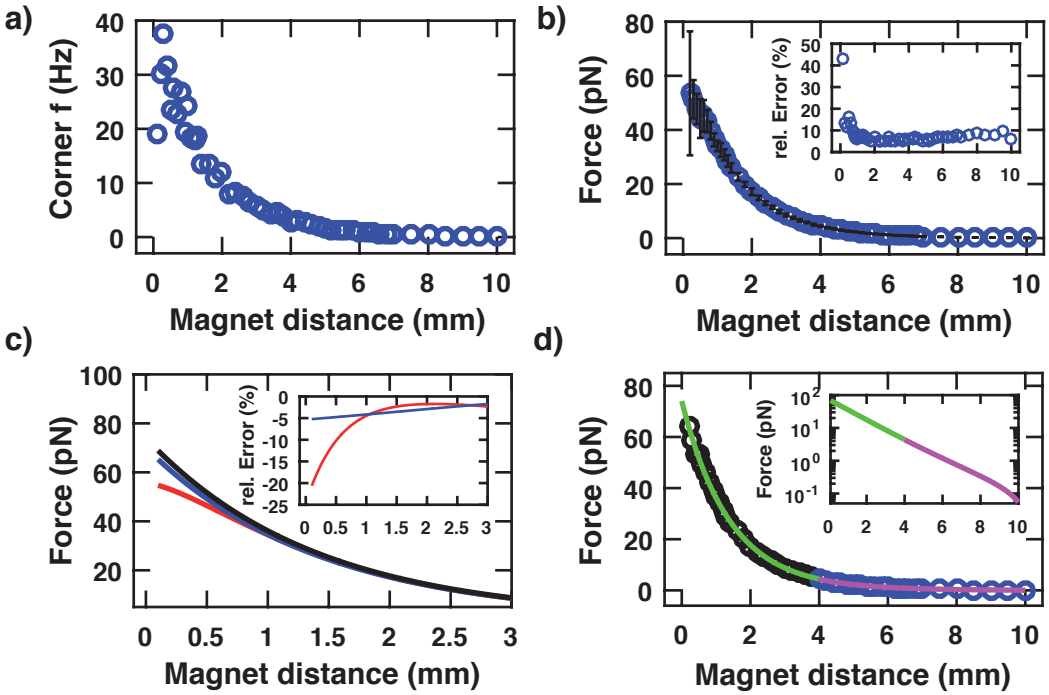

Figure 4.6: Force calibration of M270 Beads. a) Corner frequency f_C for different distances between the magnets and the flow cell. Close to the flow cell, the f_C increases and surpasses the Nyquist frequency. Data recorded at 58 Hz. b) Forces and errors at different magnet position. By decreasing the distance between the magnets and the flow cell, the force increases. The relative errors (inset) are approximately constant for magnet distances larger than 1 mm, representing mainly the bead to bead variation, and increases below. Errors are standard deviation between different beads. Data recorded at 58 Hz. c) Forces at different acquisition frequencies and fit regions. Black: single exponential fit at 400 Hz; blue: double exponential fit for magnet distances > 0.7 mm at 58 Hz; red: double exponential fit over all magnet positions at 58 Hz. Insert shows the relative deviation regarding to the data measured with 400 Hz. In the regime of high corner frequencies, i.e. magnet distances ≤ 1 mm, the discrepancies increase especially for the fit over all magnet positions at 58 Hz. d) Final force calibration for M270 beads. For magnet positions close to the surface (d ≤ 3.98 mm) data recorded at 400 Hz are considered (black circle: measurement values; green solid line: single exponential fit) while for larger distances a double exponential fit from magnet distances > 0.7 mm at 58 Hz is used (blue circle: measurement values, magenta solid line: double exponential fit). For details of the fit range and final formula see text. $\chi_r^2 = 0.3$

errors of every single force plateau increase for these magnet positions (Fig. 4.6 b) and stay approximately constant for magnet distances > 1 mm, again, representing the variation of the magnetic properties of the beads. To address the uncertainties at high forces, two approaches were considered: extrapolation from larger distances between the magnets and the flow cell, and measurements with higher camera frequency. Considering the high force regime (> 15 pN) and performing measurements with a camera frequency of 400 Hz as reference measurement, the extrapolation of a double exponential fit with a fit range over all motor plateaus with a magnet distance > 0.7 mm differs only slightly (maximal ≈ 5 %), while a double exponential model with a fit range over all magnet distances differs more pronounced, up to ≈ 20 % (Fig. 4.6

c). To take advantage of the large amount of beads that could be tracked with 58 Hz as well as the more precise measurements of less beads at higher forces, two separate exponential models were fitted for the high force and low force regime, employing the 400 Hz and the 58 Hz data, respectively (see Material and Methods, section 4.3.4 for details). The two models intersect at a magnet distance of 3.98 mm, leading to:

$$F = 73.722 \cdot e^{-0.722 \cdot z} + 0.322 \tag{4.4}$$

for magnet distances larger as 3.98 mm and

$$F = 69.410 \cdot e^{-0.713 \cdot z} + 1.637 \cdot e^{-0.053 \cdot z} - 0.963 \tag{4.5}$$

for magnet distances equal or smaller than 3.98 mm (Fig. 4.6 d).
For the MyOne beads as well as the M270 bead force calibration, the forces are in good agreement with published reference values [26, 33]. Furthermore, the M270 force calibration was validated by the characteristic phase transition of B-form dsDNA (BS-transition), a lengthening of the DNA by ≈ 70 %, which could be detected at ≈ 65 pN and thus in good agreement with literature[33, 72, 317–319].

An inhomogeneity in the gradient of the magnetic field within one FOV could lead to different forces at different positions of the FOV. A simple comparison of the single beads of the force calibration cannot be taken into account to test the force homogeneity, since differences in the magnetic properties of the beads can mask the force inhomogeneity. To examine differences in the magnetic field gradient, one bead was measured at five different positions of the FOV and only compared to itself. This was repeated for four molecules. The midpoint of the FOV was used as the reference position, the other positions were at the limits of the FOV as denoted in Fig. 4.7.
The forces vertical to the gap vary by ≈ 3 % and parallel to the gap by ≈ 2 %, hence show only minor changes. Consequently, the force defined by the magnetic field can be considered to be constant over the whole FOV.

In conclusion, the force applied by the magnets and the bead to the tether can be extracted from the force calibration and can be considered to be constant in the whole FOV. Regarding the small reduced chi-squared values χ_r^2 of 0.1 and 0.3 for MyOne and M270 beads, respectively, and the final approximately constant relative error over the whole force regime, the only significant uncertainties arise from the bead to bead variation, which was determined to be ≈ 15 % and < 10 % for the used batches of MyOne and M270 beads.

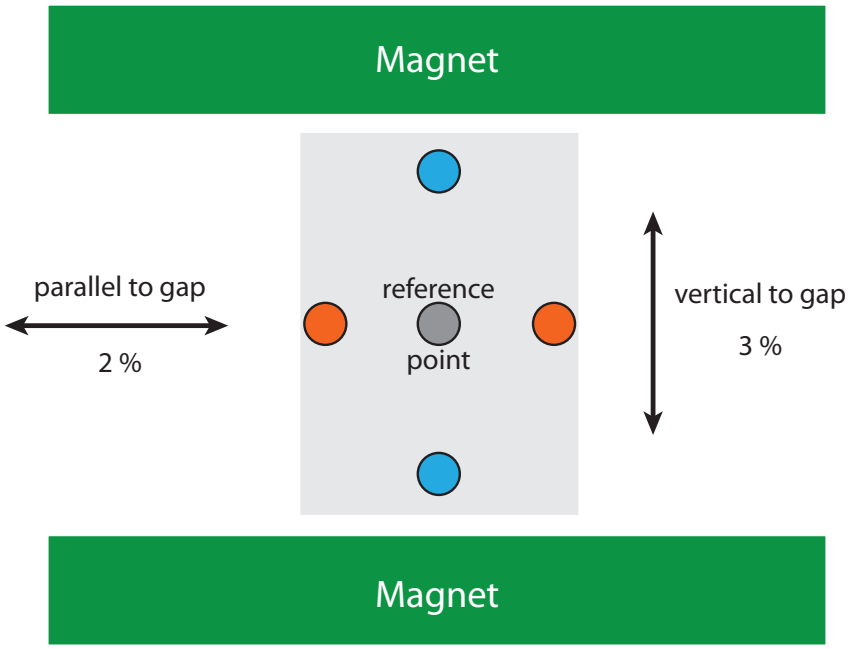

Figure 4.7: Force homogeneity within one FOV (topview). The mean force of the same four molecules differs at the limits of the FOV parallel to the gap (red spots) ≈ 2 % and in vertical direction (blue spots) ≈ 3 % from the reference point in the center of the FOV. Size of all figure components not to scale.

4.3.4 Setup: Material and Methods

Flow Cell Preparation for Resolution Measurements

Flow cells for the resolution determination in section 4.3.2 were built from an epoxy silane covered coverslip as bottom and an uncoated coverslip as top. A rectangular sheet of parafilm serves as walls for the rectangular flow channel. Before the assembly of the single components, 1 µl stock solution of polystyrene beads were mixed with 1000 µl or 500 µl ethanol for 1 µm (07310-15 Polybead, Polysciences Inc, USA) and 3 µm (09850-5 Polybead, Polysciences Inc, USA) beads, respectively. 200 µl of the final mixture were pipetted onto each flow cell bottom coverslip. After evaporation of the mixture, the beads were baked onto the coverslip for 1 min at ≈ 90° C. Finally, the bottom and top coverslip were connected by melting with the parafilm at ≈ 70° C for ≈ 30 s and filled with 1× PBS buffer.

Measurement Conditions and Reference Bead Identification for Resolution Measurements

For the resolution tests, all beads within one FOV that had no overlaps in their diffraction rings were measured and analyzed. Hence beads all over the FOV were used. Within one setup configuration, the same beads were tracked. For every bead and setup combination, a minimum of 15 beads were measured. All tracked beads were considered as potential reference beads. As optimal reference bead, the bead minimizing the sum of standard deviation of all other beads was used. This approach was repeated for every tracker setting and setup configuration. The same reference bead was used for the standard deviation comparison and for the AD. If not otherwise denoted, measurements last 10 min at 58 Hz.

Bead Selection and Reference Bead Identification for Height Resolution Determination

For the measurement of the position change in z at different distances between the flow cell and the magnets, the 3 µm beads were tracked with the 3xQI tracker and the amount of pixel covered in angular and radial direction was set to 0.7 and 2 respectively. 110 px were used as ROI. The magnets were moved from 1 mm to 10 mm distance between the magnets and the flow cell, and the measurement duration was 30 s per position. To determine the change in the measured z position of the beads baked onto the surface, the mean values obtained for both positions were subtracted from each other. A random bead was used as reference bead. For an offset calibration, another FOV was analyzed in the same manner and the offsets were subtracted from the FOV of interest. Therefore, as reference bead of the calibration FOV the one closest to the reference bead of the FOV of interest was used. Finally, the difference in height of the nearest bead of the calibration FOV was subtracted from the determined height change in the FOV of interest.

Flow Cell Preparation and Buffer Conditions for Force Calibration

Flow cells for the force calibration in section 4.3.3 were mechanically built and prepared as described in section 6.6. All force calibrations were performed in 1× PBS.

DNA Constructs for Force Calibration

For the force calibration, the bead-DNA mixture was prepared analogously to the one described in section 6.6. However, a longer DNA construct was used, consisting of ≈ 21 kbp.

Characteristic Time for Force Calibration

The characteristic time of a system defines the lower limit of the sampling frequency as well as a minimum for the total measurement duration at a single force plateau to obtain an accurate result. The camera frequency should be fast enough to capture the fluctuations, while the total measurement time should be sufficiently longer than the characteristic time [33, 316]. For a DNA-bead system such as used in magnetic tweezers, the time required to obtain a desired accuracy depends on the bead radius as well as the DNA length and can be calculated by:

$$\tau_{meas} = \frac{8 \cdot \pi^2 \cdot \eta \cdot R \cdot L_p \cdot L_C}{F \cdot \epsilon^2} \tag{4.6}$$

for $F \leq 1$ pN and

$$\tau_{meas} = \frac{12 \cdot \pi^2 \cdot \eta \cdot R \cdot L_C}{F \cdot \epsilon^2} \tag{4.7}$$

for $F > 1$ pN [33, 320]. Here, η is the viscosity (0.001 Pa s), L_p the DNA persistence length (≈ 47 nm [70]), R the bead radius, L_C the DNA contour length (≈ 7.1 nm), F the force at a particular magnet position and ϵ the statistical accuracy.

Details of Force Calibration

The same 13 MyOne beads (Life Technologies, USA) were measured and analyzed for the force calibration at 58 Hz and 400 Hz, respectively. The M270 (Life Technologies, USA) force calibration at 58 Hz consists of 16 beads, a subset of 5 beads were measured at 400 Hz. The smaller amount of beads results from the smaller FOV and hence lack of suitable reference beads. The diffraction rings of the investigated beads did not overlap with any other beads and no further pre-selection was used or needed.
For every single magnet distance of the force calibration, the measurement duration was chosen to result in a statistical error of less than 5 % and 10 % for MyOne and M270 beads, respectively [33, 320].
The position of the surface, necessary to determine the DNA length, was obtained without force by the lowest point of an 11-frames-smoothed trace at 58 Hz.
The zero point of the magnet distance was defined as 0.1 mm above contact with the FC.
The induced magnetic field in the superparamagnetic beads, geometrically correlated with the anisotropy axis of the bead, restricts the degree of freedom of the beads [321]. Hence, the beads can rotate around, but not vertical to, the magnetic field lines [38]. Consequently, the observed total tether length appears to be different for the two lateral dimensions, parallel and vertical to the magnet gap (Fig. 4.7), as in the former case the bead dimension has influence and lengthens the total tether by the radius of the bead. This results in a larger fluctuation and variance parallel to the magnet gap compared to the vertical direction. For the final force calibration, only fluctuations vertical to the magnet gap were analyzed.
To overall reduce effects of the bead size as well as surface effects close to the cover slip, a long

DNA of ≈ 21 kbp (≈ 7.1 µm) was used. To correct for the refractive-index mismatch between oil and water, a correction factor of n_{water}/n_{oil} = 1.33/1.51 = 0.88 was used in all measurements. All beads examined were tested by rotation curves at ≈ 0.4 and ≈ 6 pN to only possess a single DNA tether. For the force homogeneity tests, four individual MyOne beads were fully calibrated at different positions as indicated in Fig. 4.7. In other words, all four beads were measured in all five FOV positions. The center position of the FOV was used as reference position and the force at the four other spots in the FOV was compared at a magnet distance of 0.2 mm.

Chapter 5
Analysis Software "MT GUI"

To analyze all MT data generated within the framework of this thesis, thus with the setup described in chapter 4, a graphical user interface (GUI) was coded in MATLAB. In this chapter an overview of the GUI is giving. However, not all functions and details are described. A more detailed description can be found in the help file accessible directly from the main GUI. A more detailed description of the physical background of the analysis procedures implemented in the GUI and used in this thesis can be found in the corresponding chapters. The flowchart of the main components of the main GUI is presented in this chapter, the flowcharts of the other sub-GUIs introduced in this chapter can be found in appendix 10.4.

5.1 Practical Structure to Address Challenges Regarding the Analysis of MT Data

Recent MT setups, such as described in chapter 4, enable to track ≈ 100 beads in daily use and even more if required for the system of interest [31]. Furthermore, by reducing the FOV it is possible to measure with camera frequencies above 1 kHz while retaining its ability to track several beads in parallel [35, 37, 299]. In both cases the amount of produced data can be extremely large and difficult to handle, making the data analysis a computational challenging and time consuming aspect [37]. For simplicity, the position of every bead in every frame is saved in a simple text (ASCII) file [31, 308], thus easily accessible and highly compatible. Although other formats, such as binary files without ASCII codes, can decrease the data size [322, 323], the underlying amount of data for analysis is not reduced and hence, the main problem of the analysis cannot be solved by the tracking software.
To address the large amount of data generated by MT measurements, a software GUI "MT GUI" (current Version 1.8) was coded in MATLAB (MATLAB R2015b, The MathWorks). Special attention was paid to the capability to handle different types of MT measurements, enabling to analyze all data generated within this thesis. Furthermore, the software contains many options that can be differently combined and the code itself is easily extensible, which taken together, makes it flexible and easy to customize for new tasks. However, the many options available for data analysis are likely to generate errors by the user, such as combinations of options

which contradict and therefore do not lead to any meaningful results. In many cases this is only noticeable after a time consuming analysis. To minimize this issue, “MT GUI” is able to detect contradicting options and stop the analysis at the beginning, including an error message that contains a short help information for the user. Furthermore, the software is able to detect options that are likely to be chosen by mistake. In this case, the user is warned by a warning message, however is able to continue his analysis. Thus, the user-friendly interface reduces the possible errors by the user.

“MT GUI” consists of one main GUI, which is capable to open several small sub-GUIs, but also seven further large sub-GUIs. Some of the large sub-GUIs themselves contain again more small sub-GUIs. All large sub-GUIs are able to work independently after receiving the data from the main GUI “MT GUI”. An overview flowchart containing the large GUIs is presented in Fig. 5.1. For a more detailed description of the individual GUIs and their functions see sections 5.2 to 5.8. All GUIs include code for error checking, e.g. if data are loaded before an action can be performed. Computational tasks are transferred to functions and sub-functions. When possible, the functions work in a sequential combination, only interacting by sharing their outputs with the main GUI and consequently receiving input only from the main GUI. This makes the code easy-to-read, flexible and easy to be extended, while keeping its simplicity.

“MT GUI” is able to not only handle MT data, but also to analyze traces measured with an acoustic force spectroscopy instrument (AFS) [22, 23, 324]. Besides the different structure of the AFS-generated ASCII files, every bead is saved in one single text file. Loading AFS data with “MT GUI” automatically reads the bead number from the file name and saves the complete file names into the memory. Hence, all options that save information automatically connected to the measurement file name are also available for AFS measurement data. Nevertheless, a few options, mostly related to rotation measurements, are not available due to the restriction that no torque can be applied with an AFS setup [22, 23]. The amplitude of the acoustic wave is handled analogous to the magnet distance of a MT measurement. Predefined variables to determine plateaus of constant amplitudes can be selected by the user. Although often compatible with AFS measurement, this chapter focuses on the functions and options of “MT GUI” that are used for MT measurements.

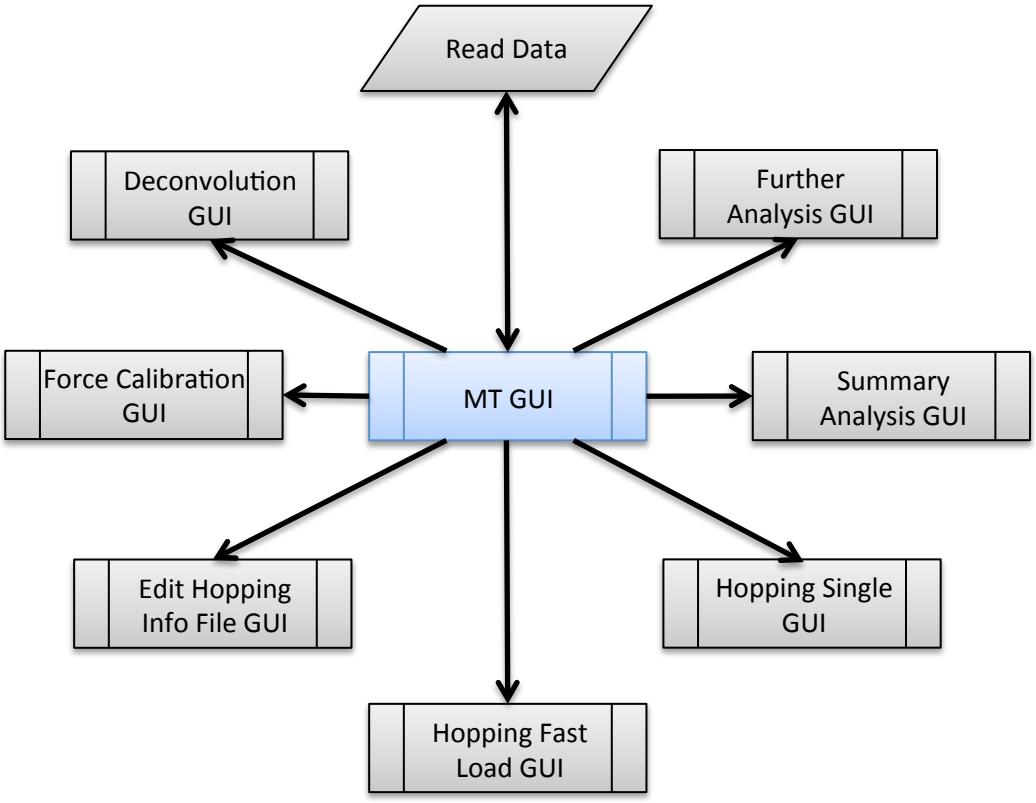

Figure 5.1: Flowchart of "MT GUI" according to DIN 66001:1983-12. Only large GUIs are presented. Every GUI has several sub-GUIs and functions. All large GUIs are able to receive data from the main GUI "MT GUI", but cannot transfer data back. "Read Data" is not a GUI but a function to load the measurement data.

5.2 “MT GUI” Main GUI

The main GUI “MT GUI” (Fig. 5.2) starts and controls all functions and sub-GUIs included in the software. Its main task is to load the data from a file and receive necessary input from the user to plot the data or transfer this information to other GUIs (Fig. 5.3). Besides loading the data, it is generally used for every measurement to get a first overview. Although its main task is to act as a control center of the whole software, it can also already perform simple tasks often used in daily MT data analysis.
“MT GUI” is able to read “.txt” files produced by the MT setup, modify them by options defined by the user, and plot the data. Here, different plot options are available, such as position (x,y,z) traces as a function of time or rotation, as well as histograms of the data. The user can choose if no reference bead, one reference bead or one out of a list should be subtracted, in the latter case depending on the distance between the beads. To handle plotting of large datasets, three simple but effective options are implemented: 1) it is possible to plot only selected beads to reduce the overall number of open MATLAB figures and hence the graphics board is significantly relieved; 2) it is possible to plot not all data points within one trace (e.g. only every second time point), reducing the number of plotted values; 3) for data plots as a function of time, the start and end time points can be selected, again resulting in less points within one figure.

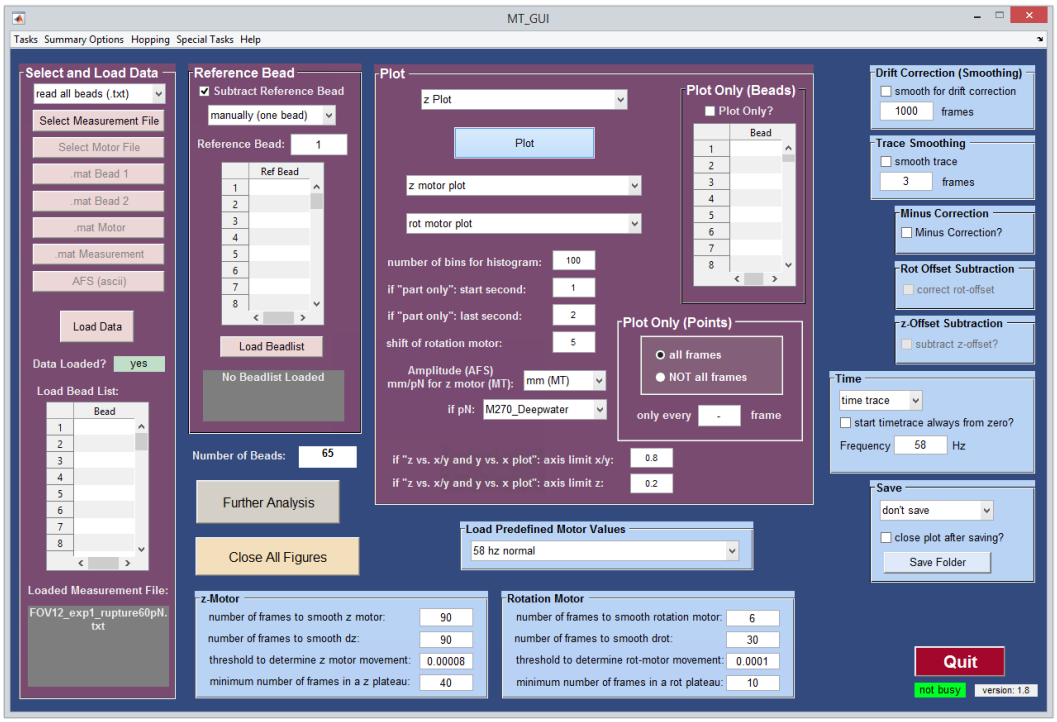

Figure 5.2: Main GUI of “MT GUI”. To improve user friendliness, functions and tasks are separated into different panels. If possible, options are disabled if a combination is not possible or data are not loaded. Other GUIs can be opened by the corresponding buttons.

“MT GUI” is able to automatically find plateaus with constant magnet position between motor movements. Due to the finite motor velocity (typically 5 cm/s for the magnet distance motor and 5 Hz for the rotation motor) the motor position obtained from the motor controller does not change instantaneously, but continuously. For both motors a slight overshoot which is

corrected within approximately half a second is observed. To define a constant motor plateau, the motor traces are smoothed by a moving average filter, the derivative is determined and again smoothed by a moving average filter. A threshold for the derivative is chosen to determine if the motors are moving. The number of frames for the filter depends strongly on the camera frequency and hence has to be adjusted.
To improve performance, “MT GUI” offers the possibility to save a “.txt” measurement file as a “.mat” MATLAB file, containing all bead and motor information. These “.mat” files can be loaded ≈ 20× faster than the “.txt” files, still containing the same information without any disadvantages. In both cases the full measurement is loaded and stored into the memory. If memory is an issue, it is possible to save every bead separately as “.txt” or “.mat” files. Two of these single bead files and one file containing the motor information can be loaded and analyzed.
Furthermore, the “MT GUI” can create an empty “summary file” that can be used to save many different types of information gained in the “Further Analysis GUI”, and analyzed with the “Summary Analysis GUI” (see section 5.3 and 5.4). The summary file is designed to be a MATLAB “struct” object and hence can be easily extended, making it adaptive for new tasks and functions of the GUI.
“MT GUI” contains many more option to adjust the plots, such as trace smoothing and drift correction, as described in the help file of the GUI.

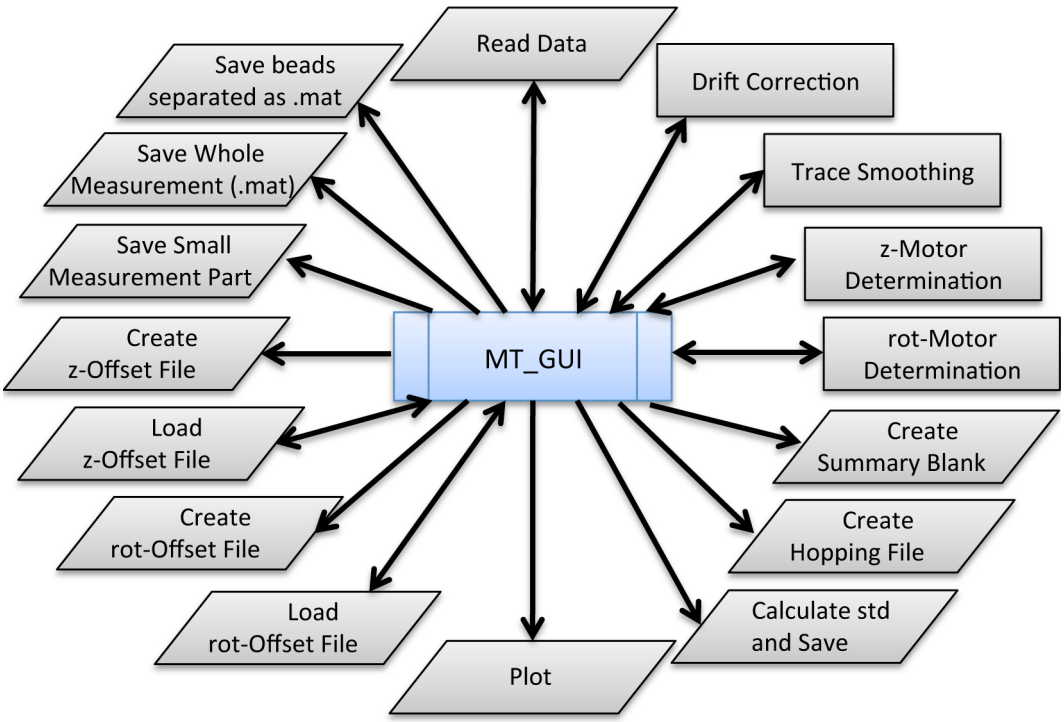

Figure 5.3: Flow chart of the main GUI of “MT GUI”. For clarity, only selected functions and small sub-GUIs are presented. The GUI controls all connected functions which cannot interact with each other, but only with the GUI. A detailed description of all functions can be found in the help file embedded in the GUI.

As an example of the sequential software part of the GUI, a programming language independent pseudo code for the plot task is presented. The pseudo code only consists of the GUI code, but no additional sub-functions. “MT GUI” is able to detect many mistakes by the user and returns

helpful error messages. However, for clarity most of the error checks are not included in this pseudo code. These tests include different controls, for example if the selected reference beads are available, or, more specific, if “z-offset subtraction” is activated, or if the number of beads in the measurement and in the z-offset file is the same. All “break” statements include an error message with help to fix the issue.

- **set busy tag to red**
- **only motor file plot option activated?**
  - **yes: break**
  - **no: continue**
- **measurement loaded?**
  - **yes: continue**
  - **no: break**
- **copy measurement data**
- **all beads loaded and selected?**
  - **yes: continue**
  - **no: get bead lists (loaded and selected) and combine**
- **minus correction?**
  - **yes: multiply z-trace with -1**
  - **no: continue**
- **subtract reference bead?**
  - **no reference bead: continue**
  - **single reference bead: subtract reference bead**
  - **multiple reference beads: find nearest reference bead and subtract it**
- **subtract z-offsets?**
  - **yes: subtract previously determined z-offsets**
  - **no: continue**
- **drift correction?**
  - **yes: smooth over long trace and subtract drift**
  - **no: continue**
- **smooth trace?**
  - **yes: smooth with moving average filter**
  - **no: continue**
- **time trace or frames?**
  - **time trace: use measurement time trace for time labels**
  - **frames: use frame number divided by the user specified frame rate for time labels**
- **which plot?**
  - **plot data according to specified plot option, e.g. z-trace vs. time**
- **save figures?**
  - **yes: save figures as specified**
  - **no: continue**
- **set busy tag to green**

5.3 “Further Analysis GUI”

“Further Analysis GUI” provides tools for a more detailed analysis. It can be directly opened from the “MT GUI” and receives reference bead corrected measurement data as well as the separated motor plateaus. The main task of the GUI is divided into two parts, with and without the possibility to load and save into a “summary file”.
The group of options where the results cannot be saved into a summary file is able to perform general analysis, such as an x-y histogram that can be used to visualise the x-y pattern, e.g. a circle in case of FOMT measurements [32]. In addition, it is possible to analyze the variance in x and y by three different methods, including the square root of the quadratic sum of both variances $\sqrt{x^2 + y^2}$ as well as a comparison of the asymmetry of both variances, by a direct visualisation and calculation of the ratio. Furthermore, the Allan deviation and variance can be calculated. This feature was used in chapter 4.3.2 to characterise the setup.
The second group of functions offer the possibility so save the results into a summary file. Furthermore, the beads that should be analyzed can be selected, reducing the total computational time. This can be achieved by manually selecting the bead numbers or loading the previously selected bead numbers defined in a summary file. The tasks of the panel include a manual selection of beads which ruptured during the measurement, e.g. to exclude these beads from further analysis. Additionally, it is possible to find the frame number of the rupture event. Furthermore, the length difference of the tether between two motor plateaus and the x-y fluctuation asymmetry can be determined. To quantify the lateral asymmetry based on the magnetic anisotropy of the bead [38, 321] (see section 4.3.4 for details), the measurement has to be performed at constant force for two rotation motor plateaus separated by 90°. “Further Analysis GUI” also contains a stepfinder [325]. Hereby, the measurement trace is separated first into the magnet distance plateaus and second into the rotation motor plateaus. All information about the steps, including the plateau level before and after the step as well as the frame number, can be stored into a summary file. Another task of the GUI is to fit the WLC model to the data. Hereto, a previously determined force calibration of the setup is used.
The latter two options have in common that they can use the previously determined last frame before a rupture event and therefore only analyze data up to this frame.

The functions connected to the summary files are used in chapter 7 to analyze protein unfolding and folding data. The options to analyze the variance of the tether can help to discriminate between a single and multiple tethers between the bead and the surface. The rupture analysis is used to determine the total tether lifetimes, the WLC fit to examine the persistence length as well as the contour length of the spacers and tethers, and the stepfinder is used to analyze the folding and unfolding events as presented in chapter 7.

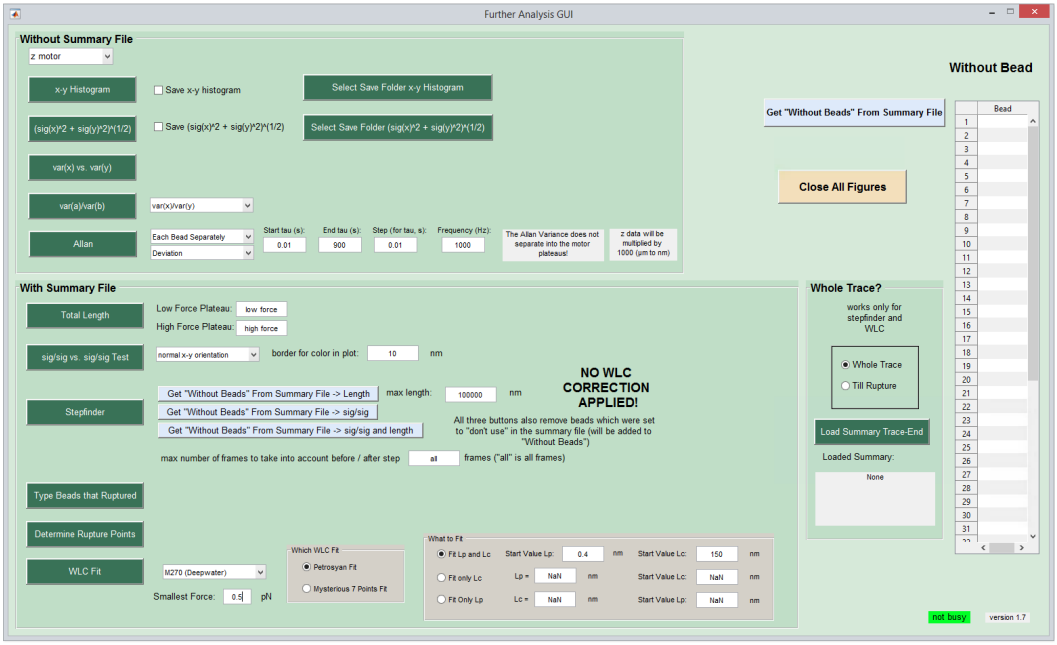

Figure 5.4: The “Further Analysis GUI” receives the measurement data from the “MT GUI” and performs more detailed analysis. Main tasks are to analyze the x-y pattern and determine features to identify specific from unspecific tethers, but also to perform WLC fits and find steps in the traces and export their information. The compatibility with the “summary file” enables to store the information for further analysis.

5.4 “Summary Analysis GUI”

The “Summary Analysis GUI” (Fig. 5.5) is able to extract the features saved in one or multiple “summary file(s)” and make the data and information visible for the user. Its main focus is to help analysing MT measurements of protein data (chapter 7) but can in general also be used for different kinds of MT data. The GUI is divided into two sections: the first one serves to distinguish specific beads, which should be analyzed further, from non-specific beads, the second part serves to present the user the information stored about the beads of interest. For all options, the data have to be prepared and saved with “Further Analysis GUI”.
The “Bead Selection” panel enables to preselect beads that should be analyzed. To this end, a maximum tolerable length can be defined and a test of the ratio of the x and y fluctuations can be performed. The variance test calculates the ratio of the x and y fluctuations $\frac{var(x)}{var(y)}$ of the first rotation plateau as well as the ratio $\frac{var(y)}{var(x)}$ of the second plateau. This can be used to discriminate between single and multiple tethers, where only single tethers behave as defined by the anisotropy of the beads. For the length exclusion, a WLC correction can be applied. Furthermore, it is possible to combine both tests and use only beads within an expected length range, which also fulfill the expected fluctuation behaviour.
The analysis options are separated into three parts, one panel (“Analysis”) containing basic visualisation of the data, another panel (“Step Analysis”) to analyze steps and rupture events, and a button (“WLC Analysis”) which opens a sub-GUI containing the analysis options for the WLC fits.
The “Analysis” panel is separated into three kinds of functions: plotting of a length histogram, visualization of the x and y fluctuations, and showing an overview of the number of rupture

events. In all cases it is possible to select individually which criteria of the “Bead Selection” panel should be applied.
For the length histogram, “Summary Analysis GUI” calculates the difference of the two positions previously determined with “Further Analysis GUI”. A WLC correction can optionally be applied. As for the bead pre-selection, a ratio of the variances of x and y can be calculated for two different rotation motor positions. The ratio can be visualized by a simple plot with one axis being the ratio $\frac{var(x)}{var(y)}$ of the first plateau and the other axis being the ratio $\frac{var(y)}{var(x)}$ of the second plateau. A color code separates the obtained values of the variances into small and large ones according to a manually selected threshold.

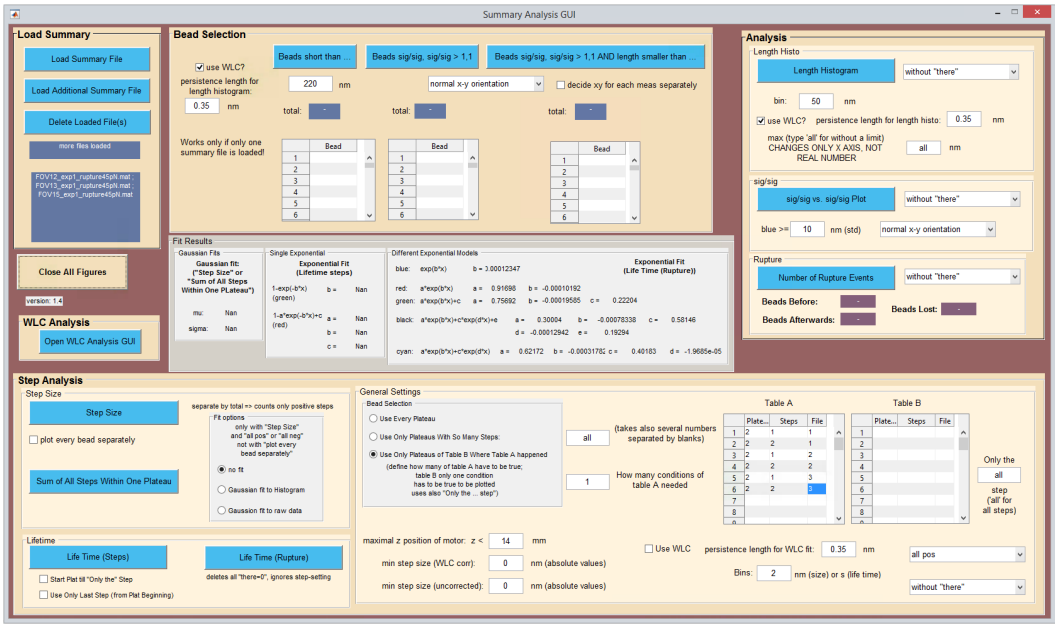

Figure 5.5: The “Summary Analysis GUI” is able to extract information saved in one or multiple summary files, apply selection rules for beads, and visualize the information. This includes a histogram of the length distribution, analysis of the x and y fluctuations, an overview of the number of ruptured beads, as well as step and WLC analysis including corresponding fits. Several criteria can be defined to distinguish if a bead should be analyzed or not.

The panel “Step Analysis” contains all options available to analyze steps previously detected and examined with the “Further Analysis GUI”, as well as a lifetime analysis. It is able to fit a Gaussian distribution to the histogram and raw data of the step sizes. Furthermore, the software allows to fit an exponential distribution with and without offset to the lifetimes of single plateaus between steps. The lifetimes of the tethers before their rupture can be fitted by single as well as double exponential distributions, with and without offset. The different exponential functions can be used to distinguish between reactions which could be completely detected and from reactions which are not fully captured (e.g. missing events at the beginning or end, see chapter 7).
In chapter 7 multiple steps within one plateau had to be analyzed. To facilitate this, the “Step Analysis” panel contains a sub-panel capable off precisely defining which steps should be analyzed. As general selection criteria, it can be distinguished between positive and negative

steps, the maximum allowed motor position can be used to delete all low force plateaus, and a minimum step size (with and without WLC correction) can be defined.
However, more precise criteria can be chosen. This includes an option to only analyze steps of a plateau that has a defined amount of steps. Here, also several numbers of steps can be selected, e.g. so that only plateaus with two or three steps are analyzed. To enable an even more complex selection of plateaus, it is possible to define criteria which have to be fulfilled, which are not limited to one single plateau. For example, it can be defined that a tether has to have one or two steps in the second and third plateau in order for the fifth plateau to be analyzed.
The analysis of the WLC fits previously performed in “Further Analysis GUI” is located in another sub-GUI (Fig. 5.6). It is able to extract the persistence and contour lengths and presents the distributions as histograms. The histogram as well as the raw data can be fitted with a Gaussian distribution.

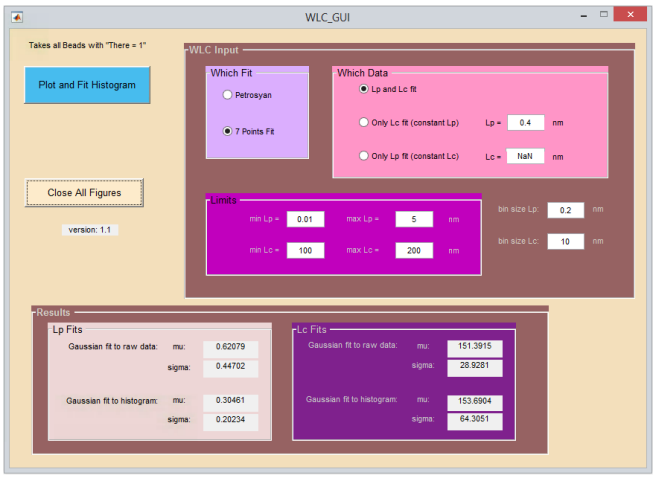

Figure 5.6: The “WLC GUI” is able to analyze WLC fits saved in one or several summary files. It extracts the persistence length as well as the contour length. A Gaussian fit to the histogram as well as to the raw data is performed.

For all kinds of fits possible with the “Summary Analysis GUI”, the user has to select by himself which one is suitable for his model. In general, the exponential models including an offset variable are capable to compensate for a limited total measurement time, however, for a specific system the physics behind the mathematical models has to be interpreted by the user (see chapter 7). Furthermore, the Gaussian distribution fits to the histogram and to the raw data can, but do not have to, lead to very similar results. In general, the fits to the histogram are more robust against outlier, however the manually selected bin size can have an impact on the result. Again, the user has to decide by himself which fit describes his data more precisely. The “Summary Analysis GUI” was used in chapter 7 to analyze protein folding and unfolding data.

5.5 “Force Calibration GUI”

The “Force Calibration GUI” can be used to calculate and calibrate the force of an MT setup. The Allan variance is used for the calibration. However, for completeness, and to give the user an overview, the force is also calculated with the PSD [313, 314, 316], but not used for the final, different, exponential fits. The physics behind, and limitations of the force calibration are explained in chapter 4.3.3. In brief, the x or y fluctuations of a bead tethered to a DNA molecule, combined with the extension of the molecule, can be used to determine the applied force originating from the magnetic field gradient. This procedure has to be repeated for different distances between the magnets and the flow cell and the resulting forces as a function of the magnet distances are commonly fitted by one or several exponential models [25, 33, 38, 313]. For the force calculation, the panel “Calculate and Save” offers to choose the coordinate (x or y) that should be analyzed (see chapter 4.3.3). Beads can be excluded from the force calibration (e.g. stuck reference beads bound to the surface) and the resulting forces of the remaining beads are saved in separate ASCII files with the bead number included in the file names. Hence the user can easily modify each “force-file” of every bead, if necessary. This feature is normally used to delete motor plateaus of single beads if the bead got temporarily stuck while touching the surface at very low forces, hence resulting in wrong force values.

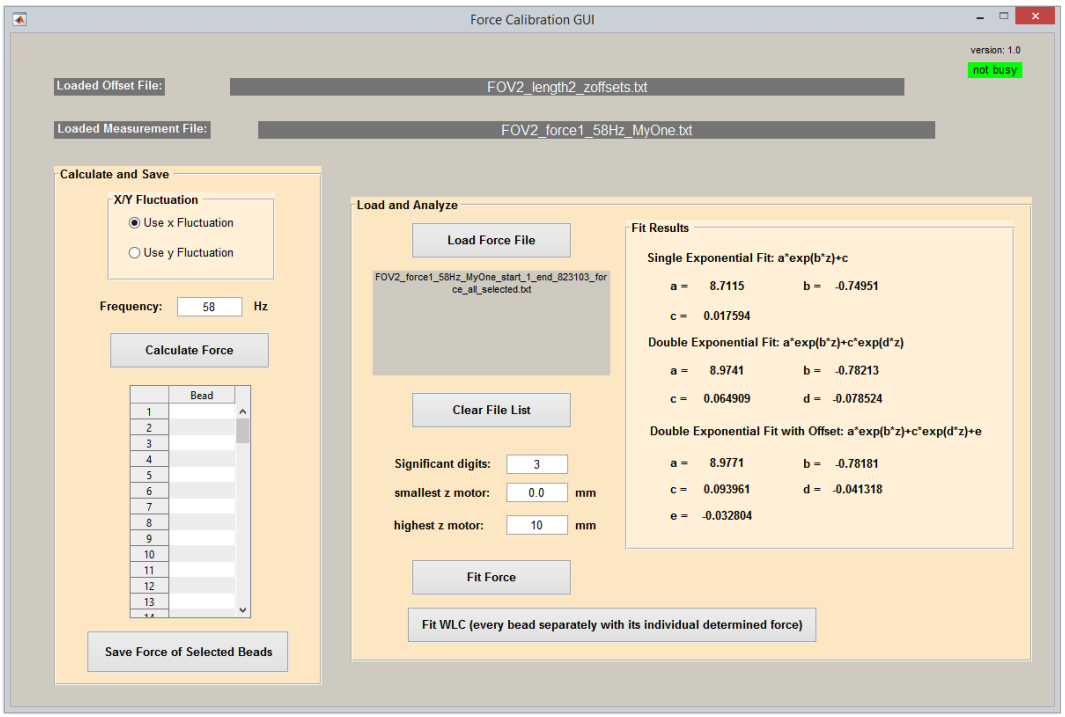

Figure 5.7: The “Force Calibration GUI” is able to calibrate the force based on Brownian motion. The forces are calculated with the Allan variance at a fixed distance between the magnets and the flow cell and can be saved in an ASCII file. Three different types of exponential models can be fitted to the data, a single exponential model with an offset, a double exponential function without offset and a double exponential with offset. For a fit of the WLC model to every single bead, the force of the particular bead is used.

In a second step, the panel “Load and Analyze” serves to extract the pre-calculated forces and distances between the magnets and the flow cell. The force is fitted with three different

exponential models, a single exponential function with offset, a double exponential model without offset and a double exponential model with offset. Furthermore, the range of the distances between the magnets and the flow cell to be taken into account can be chosen. For the force calibration the mean value of all loaded bead files is used. However, a fit of the WLC model to every single bead individually with its individual calibrated force can be performed and the persistence length and contour length extracted.
The different force calibrations of the MT setup in chapter 4 were performed with the “Force Calibration GUI”. For the composite M270 calibration curve, the fitting range of the motor position was limited as described in the corresponding chapter and finally manually combined. Different setups are calibrated with different fit functions [26, 33, 38], hence the GUI uses different exponential models. Therefore, the user has to decide by himself which fit he should use for the final calibration. For a more detailed description of a force calibration of an MT setup, see section 4.3.3.

5.6 “Hopping Single GUI”

The “Hopping Single GUI” can be used to analyze an MT measurement trajectory, which is often jumping between two different states in the extension while the magnets do not move or rotate (see chapter 6). The analysis algorithm is close to Ref. [26], but improved in stability and usability. A detailed description, especially regarding the biological relevance, can be found in chapter 6. Here, only the functions implemented into the GUI are described. The software focuses on dwell time analysis and facilitates extraction of the probability to be in one state of the two state system. In brief, it is possible to analyze a measurement trace which consists of consecutive rotational magnet positions. Every measurement trajectory, which is jumping between two states in the extension at constant magnet position, is separated by one out of one hundred equally separated trial threshold values over the full range of extension values (see Fig. 6.2a in chapter 6). The threshold with the local maximum of the first derivative of the counts in the upper state with respect to the trial thresholds is used as the optimal threshold. Only trial thresholds within the two peaks of the extension histogram are considered as feasible thresholds. This reduces artifacts of global maxima of the derivation at the limits of the extension histogram. If zero or more than one optimal threshold is found (e.g. two local maxima due to noise), the user can manually select a threshold.
For every motor position a probability to be in the upper state is calculated and fitted by a two state model, which is of importance for the buckling transition analysis in chapter 6 [26, 50]:

$$P_{post} = \frac{1}{1 + e^{\frac{C}{L_C}\cdot(2\pi)^2\cdot\frac{(\Delta Lk_b - \Delta Lk)\cdot\Delta Wr_b}{k_B T}}} \tag{5.1}$$

with the two fitting parameters ΔLk_b and ΔWr_b. For a detailed description of all parameters see chapter 6.
The time trace of every magnet position is separated by the threshold into binary states and the dwell times of both states are fitted with a single exponential model. Furthermore, the resulting mean dwell times of the upper and lower states are fitted by an Arrhenius relationship motivated exponential model as a function of the magnet position. Hereby, the crossing point

of both, independent, fits of the two states is determined (Fig. 6.7 and 6.2d in chapter 6). As described in chapter 6, the exponential fits lead to ΔWr_{pre} and ΔWr_{post} and consequently can be used to characterize a transition state in rotational degree of freedom.

“Hopping Single GUI” focuses on the analysis of single beads. Its difference and advantage compared to the quite similar “Hopping Fast Load GUI” (section 5.7) is the higher flexibility and larger amount of available options and tasks. However, this is achieved at the expense of fast access to predefined analysis settings. For this reason, the GUI is mainly used for first analysis, finding the perfect analysis settings and performing error and stability tests.
The plateaus of the rotational motor have to be manually selected by the user. However, for simplicity and help, “Hopping Single GUI” shows a list of automatically detected plateaus which are calculated from the motor file of the measurement. These plateaus can slightly differ from expected values due to uncertainties of the automatic plateau finding algorithm, and in addition, small readjustment movements of the motor. All motor plateaus existing in the measurement file have to be selected. Nevertheless, if required, it is possible to delete single plateaus with the “Delete Plateaus” panel. The options for error checking and stability tests further include, that the thresholds cannot only be automatically set, but also manually selected. A correction for finite acquisition times can be applied [326]. The MT setup described in chapter 4, which was used for the measurements presented in chapter 6, uses a refractive index correction of $\frac{n_{water}}{n_{oil}} = 0.88$, i.e. the quotient of the refractive index of the immersion oil and the buffer. However, an admixture, such as glycerol, can change the refraction index [327]. Therefore, the refractive index can be selected in “Hopping Single GUI”, which multiplies the extension values with a correction factor. The raw data can be filtered with different filter widths of a moving average filter.
Furthermore, a set of stability tests can be performed. These tests are used to examine the robustness of the analysis of the hopping traces. To test the influence of the acquisition rate of the setup, it is possible to take the mean value of two consecutive data points, but every data point only once. In other words, the original first two frames result in the first new data point, the original third and fourth frame result in the new second data point etc. Consequently, the effective frame rate is reduced by a factor of two. Furthermore, it is possible to reduce the total amount of frames to be analyzed. Hereby, only a part of a trace is evaluated, but within this part all frames are analyzed. This can be used to test if the total measurement time was long enough to extract robust results. Finally, the thresholds dividing the traces into two plateaus can be randomly shifted in a range of up to 5 % of the maximal trace fluctuation range, or only to higher or lower values by a percentage freely selectable by the user. Thus, the sensitivity for the chosen thresholds can be evaluated.

This GUI was used in chapter 6. For a subset of data, different filters were analyzed and the stability tests performed. Furthermore, to take care of the different refraction indices, the analysis of the glycerol data was performed with “Hopping Single GUI” .
Since “Hopping Single GUI” was developed mainly for the requirements of the analysis of the data presented in chapter 6, so far it only allows for analysis of consecutive rotational magnet positions. However, a modification and extension to also analyze the magnet distance positions is easily possible and can be implemented.

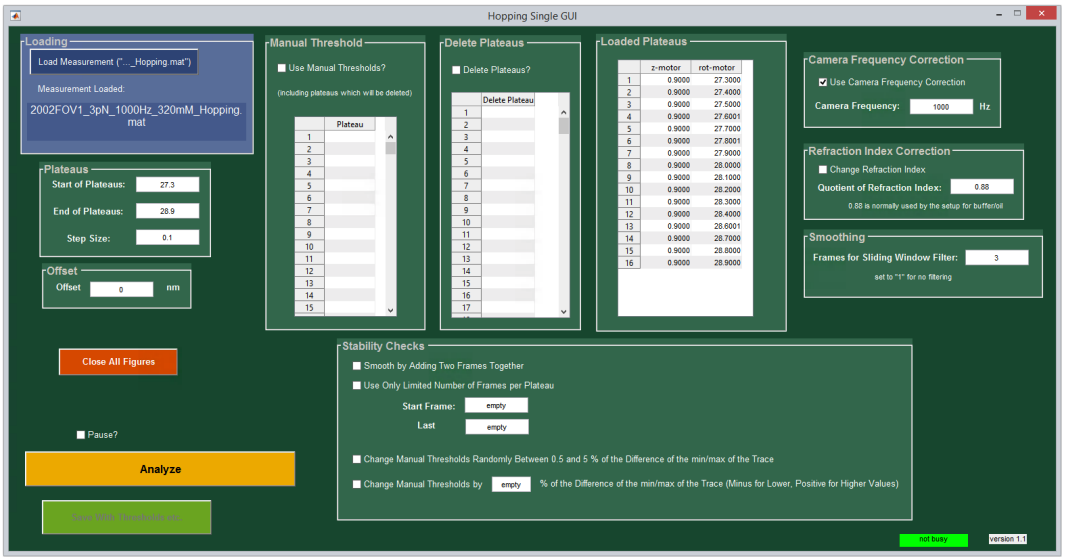

Figure 5.8: With “Hopping Single GUI” single measurements with a trajectory jumping between two separated extension states can be analyzed. Thereto, a threshold is selected to divide the extension fluctuations into two plateaus. Dwell time analyzes can be performed and related rotational information can be extracted. Different stability tests and options are available.

5.7 “Edit Hopping Info File GUI” and “Hopping Fast Load GUI”

The software package includes the two GUIs “Edit Hopping Info File GUI” and “Hopping Fast Load GUI” to analyze hopping traces with predefined settings. The former is used to specify the settings and save the information in a “.mat” file, while the latter can load the information file as well as the corresponding measurement files and analyze the data the same way as described in section 5.6. For the easy and fast selection of one measurement with its corresponding settings, one single number is allocated to every available combination of measurement and settings. However, small changes can be applied by the “Quick Change” panel. The two GUIs enable to handle and reanalyze whole data sets with a minimum of external input. This is mainly used for two different reasons: Later implemented changes in the software code that have an influence on the result, and analyzing whole data sets with different settings.
The underlying algorithm is the same as described in section 5.6 and consequently the physical and biological relevance is again described in chapter 6. In brief, dwell time analysis can be performed and related rotational information can be extracted.

Both GUIs were used in chapter 6 for the standard analysis necessary for all molecules as well as for specific comparisons, e.g. the correction of the finite acquisition time (Fig. 6.17 in chapter 6). As described for “Hopping Single GUI”, due to the close relation of both GUIs to chapter 6, only options for analysis of rotational motor positions have been implemented. However, with small changes the GUI can be generalized to analyze both rotational and translational motor plateaus.

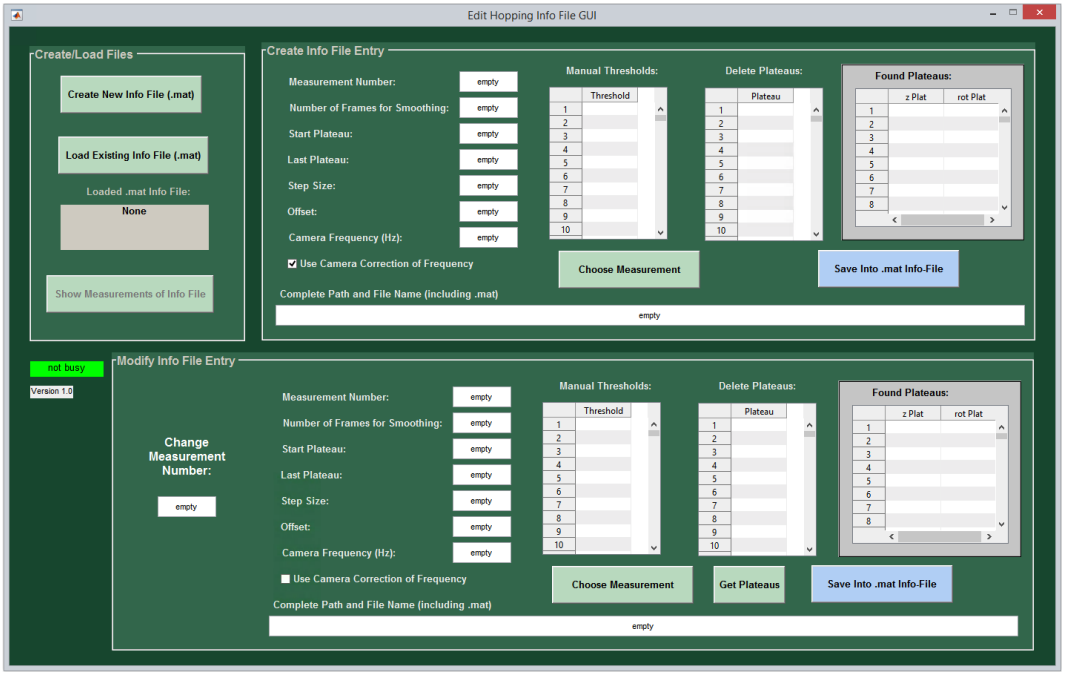

Figure 5.9: “Edit Hopping Info File GUI” enables the user to create and modify information files, which contain all required information to analyze MT hopping traces with the related GUI “Hopping Fast Load GUI”.

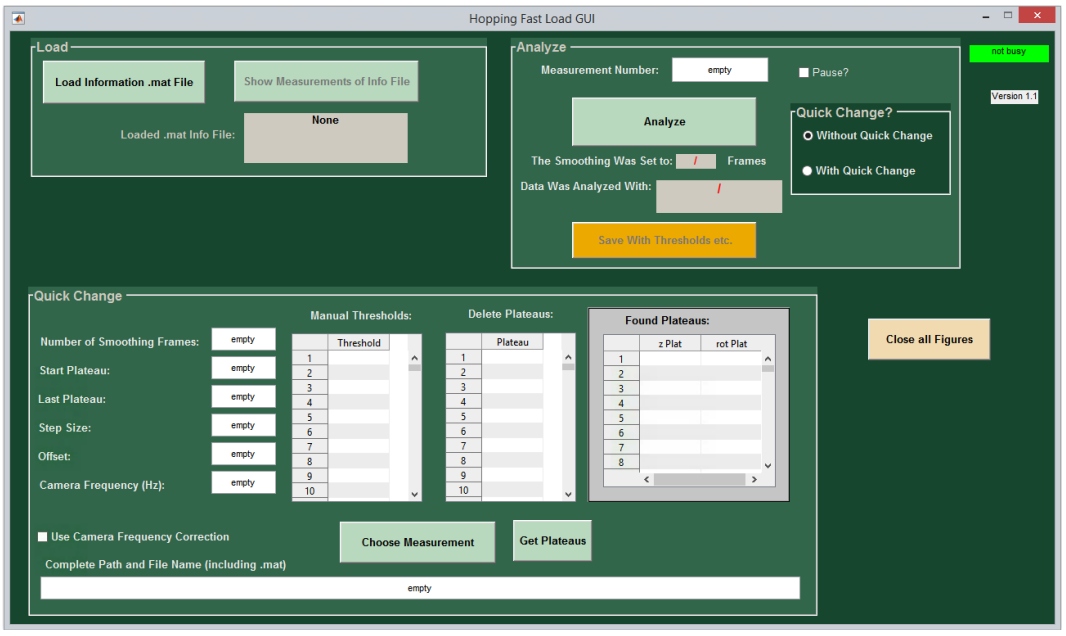

Figure 5.10: Based on an information file created with “Edit Hopping Info File GUI”, “Hopping Fast Load GUI” is able to analyze MT trajectories jumping between two different states of extension. The information file contains all necessary information and hence no further input is need. Nevertheless, with the panel “Quick Change” settings can be temporarily modified. “Hopping Fast Load GUI” enables a fast analysis of many data sets with different settings.

5.8 “Deconvolution GUI”

The software “Deconvolution GUI” is able to deconvolve MT time traces of a two state system and to extract the underlying energy landscape by the inverse Boltzmann approach. The deconvolution method is described in chapter 6 and follows the approach of Woodside et al. [328–330], applying the non-linear iterative method of Jannson [331]. In brief, the goal of the deconvolution is to obtain an extension histogram without the blur of the setup noise. First, the extension trace as a function of time is binned resulting in a histogram. This extension histogram of the raw data is deconvolved with the instrument response function S(z):

$$\hat{o}^{k+1}(z) = \hat{o}^{k}(z) + r[\hat{o}^{k}(z)] \cdot (i(z) - S(z)\ x\ \hat{o}^{k}(z)) \tag{5.2}$$

with

$$r[\hat{o}^{k}(z)] = r_0 \cdot (1 - 2 \cdot |\hat{o}^{k}(z) - \frac{1}{2}|) \tag{5.3}$$

Hereby $\hat{o}^{k}(z)$ is the deconvolved histogram after k iterations, *i(z)* the original, not deconvolved histogram and $r[\hat{o}^{k}(z)]$ a function that ensures staying in the physical boundaries with the constant r_0 controlling the speed of convergence. Furthermore, r_0 is essential in order not to overshoot the global minima of the deconvolution, but also to not get stuck in local minima caused by inhomogeneities of the histogram.

To enable fast and easy deconvolution while keeping great flexibility for different measurements, besides default settings, the software offers the user to control many options manually. As starting histogram of the raw data, a histogram can be created by selecting the bin size, or alternatively the kernel density estimation can be calculated. As setup response function, a Gaussian distribution is assumed, which is true for DNA in MT for a large force range and only differs slightly at low and high forces [332]. The width of the Gaussian distribution has to be selected manually and hence can be adjusted e.g. to capture different fluctuation amplitudes of DNA molecules at different forces [72, 333]. The number of iterations as well as r_0 can be selected manually. It is recommended to adjust r_0 depending on the error plots determined after the current deconvolution. Optionally, it is possible to smooth the original histogram, the deconvolved histogram after every iteration, and the final histogram with a boxcar filter. To reduce the impact of outlier in the raw data, e.g. caused by errors of the tracker, the lower and upper limits of the raw data can be defined. This option should be used with care in order not to accidentally distort the data.
The analysis can be performed on only one or all motor plateaus. After deconvolution, the energy landscape is determined by the inverse Boltzmann approach and the minima and maximum of the energy landscape can be automatically determined and saved together with the histograms and energy landscapes.

The GUI “Deconvolution GUI” was used in chapter 6 to deconvolve the measurements and determine the energy landscapes. It is able to deconvolve the measurement trace, determine the deconvolved energy landscape (as well as the energy landscape of the raw data) and save all information into a file. For further analysis, the saved file can be used to extract more biologically and physically relevant information (see chapter 6).

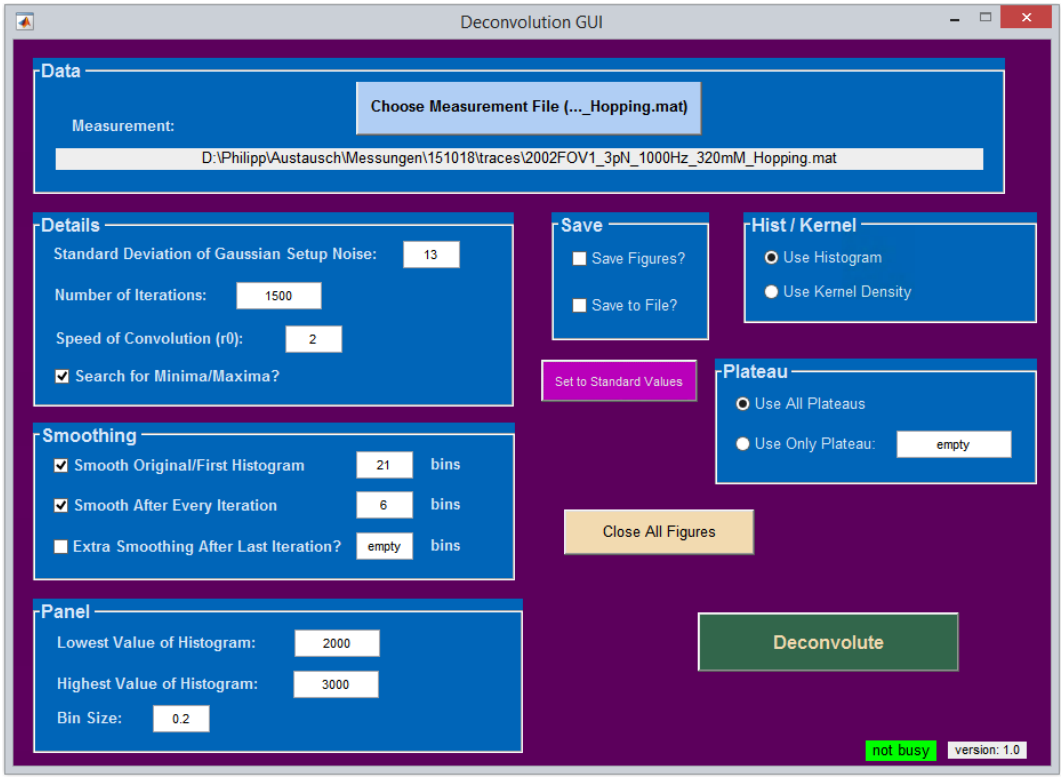

Figure 5.11: “Deconvolution GUI” is a software to deconvolve an MT extension trace as a function of time. It is based on the non-linear iterative approach of Jansson [331]. An extension trace is first converted into a histogram by a manually selected bin width or alternatively the kernel density is calculated. Subsequently, this histogram is iteratively deconvolved with the instrument response function.

Chapter 6

The Dynamics and Energy Landscape of DNA Plectoneme Nucleation

6.1 Summary

DNA buckling is the fundamental step for plectoneme nucleation and supercoil dynamics that are critical in the processing of genetic information. Here we systematically quantify DNA buckling dynamics using high-speed magnetic tweezers. Buckling times are ≈ 10-100 ms and depend exponentially on both applied force and twist. By deconvolving measured time traces with the instrument response, we reconstruct full 2D extension-twist energy landscapes of the buckling transition that reveal an asymmetry between the pre- and post-buckling states and suggest a highly bent transition state conformation.[1]

[1]This chapter is published by Walker *et al.* on "bioRxiv.org" (DOI: https://doi.org/10.1101/280719) and accepted for publication in *Physical Review E*. For this chapter I performed the measurements, analyzed the data, implemented the deconvolution procedure, and wrote the manuscript with input from of all authors.

6.2 Introduction

DNA stores genetic information as a linear sequence and consequently needs to be very long. To achieve compaction in the narrow confines of the cell, while providing local accessibility for readout and processing, genome architecture is dynamically controlled [300, 334–336]. Regulation is achieved by organizing DNA into domains, wherein DNA rotational motion is constrained. As a result, the number of links between the two single strands of the double helix, called the linking number Lk, is invariant. The topological quantity Lk partitions into the geometric parameters twist Tw and writhe Wr [337, 338],

$$Lk = Tw + Wr \tag{6.1}$$

where Tw quantifies the torsional deformations and strains of the helix, and Wr the coiling of the double helix axis in 3D. Specialized proteins maintain cellular DNA in a supercoiled state, i.e. Lk deviates from the torsionally relaxed value Lk^0 in vivo. Through topological coupling, the linking difference $\Delta Lk = Lk - Lk^0$ affects DNA structure both locally and globally, via changes in twist ΔTw and writhe ΔWr, respectively [300, 339, 340]. Supercoiled DNA, in general, is both locally untwisted and takes on interwound, plectonemic configurations of the double helix axis. The structure and mechanics of plectonemic DNA has been probed extensively by electron and atomic force microscopy of circular DNA molecules and DNA tethered between a surface and magnetic beads in magnetic tweezers (MT) (Fig. 6.1a) [12, 50, 341]. In contrast, the dynamics of plectonemes remain largely unexplored, despite their importance in the context of regulation and long-range communication in the cell [342].
A first direct measurement of plectoneme dynamics by fluorescent imaging [120] found that, within the time-resolution of the approach (20 ms), a plectoneme can disappear at one site and give rise to the appearance of a new plectoneme separated by several microns along the chain. The dynamics of this process are proposed to be rate-limited by nucleation of the newly formed plectoneme, i.e. by DNA buckling, in particular since removal of the plectoneme has been shown to be very fast [343]. Estimates for the characteristic time scale of DNA buckling range from 30-80 ms in magnetic tweezers (MT) [26, 50], to ≈ 100 ms in an optical torque wrench [344, 345], and are, surprisingly, ≈ 2 orders-of-magnitude faster than for double-stranded RNA [26]. However, a direct comparison of the different measurements is complicated as the dynamics depend on ionic strength and applied stretching force. The lack of a precise quantitation of DNA buckling dynamics is at least in part due to the difficulty of observing fast ≈ ms time scale transitions using camera based detection.
Here, we have used high-speed magnetic tweezers to quantify the kinetics of supercoil nucleation under a range of forces, ionic strength, and bead sizes. Using a deconvolution approach, we reconstruct the 2D energy landscape of the buckling transition as a function of DNA extension and twist. We propose a geometric model for the transition state and discuss how local disturbances of the helix can impact the energy landscape of supercoiling.

6.3 Results and Discussion

Bead tracking with kHz time-resolution accurately quantifies DNA buckling transitions. In our MT setup, linear ≈ 7.9 kbp DNA molecules are tethered between the flow cell surface and superparamagnetic beads, via multiple attachment points at both ends to assure

torsionally constrained attachment (Fig. 6.1a and Supplementary Information). We note that our DNA length approximately corresponds to the size of topological DNA domains *in vivo*, ≈ 10 kbp [346]. Using external magnets, one can apply precisely calibrated forces [12, 25, 310] and control the linking number of the DNA. On increasing ΔLk at forces < 6 pN [51], DNA undergoes a buckling transition and starts to form plectonemes, causing a decrease in the apparent tether extension with increasing ΔLk (Fig. 6.1b). If DNA molecules are held at a fixed ΔLk close to the buckling point ΔLk_b, the molecules undergo thermally activated transitions between the torsionally strained, but extended pre-nucleation state, and the post-nucleation state, with the first, minimal plectoneme formed (Fig. 6.1c). Here, we draw on improvements in both camera and illumination hardware as well as tracking software [35, 37, 299] to study supercoil nucleation by tracking at 1 kHz in MT. Simulations show that our experimental configuration can resolve transitions on the time scale of ≈ 10 ms or less, with an error of at most 10 % (Fig. 6.1d and Fig. 6.5 in Supplementary Information). In addition, from analysis of experimental extension time traces of torsionally relaxed DNA tethers, we find the characteristic ("corner") frequencies at 2, 3 and 4 pN to be 98 ± 3 Hz, 161 ± 6 Hz and 230 ± 12 Hz (means and standard errors from 4 independent measurements at each force), respectively, corresponding to characteristic time scales of 10, 6, and 4 ms, again suggesting that events on a time scale of ≈ 10 ms can be detected (Fig. 6.6 in Supplementary Information).

Kinetic analysis of DNA buckling. To quantify the extension time traces, we separate the extensions into two states by thresholding [38]. Upon stepwise increasing ΔLk, the time spent in the buckled state systematically increases at the expense of the population of the extended state (Fig. 6.2a). We analyze our experimental data using a two-state model [38, 50], where the energy difference between the pre- and post-buckling states is related to ΔLk and the probability to be in the post-buckling state P_{post} is given by

$$P_{post} = \left(1 + e^{(2\cdot\pi)^2\cdot(\frac{C}{L_C})\cdot(\Delta Lk_b - \Delta Lk)\cdot\Delta Wr_b/(k_B\cdot T)}\right)^{-1} \tag{6.2}$$

where C is the effective torsional stiffness (approximated in the Moroz-Nelson model [79] or using data from direct torque measurements [46], see [38]), L_C the contour length, ΔLk_b the buckling point, i.e. the number of applied turns for which $P_{pre} = P_{post}$, $\Delta Wr_b = Wr_{post} - Wr_{pre}$ the number of turns converted from twist to writhe during buckling, k_B the Boltzmann constant and T the temperature. Fitting of Eqn. 6.2 to the experimentally observed P_{post} as a function of ΔLk yields ΔLk_b and ΔWr_b (Fig. 6.2b). Over the force range investigated, ΔWr_b remains essentially constant (Fig. 6.2c), in agreement with previous experimental results for both DNA [50] and RNA [26]. We find that ΔWr_b increases by ≈ 33% on increasing the monovalent salt concentration from 100 to 320 mM, again in quantitative agreement with previous findings [26, 50].

Having characterized the equilibrium properties of the buckling transition, we now focus on its dynamics, by analyzing the dwell times in the DNA extension traces. At each imposed ΔLk, the dwell time distributions for both the pre- and post-buckling state are well described by single exponential fits, which yield the mean lifetimes τ_{pre} and τ_{post} (Fig. 6.7 in Supplementary Information). The lifetimes τ_{pre} and τ_{post} follow an Arrhenius relationship with an exponential

dependence on ΔLk (Fig. 6.2d) [50]:

$$\tau_{pre} = \tau_{buck} \cdot e^{-(2\cdot\pi)^2\cdot(\frac{C}{L_C})\cdot(\Delta Lk_b - \Delta Lk)\cdot\Delta Wr_{pre}/(k_B\cdot T)} \tag{6.3}$$

where τ_{buck} is the lifetime at the midpoint of the buckling transition ΔLk_b, and ΔWr_{pre} is the change in writhe from the pre-buckling state to the transition state. We used a similar expression for τ_{post} with ΔWr_{pre} replaced by $-\Delta Wr_{post}$, the rotational distance to the transition state from the post-buckling state (Fig. 6.1c).

Fits of Eqn. 6.3 to τ_{pre} and τ_{post} were used to determine the characteristic buckling time τ_{buck} as well as ΔWr_{pre} and ΔWr_{post} (Fig. 6.2e). The buckling time τ_{buck} increases with bead size, consistent with a model where the bead fluctuations are transmitted through the DNA molecule [347] (Fig. 6.8 in Supporting Information). For a fixed bead size, previous work [50] found a weak dependence of the characteristic buckling time on DNA length (comparing 1.9 and 10.9 kbp DNA gave a difference of 2-fold in the buckling times); our data for 7.9 kbp DNA under the same conditions falls between the previous measured buckling times, as would be expected for the intermediate length (Fig. 6.2f, differently colored points at 4 pN, 320 mM). For a fixed bead size and DNA length, the characteristic buckling time τ_{buck} is strongly dependent on force F, and is well described by an exponential model (solid lines in Fig. 6.2f, reduced X^2 = 0.4 and 0.3 for 100 and 320 mM NaCl, respectively):

$$\tau_{buck} = \tau_{buck,0} \cdot e^{F\cdot\Delta x/(k_B\cdot T)} \tag{6.4}$$

with Δx the distance to the transition state and $\tau_{buck,0}$ the buckling time in the absence of applied force. From a fit of Eqn. 6.4, we obtain $\tau_{buck,0}$ for DNA to be 8 ± 2 ms and 10 ± 3 ms (values and standard errors from the exponential fit, Fig. 6.2f) for 100 and 320 mM NaCl, respectively. These values agree with one another, within experimental error, and are close to the extrapolated buckling times at zero force for RNA [26] ($\tau_{buck,0}$ = 13 ± 7 ms and 52 ± 38 ms at 100 mM and 320 mM NaCl, respectively). The large differences between the buckling times τ_{buck} for DNA and RNA under tension can primarily be attributed to differences in Δx, which is much smaller for DNA than for RNA under otherwise identical conditions (Fig. 6.2f inset), supporting our previous hypothesis that the striking difference in the buckling dynamic between DNA and RNA is mostly driven by differences in the transition state. We note that supercoil nucleation does not merely depend on force, but on torque as well (the different points in Fig. 6.2f are not only at different forces, but also at different torques, since the buckling point ΔLk_b shifts significantly with applied force). Therefore, Δx is a value that quantifies the position of the energy barrier in a simplified 1D representation of the energy landscape. Its value does not directly reflect a physical position of the transition state, but should rather be interpreted as a characteristic length that describes the cooperativity of the transition. A full description of the transition requires considering the energy landscape along rotational (twisting, writhing, and linking) and extension (DNA end-to-end distance) degrees of freedom, see below.

To quantify the energy landscape of supercoil nucleation along the rotational degree of freedom, we first determined the distances to the transition state from the pre-buckling and post-buckling states ΔWr_{pre} and ΔWr_{post} from fits of Eqn. 6.3 (Fig. 6.2d). Both ΔWr_{pre} and ΔWr_{post} change systematically with salt concentration, but remain approximately constant

with increasing force (Fig. 6.2e) and bead size (Fig. 6.8 in Supporting Information). Notably, ΔWr_{post} and ΔWr_{pre} add up to the measured value for ΔWr_b, within experimental error (Fig. 6.9 in Supporting Information), as would be expected, since they are measured along the same coordinate. The ratio $\Delta Wr_{pre} / \Delta Wr_{post}$ is independent of force and ionic strength, within experimental error, and suggests the transition state along the writhing degree of freedom to be closer to the pre-buckling state than the post-buckling plectonemic state ($|\Delta Wr_{pre} / \Delta Wr_{post}|$ = 0.68 ± 0.05 and 0.65 ± 0.03 for 100 mM and 320 mM NaCl, respectively). Since the transition occurs at a constant ΔLk, the measured ratio of $|\Delta Wr_{pre} / \Delta Wr_{post}|$ implies that the transition state in the twisting degree of freedom is closer to the post-buckling state than the pre-buckling state.

Energy landscape reconstruction at buckling equilibrium. To obtain a full quantitative description of the buckling transition and to account for its mutual dependence on extension and rotation, we reconstructed the 2D free energy landscape $\Delta G(z, \Delta Lk)$. At a given ΔLk, $\Delta G(z) = -k_B \cdot T \cdot ln[p(z)]$ with the probability density $p(z)$ [328]. To account for the effect of the force probe, we deconvolved the extension histogram of the DNA tether with the setup response function $S(z)$ [328–331]. For the deconvolution procedure, we used the bead fluctuations of torsional unconstrained DNA molecules at the same force and buffer conditions as the instrument response function (see Supporting Information). The deconvolution sharpens the extension histogram (Fig. 6.3a), which is then converted to the corresponding 1D energy landscape to enable the analysis of the buckling transition along the extension coordinate. We compared the energy landscape obtained by deconvolution to the energy barrier reconstructed by a different approach, based on the splitting probability [348, 349] with no need for deconvolution [329], and obtained very good agreement between the two methods (see Supporting Information and Supplementary Fig. 6.10). Finally, by assembling a series of 1D extension energy landscapes while systematically varying ΔLk, we reconstruct the full 2D extension-linking number energy landscape (Fig. 6.4b).

We analyze the reconstructed energy landscape focusing on the extension coordinate at ΔLk_b, i.e. at the point where the forward and backward rates are equal [38]. At ΔLk_b, the distances to the transition state along the extension coordinate from the pre- and post-buckling state minima, Δz_{pre} and Δz_{post}, were found to be dissimilar, independent of force (Fig. 6.11 in Supporting Information). The values suggest that the transition state along the extension coordinate is closer to the pre- than to the post-buckling state (Fig. 6.3d). Notably, Δz_{pre} and Δz_{post} add up to the total jump size as determined directly from extension distributions (Fig. 6.12 in Supporting Information). At ΔLk_b, the reconstructed energy landscape (Fig. 6.3b and Fig. 6.12b in Supporting Information) shows a broader energy minimum for the post-buckling state compared to the pre-buckling state, corresponding to a larger conformational space after buckling. The broader energy minimum after buckling corresponds to a smaller curvature (Fig. 6.13 and 6.14 in Supporting Information) and, applying Kramers theory [330, 350, 351], to a smaller attempt rate k_0 for barrier crossing at buckling equilibrium compared to the pre-buckling state. Since the forward and backward rates are identical at ΔLk_b, the difference in k_0 is compensated by different barrier heights $\Delta G^{\ddagger}_{pre}$ and $\Delta G^{\ddagger}_{post}$ (Fig. 6.11c,f and 6.13c,d in Supporting Information) measured from either side of the transition state. We conclude that the energy barrier, measured along the extension coordinate, is significantly asymmetric and steeper for buckling than for plectoneme removal.

The reconstructed energy landscape enables, in addition, the calculation of diffusion coefficients for barrier crossing, again from Kramer's theory (see e.g. Equation 10 from Ref. [330]). We find diffusion coefficients D $\approx 10^{-15}$ m^2/s, whereby the diffusion constants for the pre- and post-buckling wells are essentially within error, but slightly force and salt dependent. Values of D $\approx 10^{-15}$ m^2/s are in the same order of magnitude as reported for protein relaxation times and refolding landscapes [352, 353] and smaller than DNA hairpin diffusion coefficients [330]. The estimated diffusion coefficient of 10^{-15} m^2/s implies significantly slower diffusion than what would be estimated for purely translational diffusion of DNA with length corresponding to the loop size, which is in the range of $\approx 10^{-11}$-10^{-12} m^2/s [354]. Thus, diffusive barrier crossing is several orders of magnitude slower as compared to simple translational diffusion, which in turn implies substantial internal friction in the DNA as it evolves to the transition state.

The energy landscape reconstruction is not limited to the extension coordinate (Fig. 6.3); we can also quantitatively describe the energy landscapes along the rotational degree of freedom (Fig. 6.4a). Using the values for ΔWr_{post} and ΔWr_{post} (Fig. 6.2e) to determine the relative position along the writhe coordinate and the free energy barrier heights from the energy landscape (Supplementary Fig. 6.11c,f), we obtain a free energy landscape along the ΔWr coordinate at fixed ΔLk_b that again reveals an asymmetrical distance to the transition state. The energy barrier flattens with a decrease in force (see also Supplementary Fig. 6.11) in line with previous observations for force dependent energy barriers [355].

6.4 Conclusion

In summary, taking advantage of the ability of MT to control both the applied force and twist, we have reconstructed the full 2D energy landscape along the extension and twist degrees of freedom. Along the rotational degree of freedom the energy landscape is asymmetric, with ΔWr_{pre} close to unity, and roughly 30 % smaller as compared to ΔWr_{post}. Likewise, the energy landscape along the extension coordinate exhibits significant asymmetry, with the distance from the extended to the transition state Δz_{pre}, approximately 15 % smaller than the distance from the buckled to the transition state Δz_{post}. Combining both results, we conclude that the transition state is a small, highly twisted, single loop.

We hypothesize that the strong bending and twisting deformations in the transition state for DNA buckling lead to a breakdown of isotropic elasticity and result in the formation of a kinked loop [356]. A breakdown of harmonic elasticity for DNA could explain the finding from the force dependence of τ_{buck} that the buckling transition exhibits a three- to four- fold steeper energy barrier for DNA as compared to RNA (Fig. 6.2f). Barrier steepness quantifies the cooperativity of molecular rearrangements to achieve the transition state geometry; since the (harmonic) elasticity properties of both nucleic acids are roughly the same, it is plausible that the transition involves the breakdown of DNA harmonic elasticity. This hypothesis is further supported by the observation that factors that destabilize double-stranded DNA, notably glycerol or low salt concentrations (Fig. 6.15 and 6.16 in Supporting Information), increase the rate of buckling, consistent with a lower transition state energy barrier. Disruption of DNA base pairing upon negative supercoiling under stretching forces has been clearly established previously [13, 90].

Our hypothesis of kinking and local disruption of base pairing is in line with biochemical and structural experimental results [357] and with all-atom molecular dynamics simulations of small DNA circles [358] that indicate the formation of local kinks also upon positive supercoiling

Our findings suggest that local defects [50, 359], e.g. introduced by DNA damage or protein-binding [119], would enhance the rate of supercoil nucleation by transition state stabilization, and help positioning plectonemes. The rates of supercoil location hopping, previously determined using identical beads [120], are similar to the rates of supercoil nucleation determined in this study, which strongly suggests that long-range communication along DNA is rate-limited by supercoil nucleation. In summary, the quantitative framework presented here will enable making testable predictions of DNA topology-mediated regulatory dynamics and provides a critical baseline for models of DNA dynamics *in vivo*. In addition, our work highlights the necessity to decouple the energy landscape of supercoil nucleation along both extension and rotational degrees of freedom, and demonstrates how high-speed magnetic tweezers experiments allow reconstruction of full 2D free energy landscapes, which opens up exciting possibilities to extend the more commonly used 1D free energy description of macromolecular transitions [360] into multiple dimensions [361].

6.5 Acknowledgements

We thank Samuel Stubhan for help with initial measurements, Daniel Burnham for sharing code for the bead-DNA simulations, Enrico Carlon and Stefanos Nomidis for stimulating discussions, Angelika Kardinal and Thomas Nicolaus for help with sample preparation, and the German Research Foundation (DFG) through SFB 863, KU Leuven through IDO, and FWO Flanders, for funding.

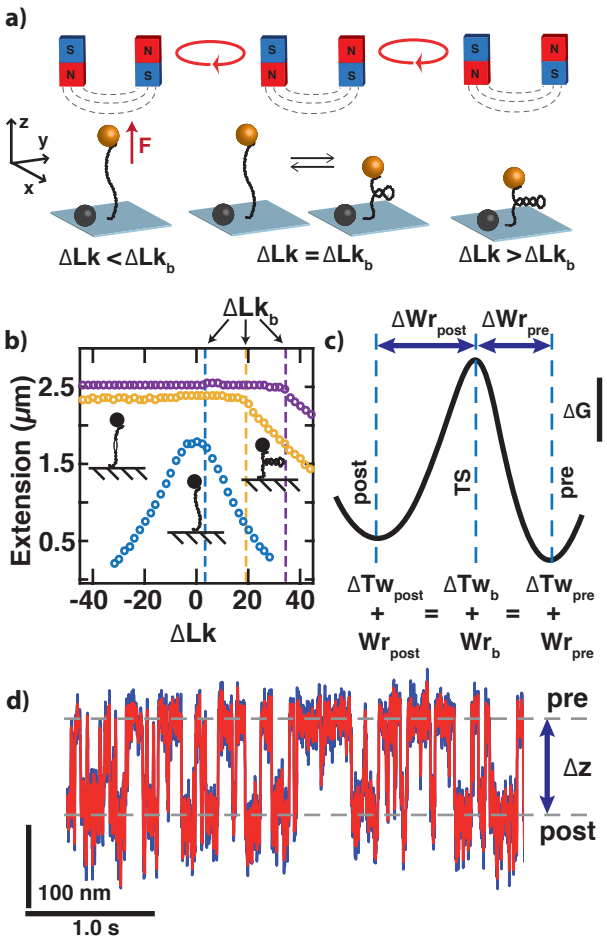

Figure 6.1: DNA buckling measurements in the MT. a) Schematic of the MT setup. A DNA molecule is tethered between the surface and a superparamagnetic bead. Magnets exert a force on the bead and rotation of the magnets controls the linking number. Close to the buckling point ΔLk_b the DNA extension jumps between two states. b) Rotation-extension curves for different forces. At low forces (blue, 0.2 pN) DNA forms plectonemes at positive and negative turns. At higher forces (yellow, 2 pN; purple, 5 pN) plectonemes appear only at positive turns, while DNA melts at negative ΔLk. c) Schematic representation of the buckling energy landscape along the rotational coordinate at ΔLk_b. d) Extension trace close to ΔLk_b, depicting the dynamic hopping of the DNA molecule between the pre-buckling and post-nucleation states. Δz indicates the jump size (raw data at 1000 Hz, blue; smoothed data at 333 Hz, red).

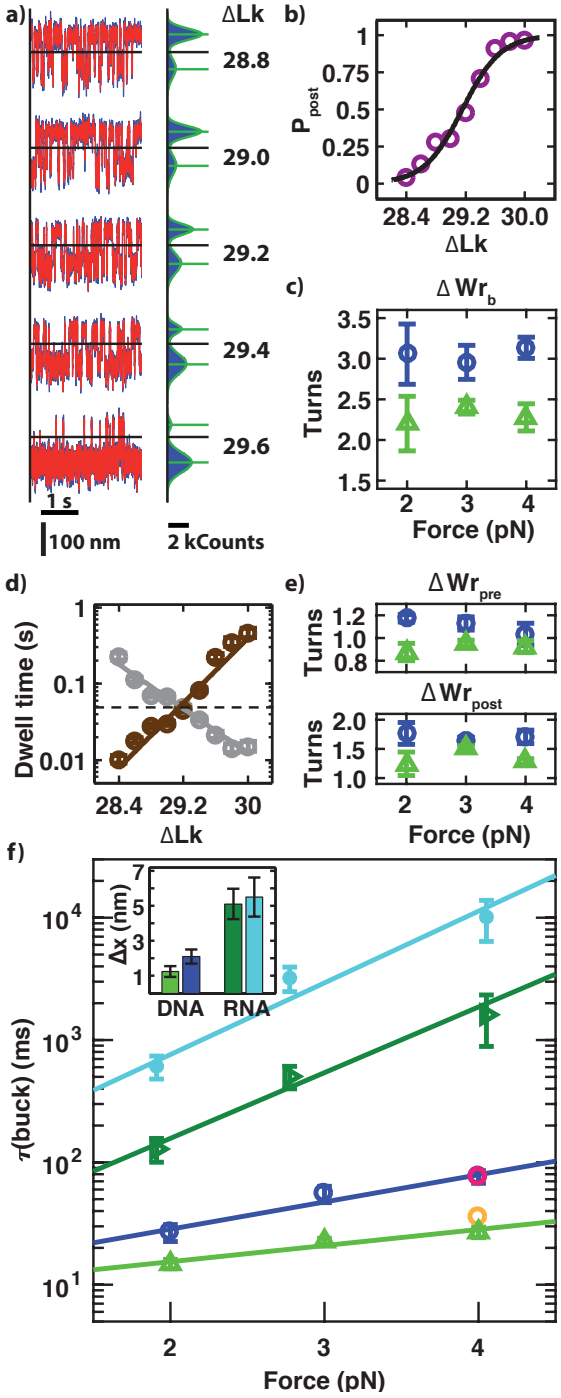

Figure 6.2: Quantification of DNA buckling dynamics. a) Extension time traces as a function of ΔLk (raw data 1000 Hz, blue; smoothed data 333 Hz, red). Black lines indicate thresholds for analysis. Histograms on the right are based on raw data and fitted by a double Gaussian. Horizontal green lines depict the mean extension of pre- and post-buckling state, respectively. b) Fraction in the post-buckling state vs. ΔLk and fit of Eqn. 6.2 (solid line) at 3 pN and 320 mM NaCl. c) Salt- and force dependence of ΔWr_b (green triangles 100 mM NaCl, blue circle 320 mM NaCl). d) Mean dwell time for the pre- and post-buckling states vs. ΔLk and fits of Eqn. 6.3 (solid lines). The dashed line indicates the fitted buckling time τ_{buck}. e) Distances to the transition state $|\Delta Wr_{pre}|$ and $|\Delta Wr_{post}|$ (same color code as in c). f) Buckling times vs. force for DNA (bottom two data sets; same color code as panel c) and RNA (top two data sets; dark green right-pointing triangle data are for 100 mM and cyan asterisk data for 320 mM NaCl) for different salt concentrations and exponential fits (Eqn. 6.4; solid lines). Magenta and orange circles for 4 pN, 320 mM NaCl taken from Ref. [50] for 10.9 and 1.9 kbp DNA, respectively. Inset: Distances to transition state Δx for DNA and RNA. All RNA data taken from [26].

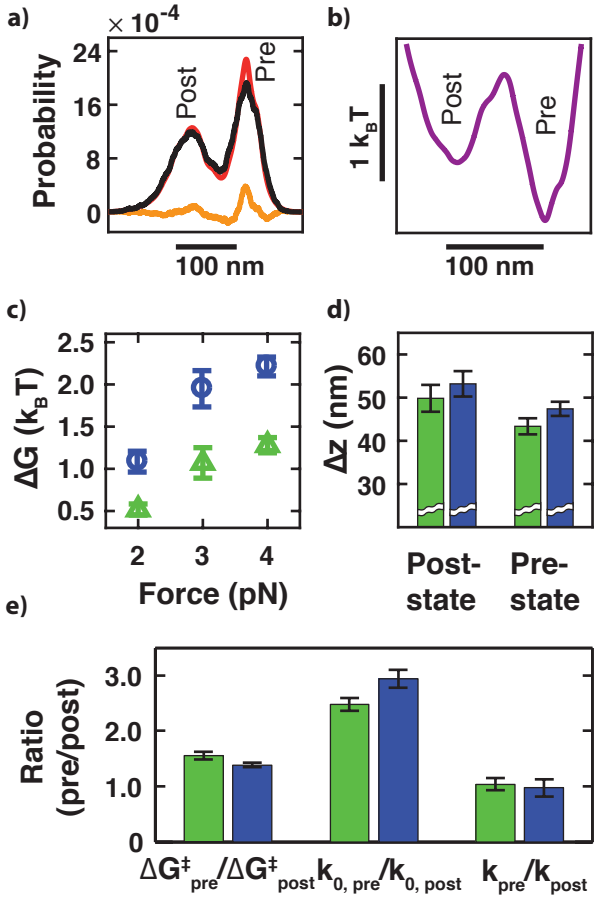

Figure 6.3: Reconstruction and quantification of the energy landscape. a) Deconvolution of extension histograms. Extension histogram before (black) and after (red) deconvolution with the setup response function and difference due to deconvolution (orange). b) Reconstructed energy landscape computed as $\Delta G(z) = -k_B T \cdot ln[p(z)]$ from the deconvolved probability density $p(z)$. c) Mean value of the energy barrier at ΔLk_b of pre- and post buckling state vs. force (color code for panels c-e: 100 mM NaCl green and 320 mM NaCl blue). d) Distances to the energy barrier along the extension coordinate (absolute values). e) Comparison of post and pre-buckling state parameters at ΔLk_b: The energy barrier for the pre-buckling state $\Delta G^{\ddagger}_{pre}$ is larger than for the post buckling state $\Delta G^{\ddagger}_{post}$ resulting in $\Delta G^{\ddagger}_{pre}/\Delta G^{\ddagger}_{post} > 1$. The ratio of the attempt frequency of the bead to cross the energy barrier of the pre-buckling state by the post-buckling state $k_{0,pre}/k_{0,post}$ determined by the ratio of the curvature of the energy landscape is larger than 1. The overall rate to cross the energy barrier $k_{pre}/k_{post} \approx 1$ in line with equilibrium at ΔLk_b.

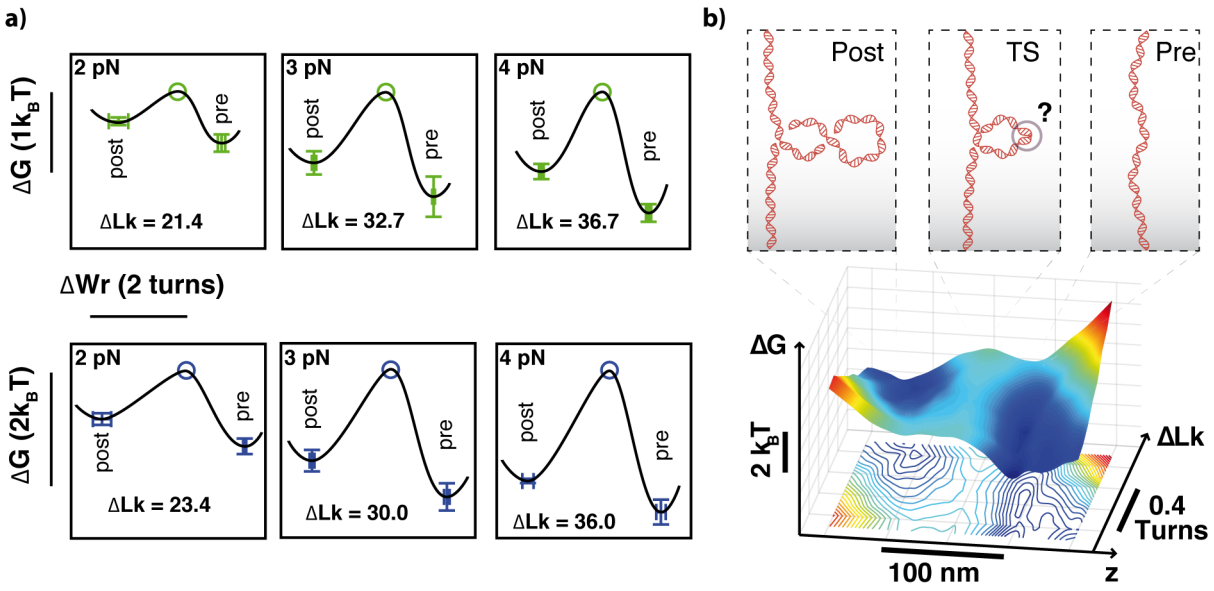

Figure 6.4: Energy landscape of the DNA buckling transition. a) Quantitative energy landscape along ΔWr for different forces and salt concentrations (upper row 100 mM NaCl, lower row 320 mM NaCl). Green and blue markers are determined from the analysis described in the main text. The energy landscape flattens for lower forces. Since the analysis only provides energy differences, the top of the barriers are set to the equal height for ease of comparison. b) A full 2D extension and rotation energy landscape was obtained by subsequently constructing 1D extension energy landscapes (as in Fig. 6.3) while systematically changing ΔLk (in steps of 0.1 turns). The iso-energy lines in the projection of the landscape into 2D have a spacing of 0.15 k_BT. The asymmetry of the pre- and post-buckling energy wells is apparent.

6.6 Supplementary Information

6.6.1 DNA Constructs and Magnetic Beads

Measurements employed a 7.9 kbp DNA construct described previously [46, 362]. For specific attachment to both the magnetic bead and the flow cell surface, ≈ 600-bp PCR-generated DNA fragments labeled with multiple biotin and digoxigenin groups, respectively, were ligated to the DNA. Measurements used either 1.0 µm diameter MyOne or 2.8 µm diameter M270 magnetic beads (Life Technologies, USA). The DNA construct was attached to the streptavidin coated beads by incubating 1 µl of picomolar DNA stock solution and 2 µl MyOne beads in 10 µl 1x PBS (Sigma-Aldrich, USA) for 12 min. Subsequently, 500 µl 1x PBS was added to get the final bead concentration and the bead-coupled DNA constructs were introduced into the flow cell, see below. Alternatively, 0.5 µl DNA stock solution, 5.5 µl M270 beads were incubated in 20 µl 1× PBS for 8 min and diluted into 150 µl 1× PBS.

6.6.2 MT Setup

The custom built MT setup uses a pair of $5 \times 5 \times 5$ mm^3 permanent magnets (W-05-N50-G, Supermagnete, Switzerland), oriented in a horizontal configuration [25]. The distance between beads and magnets is controlled by a DC-Motor (M-126.PD2, PI, Germany), rotation of the magnets is performed by another DC-Motor (C-150.PD, PI, Germany). Beads are observed with a 40× oil immersion objective (UPLFLN 40×, Olympus, Japan) and imaged with a CMOS sensor camera (12M Falcon2, Teledyne Dalsa, Canada). Reducing the field of view to 5 % of the original area (to 1792×282 pixel with 1 pixel ≈ 110 nm) enables a frame rate of 1 kHz. Images are transferred to a frame grabber (PCIe 1433, NI, USA) and analyzed with a custom-written tracking software [31]. A simple LED (69647, Lumitronix LED Technik GmbH, Germany) is used for illumination. A piezo stage (Pifoc P-726.1CD, PI, Germany) moves the objective to produce the look-up table (LUT) necessary for the bead tracking. Forces were calibrated as described by Te Velthuis *et al.* [313].

6.6.3 Flow Cells and Measurement Buffers

Flow cells are built of two coverslips (24×60 mm, Carl Roth, Germany). The bottom coverslip, to which the DNA molecules will attach, is first coated with (3-Glycidoxypropyl)trimethoxysilane (abcr GmbH, Germany). Afterwards, 200 µl of a 2000 times diluted stock solution of polystyrene beads (Polysciences, USA) in ethanol (Carl Roth, Germany) is dried in air and baked at 100°C for 5 min as reference beads. The two coverslips are glued together by one layer of melted Parafilm (Carl Roth, Germany), precut to form a flow channel. 100 µg/ml anti-digoxigenin (Roche, Switzerland) in 1× PBS are incubated in the assembled flow cell for 1 h. To minimize non-specific interactions, the flow cell is flushed with 800 µl of 10 mg/ml bovine serum albumin (BSA) (Carl Roth, Germany), incubated for 1 h and rinsed with 1 ml of 1× PBS. The premixed DNA-bead solution is added to the flowcell for 12 min for MyOne beads, and 7 min for M270 beads to allow for the digoxigenin-anti-digoxigenin bonds to the surface to form. Subsequently, the flow cell is rinsed with 1 ml of 1× PBS to flush out unbound beads. The buffer was exchanged to the final measurement buffers by flushing 2 ml of buffer while applying 5 pN. Measurements were performed in Tris-EDTA buffer (TE) (Sigma-Aldrich, USA) containing 10 mM Tris-HCl

and 1 mM EDTA at a pH of 8.0, with varying amounts of NaCl added, as indicated in the text. For some experiments, glycerol (Sigma-Aldrich, USA) was included in the buffer as noted in the relevant section.

6.6.4 Measurement Protocol to Detect the Buckling Transition

For every molecule included in the analysis, two initial tests were performed to test whether beads are attached via single double-stranded DNA tethers. First, the length of the tether was determined by applying a stretching force of 5 pN. Tethers within 10 % of the expected length (assuming a contour length of the molecule equal to 0.34 nm/bp · 7900 bp ≈ 2700 nm and taking into account the WLC-like stretching response [72]) were considered for further analysis. To test whether DNA tethers were free of nicks and suitable for supercoiling experiments as well as to exclude beads attached to the surface via multiple DNA molecules, extension-rotation curves at 5 pN as well as at 1 pN were measured. Only beads behaving as in Fig. 6.1b (no length change at 5 pN within ± 30 turns, asymmetric extension trace at 1 pN) were used for experiments. The torsionally relaxed position of the DNA molecule was determined by a rotation curve at 0.4 pN. The buckling point of the DNA molecule was determined by rotating the molecule in positive turns until a clear jump in the extension is visible. Buckling transition measurements started around one turn before jumps and ended around one turn after jumps in the extension trace were observed. Traces were recorded for each number of applied magnet rotations for 100 s and the number of rotation was systematically varied in steps of 0.1 turns (Fig. 6.2a). Unless otherwise noted, for all reported points at least 4 molecules were measured. All errors given are standard errors of the mean.

6.6.5 Analysis of Hopping Traces

Extension-time traces were recorded at 1 kHz and smoothed with a moving average filter of three milliseconds. Control calculations with filter times in the range of 3-9 ms gave identical results, within experimental error (see also “Correction for finite acquisition times”). Data analysis was performed similar to Ref. [26]. In brief, an optimal threshold for separating the pre- and post-buckling state was determined by using one hundred equally separated “trial thresholds” between the minimum and maximum extension value. The maximum of the first derivative of the fraction in the pre-buckling (“up”) state with respect to the threshold position was used as the optimal threshold. To avoid artifacts due to the tails of the extension histogram where the derivative of the of the fraction in the pre-buckling is also close to zero, only the thresholds between the two peaks of the double-Gaussian shaped extension histogram were considered as candidates for the optimal threshold. Control calculations were carried out by randomly changing the threshold position by up to 5 % of the maximal difference in the z trace; the resulting change in the characteristic buckling time was less than 10 %, suggesting that our results are insensitive to the exact position of the threshold.
Extension traces were divided into pre- and post-buckled states by the optimal threshold. Time points of the jumps from one state into the other were used to determine the dwell time distributions in the pre- and post-buckling states for all traces. The buckling time distributions were fitted with a single exponential using a maximum likelihood fit, resulting in the mean residence time for both states at every number of applied turns (Fig. 6.7). These τ_{pre} and τ_{post}

values were corrected for the finite acquisition time due to the camera frequency and filter by applying a statistical correction method based on the moment equations for a two-state Markov model (see "Correction for finite acquisition times") [326]. The corrected mean dwell times τ_{pre} and τ_{post} and their corresponding rotation number were used to determine the characteristic buckling time τ_{buck} (Fig. 6.2f).
The force dependency of the characteristic buckling time (Eqn. 6.4, Fig. 6.2f) was fitted using the standard X^2-criterion and the *fitnlm* function in MATLAB (MATLAB R2013b, The MathWorks), i.e. using $1/\sigma^2$ with σ the standard deviation as weighting factors. The reported errors for $\tau_{buck,0}$ and Δx are the standard errors of the estimate.

6.6.6 Two-State Model of the Buckling Transition

To quantify the different extension plateaus of the DNA molecules, we used the two-state model by Brutzer *et al.* [50]. Briefly, the free energy of the DNA molecule related to the twist before the buckling point is given by

$$E_{pre}(\Delta Lk) = \frac{1}{2} \cdot \frac{C}{L_C} \cdot (2 \cdot \pi)^2 \cdot \Delta Lk^2 \tag{6.5}$$

Where ΔLk is the number of applied turns, L_C the contour length and C the effective torsional modulus in $k_BT \cdot nm$ [79]:

$$C = C_{mod} \cdot (1 - \frac{C_{mod}}{4 \cdot L_p \cdot k_BT} \cdot (\frac{k_BT}{L_p \cdot F})^{0.5}) \tag{6.6}$$

with C_{mod} the DNA torsional modulus, F the applied force and L_p the persistence length. We used 100 $k_BT \cdot nm$ and 45 nm for C_{mod} and L_p, respectively. Using experimental data for the effective torsional modulus instead [46] did not significantly change the results of the fits of Eqn. 6.2 and 6.3 in the main text. After buckling, the free energy is given by

$$E_{post}(\Delta Lk) = E_b + \frac{1}{2} \cdot \frac{C}{L_C} \cdot (2 \cdot \pi)^2 \cdot (\Delta Lk - \Delta Wr_b)^2 \tag{6.7}$$

where E_b is the energetic penalty that must be overcome for the formation of the buckling structure and ΔWr_b the number of turns converted from twist to writhe during buckling. Using Boltzmann statistics, the probability to be in the post-buckling state P_{post} is given by

$$P_{post} = \frac{1}{1 + e^{\frac{E_{post} - E_{pre}}{k_BT}}} \tag{6.8}$$

With the expressions for E_{pre} and E_{post} (Eqn. 6.5 and 6.7), the probability can be rewritten as:

$$P_{post} = \frac{1}{1 + e^{\frac{C}{L_C} \cdot (2 \cdot \pi)^2 \cdot \frac{(\Delta Lk_b - \Delta Lk) \cdot \Delta Wr_b}{k_BT}}} \tag{6.9}$$

where ΔLk_b is the number of applied turns where $P_{pre} = P_{post}$, i.e. the point of buckling equilibrium. Fitting of Eqn. 6.9 to the probability to be in the post-buckling state regarding the number of applied turns, we determined ΔLk_b as well as ΔWr_b (Fig. 6.2b).

We determined the mean dwell times in the pre- and post-buckling state from a maximum likelihood fit of exponential distribution to the data (Fig. 6.7). To describe the dependence of the mean dwell times in the pre- and post-buckling states, τ_{pre} and τ_{post}, we assume an Arrhenius relationship with exponential dependence on the number of applied turns, resulting in Eqn. 6.7 of the main text [50].

6.6.7 Simulations of the DNA-Bead System in the MT

To test our ability to resolve fast transitions in the MT, we carried out numerical simulations of our measurement system: an ≈ 8 kbp DNA tether attached to a 0.5 or 1.4 μm radius bead. In the simulations, the Langevin equation for the bead motion was solved numerically following the approach of Burnham *et al.* [332], taking into account the viscous drag of the bead (with appropriate modifications due to the proximity of the flow cell surface [363, 364], the magnetic force which is constant for a given setting of the magnets [25] and the force exerted by the DNA, which is modeled using the WLC model [72]. To this basic simulation framework of a magnetic bead tethered in the MT, we add stochastic jumps in the tether extensions. The simulated jumps are instantaneous in the simulations and increase or decrease the tether extension by 100 nm (similar to the buckling transition observed for DNA). The simulated steps occur at a predefined rate (Fig. 6.5a). The simulation code includes the effect of the camera, by averaging the simulated positions (calculated for every 0.01 ms) over subsequent time intervals corresponding to the frame rate of the camera (1 ms). Simulated time traces are subjected to the same dwell time analysis routines as the experimental data: traces are filtered with a moving average filter, a threshold is selected and dwell time distributions are computed. The simulation only examines the 50-50 point that has identical dwell times in both states, thus no maximum likelihood fits of exponential distributions are required to extract the corresponding apparent mean dwell times, and we report simply the mean dwell time values for the upper and the lower state. The fitted dwell times are compared to the dwell times used as inputs in the simulations (Fig. 6.5b). The results suggest that for our measurement parameters stochastic jumps in the trace with a characteristic time down to ≈ 10 ms can be resolved with at most 10 % error using MyOne (0.5 μm radius) beads. For M270 (1.4 μm radius), the time resolution is worse, but even for these larger beads jumps with a time scale down to 20 ms can be resolved with less than 10 % error.

6.6.8 Correction for Finite Acquisition Times

Limited time resolution of the instrument as well as the need to filter the data slightly (Fig. 6.2a), could produce a bias in our measured values for τ^*_{pre} and τ^*_{post}, leading to biased values for τ_{buck}. For the simulated data, as well as for the measured data, we tested down sampling with different width for a sliding average filter from 3 ms to 9 ms, which did not affect τ_{buck} within the error. Furthermore, we tested the effect of correcting for finite acquisition time by applying a statistical correction method based on the moment equations for a two-state Markov model [326]. In brief, the influence of the detection limit of time ξ (due to camera frequency and width of the filter) to the true, intrinsic values τ_{pre} and τ_{post} of the system resulting in the observed

time values τ^*_{pre} and τ^*_{post} is corrected by numerically solving the two equations [326]:

$$\tau^*_{pre} = (\tau_{pre} + \tau_{post}) \cdot e^{\frac{\xi}{\tau_{post}}} - \tau_{post} \tag{6.10}$$

$$\tau^*_{post} = (\tau_{pre} + \tau_{post}) \cdot e^{\frac{\xi}{\tau_{pre}}} - \tau_{pre} \tag{6.11}$$

The resulting corrected values τ_{pre} and τ_{post} were slightly smaller than the uncorrected values, but within the error (Fig. 6.17). Consequently τ_{buck} was not significantly smaller. The largest effect was determined to be at the fastest buckling conditions and changed the characteristic buckling time by 15 %. All data shown are corrected values.

6.6.9 Deconvolution Procedure

To reconstruct the energy landscape without the blur of setup noise, the extension histograms from the measured time traces at fixed numbers of rotation were deconvolved with the instrument response function. We followed the approach of Woodside *et al.* [328–330] and utilize the non-linear iterative method of Jansson [331]:

$$\hat{o}^{(k+1)}(z) = \hat{o}^{(k)}(z) + r[\hat{o}^{(k)}(z)] \cdot (i(z) - S(z) \times \hat{o}^{(k)}(z)) \tag{6.12}$$

$$r[\hat{o}^{(k)}(z)] = r_0 \cdot (1 - 2 \cdot |\hat{o}^{(k)}(z) - \frac{1}{2}|)$$

with *i(z)* the measured histogram, *S(z)* the setup noise, $\hat{o}^{(k)}(z)$ the deconvolved histogram after k iterations. $r[\hat{o}^{(k)}(z)]$ is the function to remain within the physical boundaries with the constant r_0 to control the speed of convergence.
We first generated the extension histogram from the raw measurement trajectories. The z-traces were binned to 0.2 nm and the resulting histograms were smoothed with a moving average filter of a width of 4.2 nm. To reduce spurious fluctuations in the deconvolution, after every iteration the histograms were smoothed with a moving average filter of a width of 1.2 nm. For every measurement we performed 1000 iterations with $r_0 = 2$.
Woodside *et al.* deconvolved their measurements on DNA hairpins with the noise of the DNA handles in their optical trap determined with a hairpin that is always in a closed configuration. In our case the DNA tether serves both as the handle as well as the system of interest itself. Hence, we cannot directly use the DNA handle with a modified version of the system of interest, which is always in one fixed configuration as the instrument response function to deconvolve the measurement. Instead, we use the extension fluctuations of torsionally relaxed molecules, which are well approximated by a Gaussian, as the instrument response function *S(z)* (Fig. 6.18) [332]. To address the effect of force on the fluctuations, we measured the extension fluctuations in the absence of supercoils for every force used in our analysis. Furthermore, the fluctuations of torsional unconstrained DNA molecules were determined for 100 mM and 320 mM NaCl buffers. The results are well described by a model based on the worm-like chain model for DNA (Fig. 6.18) and we did not observe a significant change in fluctuations depending on salt concentration. Nevertheless, all energy landscape reconstructions were performed with the characteristic setup noise of the corresponding force and buffer, approximated by Gaussian distributions with standard deviations ranging from $\sigma \approx 10$ nm to ≈ 19 nm.

We note that the noise of the tracker (quantified by the standard deviation of the tracked z-position of bead fixed to the surface) of $\sigma \approx 1$ nm is more than one order of magnitude smaller than the z-fluctuations of DNA-tethered beads. Therefore, the instrument response function *S(z)* is dominated by the thermal fluctuations of the bead-DNA tether and not by the optical or tracking resolution. The deconvolution procedure resulted in stable solutions with small residuals and is robust against changes of reasonable dimensions (e.g. a factor of 2 in every parameter). Using a kernel density estimate with MATLAB (MATLAB R2013b, MathWorks) instead of the histogram did not result in significant changes of the energy landscape.

6.6.10 Determination of the Energy Barrier from Splitting Probability Analysis

As an alternative approach to our deconvolution analysis for the energy landscape reconstruction, we applied an independent method to determine the energy barrier following Manuel *et al.* [328]. In brief: The splitting probability $p_{buck}(z)$ measures the likelihood that the DNA goes into the buckled state as a function of its extension position z [348]. Therefore, $p_{buck}(z)$ is approximately 0 for the pre buckling state, ≈ 0.5 at the transition state, and ≈ 1 in the post buckling state. The probability $p_{buck}(z)$ can be directly determined from the measured trajectory of finite duration T for a given value of z_0:

$$p_{buck}(z_0) = \int_0^T \delta(z_0 - z(t)) c_{z_{buck}}(t) dt \Big/ \int_0^T \delta(z_0 - z(t)) dt \tag{6.13}$$

The function $c(t)$ is 0 unless the trajectory reaches the absorbing boundary z_{buck} before it reaches the boundary at z_{elong}, in which case its value is 1; z_{buck} and z_{elong} are the location of the post buckling as well as the elongated pre buckling state, respectively [349]. Hence the denominator counts the crossing events of the bead at the position z_0, whereas the numerator counts how often the trajectory hits the position z_{buck} before z_{elong} [330]. Assuming Langevin dynamics, $p_{buck}(z)$ can be used to determine the underlying 1D energy landscape $G(z)$ [330, 365, 366]:

$$p_{buck}(z) = \int_z^{z_{elong}} D(z')^{-1} e^{\beta G(z')} dz' \Big/ \int_{z_{buck}}^{z_{elong}} D(z')^{-1} e^{\beta G(z')} dz' \tag{6.14}$$

With the diffusion coefficient D and β the inverse thermal energy. Inversion and rewriting formula 6.14 leads to, up to a constant:

$$G(z) = \beta^{-1} ln\Big(-D(z) \cdot \frac{dp_{buck}}{dz}\Big) \tag{6.15}$$

Hence, the energy landscape can directly be determined from $p_{buck}(z)$. The splitting probability was calculated from the same experimental traces that were used for the deconvolution approach, with code provided by [349]. The absorbing boundaries were placed close to the peaks of the extension histograms; more precisely z_{buck} was placed 5 nm below the histogram peak of the post-buckling state and z_{elong} 5 nm above the histogram peak of the pre-buckling state. We found that the exact location of both absorbing boundaries did not change the energy landscape significantly. To reduce noise, the numerical differentiation $dp_{buck}(z)$ as well as the finally reconstructed energy barrier was smoothed with a moving average filter of 15 nm each.

The filtering windows were chosen to be large enough to remove regions of locally positive slope in $dp_{buck}(z)$, such that the logarithm was undefined.
Manuel *et al.* have demonstrated that the landscape recovered with $p_{buck}(z)$ leads to the same energy landscape as for the deconvolved extension histograms, without the need of deconvolution [330]. We used the stiffness, i.e. the curvature of the energy barrier top to compare both methods. We performed a quadratic fit of an area of ± 20 nm around the top of the energy barrier and determined the curvature of the quadratic fit. For 2 pN and 320 mM NaCl we find mean curvature values of $(-2.39 \pm 0.3) \cdot 10^{-3}$ k_BT/nm^2 and $(-2.37 \pm 0.7) \cdot 10^{-3}$ k_BT/nm^2 for the deconvolved and splitting probability reconstructed barriers, respectively. Furthermore, the shapes of the energy landscapes overlap very well (Fig. 6.10) and hence we conclude that both reconstruction methods give similar results within experimental error.
For our experimental data, we found the deconvolution method to reconstruct the energy landscape to be more robust and less sensitive to smoothing than the splitting probability approach. Furthermore, the splitting probability approach can only reconstruct the energy barrier, but not the complete wells [329], e.g. lacking the possibility to determine the curvature of the minima for Kramers escape theory and hence the comparison of the attempt frequency for barrier crossing events. Therefore we only used deconvolved histograms and the inverse Boltzmann approach for further analysis.

6.6.11 Analysis of the Energy Landscape and Determination of the Attempt Rate

To calculate the attempt rate ratio between the pre- and post-buckling state k_{pre}/k_{post} we applied Kramers escape theory [350, 351]:

$$k = \frac{\beta \cdot D_x}{2 \cdot \pi} \cdot \left(\frac{G''(x_{min})}{|G''(x_{max})|}\right)^{\frac{1}{2}} \cdot e^{-\beta \cdot \Delta G^{\ddagger}_{side}} \tag{6.16}$$

with k the Kramers escape rate, $\beta = 1/k_BT$, D_x the diffusion constant, $G''(x_{min})$ the curvature at the minimum of the energy well, $G''(x_{max})$ the curvature at the maximum of the energy barrier and the height of the energy barrier of the particular side $\Delta G^{\ddagger}_{side}$, where "side" can be "pre" or "post" buckling state. Consequently the ratio of the attempt rates of the pre- and post-buckling state is:

$$\frac{k_{pre}}{k_{post}} = \frac{(G''_{pre}(x_{min}))^{\frac{1}{2}}}{(G''_{post}(x_{min}))^{\frac{1}{2}}} \cdot \frac{e^{-\beta \cdot \Delta G^{\ddagger}_{pre}}}{e^{-\beta \cdot \Delta G^{\ddagger}_{post}}} \tag{6.17}$$

with the labels "pre" and "post" for the pre- and post-buckling state, respectively. The curvature was determined from a quadratic fit of the minimum of the energy wells that included extension information up to 20 nm to either side of the minimum.

6.6.12 Determination of the Buckling Equilibrium Point

For several analyses, in particular for the data shown in Fig. 6.3, Fig. 6.11, Fig. 6.13 and Fig. 6.14, we analyzed the reconstructed energy landscape at the buckling equilibrium. Since we obtained extension traces in fixed steps of 0.1 turns, we used the following approach to approximate the energy landscape at $P_{post} = 0.5$: we used the data sets closest to $P_{post} = 0.5$ with $P_{post} < 0.5$ and

with $P_{post} \geq 0.5$ and calculated the mean values of Δz_{pre}, Δz_{post}, $\Delta G^{\ddagger}_{pre}$, $\Delta G^{\ddagger}_{post}$, and the curvature, weighted by their distance to $P_{post} = 0.5$. This procedure reduced the variability and, therefore, the error bars without a significant change of the mean values compared to using only the data set closest to $P_{post} = 0.5$.

6.6.13 Reconstruction of 2D Energy Landscape

The 2D energy landscape (Fig. 6.4b) was assembled from sets of 1D extension energy landscapes determined for every measured number of turns. Interpolation was performed in MATLAB (MATLAB R2013b, The MathWorks) using the "surf" and "shading interp" routines. The underlying 1D energy landscapes were aligned in the extension axis to the position of the maxima of the energy barriers to exclude errors due to tracking variability from changes in the light intensity for different rotation positions. We note that the height of the barrier was not aligned, but is determined by the analysis.

6.6.14 Influence of Bead Size on the Properties of the Buckling Transition

Manipulation of individual molecules in single-molecule torque and twist assays requires the attachment of ≈ µm-sized magnetic beads or nanofabricated cylinders to enable external control of the molecules [46, 344, 367]. Attachment of ≈ µm-sized particles can affect the observed dynamics of conformational changes [343, 347], as the attached particles influence both the friction coefficient and magnitude of the thermal fluctuations. To systematically test the influence of the bead size in our assay, we measured the dynamic as well as the steady state properties for two different bead sizes for one set of conditions (3 pN and a salt concentration of 100 mM NaCl). We used two different bead sizes, one with radius 0.5 µm and the other one with a radius of 1.4 µm, hence the ratio of the bead sizes is 2.8.

We find that the equilibrium properties of the buckling transition are not affected by bead size. The angular distance to the transition state from the pre-buckling state ΔWr_{pre}, as well as from the post-buckling state ΔWr_{post}, and the amount of twist converted into writhe ΔWr_b does not change within the measurement error (Fig. 6.8a). Consequently, also for the larger beads ΔWr_{pre} and ΔWr_{post} add up to ΔWr_b and show the same asymmetry as for the smaller bead results presented in the main text (Fig. 6.8a and Fig. 6.2c,e). Furthermore, the widths of the peaks in the extension histograms corresponding to the pre- and post-buckling states do not show any dependence on bead size (Fig. 6.8b). Similarly, the total size of the extension jump between the pre- and post-buckling states is independent, within error, of bead size: we find a jump size of (94.8 ± 0.9 nm) for the 1.4 µm beads (95.9 ± 1.6 nm) for the smaller 0.5 µm radius beads (Fig. 6.8c).

In contrast to the static properties, the buckling times change significantly with bead size. For 3 pN, 100 mM NaCl we measured a characteristic buckling time of 22.7 ± 1.3 ms for 0.5 µm beads and 42.8 ± 1.1 ms for 1.4 µm beads (Fig. 6.8d). We note that the observed differences in buckling times are not due to a lack of spatio-temporal resolution of the instrumental setup. Our simulations (see "Simulations of the DNA-bead system in the MT") demonstrate that different bead sizes of 0.5 µm and 1.4 µm radius give rise to deviations due to limited spatio-temporal resolution of less than 5 % for the observed buckling times and cannot explain the observed

difference.
To understand the effect of the bead size on the buckling times, we consider the model by Bai *et al.* [347]. Briefly, due to the slower fluctuations of the bead compared to the DNA conformational fluctuations, bead induced fluctuations in tension and twist are transmitted through the DNA molecule. The rate of energy barrier crossing events depends on the attempt frequency, which in turn is influenced by the viscous drag of the bead and the DNA molecule. Therefore, at a given constant force, the characteristic dwell time before a thermally driven barrier crossing event is given by:

$$\tau = \frac{\zeta_{bead} + \zeta_{DNA}}{k_{DNA}} \cdot e^{\frac{\Delta G}{k_B T}} \tag{6.18}$$

where the drag coefficient of the bead is $\zeta_{bead} = 6 \cdot \pi \cdot \eta \cdot R$ with η the viscosity of the solution and R the bead radius, $\zeta_{DNA} = 2 \cdot \pi \cdot \eta \cdot z/ln(z/b)$ the drag coefficient of the DNA [368] with z the extension of the DNA and b = 2 nm the DNA thickness, k_{DNA} the spring constant of the DNA, ΔG the energy barrier. At constant force, the - generally force dependent - property ζ_{DNA} can be assumed to be a constant [347].
The ratio of our measured values (Fig. 6.8d) is $\tau_{buck}(R_{large}) / \tau_{buck}(R_{small})$ = 1.9 ± 0.1, which is smaller, but close to the prediction from the model of Bai *et al.* (Eqn. 6.18) of ≈ 2.4. This deviation might be partially due to the fact that fluctuations and the plectonemic loop increases the DNA friction term compared to the model's assumption of a simple elongated cylinder. In summary, the data strongly suggest that the observed dependence of buckling times on bead size is due to coupling of the Brownian dynamics of the bead through the DNA, which sets the intrinsic frequency of barrier crossing attempts. Together with the results of our simulations, we conclude that the bead strongly influences the attempt frequency to cross the energy barrier, but that we do not fail to observe buckling transitions due to limited spatio-temporal resolution.

6.6.15 Impact of Glycerol on the Buckling Transition

To further investigate the effect of friction on the observed buckling dynamics, we adjusted the viscosity of our buffer by adding varying amounts of glycerol and carried out buckling measurements for F = 3 pN and 100 mM NaCl. According to the model of Bai *et al.* [347] the friction should linearly affect the characteristic buckling time τ_{buck}. Importantly, the predicted effect is independent of the relative size of the friction coefficients of bead and DNA, since both DNA and bead friction coefficients are linear in η.
Analyzing the equilibrium properties of the buckling transition with different amounts of glycerol in the buffer, we again see essentially no dependence: ΔWr_{pre}, ΔWr_{post} and ΔWr_b are identical, within error, for different glycerol concentrations (Fig. 6.15a). Similarly, ΔLk_b and the widths of the peaks in the extension histograms for the pre- and post-buckling states are independent of glycerol concentration (Fig. 6.15b). Only the size of the jump between the pre- and post-buckling states changes by ≈ 10 %, decreasing from ≈ 96 nm to ≈ 86 nm upon increasing the glycerol concentration from 0 % to 35 %, corresponding to an increasing of the viscosity from 0.89 mPa·s to 3.2 mPa·s (Fig. 6.15c).
In contrast, the buckling time scale τ_{buck} changes significantly with increasing glycerol concentration (Fig. 6.15e), τ_{buck} slowing down approximately ≈ 1.8-fold for a ≈ 3.5-fold increase in viscosity. While this increase is qualitatively consistent with the prediction of the model by Bai

et al., both the magnitude of the observed increase and its functional form deviate significantly from the model. While the Bai *et al.* model predicts a linear dependence on viscosity, the data are sub-linear. Comparing the data at the lowest (buffer, with no added glycerol) and highest (buffer with 35 % amount glycerol) viscosities, the Bai *et al.* model significantly, by ≈ 2-fold, over-predicts the slowdown of the buckling dynamics upon increasing glycerol concentration. The fact that the addition of glycerol slows down the buckling dynamics significantly less than would be predicted from the effect of the change in viscosity alone suggests that glycerol has other, offsetting, effects on DNA buckling. We now examine several possibilities for secondary glycerol effects and how they might explain the observed behavior: changes in the dielectric constant, crowding effects, and destabilization of the double helix.

Glycerol lowers the dielectric constant of the solution (for 35 % Glycerol roughly by 15 %) [327] and, therefore, increases charge-charge interactions; by trend, we would expect this to have similar effects as reducing the salt concentration, which also increases charge-charge interactions by reducing screening. Lower salt concentrations result in faster hopping, i.e. reduces τ_{buck} (Fig. 6.2f), which could explain the observed trend with glycerol. However, we note that changing salt concentration from 100 to 320 mM monovalent changes e.g. the Debye length by roughly ≈ 2-fold, a much more pronounced effect than the at most 15 % change in dielectric constant due to glycerol. If the change in charge-charge interaction would play an important role, we would also expect a change in the steady state behavior with glycerol, as observed for different salt concentration (Fig. 6.2). The fact that an increase in glycerol concentration does not appear to affect the equilibrium properties of the transition (Fig. 6.15a-c) suggests that the change in the dielectric constant cannot account for the observed changes in buckling behavior.

Molecular crowding can influence the characteristic time of loop formation in DNA molecules τ_{loop} [369]. In simulated DNA looping events, Shin *et al.* obtain an increase in the characteristic looping time in the presence of small crowders, such as glycerol [369, 370], for which viscosity effects dominate. In addition, in particular for larger crowders, Shin *et al.* observe an increasing in the probability of the looped compared to the unlooped-state, due to caging interactions. Therefore, it appears plausible that crowding effects might stabilize the tight loop involved in the transition state, which could increase the buckling rate, in line with the observed trends. However, the effect of loop stabilization for a small crowder like glycerol is likely to be limited. In addition, if crowding has a pronounced effect on looping, the buckling point ΔLk_b would be expected to decrease to smaller values with increasing crowding, again contrary to what is observed experimentally (Fig. 6.15d), suggesting that the crowding effects of the glycerol concentrations used are relatively unimportant in our experimental situation.

Polyols, including glycerol, have been shown to destabilize the DNA helix [371]. The destabilization has been attributed to the different capability of polyhydric alcohols to interact with the polynucleotide solvation sites replacing water and to modification of the local electrostatic interactions [371]. Our results (discussed in the main text) suggest that the transition state involves strong bending of the DNA and quite possibly temporary local melting. A destabilization of the helix by glycerol would facilitate melting and, therefore, would lower the transition state and thus making the hopping faster than what is expected from the viscosity only. The observed two-fold faster buckling compared to the estimate from viscosity alone would only require a $ln(2)\ k_BT \approx 0.7\ k_BT$ reduction of the free energy barrier, which appears plausible given the ≈ 10 $°C$ reduction in melting temperature for calf thymus DNA over the glycerol

range used in our experiments.

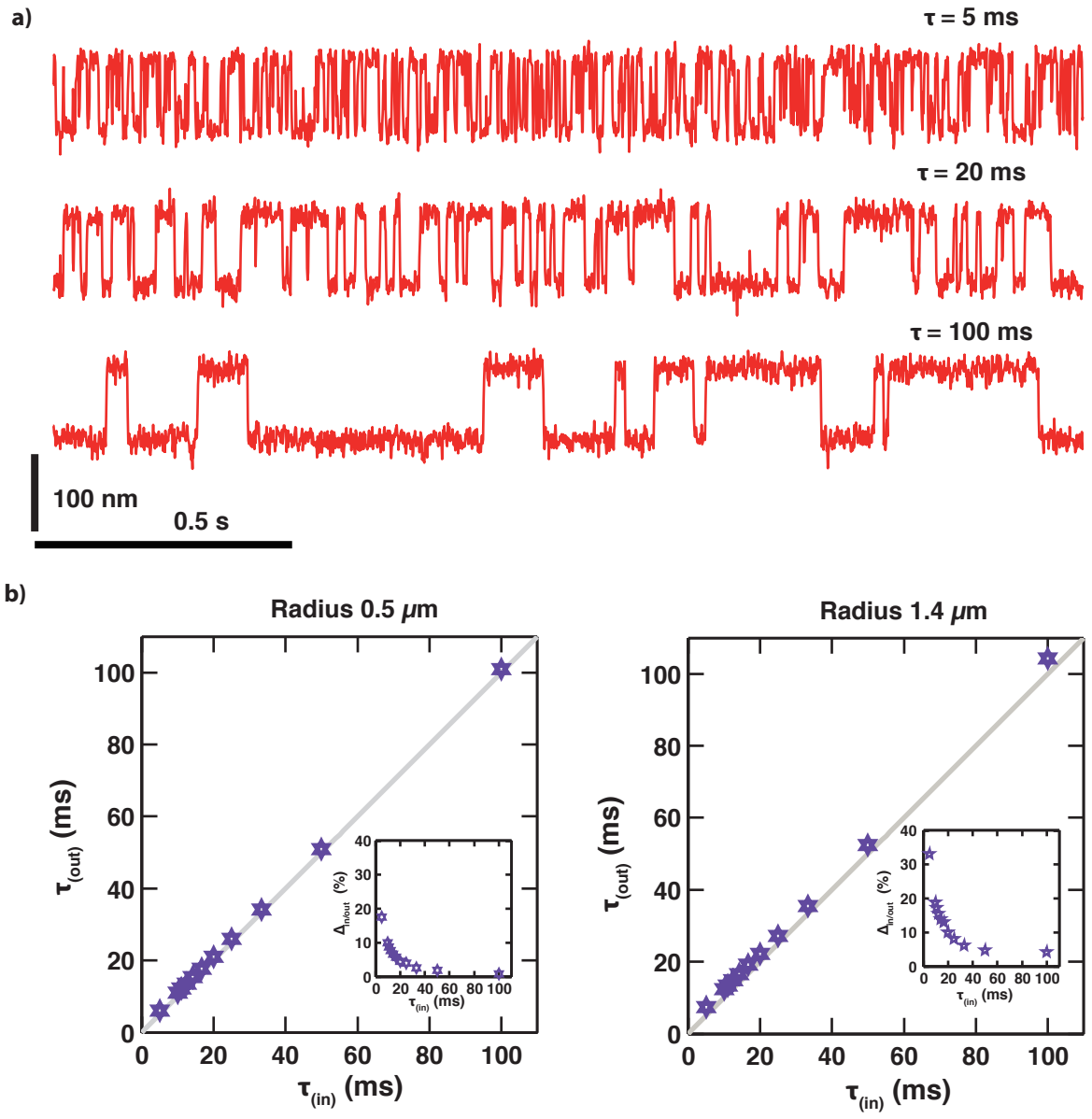

Figure 6.5: Testing the time resolution limits using Brownian dynamics simulations of the bead-DNA system. a) Simulated extension traces for different hopping rates (mean dwell time from 5 to 100 ms) at buckling equilibrium. Traces are obtained by numerically simulating the Langevin equation of the bead subject to external forces from the magnets and the DNA tether (see "Simulations of the DNA-bead system in the MT"). Instantaneous 100 nm jumps in the extension were added randomly with exponentially distributed dwell times and a predefined rate. b) Mean dwell time used as input parameter in the simulation τ_{in} vs. mean dwell time determined by the analysis of the final simulated traces τ_{out} for two different bead sizes used in the measurements. Gray line is the line $\tau_{in} = \tau_{out}$. The insets give the relative error of τ_{out} compared to the known τ_{in}. Time steps for the simulation were set to 0.01 ms, the camera frequency to 1 kHz. The analysis of the simulated extension traces was performed using the same filters and analysis routines as used in the analysis of the measured traces.

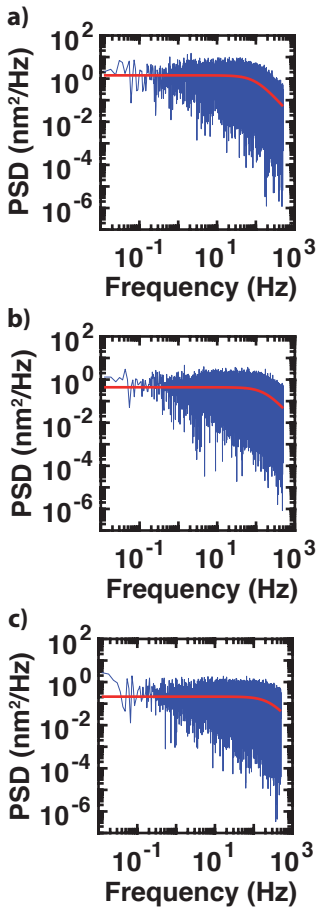

Figure 6.6: Power spectral density of extension fluctuations for DNA-tethered beads. The PSD of a torsional unconstrained DNA molecule at 100 mM NaCl at a) 2 pN, b) 3 pN, c) 4 pN. The corner frequencies differ with force, but not with salt and lead to a mean value of 98 ± 3 Hz, 161 ± 6 Hz and 230 ± 12 Hz for 2, 3 and 4 pN (means and standard errors from 4 independent measurements at each force), respectively. Red lines are Lorentzian fits to the data.

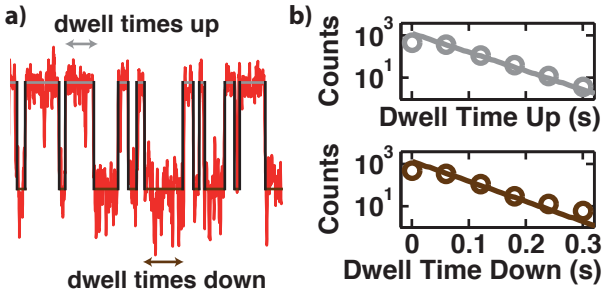

Figure 6.7: Examples of dwell times for pre- and post-buckling states. a) Example extension time trace indicating conversion of the filtered trace (red) into a binary signal (black) after selection of the threshold. Examples of dwell times in the pre ("up")- and post-buckling ("down") are indicated in the plot. b) Example histograms and exponential fits (solid lines) of dwell times for constant ΔLk close to ΔLk_b (3 pN, 320 mM NaCl).

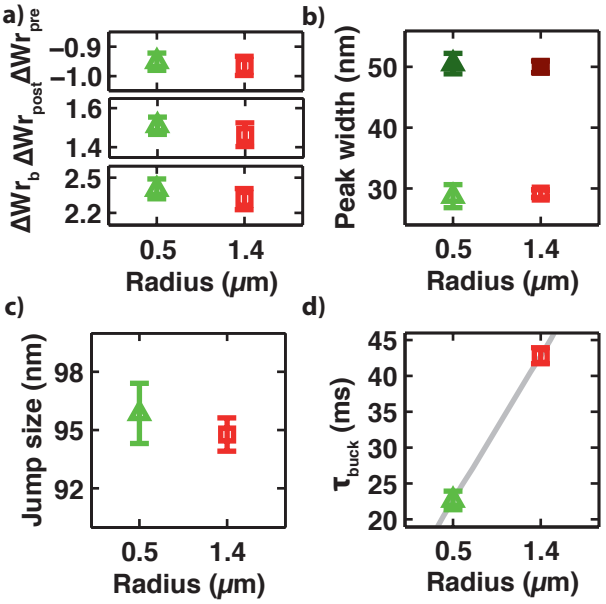

Figure 6.8: Influence of bead size on DNA buckling transitions. a) Effect of bead size on rotational distance to the transition state in number of turns. For ΔWr_{pre}, ΔWr_{post}, and ΔWr_b no dependence on bead size is observed. b) Influence of bead size on the widths of the pre- and post-buckling peaks in the extension histograms. The peak widths of the pre- as well as of the post-buckling state show no dependence on bead size (bright empty symbols pre-buckling state, dark filled symbols post-buckling state). c) Effect of bead size on the size of the jump, i.e. on the distance along the extension coordinate between the pre- and post-buckling states. For the jump size no influence of the bead size can be observed. d) Effect of bead size on characteristic buckling times τ_{buck}. An increase of the bead radius by a factor of 2.8 results in a change in the buckling time of ≈1.9-fold. All data shown are for 100 mM NaCl and 3 pN applied force; throughout, the green upward-pointing triangles are data obtained with MyOne beads, red squares correspond to data recorded using M270 beads. For a detailed discussion see "Influence of bead size on the properties of the buckling transition" in the Methods section.

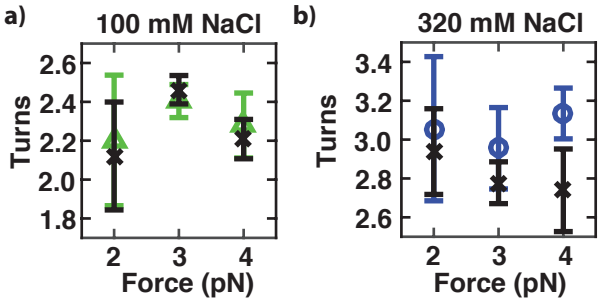

Figure 6.9: Comparison of the sum of ΔWr_{pre} and ΔWr_{post} compared to directly measured ΔWr_b. For 100 mM NaCl (a) as well as 320 mM NaCl (b) the absolute values of ΔWr_{pre} and ΔWr_{post} add up to ΔWr_b to within experimental error (color code according to Fig. 6.2, black crosses are the sum of ΔWr_{pre} and ΔWr_{post}.

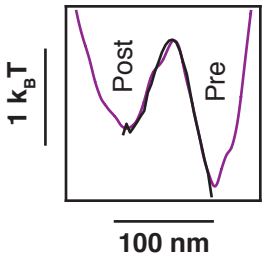

Figure 6.10: Comparison of different energy landscape reconstruction approaches. The energy landscape was reconstructed with a deconvolved histogram and the inverse Boltzmann approach (purple) as well as with the underlying splitting probability (black). The presented data were recorded at 2 pN and 320 mM NaCl for 100 s, the inverse Boltzmann approach is the same as presented in Fig. 6.3 of the main text.

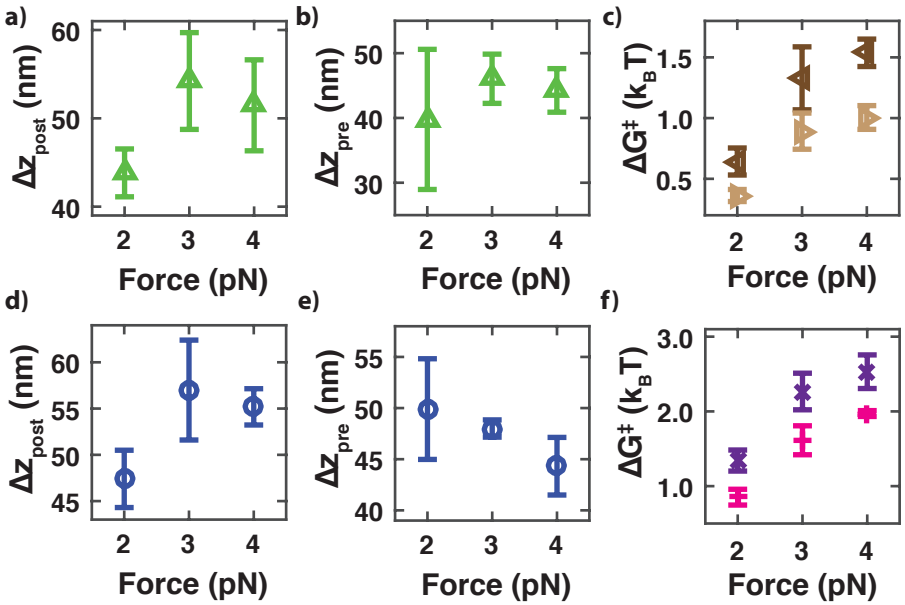

Figure 6.11: Additional analyses of the buckling energy landscape. a) and d) Distances of the maximum of the energy barrier to the post-buckling minimum along the extension axis determined from the reconstructed energy landscapes for 100 mM NaCl (a) and for 320 mM NaCl (d). No force dependency of the distances between the maxima and the minima is observed. b) and e) Distances of the maximum of the energy barrier to the pre-buckling minimum along the extension axis determined from the reconstructed energy landscape. The distances to the transition state obtained by the energy landscape indicate no significant force dependency for 100 mM NaCl (b) or for 320 mM NaCl (e). (c) and (f) Height of the energy barriers at P_{post} = 0.5 from the post-buckling state and from the pre-buckling state. The energy barrier $\Delta G^{\ddagger}_{pre}$ was determined from the minimum of the pre-buckling state to the maximum of the energy barrier (dark brown left-pointing triangle: 100 mM NaCl, purple cross: 320 mM). Analogously, $\Delta G^{\ddagger}_{post}$ from the minimum of the post-buckling state to the maximum of the energy barrier was obtained (brown right-pointing triangle: 100 mM NaCl, pink plus: 320 mM NaCl). For both salt conditions and at every force measured, $\Delta G^{\ddagger}_{post}$ is smaller than $\Delta G^{\ddagger}_{pre}$.

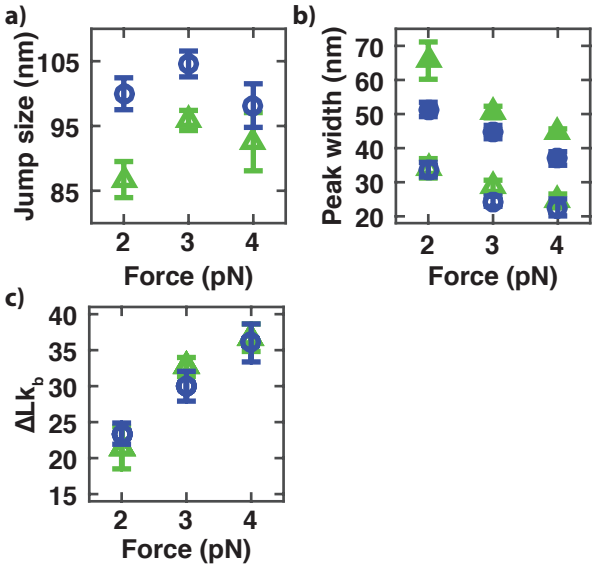

Figure 6.12: Equilibrium properties of the buckling transition for DNA. a) Sizes of the jump between the pre- and post-buckling states vs. force for 100 mM and 320 mM NaCl. The jump size within one salt concentration stays nearly constant for the investigated forces. A larger jump size of 100.9 ± 4.6 nm for 320 mM NaCl compared to the 91.7 ± 5.5 nm for 100 mM NaCl indicates a salt dependency. The sum of Δz_{pre} and Δz_{post} for 100 mM NaCl is 93.2 ± 3.6 nm and thus in good agreement with the directly determined jump size. For 320 mM NaCl Δz_{pre} and Δz_{post} sum up to 100.6 ± 3.4 nm and consequently fit also to the jump size. b) Widths of the peak of the pre- and post-buckling states in the extension histograms. For both salt concentrations, the peak width of the Gaussian distributed histograms for the post-buckling state (filled symbols) is significant larger than the peak width of the pre-buckling state (empty symbols). In all cases the peak width decrease with increasing force. For the pre-buckling state at one given force, no or only a small salt dependency is observed, while for the-post buckling state the error bars do not overlap. c) Number of twist applied at the buckling point ΔLk_b vs. force. ΔLk_b increases with force, but does not depend on salt. Color code as in Fig. 6.2.

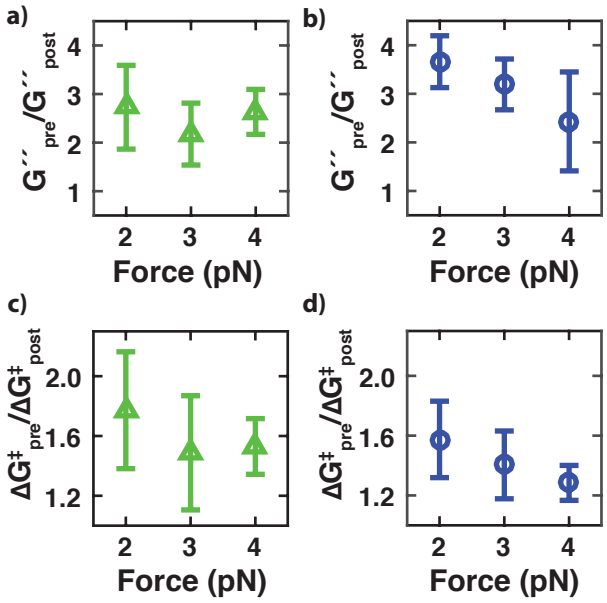

Figure 6.13: Analysis of energy barrier height and curvature at P_{post} = 0.5. a), b) Ratio of curvature of the pre- and post-buckling minima vs. force for 100 mM NaCl (a) and 320 mM NaCl (b). For each salt condition, the ratio is constant, within experimental error, for all forces. c), d) Ratio of energy barrier height $\Delta G^{\ddagger}_{pre} / \Delta G^{\ddagger}_{post}$ for 100 mM NaCl (c) and 320 mM NaCl (d). The ratios of the energy barrier show no significant force dependency for either salt condition.

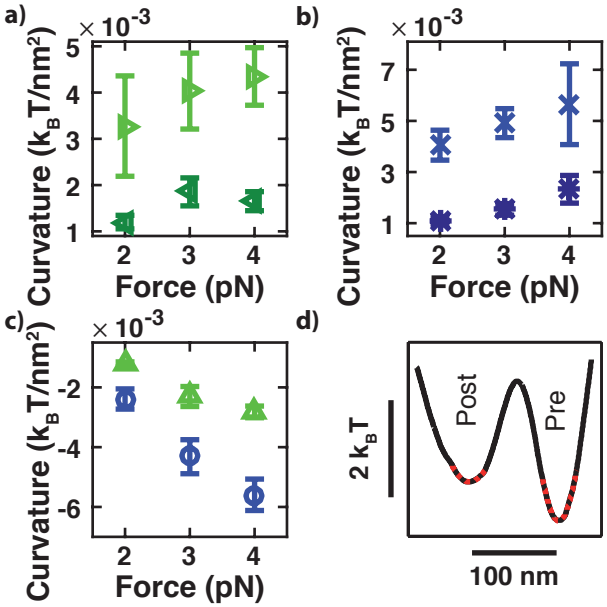

Figure 6.14: Curvature of the reconstructed energy minima and maxima. a) Curvature of energy valleys at 100 mM NaCl. No significant trend in force is observed, neither for the pre-buckling state (green right-pointing triangle) nor for the post-buckling state (dark green left-pointing triangle). The curvature of the pre-buckling state is always larger than for the post-buckling state. b) Curvature of energy valleys at 320 mM NaCl. Again, no significant change in the curvature for all forces is obtained (blue cross: pre-buckling state, dark blue asterisk: post-buckling state). As determined in panel a), the curvature of the post-buckling state is smaller than for the pre-buckling state. c) Curvature of the energy barrier top. The absolute value of the curvature for 100 mM NaCl (green upward-pointing triangle) is for every force probed smaller than for 320 mM NaCl (blue circle). For both salt concentrations a trend to higher absolute values of curvature at higher forces is observed. This is in qualitative agreement with the higher energy barrier at higher forces but force independent curvature of the energy valleys and roughly constant jump size over all forces. d) Curvatures were determined by a quadratic fit (dotted red line) around the minima of the wells that included the extension range of ± 20 nm around the minimum.

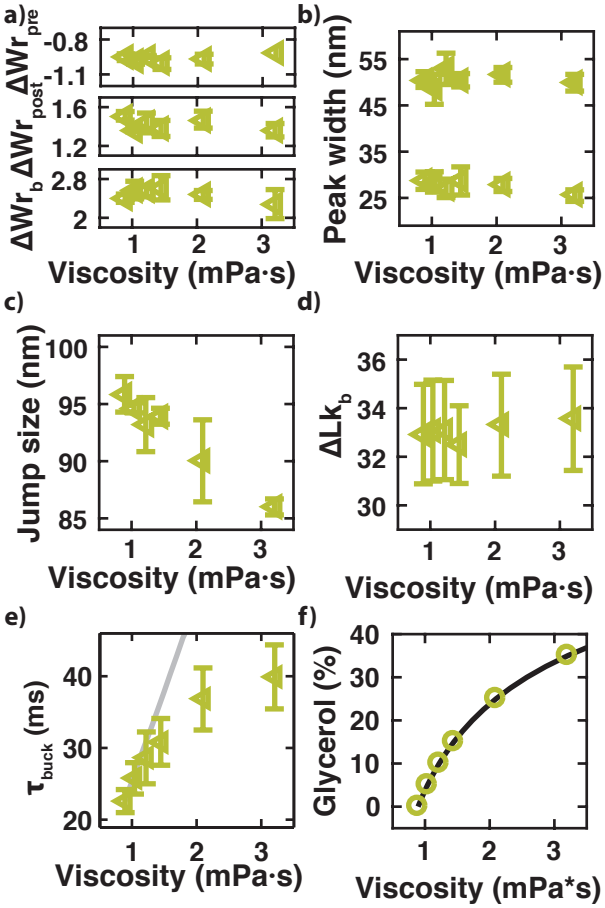

Figure 6.15: Effect of glycerol on buckling dynamics and equilibrium properties. All data were recorded at constant force and salt (3 pN, 100 mM NaCl). a) Effect of friction on distance to transition state in turns. Addition of glycerol does not change the distance to the transition state in number of turns, neither for the pre- nor post-buckling state. Furthermore the number of turns converted from twist to writhe does not change by friction. b) Peak width of pre- and post-buckling state vs. friction. The peak widths of all measured frictions remain constant and show no influence by glycerol. c) Jump size at the buckling point vs. friction. A slight trend of reduction in the jump size with higher glycerol concentration and therefore higher friction is observed. Nevertheless we note that most of the data points lie within the error bars. d) Buckling point ΔLk_b vs. friction. An increase in glycerol concentration and thus in friction does not change ΔLk_b. For every measurement point in all panels three different DNA-bead combinations were measured. Before analyzing, all extension traces were corrected for the change in the index of refraction due to glycerol. e) Influence of friction on the characteristic buckling time. An increase in friction by glycerol leads to a longer characteristic dwell time. A simple linear fit does not describe the behavior. Gray line extrapolated according to Bai *et al.* with measurement value without glycerol as starting point [347]. f) Relationship between viscosity and glycerol concentration. Data were taken from Ref. [372].

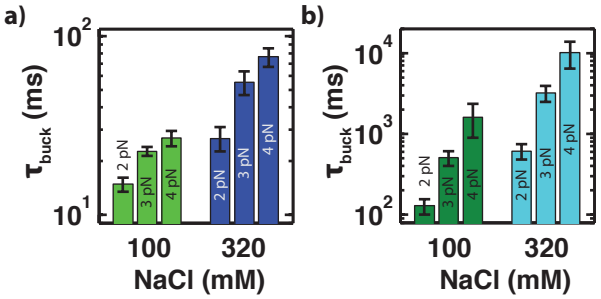

Figure 6.16: Buckling times vs. monovalent salt concentration at different forces. Increase of force and/or salt concentration results in an increase in the buckling times for DNA (a) as well as for RNA (b) (colors according to Fig. 6.2). Note the very different scales for the y-axes in panels a) and b).

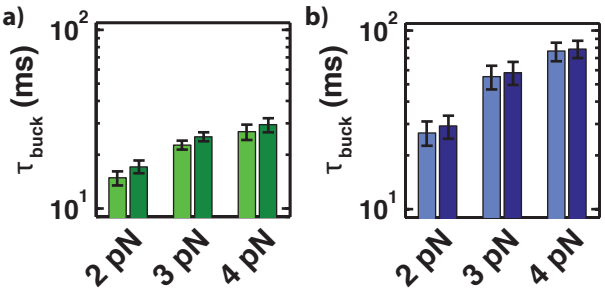

Figure 6.17: Effect of the correction of the buckling times for finite acquisition time. All buckling times reported in the manuscript, unless indicated otherwise, were corrected for the effect of finite acquisition time (see "Correction for finite acquisition times" section above). Biases due to the finite camera frequency are corrected by applying a correction based on the moment equations for a two-state Markov model. All corrected τ_{buck} are faster than the uncorrected τ^*_{buck}, but within the experimental error. a) Buckling times for DNA in 100 mM NaCl; light green: corrected values; dark green: uncorrected values. b) Buckling times for DNA in 320 mM NaCl; light blue: corrected values; dark blue: uncorrected values.

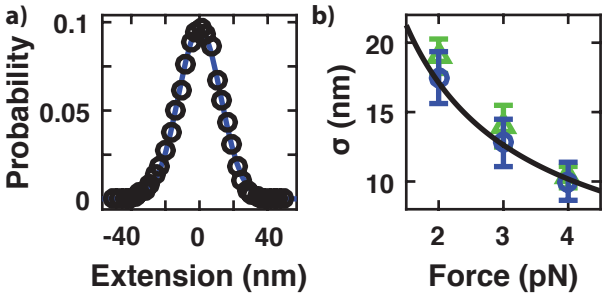

Figure 6.18: Magnitude of the extension fluctuations and estimate of the instrument response function *S(z).* a) Histogram of extension fluctuations (black circles) and Gaussian fit (blue line), at 2 pN and 320 mM NaCl. The histogram of tether extension measurements for a torsional relaxed DNA tether is well described by a single Gaussian fit. Therefore, the point spread function or instrument response *S(z)* used in the deconvolution procedure was set to a Gaussian distribution with peak width determined for every salt and force separately. b) Standard deviation of extension fluctuations (σ_z) vs. applied force for 100 mM (green triangle) and 320 mM (blue circle) NaCl. The magnitude of the extension fluctuations in the magnetic tweezers can be modeled by considering the Taylor expansion around the equilibrium position of the DNA-tethered bead and equipartition [333], yielding $\sigma_z = (k_B T/(\partial F/\partial L))^{1/2}$; $\partial F/\partial L$ is the derivative of force response of the tether with respect to the tether extension L. We approximate $\partial F/\partial L$ with the analytical derivative of the approximation formula by Bouchiat *et al.* [72] to the worm-like chain (WLC) model. The WLC model has two parameters: for the contour length, we use the value expected from the crystallographic length, 2700 nm for our 7.9 kbp DNA constructs; for the bending persistence length we use 45 nm, an average value determined previously for DNA under the salt conditions considered in our measurements. The prediction for σ_z of the WLC model (black solid line) provides an excellent description of our data (reduced X^2 = 1.08 and 0.02 for 100 and 320 mM NaCl, respectively).

Chapter 7

Introducing a New Attachment Strategy for Protein Unfolding Experiments in Magnetic Tweezers

In the framework of this thesis, a new attachment strategy to investigate proteins as tethers in MT experiments is introduced. This includes a one-side covalent (using "sortase A" enzyme-mediated chemistry) and one-side protein-ligand (*streptavidin-biotin*) bond. The final attachment strategy includes a linker between the coverslip and the protein. In this chapter, the surface chemistry is described, two kinds of linkers are compared, different passivation strategies evaluated, and preliminary successful measurements presented. The force response of the protein domain "ddFLN4" was examined as a reference and future fingerprint for other experiments. To proove universality of the attachment strategy, example traces of a second protein (von Willebrand Factor (VWF)) are presented.[1]

7.1 Introduction

Proteins adopt different kinds of functions in a cell and therefore are an essential tool for cells [125]. Hereby, a subset of proteins has to withstand external forces [139–142]. Depending on their function, proteins can bear different forces with a force-dependent lifetime before unfolding of the protein occurs. MT can apply low to medium forces ($0.001 - 100$ pN [4, 5, 33]) and therefore are a suitable tool to apply physiologically relevant forces. Its natural force clamp mode without the need for feedback makes it possible to measure for hours or even days [29] at constant force. This allows to determine the lifetime even at very small unfolding rates, where

[1] For this chapter, I performed most of the PEG related experiments. The experiments with ELP linkers were performed in close collaboration with Achim Löf (LMU Munich). Here, we contributed equally to the experimental design and to the development of the attachment strategy employed for the presented *ddFLN4* and *VWF* data. Achim Löf performed the majority of the *ddFLN4* and *VWF* measurements. I coded the software to analyze the data, and Achim Löf analyzed the single traces. The contributions to the interpretation of the *ddFLN4* data were equally split.

other techniques are limited [373–376]. Furthermore, due to the force clamp the lifetime can be measured directly without need for any theoretical assumptions and calculations [137]. Protein unfolding events under force are a thermally driven process, hence stochastically distributed. To gain a distribution of lifetimes, many unfolding events must be observed. Especially at low unfolding rates this can be a limiting factor if only one molecule at a time can be measured, such as in common AFM and OT experiments. However, highly multiplexed MT setups, such as the setup described in chapter 4, are able to measure many molecules in parallel, allowing to obtain good statistics in a minimum amount of time.

Commonly, MT are used to measure DNA mechanics [14, 44, 50, 93, 377], protein-DNA interactions [378, 379] or similar systems [26, 380], using the DNA as the tether between the surface and bead [14]. However, recent efforts towards an increase in the scope of application have led to systems with different tethers, such as proteins [27–30, 52, 141, 163, 381, 382].
A powerful property of MT is that it operates naturally in a force clamp mode. Therefore, the lifetime at one force can be examined. However, the usability for long measurements at one constant force depends on the lifetime of the attachment of the tether. A common approach for DNA-tethers is on one side an antibody attachment (*Digoxigenin-AntiDigoxigenin*, abbreviated "*Dig-AntiDig*") and on the other side a protein-ligand bond (*streptavidin-biotin*) [12, 25, 50, 383]. Common DNA constructs have multiple binding sites on both ends to enable a torsionally constrained attachment, but also to allow a long lifetime over a large force range. At high forces, the lifetime of a DNA tether is limited by the *Dig-AntiDig* binding sites [383]. The bond of the antibody allows a reasonable lifetime for common measurements with DNA, which are typically in a force range below $\approx$ 20 pN or only a short amount of time at higher forces. However, many proteins can bear higher forces for a longer time [52, 373, 384, 385], making a strong attachment necessary. Besides the limited lifetime of the multiple *Dig-AntiDig* binding sites (e.g. $\approx$ 7 min at 45 pN [383]), a second drawback of this attachment strategy is the need for multiple binding sites. Therefore, a break of one binding site can result in a jump in the extension trace without a rupture event of the tether, which can be falsely attributed to the tethered protein and therefore interfere with the protein signal. For this reason, a new attachment strategy with a long lifetime is needed, which does not produce artifacts in the extension trace of the beads.

In single-molecule force spectroscopy, different covalent bonds have been introduced, e.g. an *Sfp phosphopantetheinyl transferase* induced *coenzyme A* (*CoA*) – *ybbR-tag* bond [386, 387], formation of a covalent peptide bond with a *sortase A* mediated reaction [385, 388], a *HaloTag protein-ligand* bond [389, 390], *SpyTag-SpyCatcher* bond [391], and disulfide (thiol) bonds [392, 393]. The advantage of a covalent attachment is the high force needed to break the bond, which is in common experiments not accessible with MT. However, the thiol bond is in general not suitable, since many proteins contain naturally the amino acid *cysteine*, which can react with other thiol groups and therefore contain several binding sites, making it difficult to attach the protein in a well-defined, single geometry. The *HaloTag-ligand* and *Spytag-SpyCatcher* strategies have been recently implemented in MT experiments [29, 52, 382, 394, 395]. However, the drawback of the *HaloTag* attachment strategy is the potential unfolding of the binding complex, resulting in a step in the extension trace, which can interfere with the signal of the protein of interest [395, 396]. The *SpyCatcher* of the *SpyTag-SpyCatcher* bond is a large protein

by itself. However, in this case the force does not propagate through the protein, preventing it from unfolding. Nevertheless, in general, proteins don't have to, but can nonspecifically interact. Any interaction of the *SpyCatcher* protein with the protein of interest is difficult to distinguish from internal conformational changes of the tethered protein and results in an artifact to the measurements which can be easily misinterpreted.

Proteins close to surfaces can interact nonspecifically with the surface [397–400]. To address this problem, it is of interest to introduce a spacer between the glass surface and the protein of interest. One common linker in single-molecule force spectroscopy is *poly(ethylene glycol)* (PEG) [401–403] whose ends can be modified with functional groups and therefore can be (covalently) attached to surfaces and proteins. A recently introduced alternative approach are the so called "*elastin-like polypeptides*" (ELPs). In comparison to PEG, the force response of ELPs are better described by the qmWLC model, a WLC like model with an approximation for the stretching of the backbone by a *ab initio* quantum mechanical correction [404, 405]. For PEG, the force extension behavior is difficult to describe because of its linear regime between $\approx 100 - 300$ pN [404]. Nevertheless, in the force range commonly accessible with MT setups (< 100 pN) this drawback of PEG is not present. Furthermore, in force clamp measurements, the force acting on the linker is constant independent of protein un- or refolding events. Therefore, the exact stretching behavior of the linker is not expected to influence the measurement.
The thermal fluctuations of a linker increase the noise of a measurement. To reduce noise, a short linker is favorable, whereas a long linker minimizes risk of nonspecific interaction with the surface. Furthermore, the persistence length of the linker has influence on the additional noise. Although it is difficult to specify one value for the persistence length of PEG because of its linear force response regime, the persistence length of PEG and ELP is in the same order of magnitude. To obtain a maximum in resolution while minimizing surface interactions, the type and length of a linker has to be carefully chosen.
To sum up, it is of interest to use an attachment strategy which does not nonspecifically interact with the protein of interest, has a long tether lifetime, and implements a linker between the glass surface and the protein of interest. To allow long measurements times at high forces, only attachment strategies with at least one site covalent bond to the protein have been investigated.

7.2 Challenges of New Surface Attachment Strategies

For a new attachment strategy, in particular four properties are essential: 1) the bond has to form, 2) the surface has to be passivated to minimize unspecifically interactions, 3) the lifetime of the bonds have to be sufficient, 4) the lack of a "fingerprint" has to be considered.

The protein and the non-elongated spacers have typically a size of a few nanometers. Consequently, to form the bond(s), the bead and the surface have to get close together. The short distance to both the surface and the bead, can have an impact on the efficiency of the bond formation.
For many kinds of force spectroscopy, surface passivation plays an important role. In the case of MT, not only the proteins have to be prevented from nonspecifically binding to the surface, but also nonspecific binding of the bead to the surface have to be considered. The long incubation time needed for some of the covalent bonds can increase the importance of

surface passivation. Beads bound nonspecifically to the surface are critical in two ways. First, a specifically bound protein cannot be examined if the bead has a second unspecifically bond, second, tests revealed that nonspecific bound beads can exhibit steps in their extension trace which can interfere with the signal of the molecule of interest (Fig. 7.1).

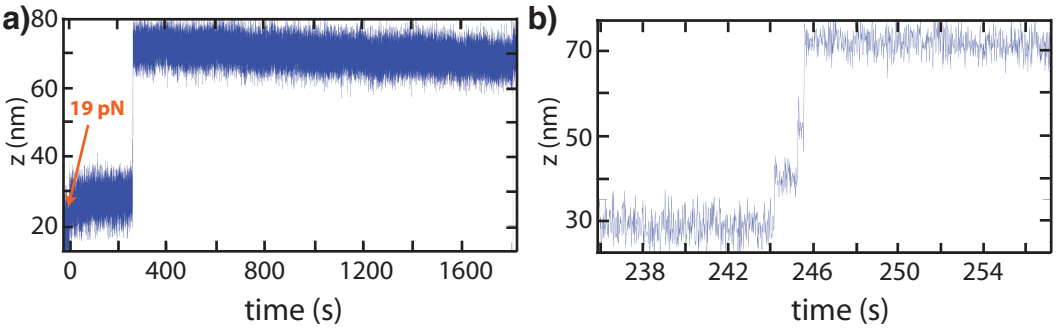

Figure 7.1: Multiple steps in the extension trace caused by a nonspecific bound bead. *Streptavidin* coated beads were incubated for 1 h to a nonreactive $-CH_3$ modified PEG surface within the flow cell. Beads that remained after rinsing with 1× PBS buffer were measured at a constant force of 19 pN (starting point as labeled in the figure) to determine the force response of nonspecific bound beads. a) whole trace and b) zoom in of the step(s) of (a). In the zoom in, multiple steps can be observed. The order of magnitude of the jump size is comparable to protein unfolding events. Time trace is set manually to 0 when force was applied. Note that no protein was attached to the beads or the surface.

As mentioned above, protein unfolding events can occur over a large force range. Therefore, the bonds have to withstand small as well as large forces for a long time before rupture of the bond. Hence, it is practical to have a covalent attachment for at least one terminus of the protein.
Common MT experiments with DNA as tether between the surface and the bead can use the DNA as a fingerprint to identify beads with single molecules between the surface and the bead. Therefor, the known behavior of DNA upon rotation as well as its easy-to-measure (long) length (in the order of a few micrometers) can be used (see chapter 6). However, single attachment points, as considered for protein attachment, are in general not torsionally constrained and thus the protein and the linkers are not subjected to any torque applied by the magnets and beads. As mentioned above, the typical size of an nonstretched linker-protein construct is in the order of a few nanometers, hence much short than for DNA and therefore the absolute length is more difficult to determine.

7.3 Surface Attachment with Linker (PEG)

PEG is commonly used as linker in single-molecule force spectroscopy. Both ends of PEG can be chemically modified to enable different kinds of attachments. It can be produced in different lengths and therefore an optimum of space between the surface and the molecule of interest to prevent from nonspecific binding, combined with a minimum of noise caused by the linker, can be found. PEG passivates surfaces and minimizes nonspecific interaction.
PEG has been introduced to MT experiments, but is not a common approach to attach a DNA or other molecule [383]. However, first attempts with PEG as linker in MT and its common use in other single-molecule force spectroscopy methods [401–403] made it a promising candidate

for a future standard in MT attachment strategies.
The two properties, successful bond formation and surface passivation, described in section 7.2, were investigated for different PEG lengths, binding sites, flow cell designs, buffers, and additional surface passivation admixtures. For a subset of tests, beads were modified with PEG (see Materials and Methods, section 7.8).

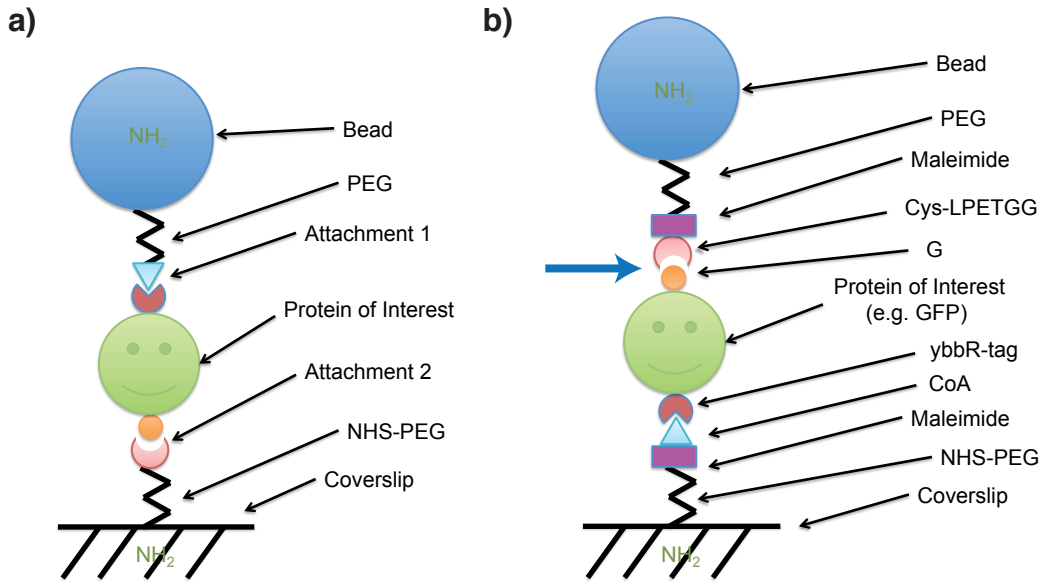

Figure 7.2: Surface attachment strategy with PEG. a) Basic idea of surface attachment. The protein of interest is tethered between the surface and the bead with PEG on both sites as a linker. For a subset of experiments, PEG was only attached to the coverslip and not to the bead. "Attachment 1" and "Attachment 2" are in general different types of bonds. One attachment site can consist of multiple successive bonds. b) Detailed attachment for *sortase A* mediated reaction (peptide binding) as *attachment 1* and a *CoA – ybbR-tag* bond as *attachment 2*. All bonds in the whole attachment strategy are covalent bonds. The blue arrow indicates the last bond formation.

7.3.1 External and Within Flow Cell Attachment Experiments

To evaluate PEG as a future linker for MT experiments, external tests with only coverslips and beads were performed, thus without a whole flow cell. Hereto, the coverslip and beads were coated with PEG containing functional groups (Fig. 7.2 and Material and Methods, section 7.8) and a protein (*green fluorescent protein* (GFP)) was tethered between the surface and the beads. To test the ability of bond formation, a maximum of tethers was targeted, hence it is expected that multiple proteins bind between the coverslip and the bead.

GFP was first attached via the covalent *CoA – ybbR-tag* bond to the PEG on an approximately round spot of the coverslip and secondly attached to the PEG of the bead with either *Streptag-Streptavidin* or *sortase A* mediated peptide bond, or the *SpyTag-SpyCatcher* system. After 1 h of incubation, loose beads were removed by rinsing with a pipette. In all three cases, a clear spot of beads could be observed (Fig. 7.3), whereas outside of the protein covered spot (almost) no beads remained.

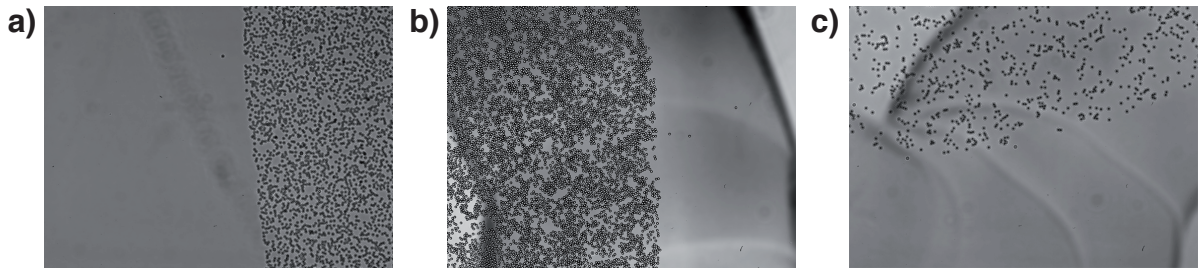

Figure 7.3: External, specific attachment of beads to the coverslip without a flow cell. After incubation of beads for one hour on the PEG- and partly protein-coated coverslips, the coverslips were rinsed with a pipette with 1× PBS. In all three cases, a specific attachment was possible: a) *Streptag-Streptavidin* and *CoA − ybbR-tag*, b) *SpyTag-SpyCatcher* and *CoA − ybbR-tag*, c) *sortase A* mediated peptide bond and *CoA − ybbR-tag*. The high concentration of proteins facilitates multiple tethers between a bead and the surface. In all three cases, only one (approximately round) spot was functionalized with protein. Broad gray shades are markers on the back of the coverslips to mark the border of the functional spot. In all three cases only within the functionalized spot a large amount of beads remained after rinsing with buffer, indicating specific binding. However, the *sortase A* mediated bond in (c) exhibits less beads compared to (a) and (b). It should be noted that approximately the same amount of beads were incubated in a, b, and c, however the concentration can slightly vary. In all three cases, the *CoA − ybbR-tag* was formed first, before the beads were added to the coverslip.

The same three attachments were furthermore tested in flow cells. Therefor, the bottom coverslips of the flow cells were covered with PEG before the flow cell was built. Again, protein was only attached to one spot of the coverslip. As for the external binding tests, the *CoA − ybbR-tag* reaction was performed as first bond before the flow cell was built. The beads were added within the flow cell. After 1 h of incubation, loose beads were removed by rinsing with 2 ml (i.e. 40× the volume of the flow cell) of buffer. For all three attachment strategies, the flow cells were covered with beads inside as well as outside of the spots. However, for the *SpyTag-SpyCatcher* as well as the *sortase A* mediated attachment, beads outside the spot could be partly removed by high force (≈ 70 pN) combined with rotation of the beads (Fig. 7.4). For the *streptavidin* coated beads, this was not possible. The difference in the amount of nonspecifically bound beads between the external and inside flow cell binding tests is most likely attributed to a higher force while rinsing with a pipette compared to the flushing of buffer inside a flow cell, therefore removing nonspecific bound beads in the former case. However, applying high force before a measurement is in general not feasible, since the protein of interest can unfold and may not refold into its natural conformation.

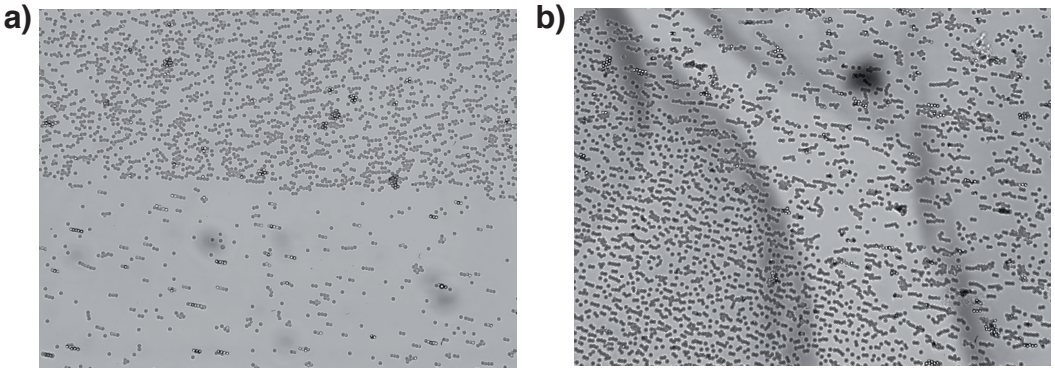

Figure 7.4: Specific binding to a functional spot inside a flow cell. Bottom-coverslip were covered with PEG. The protein was first attached to the PEG within a spot with the *CoA − ybbR-tag* bond before the flow cell was built. Outside the spot only PEG was present. The high concentration of protein facilitates multiple tethers between the coverslip and the bead. After mounting the flow cell, buffer was rinsed and beads were incubated for 1 h, than removed by rinsing of 2 ml of buffer. The spots were not clearly visible. Pulling with ≈ 70 pN while rotating the magnets could remove a subset of beads outside the functional spot. a) *SpyTag-SpyCatcher* and *CoA − ybbR-tag*, b) *sortase A* mediated peptide bond and *CoA − ybbR-tag*.

7.3.2 Surface Passivation (PEG)

Different strategies were examined to achieve a good surface passivation to minimize the number of unspecifically bound beads. For the following tests, the number of residual beads was examined, which were left in the flow cell after rinsing with buffer. The lack of at least one of the two attachment sites prohibits specific binding, hence, a low number of beads bound to the surface is favorable.
For all flow cells covered with PEG, the results were difficult to reproduce. An attachment strategy with a bad passivation was in general also sticky in a repeat measurement, however, the number of beads left in a flow cell can vary by a factor of up to ≈ 3. Flow cell preparation combined with attachment of PEG to the surface is a time consuming task, therefore only one to two flow cells per condition were built. Consequently, only a qualitative analysis of the experiments is reported. However, the results are typically sufficient clear that final conclusions can be drawn.

All tested flow cells coated with a PEG layer had in common, that they were very sticky for beads. Passivation tests under various conditions were performed to improve the passivation and reduce nonspecific binding. For these tests, beads were incubated in the flow cell, however, no specific binding could occur due to the absence of at least one binding partner. For many tests, no protein was used. For a subset of tests which exhibited an acceptable passivation without a protein, consecutive tests were performed, including *GFP* or several consecutive *Ig-domains* bound to the beads or coverslips. Therefore, the passivation efficiency under realistic conditions with proteins was examined.

For different lengths of PEG (from ≈ 500 to ≈ 10000 dalton) the flow cells were sticky, resulting in a large number of nonspecific bound beads, which could not be removed by rinsing the flow cell with buffer. This result was independent of the tested functional groups at the end of the PEG (including the nonreactive $-CH_3$).

For a subset of conditions, two attachment strategies of the PEG layer were tested: binding the PEG layer before or after the flow cell was built. However, no significant difference in the passivation could be observed. However, coating the flow cell with a layer of PEG after the flow cell was built resulted in small, local, gray shades on the surface after rinsing with 1× PBS or Coh-Doc buffer (Fig. 7.5, see Materials and Methods for details of buffer compositions, section 7.8). However, the shades could be removed with *dimethyl sulfoxide (DMSO)* and are likely clusters of PEG which were not removed while rinsing with buffer. Since *DMSO* can be used as solvent for attaching *N-Hydroxysuccinimid (NHS)* functionalized PEG to the *amine* (NH_2) functionalized glass surface, the resulting layer is not expected to be damaged by rinsing with *DMSO*.

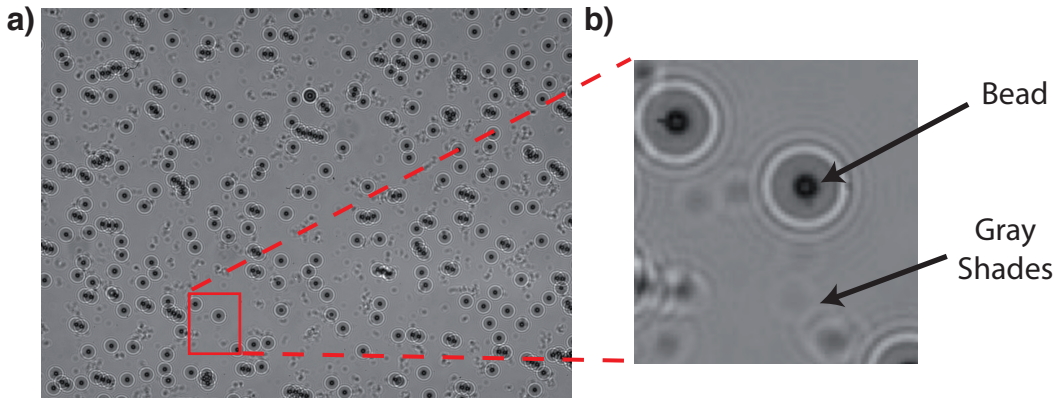

Figure 7.5: Gray shades after PEG attachment within the flow cell. If PEG was attached to the coverslips within the mounted flow cell, residual gray shades remained in the flow cell after rinsing with 1× PBS or Coh-Doc buffer. These residual shades remained independent of the amount of buffer and the velocity of rinsing. However, rinsing with *DMSO* could remove the shades. Whole FOV (a) and insert (b) as marked in (a) after PEG attachment and buffer flushing.

A repeat of binding PEG to the surface, thus a second step of attachment, and therefore reducing areas not covered with PEG [400], did not improve the passivation of the PEG-coated flow cells. The walls of MT flow cells are commonly made of parafilm (see Materials and Methods, section 7.8) and have to be baked to form a sealed chamber. To exclude any influence of the baking to the surface, which could potentially worsen the PEG layer, for a subset of PEG and buffer conditions, flow cells were produced with silicone sheets with no need for baking. However, for all conditions tested, no improvement of the surface passivation was observed. Taken together, it can be assumed that the PEG layer attached to the surface of the flow cell is comparable to other experiments using PEG as surface functionalization [401–403].

To test the impact of buffer on nonspecific binding, different buffer conditions containing different amounts of monovalent and divalent ions were tested during incubation of the beads and rinsing the flow cell afterwards. It was observed that the composition of the buffer influences the passivation of the PEG covered coverslips (Fig. 7.6). The buffer containing borate ("borate buffer" described in Material and Methods, section 7.8) but no salt reduced the sticking of the beads to the surface. However, many covalent attachment strategies need a defined amount of salt to form [385–388], and consequently the salt free buffer restricts the application of different attachment strategies. Furthermore, in general proteins need a certain amount of salt to not

change their conformation, unfold or aggregate. Therefore, the salt free buffer restricts the generality of the attachment strategy in a manner that this approach was not further continued.

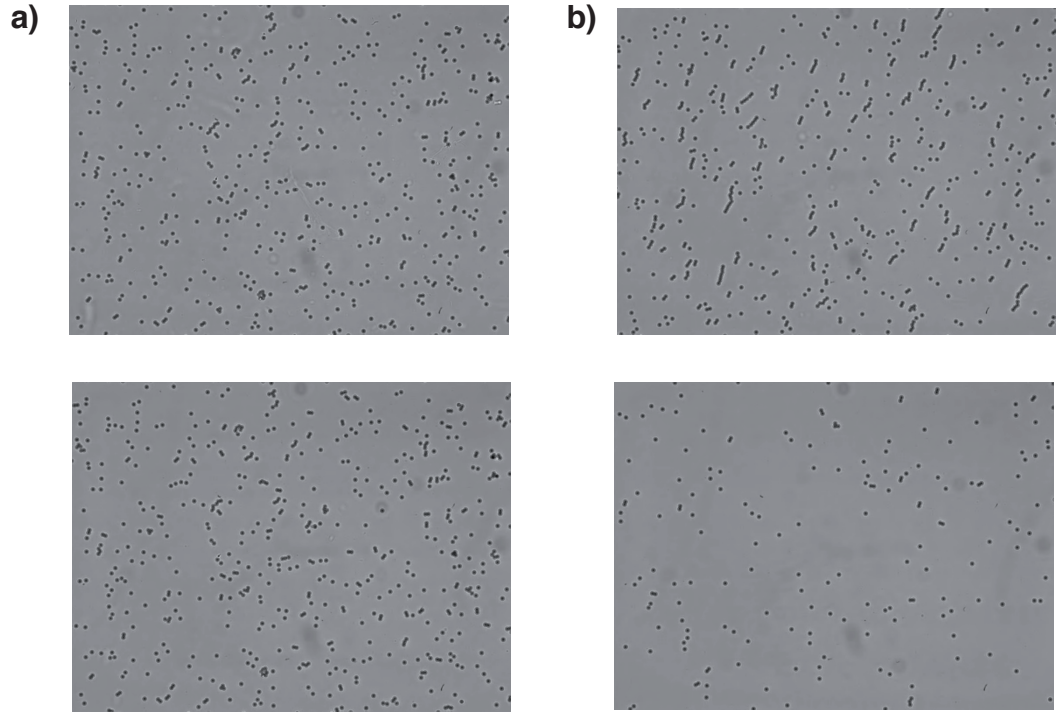

Figure 7.6: Impact of buffer conditions on nonspecific binding. Different buffers were tested for incubation of beads and rinsing the flow cell afterwards. The *borate buffer* containing no salt reduces the amount of residual beads after rinsing with buffer. Top row before flushing to remove beads, lower row after flushing with buffer. a) *Coh-Doc*, b) *borate-buffer*. The detailed composition of both buffers is given in the Material and Methods, section 7.8. Beads were covered with streptavidin and were incubated with the relevant buffer for 1 h in the flow cell. The bottom coverslip of the flow cell was covered with nonreactive (CH_3) PEG and therefore could not bind specifically to the beads.

To reduce unspecifically binding of the bead (and later protein) to the surface different detergents in different concentrations and other passivation methods have been considered. *Bovine serum albumin (BSA)* did not improve the passivation of the surface, a commercial pre-mixed blocking solution (*BlockAid*) had only minor impact. Preincubation of the flow cell with *diaminodiphenylmethan* (*DDM*) or *Pluronic F127* could not improve the passivation. However, pre-incubation of *Tween 20* could reduce the amount of beads nonspecifically bound to the surface. Further improvement in passivation was achieved by an admixture of *Tween 20* and buffer while beads incubated in the flow cell. A small tendency to better passivation at higher concentrations of *Tween 20* was observed, however, the deviations between different flow cells prevents a quantitative result. *Casein* and a commercial "blocking solution" (Candor, Germany) based on chemically modified and fragmented *casein*, could further improve the passivation. However, the deviations between different flow cells with the same passivation could not be eliminated. The deviations between the flow cells made it difficult to continue with the achieved passivation. Multiple tethers between the glass surface and the bead are expected to be difficult to distinguish from nonspecific tethers. Hence, trying to bind beads

specifically to the surface with a protein as tether and thus increasing the number of beads remaining within the flowcell, it is difficult to distinguish if a higher amount of beads is related to specific binding or deviations of the degree of nonspecific binding.

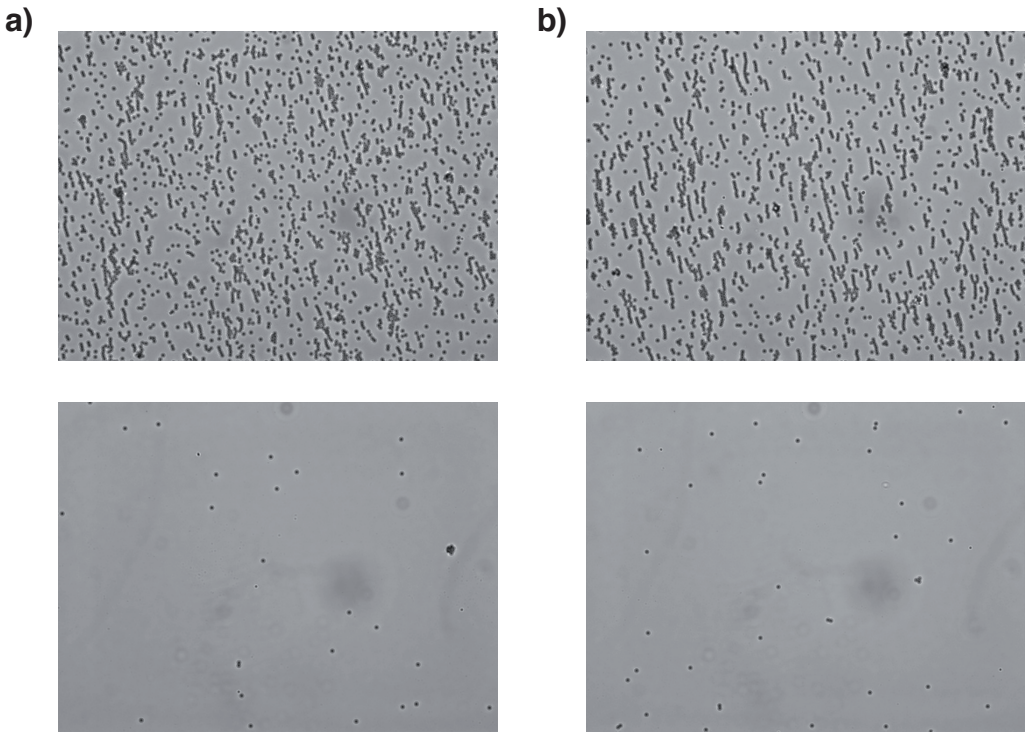

Figure 7.7: The best passivation result, thus the least amount of residual beads nonspecifically bound to the surface was achieved for beads covered with PEG with *CoA* attached to its end together with *Tween 20* (0.1 %) pre-incubated in the flow cell and also admixed to the buffer during incubation (here 0.01 %). (a) and (b) are two independent flow cells with the same conditions. Top row before rinsing, lower row after flushing of 2 ml (i.e. 40× the volume of the flow cell) of *Coh-Doc* buffer. The detailed composition of both buffers is given in the Material and Methods section 7.8. Beads were incubated 1 h before rinsing with buffer. The bottom coverslip of the flow cell was coated with nonreactive (CH_3) PEG and therefore could not react specifically with the beads.

Many covalent attachment strategies have in common that they need a long incubation time (≈ 1 h) to form the bond. However, the long incubation time could increase the number of nonspecific bound beads. To enable short incubation times, beads coated with *streptavidin* were examined. In normal MT flow cells with DNA as tethers, the *streptavidin-biotin* bonds can form within seconds. Passivation tests with *streptavidin* were performed with pre-incubated *Tween 20*. However, *streptavidin* coated beads bound nonspecifically to the PEG coated coverslips within seconds and even while flushing the beads and buffer. Hence, this approach was not further considered for future measurements.

For the best passivation tests, not only the coverslips, but also the beads needed to be covered with PEG. The least amount of residual beads nonspecifically bound to the surface was achieved with PEG coated beads containing *CoA* at their remaining reactive end. For best passivation efficiency, *Tween 20* has to be pre-incubated and at least a low concentration of *Tween 20* (≈ 0.1 %) is needed in the buffer during incubation of the beads (Fig. 7.7). This

passivation was acceptable with physiological buffer conditions.

7.3.3 Bond Efficiency (PEG)

The *CoA* covered beads with pre-incubation of *Tween 20* were the only combination which resulted in a sufficient surface passivation. Therefore, this combination was further examined to serve as a attachment strategy for a covalent bond of proteins in MT flow cells. For all binding experiments, the coverslip and the bead were covered with PEG and further modified as described in the following.

CoA can covalently attach to the *ybbR-tag* of the protein. Hereby, the *Sfp phosphopantetheinyl transferase* is needed to form the bond. To have a covalent bond on both sites of the protein, the other site was attached either with a *sortase A* mediated covalent peptide bond or the *SpyTag-SpyCatcher* system. However, the *SpyCatcher* bound to the surface resulted in an extremely sticky flow cell and therefore was not further considered for future attachment strategies.
For the *sortase A* associated reaction, only a very short, specific amino acid sequence is needed at the coverslip and protein site (see Ref. [385, 388] for details). These amino acids did not influence the passivation of the surface and the beads. To obtain best efficiency of the covalent binding process, different orders of binding steps were examined, i.e. starting with the *Sfp phosphopantetheinyl transferase* or *sortase A*, respectively. Furthermore, the attachment geometry was reversed, hence the *CoA* was attached to the surface and the the peptide for the *sortase A* mediated reaction to the beads.
Independent of the sequence of the reaction or the geometry, no effective binding was obtained. The experiments were reproduced with *GFP* and the *Titin Ig-domains* leading in both cases to no appreciable binding efficiencies. The fluorescent property of *GFP* was used to examine the binding of the protein. It was shown that the first reaction, i.e. protein attachment to the surface, worked, independent if it was the *Sfp phosphopantetheinyl transferase* or *sortase A* mediated reaction. Therefore, the second reaction must fail.
About the reasons for the inefficient attachment, it can only be speculated. However, the small distance between the surface and the bead for the second reaction suggests that it could be related to an inaccessibility of the *Sfp phosphopantetheinyl transferase* or *sortase A* to the binding sites.
An experiment with a *CoA* coated flow cell and *streptavidin* attached to the beads (hence no further supplement is needed, but only a noncovalent bond can form) did result in a large amount of unspecifically bound beads, not usable for future experiments.

7.4 Surface Attachment with Linker (ELP)

To overcome the remaining challenges of the PEG based attachment, another linker, namely ELPs, has been investigated as alternative approach. ELPs are biopolymers built up from repeats of tropoelastin domains and thus amino acids [404, 406]. They can easily be expressed in bacteria (e.g. Escherichia coli). ELPs can be considered as disordered proteins which do not form secondary or tertiary structures. Therefore, the global structure of ELPs is flexible and unfolded [404, 407]. Their bulky but flexible shape enables an effective surface passivation

combined with a high accessibility for specific reactions [404]. The geometrical unstructured shape of the ELPs makes any steps in extension at constant force unlikely and thus no signal from the linkers should interfere with the signal (e.g. unfolding and refolding) of proteins.

The synthetic production of PEG results in a distribution in length, whereas ELPs are manufactured in bacteria and can be produced completely monodisperse, i.e. with a well-defined contour length. The monodispersity in length of ELPs enables to use the stretching behavior of the linker as a fingerprint for specific attachment. However, it should be noted that the absolute length determination of a linker with a contour length of $\approx$ 120 nm (as used within this thesis), which is only partly stretched because of its qmWLC like force response and the limited force allowed to not affect the protein, is a challenging aspect for MT setups (see Fig. 4.4).
Like PEG, ELPs can be produced with a large variation of modifications at their N-/C-terminals, enabling specific (covalent) attachment methods [404]. Their global physical behavior is roughly comparable to PEG (persistence length, common (accessible) total lengths), however differs significantly in a more detailed point of view. In single molecule force spectroscopy, the most critical difference of both linkers is the good description of ELPs with the qmWLC model, whereas the above mentioned linear force regime of PEG cannot be described that easily [404]. However, as previously mentioned, this property is mainly of interest for force-ramp or similar experiments, whereas in force clamp experiments the exact force response of the linker is of minor importance.

To compare ELPs with PEG, a subset of the passivation tests as described in section 7.3.2 were performed, this time with ELP coated flow cells. However, to make use of the already optimized passivation strategy, only bare ELPs, pre-incubation of *Tween 20* combined with an admixture of *Tween 20* and buffer while bead incubation, and a pre-incubation of *casein* combined with an admixture of *Tween 20* and buffer while bead incubation were tested. Again, for the passivation tests no specific binding was possible between the glass surface and the bead due to a lack of at least one binding site. Only ELPs with an amino acid sequence of "LPETGG" at their C-terminal end for protein attachment were used for the passivation tests, thus enabling future *sortase A* mediated attachment. To face the possibility of the same inefficient specific bond formation as for PEG for *Sfp phosphopantetheinyl transferase* or *sortase A* mediated specific binding in the second reaction step (see section 7.3.3), only commercially available *streptavidin* coated beads were used. Therefore, for future attachments only one side of the attachment strategy can be covalently bound.

Throughout the passivation tests, the deviations between different flow cells were reduced compared to PEG coated flow cells. ELP coated flow cells without any additional surface passivation were much less sticky than comparable PEG coated flow cells. Further improvement was achieved with pre-incubation of *casein* for 1 h and an admixture of 0.01 % *Tween 20* in Coh-Doc buffer during incubation of the beads. As described above, *streptavidin-biotin* bonds can form within seconds in a flow cell, thus the *streptavidin* coated beads were only incubated for $\approx$ 1 min in the flow cell before rinsing with buffer. For these conditions, flow cells could be produced with essentially no remaining nonspecific beads after flushing with buffer (Fig. 7.8).

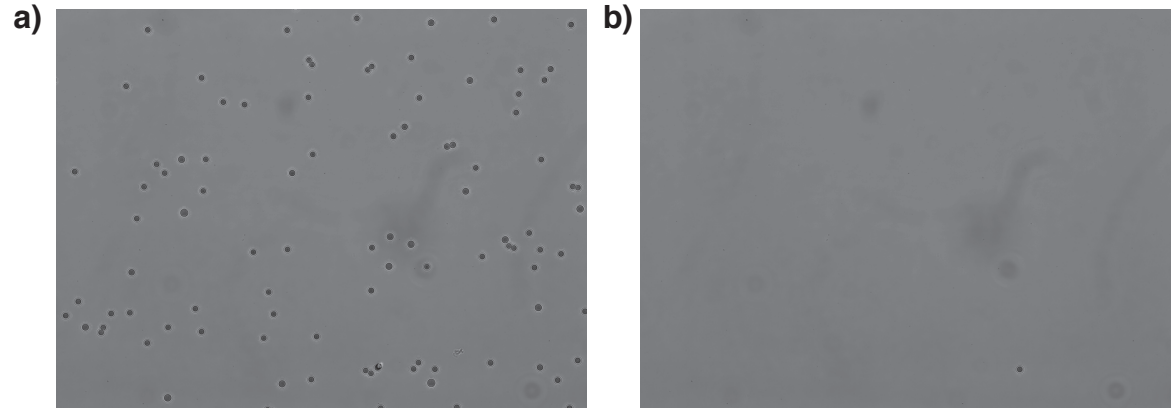

Figure 7.8: Representative picture of a surface passivation with ELP coated flow cells. ELPs were covalently attached to the bottom coverslip before the flow cell was built. *Casein* was incubated for 1 h and removed by flushing a Coh-Doc buffer admixed with 0.01 % *Tween 20*. *Streptavidin* coated beads were incubated for ≈ 1 min in the same *Tween 20* containing Coh-Doc buffer and removed by rinsing with this buffer. No protein was added to the flow cell, hence no specific interaction of the beads and the coverslip was possible. For this example FOV, only one bead remained nonspecifically bound to the surface. Image (a) was taken during incubation of beads, b) after rinsing with buffer.

7.5 Attachment Chemistry Characterization and Example Protein Un- and Refolding Events

The final attachment strategy received from the passivation tests has ELPs as a spacer between the bottom coverslip of the flow cell and the protein of interest. The protein is on one terminus covalently bound with the *sortase A* mediated peptide bond and on the other terminus noncovalently attached to the bead with a single *streptavidin-biotin* bond (Fig. 7.9).

The efficiency of this attachment strategy was tested with the protein domain *ddFLN4* as protein of interest. For these tests, the N-terminus of the protein was modified such that it possesses a single *glycine* ("G"), whereas the C-terminus contains the *ybbR-tag*. Incubation of the protein, *Sfp phosphopantetheinyl transferase*, and *CoA-biotin* results in an construct with *biotin* instead of the *ybbR-tag* at its end.
The protein domain *ddFLN4* is well characterized by constant speed single-molecule AFM measurements [7, 149, 360, 408–412]. *ddFLN4* is the fourth domain of the actin cross-linking filamin rod of Dictyostelium discoideum [7, 148]. Besides its physiological relevance, the (known) characteristic force response [7, 149] makes *ddFLN4* a suitable test-device and fingerprint to examine the protein attachment in MT. Studies of unfolding of the protein domain with AFM force spectroscopy revealed an intermediate state which comprises ≈ 60 of the 100 amino acids of the protein domain [7, 149]. These AFM experiments in constant speed pulling mode revealed a higher unfolding force for the transition from the native to the intermediate state compared to the transition from the intermediate to the completely unfolded state. Hence, in a force clamp measurements, such as in MT, a short lived intermediate state would be expected. Additionally, the single-molecule AFM measurements revealed a fast refolding within the millisecond regime at zero force [149]. Consequently, an unfolding event detected with MT should be reproducible if, for a limited time span, zero tension is applied between the force plateaus to allow refolding

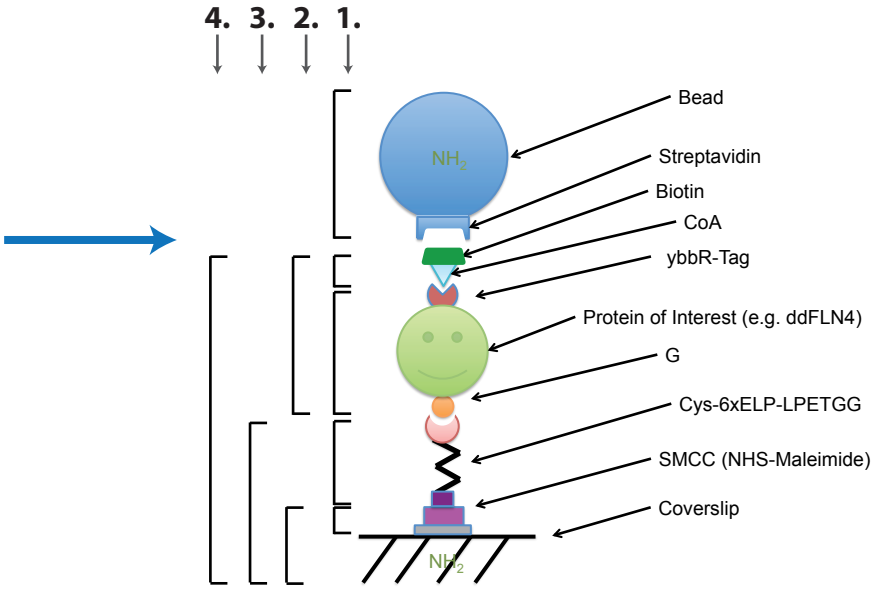

Figure 7.9: Final attachment strategy with ELPs as a spacers between the bottom coverslip of the flow cell and the protein of interest. The planes numbered with 1 to 4 picture the order (in time) of the attachment. The blue terminus indicates the last bond formation. The protein is covalently bound at one site via the *sortase A* mediated peptide bond, and noncovalent attached to the bead with the *streptavidin-biotin* bond.

of the protein domain. The average unfolding force of the native *ddFLN4* in constant speed AFM measurements was reported to be below 100 pN and therefore achievable for the MT setup introduced in chapter 4.

For a low concentration of *ddFLN4* bound to the surface of the flow cell (see Materials and Methods, section 7.8) and a force of ≈ 25 pN, two temporal nearby consecutive steps can be observed in approximately 50 % of all extension traces (Fig. 7.10). Both steps increased the extension of the tether (in the following referred to as "positive" steps). For a bead which once exhibited these two steps, the behavior was reproducible after a short (≈ 30 s) 0.5 pN force plateau. The first step in the extension trace occurred typically after several seconds, while the extension plateau of the intermediate step lasted typically less than one second. Before two positive jumps in the extension trace occurred, the absolute extension of the tether is in the order of what is expected for a partially stretched ELP. Considering only extension traces with two consecutive steps within the ≈ 25 pN force plateau, the extension before the first step, between the two steps, and after the second step are approximately at the same height for consecutive force plateaus (Fig. 7.10). The step size of the individual positive steps and the total increase in length are close to the WLC corrected extension values for *ddFLN4* obtained by single-molecule AFM measurements [7].
At lower force, e.g. 6.5 pN, steps in the extension trace can be observed, reducing the absolute extension of the tether (in the following referred to as "negative" step). However, in some traces it is more difficult to allocate two discrete steps.
Taken together, from the total length before the first step at 25 pN, the two consecutive steps with a longer lifetime before the first step, the fast refolding at low forces, and the length increase for both slightly different sized steps matching the expected length for the two subdo-

mains of *ddFLN4*, it was concluded that in these traces one single *ddFLN4* is tethered between one bead and the surface. A detailed analysis of traces with *ddFLN4* and thus the force response of *ddFLN4* can be found in section 7.6.

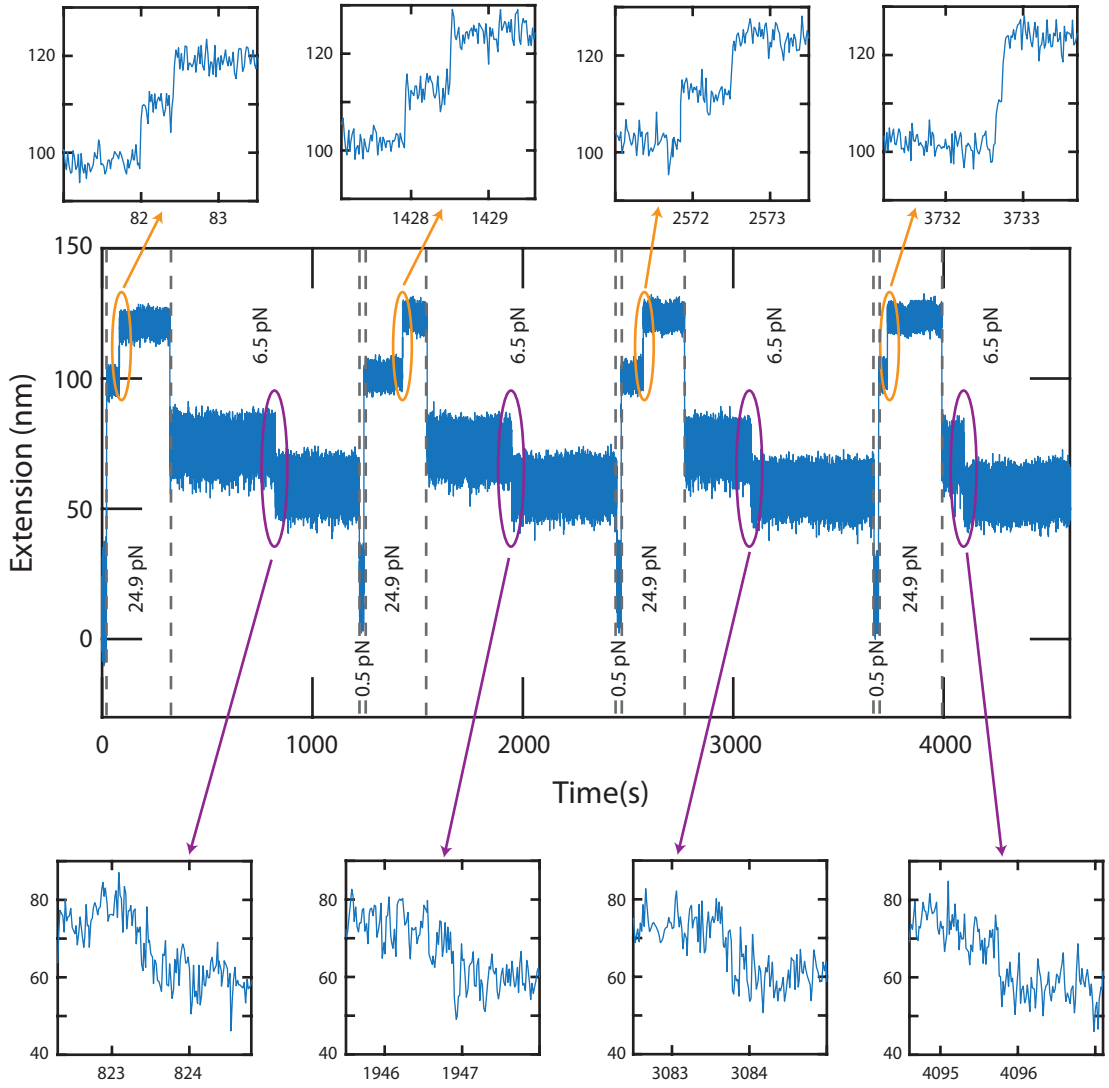

Figure 7.10: Example traces of unfolding and refolding events of the protein domain *ddFLN4* under constant force. The force was increased to a force plateau of 24.9 pN to unfold the protein domain, reduced to 6.5 pN to detect refolding events, and further reduced to 0.5 pN to enable refolding of protein domains which were not already in their native conformation. Gray dotted lines indicate force change. Upper row is a zoom in into the regions of unfolding events marked by the orange ovals. Lower row is a zoom in into the refolding events marked by the purple ovals. For unfolding, two temporally closely related consecutive steps could be observed as predicted for *ddFLN4* [7, 149]. The length increase is in good agreement as expected ones from AFM measurements [7, 149]. At 6.5 pN steps in the extension trace can be observed, reducing the absolute extension of the tether. However, in some traces it is more difficult to allocate two discrete steps. *ddFLN4* was attached to the surface via ELP linker and the *sortase A* mediated peptide bond. The other terminus of the protein domain was bound to the bead with the specific, noncovalent *streptavidin-biotin* bond. Measurements were performed in 20 mM HEPES buffer with additional amount of 0.01 % *Tween 20*. Zero point of the y-axis set arbitrarily.

In some cases, a tether that repeatedly showed two consecutive positive steps, exhibits only one step within one 25 pN force plateau. In this case the extension after motor movement of the magnets is already in the height of the intermediate state. Hence it is assumed that the first step occurred already during the movement of the magnets, which takes ≈ 1 s, or did not completely refold before. Furthermore, also tethers were observed which show sometimes no jumps within one 25 pN force plateau. Hereby, such tethers started either with the extension before two steps would be expected or with the final extension after the two consecutive steps. In these cases it is supposed that the tether did either not unfold within the plateau (lower level) or did already completely unfold within the motor movement (upper level). A lack of refolding in the previous low-force plateau can also explain the full extension of the tether.

To give further evidence for the specific attachment as well as to prove generality of the attachment chemistry, the large protein *VWF* (more precise, the large dimeric subunit of the protein *VWF*) was used for further experiments. Again from constant speed AFM measurements and optical tweezers measurements, it is known that the two *A2* domains of the *VWF* will unfold under external force. [152, 157]. These two unfolding events are expected to occur independently of each other and to obtain the same force response properties, i.e. unfolding force and contour length.
Measurements with repeated low (0.3 pN) and high (10.1 pN) force plateaus again revealed a characteristic unfolding pattern (Fig. 7.11a). The pattern of the extension trace consists of two positive steps of equal length. However, the second step is not rapidly following the first step as observed for the *ddFLN4*. Again, as for flow cells containing *ddFLN4*, not within all high force plateaus both steps are present, which can be explained the same way as for flow cells containing *ddFLN4* (unfolding while movement of magnets, to short force plateau for stochastically distributed unfolding events, or no refolding at low force). Regarding only plateaus with two steps, the three extension levels separated by positive steps within one 10.1 pN plateau are at the same height for the consecutive 10.1 pN force plateaus. After two positive steps at the high force plateau, two negative steps at an intermediate force of ≈ 4.4 pN can be observed (Fig. 7.11b).
For different forces, the positive steps are in excellent agreement with the expected, WLC corrected, length increase of a single *A2* domain unfolding event (data not shown) [157].
From the similarity between several beads within one FOV, two comparable positive steps at high force followed by two negative steps at lower force, the length change of one single step in the extension trace fitting the published length increase for *A2* domain unfolding, the conclusion can be drawn that the signal from these measurements originate from one single *VWF* protein tethered between the bead and the surface.

Between the bottom surface of the flow cell and the protein of interest, a 6×ELP linker is included. The observed extension traces as a function of the applied force shows a WLC like behavior before the two consecutive unfolding events of the attached *ddFLN4* protein domain, such as expected for an ELP linker (Fig. 7.12) [404]. Importantly, no steps or further features caused by the ELP linker were observed (here in HEPES buffer), which could interfere with the signal of the protein of interest. To further test if ELPs can produce buffer dependent steps or other signals in the trace of the bead, similar extension traces as function of force were recorded for sodium acetate buffer at pH 5.5 and HEPES buffer with 10 mM EDTA (pH 7.4) (for

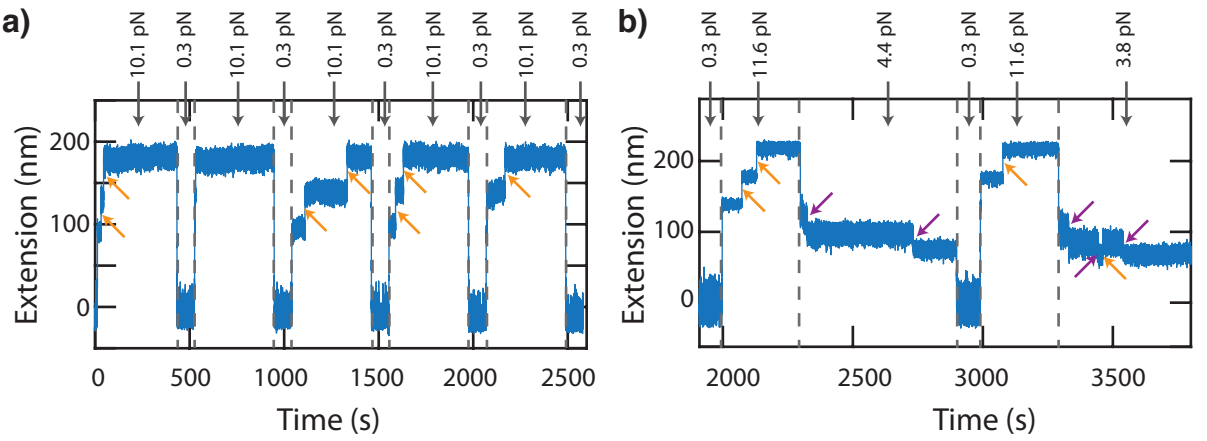

Figure 7.11: Example traces of unfolding and refolding events of the dimeric subunit of the protein *VWF* at constant force. The *VWF* construct is attached to the bottom coverslip of the flow cell with a covalent *sortase A* mediated peptide bond. A 6×ELP is used as spacer. The other terminus of the protein is attached to the bead via the specific, noncovalent *streptavidin-biotin* bond. a) Five repetitive 10.1 pN force plateaus separated by shorter 0.3 pN plateaus. *A2* unfolding events are marked with orange arrows. Two *A2* domains are present within the *VFW* construct, which unfold in the first, third, and fourth high force plateau. In the second 10.1 pN plateau the length indicates two unfolded *A2* domains from the beginning of the force plateau, in the fifth high force plateau one *A2* domain was already unfolded before the constant force plateau started. b) Unfolding (orange arrows) and refolding (purple arrows) of the two *A2* domains. The unfolded *A2* domains refold at lower forces (4.4 and 3.8 pN). Within the 3.8 pN force plateau an unfolding event after refolding is observed, followed by another refolding event. The length determined for the unfolding and refolding events are in good agreement with Ref. [157]. Measurements were performed in sodium acetate buffer with an admixed amount of 0.01 % *Tween-20*. Zero point of the y-axis set arbitrarily.

salt conditions see Materials and Methods, section 7.8).

The attachment strategy has a covalent bond only to one terminus of the protein of interest and the protein-ligand bond *streptavidin-biotin* at the other terminus. Therefore, it is possible that the bond ruptures within an MT experiment. To evaluate the possibility of a rupture event at constant force, the lifetime of the tethers were examined for different forces (Fig. 7.13). For this purpose, the *ddFLN4* was used as a fingerprint. Hence, only beads were considered which showed the two-step unfolding behavior of *ddFLN4*. For every single force investigated, the lifetime distribution of the beads at constant force can be described by a double-exponential decay (Fig. 7.13a). The rates of the first exponential (b) and second exponential (d) of the $a \cdot exp(-b \cdot t) + c \cdot exp(-d \cdot t)$ model, with t the time, are used to quantify the rupture lifetime of the protein-ligand bond (Fig. 7.13b). The force response of the individual dissociation rates $k_{off,\,F,\,speed}$ (with F the force) and also separated into the slow and fast decays (for "speed", respectively) were fitted by an Arrhenius relationship (Fig. 7.13b):

$$k_{off,F,speed} = k_{off,0,speed} \cdot e^{-F \cdot \Delta x_{speed}/(k_B \cdot T)} \tag{7.1}$$

with $k_{off,\,0,\,speed}$ the dissociation rate at zero force, k_B the Boltzmann constant and T the temperature. Δx_{speed} is the distance to the transition state. For all constants, the subscript "speed" can be "slow" or "fast" for the slow or fast decay of the double exponential model used for one constant force. For the fast decay, the zero force dissociation rate $k_{off,\,0,\,fast}$ is $\approx 1.9 \cdot 10^{-6}$ 1/s, with a distance to the transition state Δx_{fast} of ≈ 0.57 nm. For the slow decay the dissociation rate at

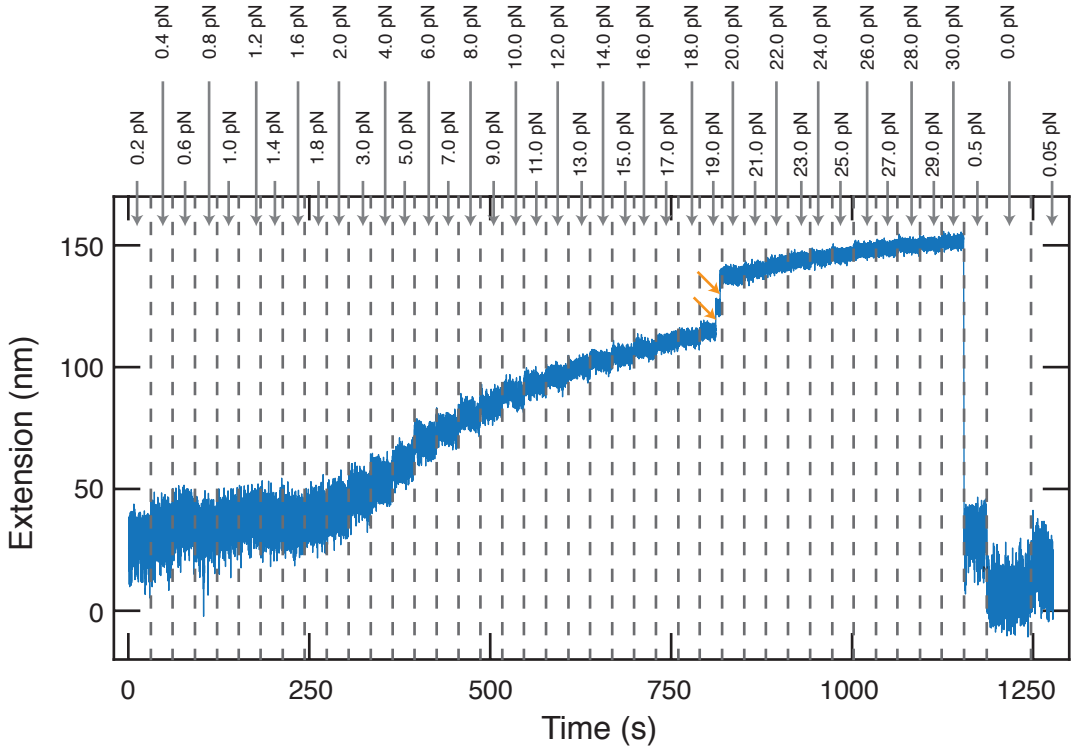

Figure 7.12: Extension trace of a 6×ELP linker for different constant force plateaus. The force is increased in steps and held constant for a few seconds. Gray dotted lines indicate force plateaus as labeled. The force response of the ELP follows a WLC-like behavior. Orange arrows indicate the two step unfolding of the *ddFLN4* protein domain. Measurement performed in HEPES buffer.

zero force is $k_{off,\,0,\,slow} \approx 0.3 \cdot 10^{-6}$ 1/s and the distance to the transition state approximately $\Delta x_{slow} \approx 0.42$ nm.

To sum up, for two different kinds of proteins successful protein (domain) unfolding as well as refolding events could be observed. The known force response pattern of these constructs, determined by AFM or OT measurements, are in excellent agreement with the data determined with the new MT attachment strategy. Therefore it can be concluded that the observed traces origin from single molecules tethered between the glass surface and the bead. Furthermore, the simultaneously, so far roughly, determined length of the ELP linker and its force response give further evidence, that a single protein is tethered between the glass surface and the bead with an ELP spacer between the glass surface and the protein. Combined with the setup described in section 4, the attachment chemistry allows for approximately 40 beads in average to measure simultaneously within one FOV that show the expected protein unfolding behavior. The lifetime of the bond is feasible for physiological forces and the accessible force range of MT setups. Therefore, measurements below 10 pN which last for more than 2 days (afterwards manually stopped) could be performed (see section 7.6, Fig. 7.18).
In the following section, the attachment strategy was used to determine detailed information about the *ddFLN4* protein domain.

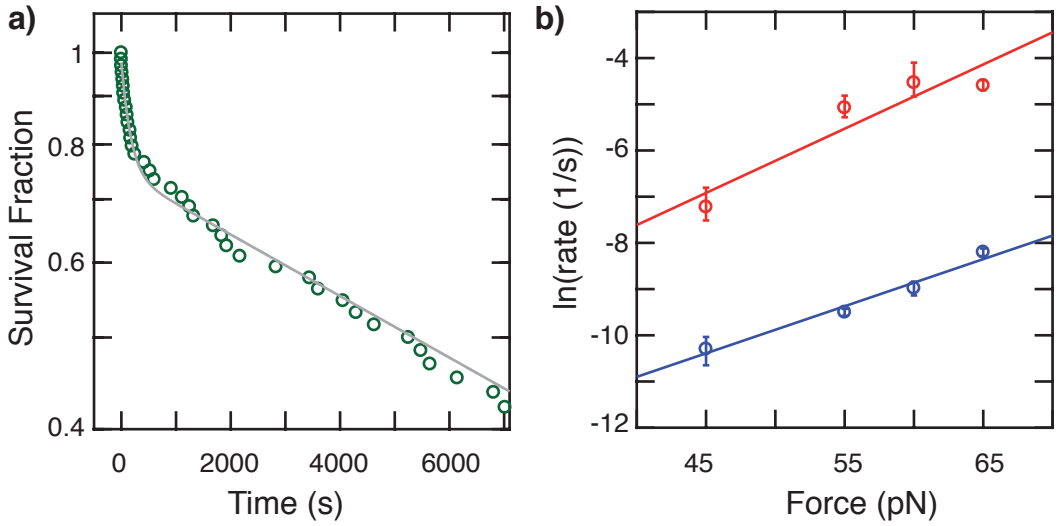

Figure 7.13: Lifetime of the *streptavidin-biotin* bond under external forces. a) Survival fraction of beads as function of time at 55 pN. At constant force, the lifetime of the bond is separated into a fast and a slow decay and thus is well described by a double exponential model (gray line). b) Force dependence of the two rupture rates within one constant force. The fast (red) and the slow (blue) rates follow each a single exponential model (Arrhenius relationship) as function of force. Error bars are 95 % confidence interval of the double exponential fits as shown in (a). Detailed measurement condition are described in Materials and Methods, section 7.8.

7.6 ddFLN4 Force Response - Preliminary Results

Section 7.4 and 7.5 introduced an attachment strategy with covalent attachment on one terminus. This chemistry can be used for high throughput measurements of the force response of proteins. To prove its prospects, the protein domain *ddFLN4* was measured and analyzed quantitatively. To this end, the rates of the different events as well as the length increase and decrease is analyzed. However, this part is an ongoing project, which so far focuses on data collection and analysis, but lacks biological interpretation (see section 7.7 for future directions).

As mentioned above, *ddFLN4* is a domain of actin cross-linking rod. Unfolding and refolding under force of this protein domain is expected to be important for its biological function. Schwaiger *et al.* [7, 149] showed that under force *ddFLN4* occupies (at least) one intermediate state for both transitions. By single molecule constant speed AFM measurements they were able to reconstruct transition rates at zero force between the different states for un- and refolding events.
To obtain the force response of the *ddFLN4* domain at different forces, i.e. different magnet positions, measurements similar to Fig. 7.10 were performed (unfolding at high forces, refolding at medium force, additional refolding phase at low force). Before the actual measurements, the protocol for protein unfolding with $\approx$ 25 pN and a measurement time of 300 s was repeated five times. Only beads that showed at least two times a two-step unfolding of the protein domain were considered for future measurements and analysis.
One main goal of this ongoing project is to compare the rates determined by AFM in constant speed pulling mode with force clamp measurements of magnetic tweezers. To show that the intermediate state in constant speed and constant force measurements is (probably) the same, the length between the native and the intermediate state and between the intermediate state and

the unfolded state is examined (Fig. 7.14). For forces equal to and higher than 9 pN, unfolding events of the protein domain were analyzed. For lower forces, the refolding event was used. In both cases, the first and the second step were analyzed separately. However, for refolding below 6 pN, two steps could not be clearly distinguished and only the total length change was determined. For unfolding of the protein domain, the first step was smaller than the second step, while for refolding the first step was larger than the second one. Schwaiger *et al.* [149] showed that for unfolding and refolding of *ddFLN4* only one (the same) intermediate state can be assumed. With the assumption of only one, single, intermediate state, the two small steps were attributed to belong to the same conformational transition, and the two large steps to the remaining conformational change. This assumption is further affirmed by equilibrium measurements (see Fig. 7.18) where an intermediate state can result into an unfolding or refolding event. The WLC model (in approximation of Petrosyan [405]) with a fixed persistence length of 0.5 nm (following Ref. [149]), can describe the determined extensions as a function of force, resulting in contour lengths (and standard deviation) of 14.95 ± 0.06 nm, 17.2 ± 0.11 nm, and 31.86 ± 0.13 nm for the small step, large step, and total length, respectively (Fig. 7.14). These results are close to the contour lengths reported by Schwaiger *et al.* [149] (≈ 14−15 nm, ≈ 16−17 nm, and 31.5 ± 0.1 nm, same steps in the same order). Therefore, it can be concluded that the intermediate state observed in the MT measurement is the same as previously reported for AFM measurements, thus a ≈ 40 amino acids long portion comprising two β strands which is related to the small step and a ≈ 60 amino acids long segment related to the large step.

The force clamp measurements enable to determine the rates between the different states of the protein domain. To describe the transitions connected to the intermediate state, four different rates have to be considered: Native to intermediate state (NI), intermediate to unfolded state (IU), unfolded to intermediate state (UI), and intermediate to native state (IN). Furthermore, the total rates from the native state to the unfolded state (NU) and vice versa (UN) are determined. The rates at one force were calculated from an exponential fit to the fraction of observed events as a function of time:

$$f(t) = 1 - a \cdot e^{(-k_{F,XX} \cdot t)} + c \tag{7.2}$$

with $k_{F,XX}$ the rate of the transition XX (i.e. NI/IU/UI/IN/NU/UN) at the force F, and t the time. The fit parameters a and c compensate for un- and refolding events which were missed by the measurements or analysis. This can occur by unfolding or refolding events within the magnet movement, but also a limited measurement duration at one force plateau defined a maximum of the detectable live times. Furthermore, very short occupations of the intermediate state, i.e. shorter than the camera acquisition time, can be addressed with the free parameters.
For the force range investigated, $k_{F,IU}$ is larger than $k_{F,NI}$ and $k_{F,NI}$ is in the same order of $k_{F,NU}$. It is concluded that the intermediate state formation is the limiting factor for unfolding of *ddFLN4*. Analyzing the refolding under force of the protein domain, $k_{F,IN}$ is approximately three orders of magnitudes larger than $k_{F,UI}$, while $k_{F,UI} \approx k_{F,UN}$. In this case it is concluded that, again, the intermediate state formation is the rate limiting transition. However, as mentioned above, for unfolding of *ddFLN4* the first step is attributed to the ≈ 40 amino acids long sequence of the protein domain, while for the refolding the first transition is attributed to the ≈ 60 amino acids long sequence.
The rates at zero force are determined from linear fits to the natural logarithm of the rates as a function of force (solid lines in Fig. 7.15, see Eqn. 7.5 in Materials and Methods). From

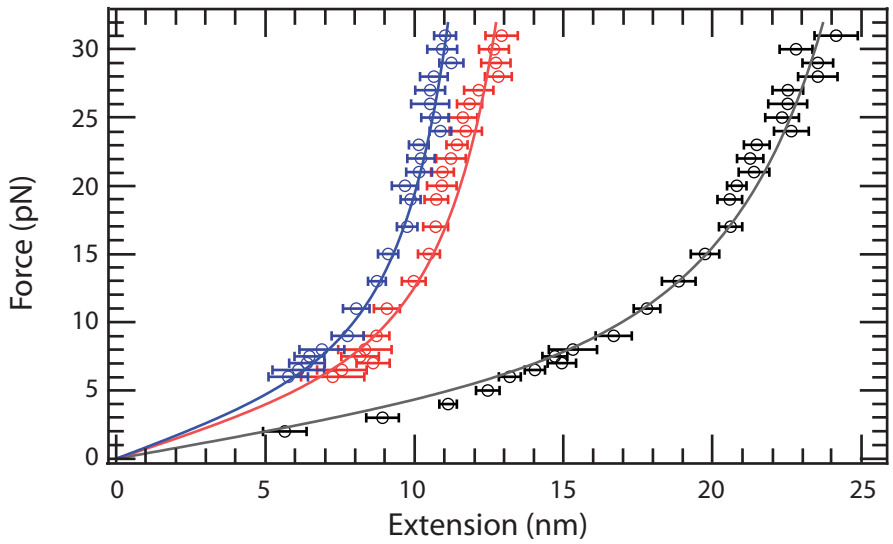

Figure 7.14: Extension curve of the small and the large step, as well as the sum of both as function of force. Data from < 9 pN are determined by refolding of the protein domain, all data from higher forces are obtained from unfolding events. The first step of unfolding and the second step of refolding are assumed to belong to the same conformational change (blue). Furthermore, the second step of the unfolding events and the first step of the refolding events are expected to belong to the same remaining conformational change (red). The force response of both individual steps as well as the sum of both steps (black) can be described by the WLC model simplified by Petrosyan [405]. The persistence length was fixed to 0.5 nm. The resulting contour lengths are ≈ 15 nm, ≈ 17 nm, and ≈ 32 nm for the small step, large step, and total length change, respectively. Below 6 pN the two refolding steps cannot be clearly identified and therefore only the sum of both steps are reported. Single extensions at one force are determined from Gaussian fits to the step length histograms (1 nm bins). Reported error bars are full width half maximum (FWHM) divided by the square root of the number of steps. It should be noted, that the force response of the ELP linker does not have to considered for constant force measurements

the force dependence, the rates at zero force $k_{0,XX}$ (with XX denoting the transition) as well as the distance to the transition states Δx_{XX} were determined. For the individual transitions, the rates at zero force are: $k_{0,NI} = 1.5^{+0.3}_{-0.2} \cdot 10^{-4}$ 1/s, $k_{0,IU} = 0.25^{+0.07}_{-0.05}$ 1/s, $k_{0,UI} = 0.52^{+0.27}_{-0.18}$ 1/s, $k_{0,IN} = 1544^{+960}_{-593}$ 1/s (Fig. 7.16). The subscripts and superscripts are the standard deviations of the linear fit. For the total unfolding and refolding of the *ddFLN4* protein domain, $k_{0,NU}$ and $k_{0,UN}$ were determined to be $1.6^{+0.3}_{-0.3} \cdot 10^{-4}$ 1/s and $0.52^{+0.27}_{-0.18}$ 1/s, respectively. The corresponding distances to the transition states are: $\Delta x_{NI} = 0.993^{+0.031}_{-0.03}$ nm, $\Delta x_{IU} = 0.320^{+0.045}_{-0.044}$ nm, $\Delta x_{UI} = 3.54^{+0.29}_{-0.30}$ nm, $\Delta x_{IN} = 3.48^{+0.28}_{-0.28}$ nm (Fig. 7.16). The distance to the transition state for the total unfolding and refolding are obtained to be $\Delta x_{NU} = 0.969^{+0.031}_{-0.03}$ nm, $\Delta x_{UN} = 3.55^{+0.29}_{-0.30}$ nm. The distance to the transition state, which is directly correlated to the force dependency of the transition and hence the slope in Fig. 7.15, shows that the transition from the native conformation of the protein domain to the intermediate state depends stronger on the force than the transition from the intermediate to the unfolded state. For refolding of the protein domain, the transition of the unfolded to the intermediate as well as the intermediate to the native state have the same dependency on force. The approximately similar values in the distance to the transition state and rates for NI and NU, as well as UI and UN indicate that the first transition is the rate limiting transition.

Extrapolation of the UN and NU transition yield an equilibrium force of ≈ 7.3 pN with $k_{7.3,NU} = k_{7.3,UN} \approx 9.3 \cdot 10^{-4}$ 1/s, which corresponds to a mean dwell time of 18 min (Fig.

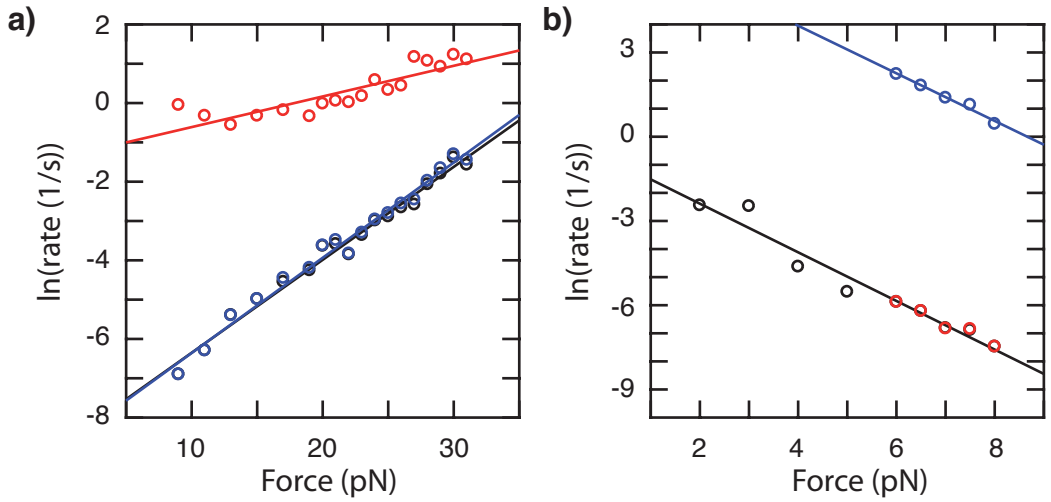

Figure 7.15: Unfolding (a) and refolding (b) rates as function of force for ddFLN4. For all unfolding transitions, the rates increase with force, while for the refolding the opposite is observed. $k_{F,NI}$ and $k_{F,UI}$ are the limiting rates for unfolding and refolding, respectively. Color code (a): IU red, NI blue, NU black. Color code (b): UI red, IN blue, UN black. Solid lines are exponential fits to the data. For determined rates at zero force and distances to the transition state see text. For *ddFLN4* refolding at forces $\leq$ 5 pN the intermediate state was not clearly detectable anymore and only the total rate is presented. Exponential fit for UI implied also total refolding rates at $\leq$ 5 pN. Fit of the UI and UN transitions overlap and therefore only solid line from fit to UN is presented. Errors of the previously determined rates at one force are within symbol size.

7.17). The equilibrium rate is verified by measurements close to 7.3 pN, however, the total amount of steps at equilibrium, even for a 66 h measurement, made a precise rate calculation difficult (Fig. 7.18). Furthermore, for a transition into the intermediate state, a transition back into the original state is sometimes observed ($k_{7.3,IN}$ = 3.17 1/s, $k_{7.3,IU}$ = 0.44 1/s, rates calculated from fits in Fig. 7.15). This makes a unique assignment of the transition (only separating into NU and UN) difficult.

Most of the rates reported in Fig. 7.16 differ significantly from the rates determined in constant speed AFM measurements of Ref. [149]. However, for the IU transition, approximately the same rate is determined ($k_{0,IU} = 0.25^{+0.07}_{-0.05}$ 1/s in MT vs. 0.33 1/s for constant speed AFM [149]). The folding rate at zero force $k_{0,IN}$ is roughly one order of magnitude larger within the MT measurements, the two folding rates $k_{0,UI}$ and $k_{0,UN}$ are approximately two orders of magnitude larger in AFM measurements. For completeness it should be noted that Schwaiger *et al.* determined the refolding rate UI and IN directly at zero force (see Ref. [149] for details). The largest deviation is observed for the transition from the native into the intermediate state (NI transition), with a three orders of magnitude smaller transition rate observed in constant force MT measurements. Remarkably, for the unfolding of the protein domain, the rates of the NI transition directly observed under force are for the force range investigated ($\leq$ 30 pN) smaller than the zero-force rate extrapolated from the AFM measurements [149].
For the IU transition, not only the rates, but also the distance to the transition state are within a comparable range ($\Delta x_{IU} = 0.320^{+0.045}_{-0.044}$ nm and 0.53 nm in MT and AFM measurements, respectively). The second distance to the transition state reported by Schwaiger *et al.* is from the native to the intermediate state (NI). Remarkably, with 0.4 nm it is by a factor of only 2–3

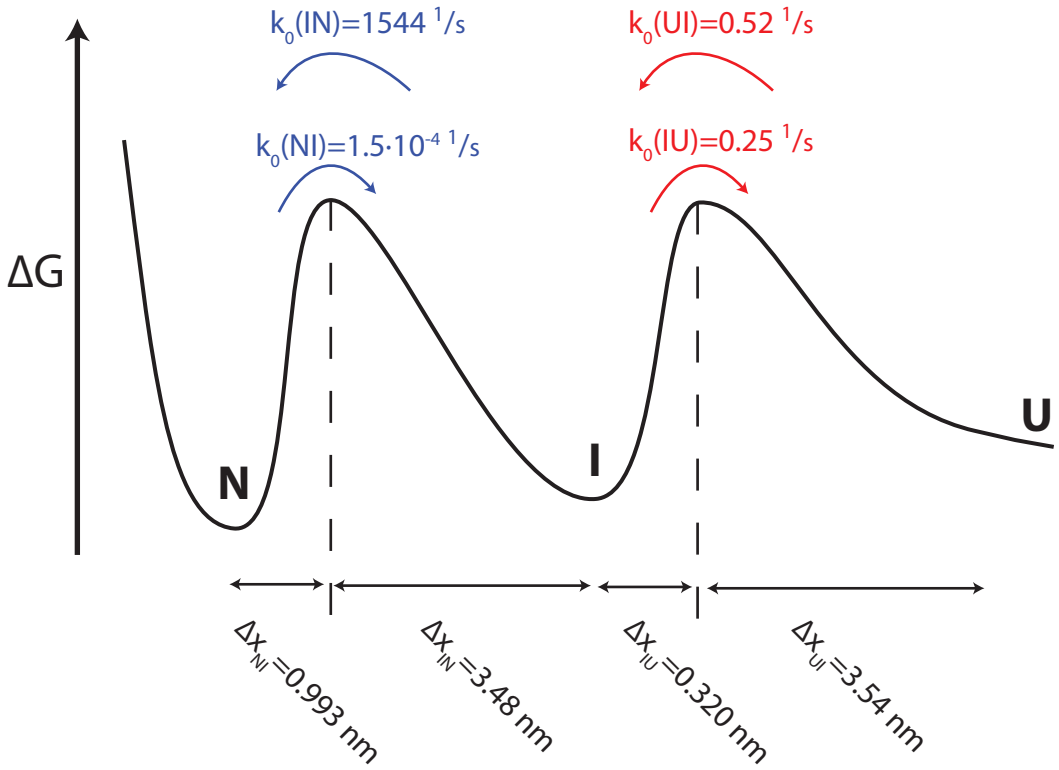

Figure 7.16: Illustration of 1D energy landscape of *ddFLN4*. Schematic not to scale. The distances to the transition state give evidence of an asymmetric energy landscape. The transitions for the complete NU and UN transitions are $k_{0,NU} = 1.6^{+0.3}_{-0.3} \cdot 10^{-4}$ 1/s and $k_{0,UN} = 0.52^{+0.27}_{-0.18}$ 1/s, respectively. The distances to the transition states are found to be $\Delta x_{NU} = 0.969^{+0.031}_{-0.03}$ nm and $\Delta x_{UN} = 3.55^{+0.29}_{-0.30}$ nm. The close overlap of NI and NU as well as UI and UN indicate that the first transition in both directions is the limiting step.

smaller than determined from the MT measurements (while as mentioned above the rate at zero force is three orders of magnitude different).

How to in general combine constant force and constant speed measurements is an ongoing discussion. For *ddFLN4*, several approaches have been employed to extract method independent rates for zero force [149, 360, 408–414]. Hereby, the exact values of the constant force MT experiments cannot be reproduced by the analysis of the constant speed AFM measurements. However, the results show that a discrepancy between the AFM data of Schwaiger *et al.* [149] and the data presented within this thesis is not surprising, as well as that the rates at zero forces have in general to be considered with care.
Schlierf *et al.* [412] compared extrapolation of the constant speed AFM measurement analyzed with the phenomenological model of Bell [138] and a model extension with the Kramer diffusion model. They found a better overlap for the raw unfolding data within the Kramers diffusion framework [137, 415] and achieved an unfolding rate of $k_{0,NU} = 10^{-2}$ 1/s (compared to 0.35 1/s with the model introduced by Bell). This extrapolation is closer to the MT unfolding data presented within the framework of this thesis, but still two orders of magnitude faster.
Constant speed AFM measurements of *ddFLN4* with a slow pulling speed of 1 nm/s (and 20 nm/s) deviated from data extrapolated with the Bell model [138] obtained from faster pulling speeds

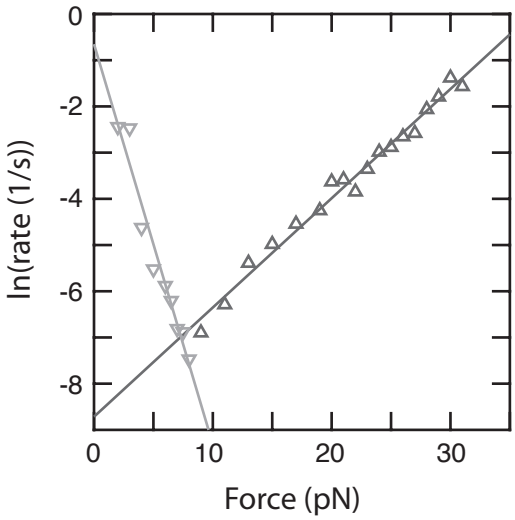

Figure 7.17: Rates of complete unfolding (NU, upward pointing triangle, dark gray) and refolding (UN, downward pointing triangle, light gray) of *ddFLN4* as function of force. Both rates are well described by a single exponential model (solid lines), which cross each other at ≈ 7.3 pN and a equilibrium rate of $k_{7.3,NU} = k_{7.3,UN} \approx 9.3 \cdot 10^{-4}$ 1/s.

[409]. Combining findings from constant speed AFM measurements and bulk denaturation of comparable protein domains [409, 416, 417], it was proposed that two parallel unfolding pathways, the mechanical and denaturant unfolding pathway, exist at low forces. With the slow constant pulling speed of 1 nm/s, an unfolding rate at zero force of $k_{0,UN} \approx 1.4 \cdot 10^{-4}$ 1/s and a Δx of ≈ 1.2 nm was achieved, thus in good agreement with our MT constant force measurement. Molecular dynamics simulations revealed differences in the (multidimensional) energy landscapes for two force regimes, separated by ≈ 2 pN. Here, below 2 pN the system consists of effectively two states, while at higher forces a third state becomes more pronounced. Above ≈ 5 pN the intermediate state is clearly observed [413].

Lucciolo *et al.* [410] determined an unfolding rate $k_{0,UN}$ of $\approx 10^{-2}$ 1/s with the concept of a critical force, which separates into two force regimes. Hereby, a thermally activated escape from a pure diffusion with external bias driven process is distinguished. For *ddFLN4* the critical force is determined to be in the order of ≈ 60 pN. However, it is assumed that also below this critical force, an influence within the low force regime can be observed [410].

Dudko *et al.* [360] and Cossio *et al.* [414] focus on the underlying energy landscape of *ddFLN4*. In this context, Dudko *et al.* assume that (in contrast to the Bell model) the distance to the transition state is force dependent. Hereby, similar to Lucciolo *et al.*, a $k_{0,UN}$ of $\approx 10^{-2}$ 1/s is obtained, thus again closer to the data determined within this thesis, however, still two orders of magnitude off. It is speculated that the pulling direction is not a good reaction coordinate and that therefore "the lifetimes can reveal richer, and even nonmonotonic, dependence on the force" [360]. However, it is mentioned that the multidimensional energy landscape could still be transformed into a 1D energy landscape with the real reaction coordinate.

Cossio *et al.* [414] focus on the unfolding of the *ddFLN4* protein domain. They describe the 1D energy landscape of *ddFLN4* to be ductile, meaning that the distance to the transition state changes with force. Ductile systems can in general resist larger force peaks and are therefore more robust than assumed from the Bell model, which assumes a perfectly brittle energy

landscape. Hereby, Cossio *et al.* determine the unfolding rate $k_{0,UN}$ to be $\approx 10^{-3}$ 1/s to 10^{-2} 1/s. Therefore, the original three orders of magnitude difference between the constant speed AFM data and the constant force MT data could be reduced to only one order of magnitude difference. The distance to the transition state Δx_{NU} was determined to be between 1.0 and 1.5 nm, thus close to the one determined within this thesis ($\Delta x_{NU} = 0.969^{+0.031}_{-0.03}$ nm). It should be noted that a ductile and a brittle energy landscape can reveal the same distance to the transition state and energy barrier [414]. While the asymmetry can be evaluated from the distances to the transition states, the exact shape of the energy landscape (and especially a force dependence of Δx) is not directly accessible in the folding and unfolding data as a function of force (see Conclusion and Outlook, section 7.7, for further access to the shape of the barriers).
It should further be noted that the buffer conditions for the AFM and the MT measurements do not completely match, but are comparable (1x PBS and HEPES buffer, respectively, see Materials and Methods for details, section 7.8). However, for completeness, a measurement with the same conditions is recommended to avoid influence of the salt concentration.

To sum up, the interpretation of the constant force and constant speed measurements is a challenging task. Different analysis methods of the same data from constant speed AFM measurements result in different values for $k_{0,UN}$ and Δx_{NU}. Later analyses tend to be closer to the results determined by constant force MT measurement obtained within this chapter. Nevertheless, it should be noted that still one order of magnitude in the refolding rate Δx_{UN} is present, but also a constant speed AFM measurement with a slow pulling rate revealed a comparable unfolding rate of the *ddFLN4* protein domain.

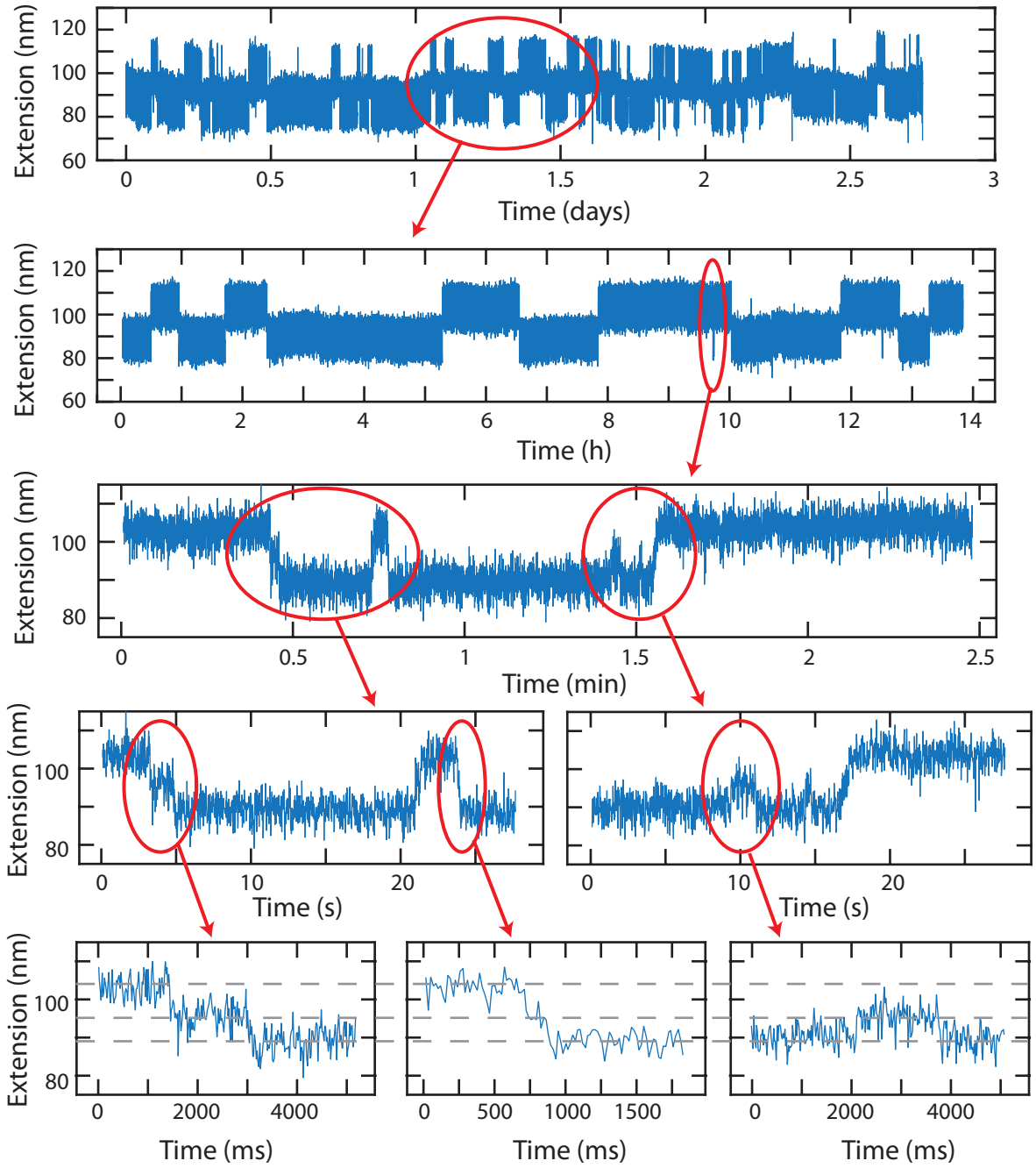

Figure 7.18: Extension trace of *ddFLN4* close to the equilibrium force. The theoretical equilibrium force and rate determined from the fits in Fig. 7.17 are 7.3 pN and $k_{7.3,equi} \approx 9.3 \cdot 10^{-4}$ 1/s (corresponding to a mean dwell time of $\approx$ 18 min), measurement performed at 7.5 pN. Reaching the intermediate state from the native or unfolded state, transitions into the original state as well as into the other state are observed. Zoom ins as marked by red ovals. Time traces set manually to zero. Gray dotted lines to guide the eye.

7.7 Discussion and Outlook

In this chapter, a new attachment strategy for proteins was introduced. Hereby, the protein of interest is attached covalently to the surface via an ELP linker and with its other terminus with a protein-ligand (*biotin-steptavidin*) bond to the bead. Single molecule attachment could be demonstrated by the two fingerprint protein domains *ddFLN4* and *VWFs A2*, which showed the previously known unfolding pattern. The bond lifetime of the protein-ligand bond was observed to follow a double-exponential model at constant force. The force response of both decays can be described by a single exponential model. One explanation of the double exponential decay of the tether lifetime is the different binding pockets of the tetravalent *streptavidin*, which is attached to the bead. Within the presented MT measurements it cannot be distinguished between the different binding sites of the *streptavidin*, hence it is not possible to assign the rupture events to one specific pocket of the tetravalent *streptavidin*. Therefore, it is also impossible to distinguish between a bond release of the *biotin-steptavidin* from a rupture event of the *streptavidin* dimer or similar conformational changes within the *streptavidin*, which lead to release of the tether [418]. However, with the use of monovalent *streptavidin* [401] the binding can be restricted to one binding pocket. If the double exponential decay of the tether lifetime at one single force originates from the different binding sites of the tetravalent *streptavidin*, monovalent *streptavidin* should have an impact on the behavior of the lifetime at constant force. Therefore, it would be of interest if the double exponential decay of the lifetime of the tethers transforms into a single exponential model for monovalent *streptavidin*. Furthermore, in this case a comparison of the lifetimes of the monovalent *streptavidin* and the double exponential decay of the tetravalent *streptavidin* could resolve which binding pocket corresponds to which decay rate, allowing conclusion about the (internal) release of the bond within *streptavidin*.

To test the monovalent *streptavidin*, beads have to be functionalized. Hereby, it is useful to implement a well characterized linker between the *streptavidin* and the bead. Introducing an ELP linker to the bead opens up the possibility for different attachment strategies. Therefore, it is useful to test if a covalent bond mediated by *Sfp phosphopantetheinyl transferase* or *sortase A* can form. However, it should be considered that this approach failed for PEG. Within the PEG passivation tests, *streptavidin* and *SpyCatcher* functionalized beads stuck highly to the PEG coated surface, so that both functionalizations were not further considered for PEG coated flow cells. However, *streptavidin* coated beads did not stick nonspecifically to ELP coated surfaces, thus *SpyCatcher* functionalized beads might also be a suitable option. This would allow covalent attachment on both termini of the protein. Therefore, the whole force range achievable with MT could be used for an unlimited amount of time.

The two step unfolding and refolding of the protein domain *ddFLN4* was measured and analyzed in detail. As mentioned at the beginning of the relevant section, this project is an ongoing project. Nevertheless, structural and temporal properties of the protein domain have already been extracted.
The determined contour lengths of the different protein domain sub-segments are in good agreement with published data. However, the different rates for the transitions of the three states differ significantly from previously determined constant pulling speed AFM data. It was discussed before that the extrapolation to zero force (for this case) is challenging and therefore

the unfolding rate at zero force for constant speed AFM measurement can differ by two orders of magnitude depending on the choice of model. However, slow pulling rates in the AFM measurements revealed comparable zero force rates as determined by constant force MT experiments within this chapter. One explanation for the difference in the extrapolated zero force rates relies on the shape of the energy landscape [414]. Deconvolution and energy landscape reconstruction as introduced in chapter 6 can give further insights into the energy landscape and therefore cannot only reveal asymmetries but also detailed shapes of the landscape which can be attributed to ductile or brittle energy barriers.
Simulations of the *ddFLN4* unfolding indicate that the intermediate state is only significantly populated at forces above $5 - 6$ pN [413]. Below 6 pN, the used time resolution of ≈ 17 ms was not sufficient to detect an (potentially still existing) intermediate state while refolding of the protein domain. As described in chapter 4, the setup is in principle able to measure with an acquisition time of 0.4 ms. However, the FOV is limited in such a way that only two to three beads can be measured in parallel. Furthermore, the relatively low unfolding rate of the first transition (UI) limits the total amount of events which can be observed in an accessible measurement duration. Both reasons limit the statistics, making a useful analysis of the lifetime difficult. The latter case relies on the biological properties of the sample and cannot be influenced by the setup (for a fixed force). However, the new generation of "scientific CMOS" (sCMOS) cameras are able to select multiple, small, FOVs which can be tracked in parallel at high frequencies. Hence, the lack of statistics at high frequencies can be reduced.

MT proved its capability of collecting a lot of data within a minimum of time. For the data related to *ddFLN4*, presented in section 7.6, only four independent flow cells were needed to gain sufficient statistics. One FOV contains ≈ 40 beads that can be analyzed. An ageing effect of the protein was not detected, hence unfolding and refolding events could be often repeated, making it easy to detect hundreds of events within a minimum of time.
Furthermore, the effectively non-existing drift in the applied force, as well as the minimum of drift in the extension trace not corrected by a reference bead enables to measure rates of the protein over minutes, hours and even days, allowing for quantitative detection and analysis of small unfolding or folding rates which are difficult to achieve for other measurement methods.

7.8 Material and Methods

7.8.1 Flow Cells and Buffers

Flow cell are built with amino-silanized (NH_2) coverslips as bottom and a nonfunctionalized coverslip with two holes as top. The two holes serve as inlet and outlet of the flow cell. The coverslips are glued together by one layer of melted Parafilm (Carl Roth, Germany), pre-cut to form a flow channel.
PEG attachment: 25 mM of ≈ 500 Da, ≈ 5000 Da, and ≈ 10000 Da (Thermo Fisher Scientific Inc., USA) PEG possessing an *N-Hydroxysuccinimid (NHS)* group at its one end is incubated for 1 h in 20 mM HEPES buffer to allow covalent attachment. The free end the nonfunctional PEG contains a *methyl group* (CH_3), whereas *maleimide* for covalent attachment is attached to the functional PEG.
ELP attachment: 10 mM *SMCC* (*NHS–Malemide* linker) (Thermo Fisher Scientific Inc., USA) is incubated in 50 mM HEPES buffer (pH 7.5) for 45 min to the surface to allow the NH_2–*NHS* bond to form. Non-attached *SMCC* was removed by rinsing with water. 50 µM 6×ELP, with *cysteine* and the peptide sequence "LPETGG" at its N- and C-terminal (Cys-6×ELP-LPETGG), respectively, was incubated at ph 7.2 for 1 h and afterwards rinsed with water to remove nonattached ELP linkers.

Before protein or beads are incubated to a flow cell or coverslip, *cysteine* is incubated for 1 h (coupling buffer, pH 7.3) to saturate *maleimide* groups if present in one of the former steps. Remaining free *cysteine* is removed by rinsing with water.

ddFLN4 and *VWF* measurements in section 7.5 and 7.6 use 3 µm, non-magnetic polystyrene beads (Polysciences, USA) baked to the surface to serve as reference beads. To this end, 70 µl of a stock solution, diluted 1:1000 in ethanol, is added to the bottom coverslip and baked for 5 min at 100°C before the flow cell is assembled.

Before *ddFLN4* or *VWF* dimers are incubated in the flow cell, the flow cells are passivated with 1 % *casein* (in water) for 1 h. Rinsing of ≈ 2 ml buffer removes remaining free *casein* from the flow cell. The *ddFLN4* construct has a *glycine* at its N-terminus to allow *sortase A* mediated reaction and a *ybbR*-tag at its C-terminus. In the case of the *VWF* dimer construct, one N-terminus contains three *glycine*, while to the second N-terminus the *ybbR*-tag is attached. In both cases, the *ybbR*-tag is first conjugated with *CoA-biotin* in bulk via *Sfp phosphopantetheinyl transferase* induced reaction. Hereto, 10 µl of protein stock (≈ µM), 14 µl H_2O, 3 µl 10× *sfp* buffer, 2 µl *CoA-biotin* (1 mM in DMSO) and 1 µl *Sfp phosphopantetheinyl transferase* (100 µM) is incubated at 4°C over night. *Sortase A* is added to the mixture and diluted with buffer containing 1 mM $CaCl_2$ to a concentration of 8 nM *VWF* and 1 µM *sortase A*, or 64 nM *ddFLN4* and 2 µM *sortase A*, respectively. The final mixture, containing the protein with *glycine* and *biotin* as well as the *sortase A* enzyme, is incubated for 30 min in the flow cell. Non-attached proteins are removed by rinsing with buffer. *Streptavidin* coated M270 beads (65305, Dynabeads, Thermo Fisher Scientific Inc., USA) are incubated for 60 s and non-bound beads are again removed by rinsing with buffer.

Within this chapter, different buffers were used as described in the relevant sections:

Coh-Doc buffer: 25 mM TRIS, 72 mM NaCl, 1 mM $CaCl_2$ (pH 7.2)
Coupling buffer: 50 mM sodium phosphate, 50 mM NaCl, 10 mM EDTA (pH 7.2)
HEPES buffer: 20 mM HEPES (in some cases adjusted as noted), 150 mM NaCl, 1 mM $CaCl_2$, 1 mM $MgCl_2$ (pH 7.4)
Borat buffer: 50 mM boric acid (pH 8.5)

7.8.2 Test of Passivation

If not otherwise noted, to test the passivation efficiency of PEG, beads are incubated for 1 h in the flow cell. For ELP coated flow cells the incubation time is reduced to 1 min. Afterwards, the flow cell is rinsed with 2 ml buffer at 150 µl / min. For all tests, approximately the same number of beads were incubated into the flow cell. However, to address uncertainties in the reproducibility of the bead concentration, the amount of beads before and after rinsing with buffer is compared, but not between different flow cells.
Attachment of PEG to the NH_2 coated beads (14307D, M270, Dynabeads, Thermo Fisher Scientific Inc., USA) was performed analogously to the coverslip coating of PEG. The *streptavidin* coated beads within the ELP related measurements are commercial available *streptavidin* covered M270 beads.
For passivation tests, *BlockAid* (B10710, Thermo Fisher Scientific Inc., USA), *diaminodiphenylmethan (DDM)* (Sigma-Aldrich, USA), *Pluronic F127* (P2443-250, Sigma-Aldrich, USA), *casein* (Thermo Fisher Scientific Inc., USA), "blocking solution" (Candor, Germany), and *Tween 20* (P9416, Sigma-Aldrich, USA) was used.

7.8.3 Lifetime Detection

The lifetime of the *biotin-streptavidin* bond was measured in HEPES buffer. The measurement duration was adjusted to the force. For 65 pN, 60 pN, 55 pN, and 45 pN the total time of the measurements was 1, 3, 3, and 15 hours, respectively. Only beads that showed specific unfolding of *ddFLN4* in at least one of two 20 pN force plateaus were used for later rupture measurements and analysis. Lifetimes at one constant force are fitted with a double-exponential model $a \cdot exp(-b \cdot t) + c \cdot exp(-d \cdot t)$, with t the time and the two rates for the lifetimes b and d. The force dependency of the lifetime was analyzed by an Arrhenius relationship as described in the main text.

7.8.4 ddFLN4 Analysis

The single extensions at one force in Fig. 7.14 are determined from Gaussian fits to the step length histograms (1 nm bins). The resulting contour lengths are calculated with a fixed persistence length of 0.5 nm and the WLC model approximation of Petrosyan [405]:

$$\frac{F \cdot P}{k_B \cdot T} = \frac{1}{4}\left(1 - \frac{x}{L_0}\right)^{-2} - \frac{1}{4} + \frac{x}{L_0} - 0.8 \cdot \left(\frac{x}{L_0}\right)^{2.15} \tag{7.3}$$

The properties in Fig. 7.15 (hence the distance to the transition state Δx and the rate at zero force $k_{0,XX}$, with XX the transition, see main text) are determined following the Arrhenius relation ship:

$$k(F) = k_{0,XX} \cdot e^{\frac{\Delta x}{k_B T} \cdot F} \tag{7.4}$$

with $k_B T$ = 4.1 pN nm. For robustness, linear fits to the natural logarithm are performed:

$$ln(k(F)) = ln(k_{0,XX}) + \frac{\Delta x}{k_B T} \cdot F \tag{7.5}$$

For *ddFLN4* refolding at forces lower than 6 pN, only one step was detectable. It is assumed that the second step occurred faster than the camera frequency. Hence the rate of the single detectable step is equal to the first step of a two step refolding event, enlarging the fit range of UI by including the UN data for < 6 pN.

Measurements were performed with the MT setup described in chapter 4 and analyzed with the software package described in chapter 5.

Part III

Small-Angle X-Ray Scattering

Chapter 8

Time-Resolved Small-Angle X-Ray Scattering Reveals Millisecond Transitions of a DNA Origami Switch

8.1 Summary

Self-assembled DNA structures enable creation of specific shapes at the nm-μm scale with molecular resolution. The creation of functional DNA assemblies will likely require dynamic structures that can undergo controllable conformational changes. DNA devices based on shape complementary stacking interactions have been demonstrated to undergo reversible conformational changes triggered by changes in ionic environment or temperature. An experimentally unexplored aspect is how quickly conformational transitions of large synthetic DNA origami structures can actually occur. Here, we use time-resolved small-angle X-ray scattering to monitor large-scale conformational transitions of a two-state DNA origami switch in free solution. We show that the DNA device switches from its open to its closed conformation upon addition of $MgCl_2$ in milliseconds, which is close to the theoretical diffusive speed limit.
In contrast, measurements on the dimerization of DNA origami bricks occur on a time scale of minutes to hours suggesting that the kinetics depend on local concentration and molecular alignment.[1]

[1]This chapter is published at *Nano Letters* by Brützel* and Walker* *et al.* (DOI: 10.1021/acs.nanolett.8b00592) (March, 2018). *contributed equally to this work.
Linda Brützel and I jointly performed the measurements and analyzed the data. I contributed to the interpretation of the data and writing the manuscript.

8.2 Time-Resolved Small-Angle X-Ray Scattering Reveals Millisecond Transitions of a DNA Origami Switch

The programmable self-assembly of DNA molecules is a new paradigm for creating structures at the nm-μm scale with potential for diagnostic, therapeutic, and engineering applications [188, 193, 419, 420]. DNA origami structures are assembled from kilobase long single-stranded (ss) DNA (scaffold) strands that fold due to a number of specific ssDNA oligonucleotides (staple strands) into pre-defined and precisely addressable ≈MDa-sized structures [172, 197, 199]. Recently, further hierarchical organization of DNA origami structures into higher-order assemblies, some of which reaching the ≈GDa range, has been demonstrated [176, 421, 422]. Moving beyond static two- and three dimensional structures [172, 197] toward building complex devices will require implementing and controlling reversible mechanical movements in DNA objects, which remains a challenging aspect in the field [423]. So far, most switchable DNA devices have been triggered by the addition of DNA single strands and toehold-mediated strand exchange, where transitions occur on time scales of minutes. Conformational changes controlled by the addition and exchange of oligonucleotides are fundamentally constrained by the maximal rate of toehold-mediated strand exchange $\approx 5 \cdot 10^5$ M^{-1} s^{-1} [157], at typical nM-μM concentrations this corresponds to changes on the time scale of seconds to minutes [201, 204, 424, 425]. Conformational transitions initiated by changes in ionic strength, pH, temperature, or light can be faster, and have been demonstrated to occur within seconds [207, 209]. A new technology to create well-defined and reversible conformational changes of DNA origami devices relies on shape complementary protrusions and recessions that interact via DNA stacking interactions [3, 175]. While salt and temperature dependent conformational changes of DNA devices based on shape complementary and stacking interactions have been characterized [3, 175], it is an open question how fast conformational transitions of these large, ≈MDa DNA origami structures can be. Friction with the solvent and energy barriers in junctions or pivots could pose fundamental speed limits for switching dynamics, similar to what is observed for folding of naturally occurring RNAs due to their rugged free energy landscapes (Supporting Fig. 8.4) [426, 427].

Fast conformational transition of a DNA origami switch device revealed by trSAXS. To address this question, we employ time-resolved small-angle X-ray scattering (trSAXS) to monitor conformational transitions in a unimolecular (two-state) DNA origami switch and in a bimolecular DNA origami reaction system. SAXS can monitor the conformational transitions of macromolecules and their assemblies in free solution under virtually arbitrary solution conditions [3, 217, 241, 428–430]. SAXS does not require any labeling and directly probes the global conformation in solution. By using a stopped-flow kinetic mixer to trigger conformational changes by rapid changes in $MgCl_2$ concentration and a high-flux synchrotron beamline for fast data acquisition [284], we achieved a time resolution of 25 ms (Fig. 8.1a). We applied trSAXS to study the dynamics of a DNA origami switch (switchD16) [175]. We have previously characterized the structure and equilibrium conformations of switchD16 [3, 175]. In brief, switchD16 consists of two ≈ 100 nm long rigid arms connected by a Holliday junction at the center that allows for reversible transitions between an open and a closed conformation (Fig. 8.1). Shape-complementary patterns of blunt-ended double helical protrusions and recessions are arranged on both arms that can form 16 basepair stacking interactions in the closed conformation of the switch. Electrostatic repulsion counteracts the stacking contacts, such that at low cation

concentration the open conformation is favored. We have previously demonstrated that SAXS can monitor and quantify the $MgCl_2$-dependent unimolecular equilibrium of the switchD16 device [3] and determined the midpoint of the open-to-close transition at ≈ 10 mM $MgCl_2$ (Fig. 8.1b and Supporting Information). In the trSAXS measurements, we started with DNA switch devices in 5 mM $MgCl_2$ where the open conformation is predominantly populated (fraction closed $f_{close} < 4$ %) [3]. Using the stopped-flow mixer (see Supporting Information), we then rapidly (within ≤ 1 ms) added $MgCl_2$ to final concentrations of 15, 25, and 35 mM (where in equilibrium f_{close} = 90 %, 98 %, and 99 %, respectively) and monitored the subsequent conformational changes. For the 15 mM $MgCl_2$ condition the transition from the open to the closed state is resolved and well described by a first-order kinetic model (Fig. 8.2 and Supporting Fig. 8.5) with a closing rate constant k_{close} = 22 s^{-1} and an opening rate constant k_{open} = 2.4 s^{-1}. For the 25 and 35 mM $MgCl_2$ conditions, the transition to the closed state occurs essentially within the dead time of our instrument (25 ms). Analysis of the data suggests a lower limit on the closing rate constants of k_{close} = 150 s^{-1} (Fig. 8.2b and Supporting Fig. 8.6). The measured closing times of $\tau_{close} = k_{close}^{-1} \leq 7$ ms are at most 1-2 orders of magnitude slower than a simple estimate of the time scale for the diffusive motion of the two arms from the open into the closed state of $\tau_{diff} \approx 100$ µs (Supporting Text and Supporting Fig. 8.7), suggesting that the DNA switch closes near the diffusive speed limit. Residual energy barriers, if any, for closing must be lower than $ln(\tau_{close} / \tau_{diff}) \approx 4\ k_B T$, where $k_B T$ is the thermal energy.

Slow dimerization of DNA origami bricks. As a reference construct, we studied the kinetics of a bimolecular reaction system consisting of two separate monomeric DNA origami bricks that dimerize via shape-complementary basepair stacking interactions, similar to the switch device (Fig. 8.3a). The SAXS profiles at 20 mM $MgCl_2$ show pronounced differences between the monomer and dimer scattering patterns (Fig. 8.3b). In particular, the scattering profile of the dimeric complex exhibits a clear peak at $q \approx 0.28$ nm^{-1} (Fig. 8.3b), which corresponds to a length scale of $2 \cdot \pi / q \approx 23$ nm that matches the cross-section of the dimer (22 nm × 24 nm) (Fig. 8.3a). This strong interference peak is largely missing in the monomeric profile due to the asymmetric cross sectional area (11 nm × 24 nm) (Fig. 8.3a). Based on a two-state model we determined the fraction of dimers at each time point (Fig. 8.3c,d, Supporting Fig. 8.8 and Supporting Information). As expected for a bimolecular system, we find concentration dependent assembly kinetics. From a fit of a bimolecular reaction kinetics model to the data we obtain a negligible dissociation rate constant k_{off} and an estimate of an association rate constant k_{on} of $1.7 \cdot 10^4$ M^{-1} s^{-1}. A simple estimate for the time scale of diffusive reaction that takes into account the global dimensions of the bricks yields a diffusion-limited reaction rate constant k_{diff} of $\approx 2.5 \cdot 10^8$ M^{-1} s^{-1} (see Supporting Information). Hence, the brick system reacts much slower than the diffusive speed limit, which points to the existence of additional barriers, likely to overcome electrostatic repulsion and to achieve the correct alignment of the brick monomers [17], that slow down the reaction.

Taken together, these data suggest that the very rapid closing transition of the DNA switch device is due to the fact that the central Holliday junction links the two arms and orients them favourably to form the 16 basepair stacking interactions that stabilize the closed state. Therefore, the central pivot link creates a high effective concentration (estimated to be $k_{close} / k_{on} \approx 1.4$ mM) of the two arms enabling them to interact on the millisecond timescale.

In conclusion, we have demonstrated that ≈ 5 MDa DNA origami devices can undergo very fast conformational dynamics on the millisecond timescale, suggesting that such devices could be employed for switching and sensing molecular capabilities with rapid response times. While the kinetics for the DNA switch device are very fast and approach the estimated diffusion controlled rate, assembly of the DNA bricks at nM-μM concentrations is much slower than both the dynamics of the DNA switch, the estimated diffusion controlled rate, and the maximal rate for toehold-mediated strand exchange. In particular since hierarchical assembly of (various types of) DNA bricks forms the basis for creating higher-order DNA structures reaching the ≈GDa-range [176, 422], it is desirable to better understand –and ultimately optimize– their assembly kinetics. Unforeseen barriers that could slow down the dimerization dynamics could be caused by deviations of the actual brick geometry from the designed one. For example, residual twist in honeycomb structures [176] may make it necessary that the bricks deform through thermal fluctuations in order to satisfy the stacking bonds. The associated energetic penalties will be likely on the order of multiple k_BT and could thus explain the slow binding rates that we have observed. Thus, one approach for increasing the speed of DNA brick association may consist in more precise design. Other approaches might include optimized temperature and salt conditions, introduction of confinement or molecular crowding agents, chemical modifications to the DNA to reduce charge repulsion, and a more symmetric design to facilitate correct alignment.

Our work establishes trSAXS as a powerful tool to monitor large-scale conformational changes and assembly of DNA origami objects on timescales from milliseconds to hours without the need for labeling or surface immobilization. The ability of SAXS to directly probe the global conformation in solution is advantageous, since it has recently been demonstrated that inferring global conformations from local distance measurements e.g. by Förster resonance energy transfer (FRET) can be problematic [431, 432] and that the addition of dyes can bias the conformational ensemble [433]. In the future, a combination of continuous-flow mixing in appropriate microfluidics with microfocus X-ray sources has the potential to push the time-resolution even into the μs-regime [289], which would allow us to directly probe conformational transitions at the molecular speed limit.

8.3 Acknowledgements

We thank Dr. Theyencheri Narayanan for assistance at beam line *ID02* and Dr. Martha Brennich for help at beam line *BM29* at the ESRF (Grenoble, France), Dr. Martin Schroer for assistance at beam line *P12* at DESY (Hamburg, Germany), Florian Praetorius for scaffold DNA preparations, and Philip Tinnefeld for discussions.

8.4 Author Contributions

L.K.B. and P.U.W. contributed equally to this work. All authors designed this study. T.G. assembled and purified DNA origami samples; L.K.B. and P.U.W. performed SAXS measurements and analyzed the data. All authors contributed to writing the paper and have given approval to the final version of the manuscript.

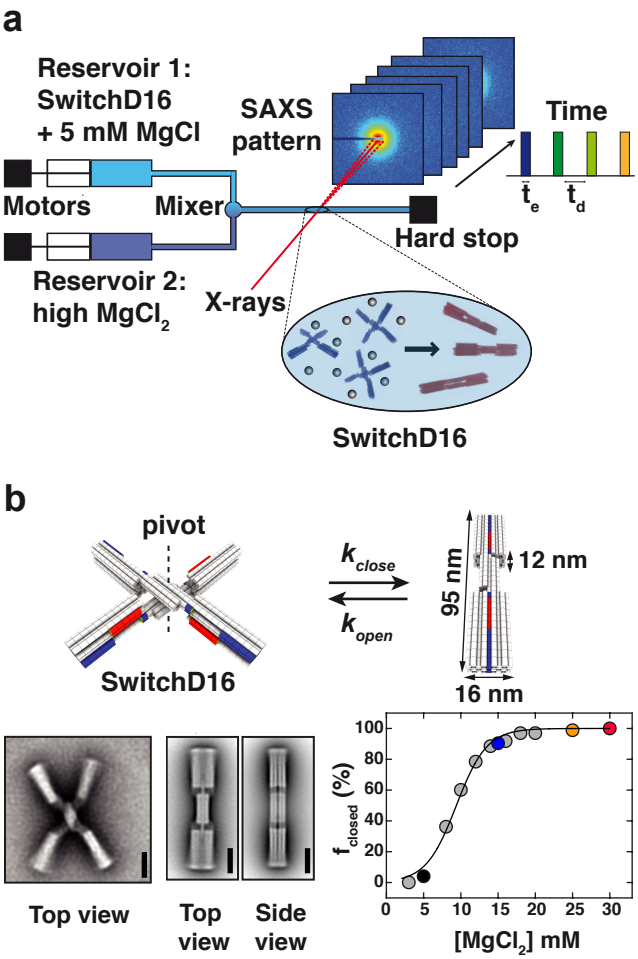

Figure 8.1: Schematic of time-resolved SAXS and a $MgCl_2$-dependent DNA origami switch device. a) Schematic of the stopped-flow mixing device coupled to the high brilliance beamline *ID02* at the ESRF. The mixing reservoirs 1 and 2 contain the switchD16 device in 5 mM $MgCl_2$ and buffer with high $MgCl_2$ concentrations, respectively. After turbulent mixing, the mixture is directed to a capillary and the flow is stopped. The beam hits the sample in a specific acquisition pattern defined by the exposure time (t_e) and a delay time (t_d) (see Supporting Information). b) (Top) Schematic view of the switchD16 device, which changes from an open to a closed conformation upon the addition of $MgCl_2$. The closed state is stabilized by 16 basepair stacking interactions occurring at the interface of shape-complementary double helical protrusions (red) and recessions (blue). (Bottom, left) Negative-stain TEM micrographs of switchD16 particles in the presence of 5 mM and 25 mM $MgCl_2$. (Scale bars, 20 nm). (Bottom, right) Equilibrium fraction of closed switchD16 devices as a function of $MgCl_2$ determined by SAXS and two-state based thermodynamic model (black line).

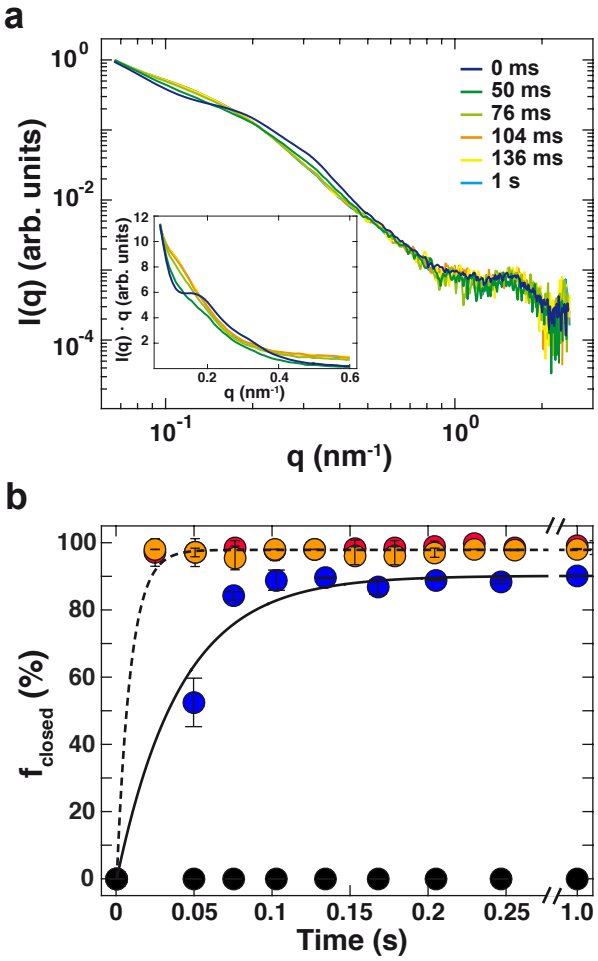

Figure 8.2: TrSAXS reveals conformational kinetics of a DNA origami switch device. a) SAXS profiles for switchD16 for selected time points after increasing $MgCl_2$ concentration to 15 mM. The inset shows a zoom of the data in Holzer representation ($I(q) \cdot q$ vs. q). b) Fraction of switchD16 devices in the closed conformation vs. time after changing to $MgCl_2$ concentrations of: 5 mM (black circles), 15 mM (blue circles), 25 mM (orange circles) and 35 mM (red circles). Symbols and error bars are the mean and standard deviation from two independent repeats of each condition. The solid black line and dashed black line represent a reversible unimolecular first-order reaction fit to the data at 15 mM and 25 mM $MgCl_2$ (see Supporting Information).

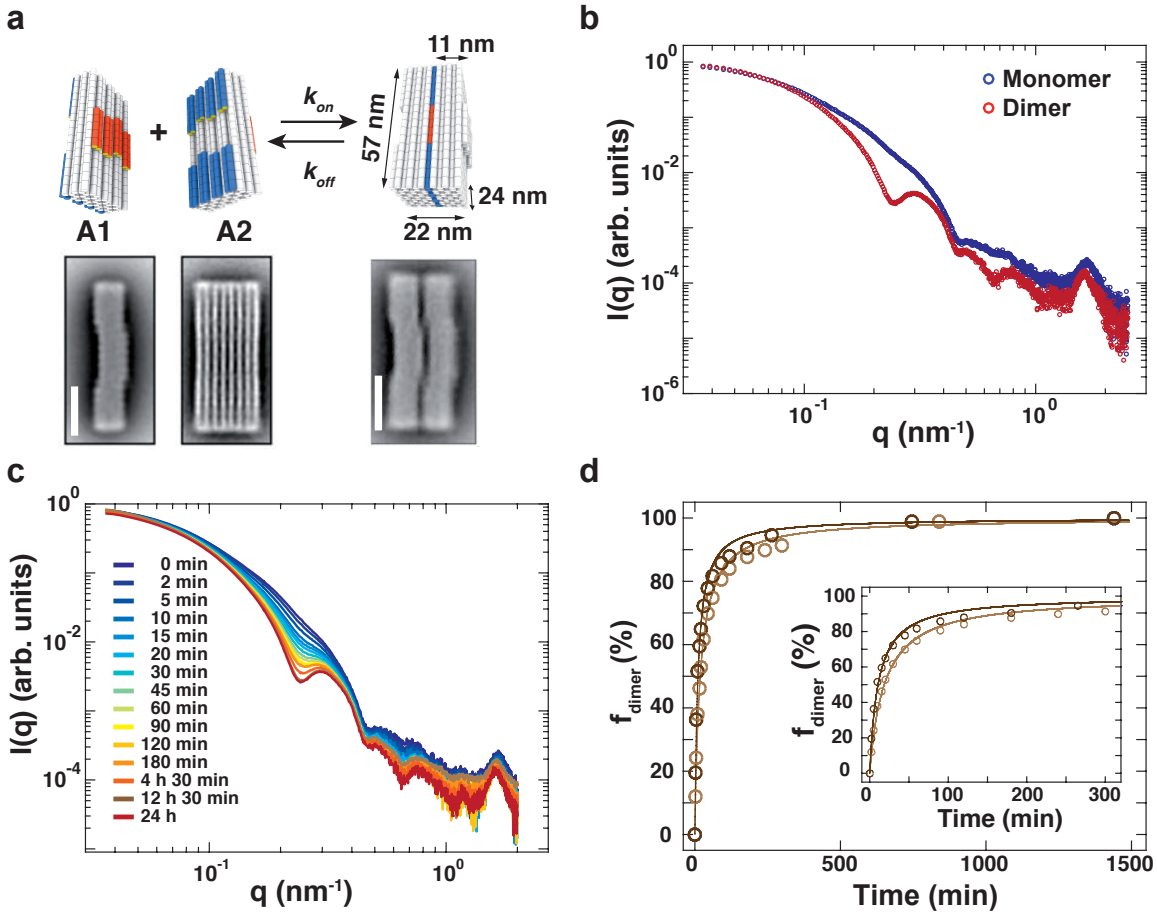

Figure 8.3: Time-resolved SAXS measurements on dimerization kinetics of DNA origami bricks. a) (Top) Schematic of DNA origami brick monomers with double helical protrusions and recessions (indicated in red and blue) allowing for the formation of a dimeric brick in the presence of 20 mM $MgCl_2$. (Bottom) TEM micrographs of DNA origami monomers and dimers. Scale bar: 20 nm. b) Experimental scattering profiles of DNA origami monomers (blue circles) and dimers (red circles) at a sample concentration of 100 nM in 20 mM $MgCl_2$. c) Time evolution of scattering profiles after 1:1 mixing of monomeric brick samples at an initial concentration of 100 nM. d) Fraction of dimeric brick particles as a function of time determined from a two-state model for initial monomer concentrations of 100 nM (dark brown circles) and 50 nM (light brown circles). Solid lines represent fits of an irreversible bimolecular reaction rate model (see Equation 8.9) yielding an average association reaction rate constant of $1.7 \cdot 10^4$ M^{-1} s^{-1}. The inset shows a close up of the early time points.

8.5 Supporting Information

8.5.1 Materials and Methods

DNA Origami Assembly and Purification

The scaffold DNA (p8064) was prepared as previously described [434]. Staple DNA strands were synthesized by solid-phase chemical synthesis (Eurofins Genomics GmbH, Ebersberg, Germany; HPSF purification). DNA origami objects were designed using caDNAno v.02 [197] and prepared as described previously [3, 175]. Objects were self-assembled by subjecting the one-pot reaction mixture to a thermal annealing ramp using a thermal cycling device (TETRAD; MJ Research - now Biorad) [181]. The reaction mixture contained 50 nM scaffold DNA (p8064), 200 nM of each staple DNA strand, folding buffer (1 mM EDTA, 5 mM TrisBase, 5 mM NaCl; pH 8), and 20 mM $MgCl_2$.

DNA Origami Switch Device

All 16 basepair stacking interactions are active in the dynamic switch variant switchD16 (Supporting Figure 8.9). After a 15 min thermal denaturation step at 65 °C, the thermal annealing ramp covered the temperature interval [58 - 55 °C] with a rate of 1 °C/90 min.
Excess staple DNA strands were removed from the reaction mixture by performing two rounds of polyethylene glycol (PEG) precipitation [183]. The resulting pellet was dissolved in folding buffer (1 mM EDTA, 5 mM TrisBase, 5 mM NaCl; pH 8) containing 5 mM $MgCl_2$. To allow for equilibration, all samples were incubated at 40 °C and 400 rpm overnight. Residual PEG was removed from the samples by performing three rounds of ultrafiltration (30K Amicon Ultra-0.5mL from Merck Millipore). Filters were equilibrated by adding 500 µL folding buffer containing 5 mM $MgCl_2$ at 2000 × g and 25 °C for 2 minutes. Then, 50 µL sample was mixed with 450 µL folding buffer and centrifuged at 8000 × g and 25 °C for 15 minutes. The flow-through was discarded and 480 µl of folding buffer was added to the recovered sample.

DNA Origami Bricks

We used a self-complementary DNA origami brick where the protrusions on its front face can click into correspondingly shaped recessions on its back face. Two samples were prepared: in brick A_1 protrusions are active and recessions were permanently deactivated (Supporting Figure 8.10) and in brick A_2 recessions are active and protrusions were permanently deactivated (Supporting Figure 8.11). Blunt end contacts were permanently deactivated by using 10-thymine-long overhangs. After a 15 min thermal denaturation step at 65 °C, the thermal annealing ramp covered the temperature interval [56 - 50 °C] with a rate of 1 °C/60 min. Excess staple DNA strands were removed from the reaction mixture by performing one round of polyethylene glycol (PEG) precipitation [183]. The resulting pellets were dissolved in HPLC buffer (1 mM EDTA, 5 mM TrisBase, 200 mM NaCl; pH 8) containing 5 mM $MgCl_2$. Then, we subjected the sample to HPLC (Agilent Technologies 1260/1290 Infinity) using the column (Agilent Bio SEC-5: 5 µm; 2000A; 21.2 × 300 mm) at a flow rate of 2 ml/min and collected fractions of the monomer peak (29.5 - 33.5 minutes). Due to dilution of the sample, we used ultrafiltration (30K Amicon Ultra-15mL from Merck Millipore) to concentrate the sample and to exchange the buffer to folding buffer (1 mM EDTA, 5 mM TrisBase, 5 mM NaCl; 5 mM $MgCl_2$; pH 8).

Filters were equilibrated by adding 15 ml folding buffer containing 5 mM $MgCl_2$ at 7000 × g and 25 °C for 5 minutes. Then, 15 ml sample was added and centrifuged at 7000 × g and 25 °C for 7 minutes. The flow through was discarded. This step was repeated until the entire volume of the sample was centrifuged in the same filter. Then, the sample was mixed with 15 ml folding buffer and centrifuged at 7000 × g and 25 °C for 7 minutes. This step was repeated three times. The concentration of all DNA origami samples was determined using a spectrophotometer (NanoDrop 8000; Thermo Scientific). All SAXS experiments were performed on SwitchD16 and brick samples dissolved in folding buffer (1 mM EDTA, 5 mM TrisBase, 5 mM NaCl; pH 8) containing varying $MgCl_2$ concentrations.

SAXS Data Acquisition

SAXS measurements were performed at beamline *P12*, DESY, Hamburg [285] and the high brilliance SAXS beamline *ID02*, ESRF [284], Grenoble.
P12. SAXS measurements at beamline *P12* were performed at an X-ray wavelength λ of 1.2 $\mathring{A}$ and a sample-to-detector distance of 3.0 m, resulting in a q-range of 0.03 to 5 nm^{-1} (with $q = 4 \cdot \pi \cdot sin(\Theta)/\lambda$, where 2Θ is the total scattering angle). For data acquisition we used a Pilatus 2M detector. For each sample condition 40 frames with an exposure time of 45 ms in "flow" mode were conducted at room temperature. Buffer samples were measured using identical procedures before and after each sample measurement. Static profiles of monomeric and heterodimeric brick constructs were measured in buffer with 20 mM $MgCl_2$ at sample concentrations of 50 nM and 100 nM, respectively. Time-resolved (tr) SAXS measurements on dimerization kinetics were performed by manual mixing of 50 nM and 100 nM monomer concentrations in a 1:1 mixing ratio.
ID02. SAXS experiments were performed at an X-ray wavelength λ of 0.99 $\mathring{A}$. Static experiments at beamline *ID02* on switchD16 samples and DNA origami brick monomer and dimer samples were performed in a temperature controlled flow through capillary operated in air using the Rayonix MX-170HS detector (Rayonix L.L.C., USA) with a sample-to-detector distance of 5 m resulting in a q-range of 0.015 nm^{-1} to 1.5 nm^{-1}. Data acquisition was performed with an exposure time of 10 ms including 50 repeats and a delay time of 0.5 s in order to reduce radiation damage. The measurements were conducted at room temperature.
SwitchD16 samples were measured at a final sample concentration of 100 nM.

TrSAXS experiments on switchD16 samples were conducted using a stopped-flow device (SFM-400, Bio-Logic, Claix, France) consisting of four motorized syringes coupled through three mixers. The last mixer is coupled to a quartz capillary with a diameter of 1.5 mm that serves as the observation volume where the sample is exposed to the X-ray beam at a constant position (Figure 8.1a). A hard-stop is placed at the end of the flow line and is activated at the end of the mixing sequence in order to stop the flow. The net dead time (≈ 1 ms) including the mixing time and the time to transfer the mixture to the beam crossing point in the capillary was determined as described elsewhere [284]. For each trSAXS measurement 150 µl each of buffer and switchD16 samples were prepared in the syringes for mixing and subsequently mixed at equal volumes. For stopped-flow based SAXS experiments the sample-to detector distance was set to 2.5 m covering a q-range of 0.04 nm^{-1} to 3.0 nm^{-1}. For each run 30 to 50 frames were recorded with an exposure time of 10 ms and a delay time t_d = (16×1.05^{i}) ms (where i denotes

the actual frame number) between consecutive frames in order to prevent radiation damage. For trSAXS experiments switchD16 samples at a concentration of 200 nM were dissolved in 5 mM $MgCl_2$ buffer. Buffer solutions with $MgCl_2$ concentrations of 65 mM, 45 mM, 25 mM, and 5 mM were prepared to achieve final $MgCl_2$ concentrations after mixing of 35 mM, 25 mM, 15 mM and 5 mM, respectively. Prior to each stopped-flow experiment static profiles of switchD16 samples (c = 100 nM) at 5 mM, 15 mM, 25 mM and 35 mM $MgCl_2$ concentrations and corresponding buffer profiles were recorded with the exposure time set to 10 ms and the number of frames to 10. For each $MgCl_2$ concentration two independent trSAXS repeats were conducted.

SAXS Data Processing

Data reduction was carried out using custom written scripts in Matlab (Matlab 2015, The MathWorks Inc., Natick, MA, USA). Scattering data were normalized to the intensity at zero angles (*I(0)*) by performing Guinier analysis of the data [240].

Static SAXS measurements. For static SAXS experiments performed at beamline *P12* and *ID02*, sample and buffer data from each run were analyzed for radiation damage, which was not observed in any of the measurement. Matching sample and buffer profiles were averaged and buffer profiles were subtracted for background correction.

Stopped-flow based SAXS measurements. For each $MgCl_2$ concentration scattering profiles at each acquisition point were checked for consistency and radiation damage; no damage was observed in any of the measurements. Matching averaged buffer profiles from static SAXS experiments were subtracted from each single frame for background correction.

SAXS Data Analysis

SwitchD16. For trSAXS data, the scattering profile at each acquisition point ($I(q,t)$) can be described by a superposition of the scattering profiles of the sample conformation at the initial solution condition ($I_i(q,t_0)$) before mixing and the scattering profile of the final state at equilibrium after mixing ($I_f(q,t_{eq})$):

$$I(q,t) = f_i \cdot I_i(q,t_0) + f_f \cdot I_f(q,t_{eq}) \tag{8.1}$$

where the coefficients f_i and f_f are fractional occupancies of the initial and final states. For stopped-flow experiments we used static reference profiles of switchD16 samples acquired at 5 mM $MgCl_2$ and 15 mM, 25 mM and 35 mM $MgCl_2$ concentrations for I_i and I_f, respectively. For some frames, portions of the scattering curves deemed unreliable at the lowest q-values due to parasitic scattering and at high q-values because of low signal-to-noise ratio resulting in an utilizable q-range of 0.08 nm^{-1} to 2.5 nm^{-1} for fitting. The fraction of closed particles was determined from two independent SAXS measurements at each $MgCl_2$ concentration and time point and the mean and the standard deviation were calculated and reported in Figure 8.2b. Fraction of closed particles were normalized to the portion of closed switchD16 particles in steady state for each $MgCl_2$ concentration (i.e. 0 %, 90 %, 98 % and 99 % for 5 mM, 15 mM, 25 mM and 35 mM $MgCl_2$ concentrations, respectively), derived from previous SAXS measurements [3]. To evaluate the goodness of the two-state fits, chi-squared values (X^2) were calculated for each fit according to the following equation:

$$X^2 = \sum_i \frac{[I_{exp}(q_i,t) - I_{fit}(q_i,t)]^2}{\sigma_i^2} \tag{8.2}$$

where I_{exp} is the experimental SAXS profile, I_{fit} the best two-state fit profile, and σ the experimental error of I_{exp}.

Bricks. Two-state fits for dimerization kinetics of DNA origami bricks were performed using Equation 8.1, where the initial and final state are given by the scattering profiles of the monomer at the respective starting concentration and the dimer at equilibrium. Each fit was evaluated according to Equation 8.2. To determine the fraction of dimers, we used the q-range from 0.1 to 2.5 nm^{-1}.

Kinetic Fits for Folding and Assembly.

SwitchD16. The (intramolecular) conformational change between the open and the closed state of the switchD16 sample was modelled as a reversible first-order reaction:

$$O \underset{k_{close}}{\overset{k_{open}}{\rightleftharpoons}} C \tag{8.3}$$

where O and C denote the open and closed state of switchD16 particles and k_{close} and k_{open} describe the closing and opening rate constants. Assuming that all objects (with an initial concentration of c_0) adopt an open conformation at $t_0 = 0$, the time dependent relative concentrations of particles in the open and closed state are given by:

$$\frac{c_O(t)}{c_0} = \frac{k_{open} + k_{close} \cdot e^{-(k_{close}+k_{open})\cdot t}}{k_{close} + k_{open}} \tag{8.4}$$

$$\frac{c_C(t)}{c_0} = \frac{k_{close} - k_{close} e^{-(k_{close}+k_{open})\cdot t}}{k_{close} + k_{open}} \tag{8.5}$$

The equilibrium constant K_{eq} of the reaction is defined as:

$$K_{eq} = \frac{k_{close}}{k_{open}} = exp\Big(-\frac{\Delta G}{k_B T}\Big) \tag{8.6}$$

where k_B is the Boltzmann constant and ΔG denotes the Gibb's free energy between the open and the closed state.

To estimate the closing rate constants for the 25 mM and 35 mM $MgCl_2$ data, we calculated the fraction of closed particles following Equation 8.5 for different closing rate constants ($20\ s^{-1} < k_{close} < 300\ s^{-1}$) with $k_{open} = 0$ (as at $MgCl_2$ concentrations of 25 mM and 35 mM the closed fractions in equilibrium are ≈ 98 % and ≈ 99 %, respectively, suggesting that the opening rate constant is essentially negligible) and calculated the reduced X^2-values for each closing rate constant given by:

$$X^2_{red} = \frac{1}{N} \cdot \left(\sum_i \frac{[f^{exp}_{closed}(t_i) - f^{theo}_{closed}(t_i)]^2}{\sigma_i^2} \right) \tag{8.7}$$

where N denotes the number of data points, f^{exp} corresponds to the experimentally determined fraction of closed particles, f^{theo} corresponds to the fraction of closed particles given by Equation 8.5 for each k_{close} value. The errors σ used in the calculation of the reduced X^2-value

are from repeat measurements, with an additional global error of 1 %. All fitting procedures were performed with custom written Matlab (Matlab 2015, The MathWorks Inc., Natick, MA, USA) scripts using "fminsearch" as optimization function.

Bricks. Heterodimerization kinetics of the DNA origami bricks were modelled as an irreversible bimolecular reaction:

$$A_1 + A_2 \xrightarrow{k_{on}} B \tag{8.8}$$

where A_1 and A_2 correspond to the brick monomer variants where either the protruding stacking pattern (1) or the recessed stacking pattern (2) had been activated, B denotes the dimer state and k_{on} describes the association reaction rate constant in M^{-1} s^{-1}. For our experimental conditions with an equimolar mixing ratio of A_1 and A_2 (with an initial concentration of A_0) and in the absence of dimers B at $t_0 = 0$, the time dependent relative concentrations of heterodimeric bricks as a function of time is given by:

$$\frac{B(t)}{A_0} = 1 - \frac{1}{1 + A_0 \cdot k_{on} \cdot t} \tag{8.9}$$

The model defined by Equation 8.9 was used to fit the fraction of dimers derived from the SAXS data for initial monomer concentrations ($A_1(t_0) = A_2(t_0) = A_0$) of 50 nM and 100 nM. We obtained an association rate constant k_{on} of 1.8×10^4 M^{-1} s^{-1} and 1.6×10^4 M^{-1} s^{-1} for a monomer concentration of 50 nM and 100 nM, respectively, and hence a mean value of 1.7×10^4 M^{-1} s^{-1}.
We also applied a bimolecular reaction model fit including the dissociation reaction rate constant for different final states of dimer fractions varying between 90 % and 100 % where a value of 100 % dimers resulted in the lowest X^2-value and a negligible small value for the dissociation reaction rate constant in line with previous experiments [175]. Assuming 100 % dimers, we tested different k_{off} rates, yielding that the fit results are insensitive towards the off-rate for $k_{off} < 10^6$. Larger k_{off} values resulted in increasing X^2-values.

To compare these values with a reaction, only limited by the diffusion dynamics of the monomeric bricks, we calculated the theoretical diffusion-limited association rate constant k_{diff} of the bricks [435]:

$$k_{diff} = 4 \cdot \pi \cdot R \cdot D \cdot N_A \tag{8.10}$$

with R as distance within the two monomers react and form a dimer and can be assumed to be ≈ 2 nm [17], D is the diffusion coefficient according to Equation 8.11 and N_A as the Avogadro constant.

8.5.2 Supporting Text

Estimation of the timescales involved in the conformational transition from the open to the closed conformation of switchD16 samples.
We estimate the timescales for several processes involved in the conformational transition from the open to the closed state of the switch device. Specifically, we obtain rough, order-of-magnitude, estimates for the timescales of i) the diffusional motion of the two arms from the open to the closed conformation, ii) the formation of DNA basepair stacking interactions, and

iii) the local conformational transitions of the central Holliday junction.

Diffusion of the switchD16 arms. After introducing a sufficiently high salt concentration to screen the (long-range) electrostatic repulsion that causes the switchD16 device to adopt the open conformation at low salt, we expect the transition from the open to the closed state to be fundamentally limited by diffusion of the arms, since the favourable stacking interactions that keep the switchD16 device in the closed conformation are short-range in nature [17] (with a range of $\leq$ 2.5 nm) and will only form once the arms are in sufficiently close proximity. Therefore, the timescale for diffusive motion of the two arms is expected to set the ultimate speed limit for closing of the switch device, similar to what has been observed for proteins [130, 436].

To assess the order of magnitude of the timescale for diffusive motion of the arms from the open to the closed state of switchD16, we applied a simple model based on rotational and translational diffusion. Each arm was considered as a rigid rod with a length L = 95 nm and a diameter of D = 16 nm (Supporting Figure 8.7) and the translational (D_t) and rotational (D_r) diffusion coefficients were calculated following Lehner *et al.* [437]:

$$D_t = \frac{k_B T}{3 \cdot \pi \cdot \eta \cdot L}\left[ln(\frac{2 \cdot L}{D}) - \xi\right] \tag{8.11}$$

$$D_r = \frac{3 \cdot k_b T}{\pi \cdot \eta \cdot L^3}\left[ln(\frac{2 \cdot L}{D}) - \nu\right] \tag{8.12}$$

where k_B is the Boltzmann constant, T the temperature in Kelvin (300 K), η the viscosity of the solvent (1 mPa s) and ξ and ν are correction factors for the end terms taken from Tirado *et al.* [438]. The distance d each arm has to travel depends on the opening angle Θ, which has a mean value of $\approx 50°$ (Supporting Figure 8.7) [175]. Translational (t_{trans}) and rotational (t_{rot}) diffusion times for each arm are given by:

$$t_{trans} = \frac{d^2}{4 \cdot D_t} \tag{8.13}$$

$$t_{rot} = \frac{\Theta^2}{4 \cdot D_r} \tag{8.14}$$

We find values for t_{rot} in the range of 20 to 70 µs for opening angles Θ between 50° to 90°. The estimate based on translational diffusion gives similar values, again varying the opening angle between 50° and 90°.

Formation of DNA stacking interactions. In the closed state, the two arms of the switchD16 device are held together by DNA stacking interactions. The timescale for the formation of nucleobase stacking interactions was investigated recently by force spectroscopy and molecular dynamics simulations [17]. The results suggest that formation of stacking interactions occurs on a timescale of $2.40 \cdot 10^{-5}$ s under conditions similar to our experiments. This implies that once the arms are positioned to form stacking interactions, the formation of the short-range stacking interactions is very fast and essentially negligible compared to the timescale for diffusion of the arms or to the overall rate of closing.

Conformational changes of the central Holliday junction. The single Holliday junction that represents the pivot point for the rotational degree of freedom of the switch object could

also influence the dynamics. Dependent on the ion concentration Holliday junctions in isolation can assume multiple conformations: an open conformation at low salt conditions and two stacked conformations at high salt conditions [439, 440]. While there are several studies on the kinetics of the conformational transitions between the two possible stacked conformations of a Holliday junction [439, 441], to the best of our knowledge there exist no experimental rate constants for the transition between the open and the stacked conformations. However, MD simulations yielded transition times in the ≈µs regime, which again is much faster than the timescales for diffusional motion or overall closing and suggests that the structural dynamics of the Holliday junction are not a rate limiting factor [442, 443].

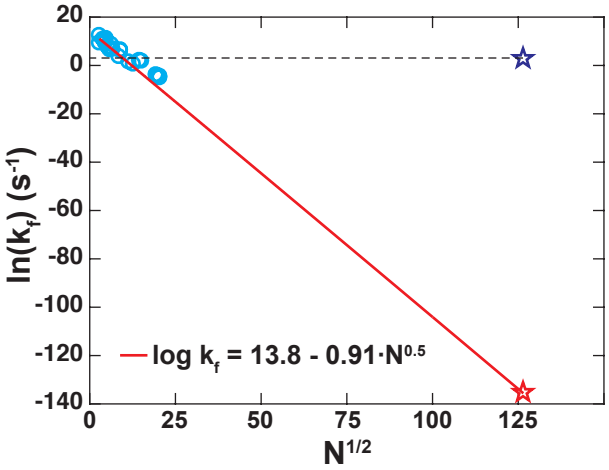

Figure 8.4: Scaling relationship for nucleic acid folding rate constants. Experimentally determined folding rate constants of a range of RNA molecules (cyan circles) as a function of the square root of the number of nucleotides and the corresponding fit of a scaling relationship using $log(k_{fold}) = log(k_0) - a \cdot N^b$ with a, b, and k_0 as fit parameters; both the data and the fit are from Hyeon *et al* [443]. The red star indicates the folding rate constant predicted for the switchD16 device by the fitted scaling relationship. In contrast, the blue star corresponds to the experimentally determined folding rate constant for the transition of switchD16 from the open to the closed state at 15 mM $MgCl_2$.

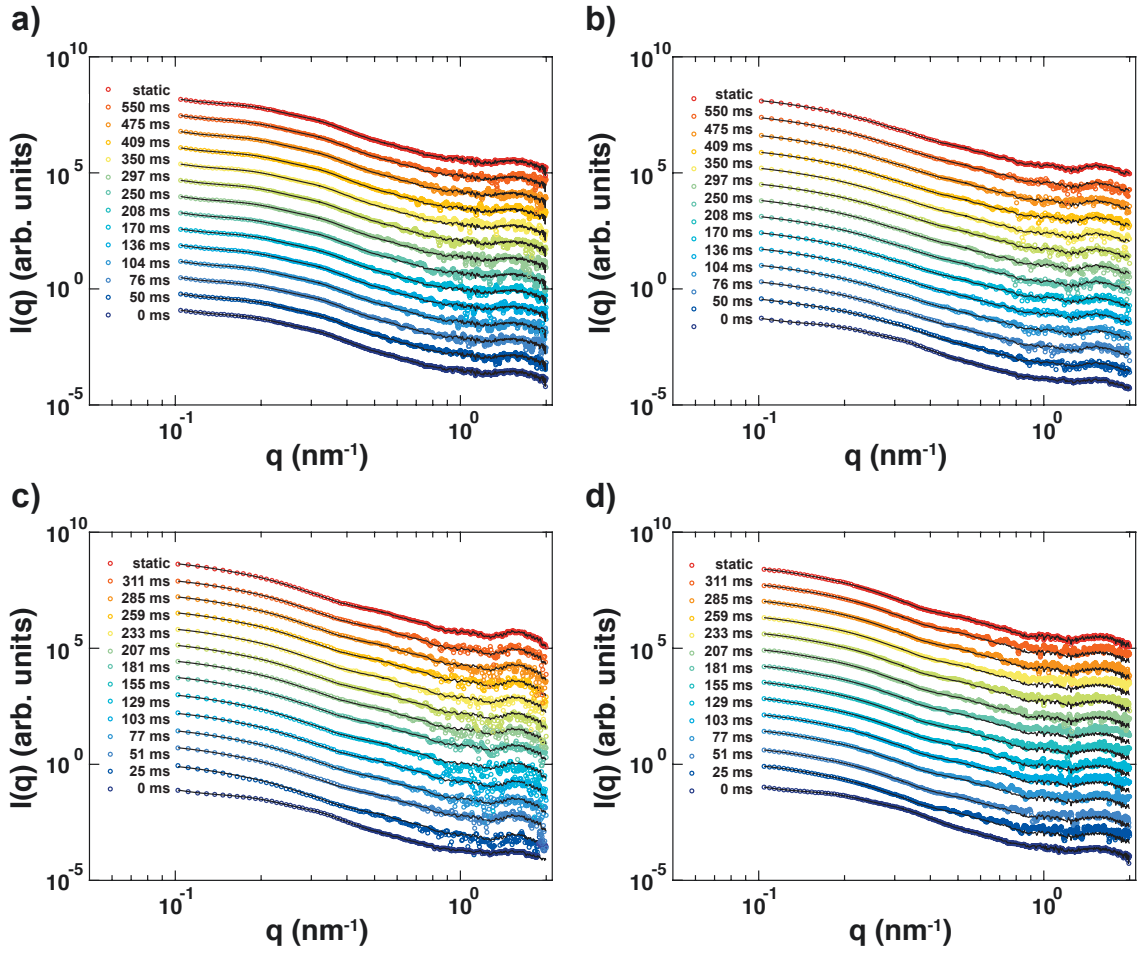

Figure 8.5: Time-dependent scattering profiles for switchD16 and two-state fits. Time-dependent scattering profiles of switchD16 samples upon mixing with varying $MgCl_2$ concentrations and corresponding fitted profiles from a two-state model (black lines) (see main text). a) Evolution of scattered intensity upon equimolar mixing of switchD16 samples with 5 mM $MgCl_2$ at different time points indicated in the legend. SAXS curves at the bottom (dark blue circles) and at the top (red circles) correspond to static reference profiles of switchD16 samples at the initial and final $MgCl_2$ concentrations (here: 5 mM). b) Scattering profiles for switchD16 samples diluted into a final concentration of 15 mM $MgCl_2$ at subsequent timepoints acquired after mixing. SAXS profiles at the bottom (dark blue circles) and at the top (red circles) are obtained from static SAXS measurements of switchD16 samples diluted in 5 mM and 15 mM $MgCl_2$, respectively. c) Scattering profiles of switchD16 samples diluted into a final concentration of 25 mM $MgCl_2$ buffer. SAXS profiles at the bottom (dark blue circles) and at the top (red circles) are obtained from static SAXS measurements of switchD16 samples diluted in 5 mM and 25 mM $MgCl_2$, respectively. d) Time-dependent SAXS data obtained from switchD16 samples after equimolar mixing with $MgCl_2$ buffer resulting in a final concentration of 35 mM $MgCl_2$. SAXS curves at the bottom (dark blue circles) and at the top (red circles) are obtained from static SAXS measurements of switchD16 samples diluted in 5 mM and 35 mM $MgCl_2$, respectively. Data are vertically offset for clarity. Data from trSAXS experiments with final $MgCl_2$ concentrations of 5 and 35 mM after mixing contain twice the number of data points as compared to the 15 and 25 mM $MgCl_2$ data due to interpolation to the q-bin size of static reference profiles, which where recorded with half of the bin size as compared to stopped-flow SAXS experiments.

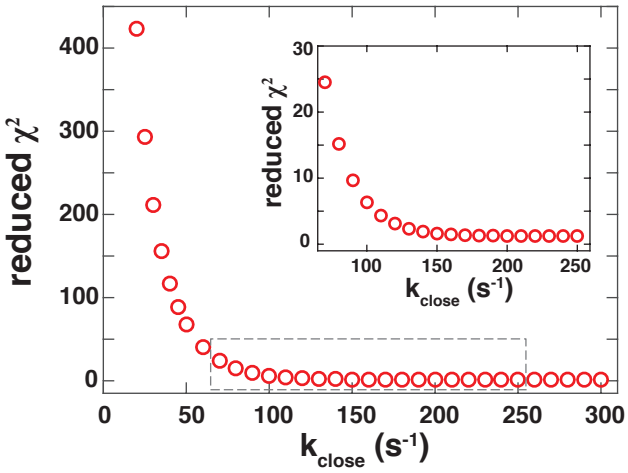

Figure 8.6: Estimate of the closing reaction rate constant of SwitchD16 particles for a final $MgCl_2$ concentration of 25 mM after mixing. We used Equation 8.5 and calculated the reduced X^2–value for different closing rate constants while setting the opening rate constant to zero (as at a $MgCl_2$ concentration of 25 mM the closed fraction in equilibrium is ≈ 98 %, suggesting that the opening rate constant is essentially negligible). The data are well described for k_{close} values equal or greater ≈ 150 s^{-1} (see inset graph corresponding to the data range indicated by the grey frame). We found very similar results for the 35 mM $MgCl_2$ data.

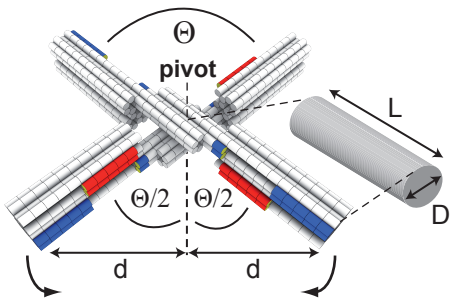

Figure 8.7: Schematic model and length scales used to estimate the diffusion times of the arms of switchD16 required to change from the open conformation (shown here) to the closed conformation.

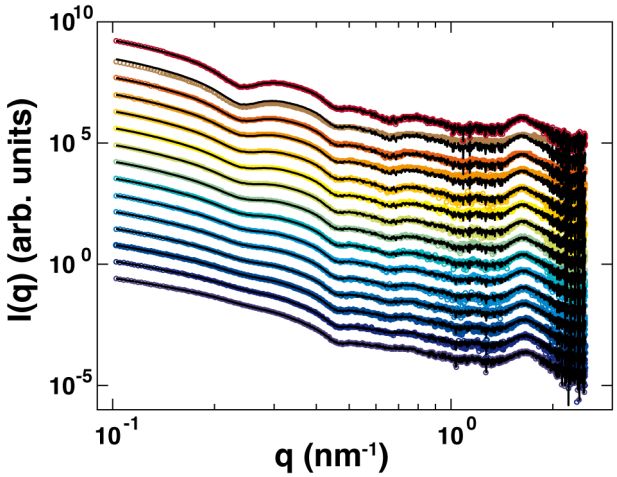

Figure 8.8: Time evolution of scattering profiles from DNA origami dimerization kinetics after 1:1 mixing of monomeric brick samples at an initial concentration of 100 nM. 0 min (dark blue circles, bottom), 2 min, 5 min, 10 min, 15 min, 20 min, 30 min 45 min, 60 min, 90 min, 2 h, 3 h, 4 h 30 min, 12 h 30 min and 24 h (red circles, top). Black lines correspond to fits from a two-state model following Equation 8.1.

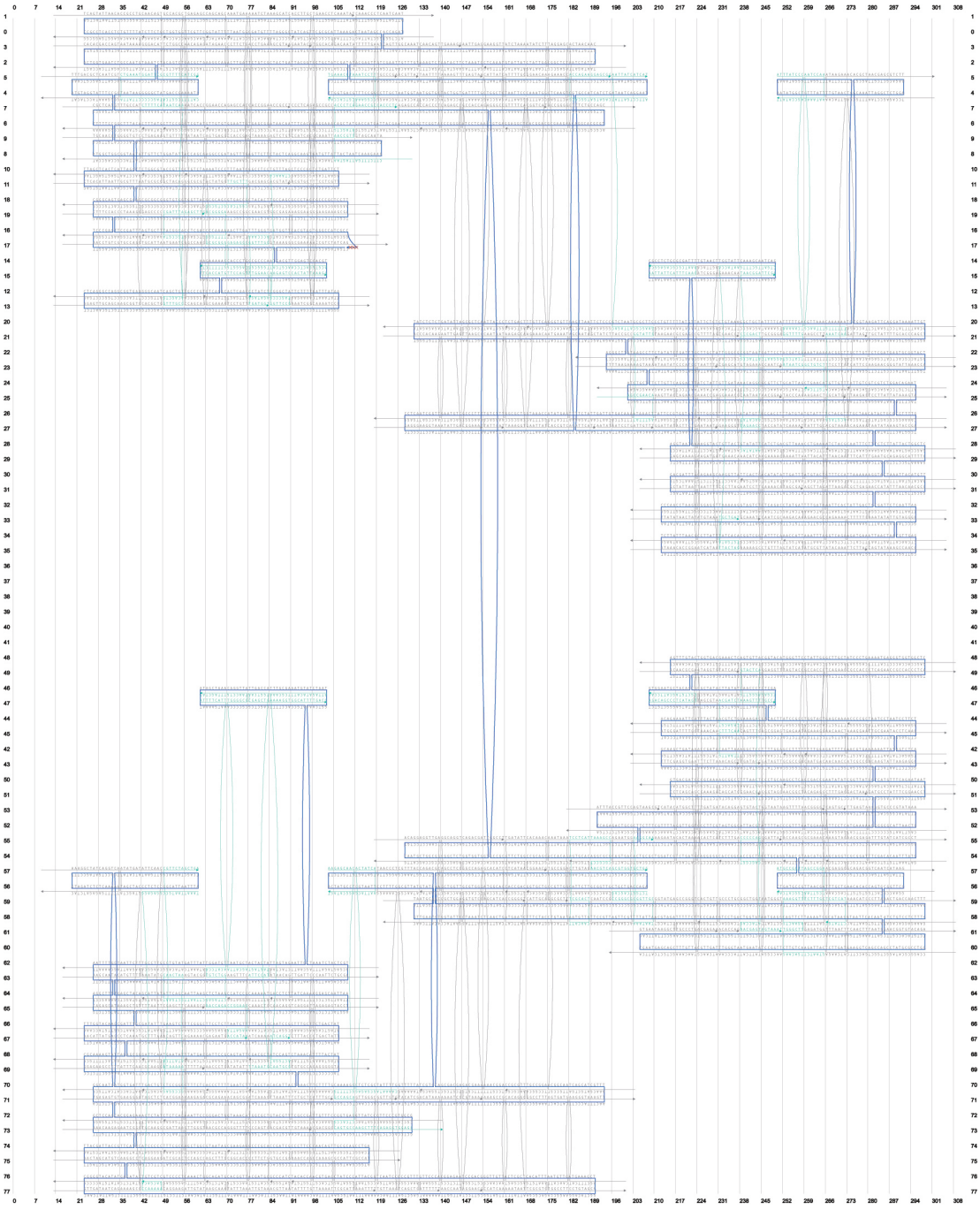

Figure 8.9: Strand diagram of the dynamic (switchD16) variant. Scaffold (shown in blue) and staple layout of the dynamic switch variant with 16 activated stacking interactions. Cyan: stacking activated. Generated with caDNAno v0.2.

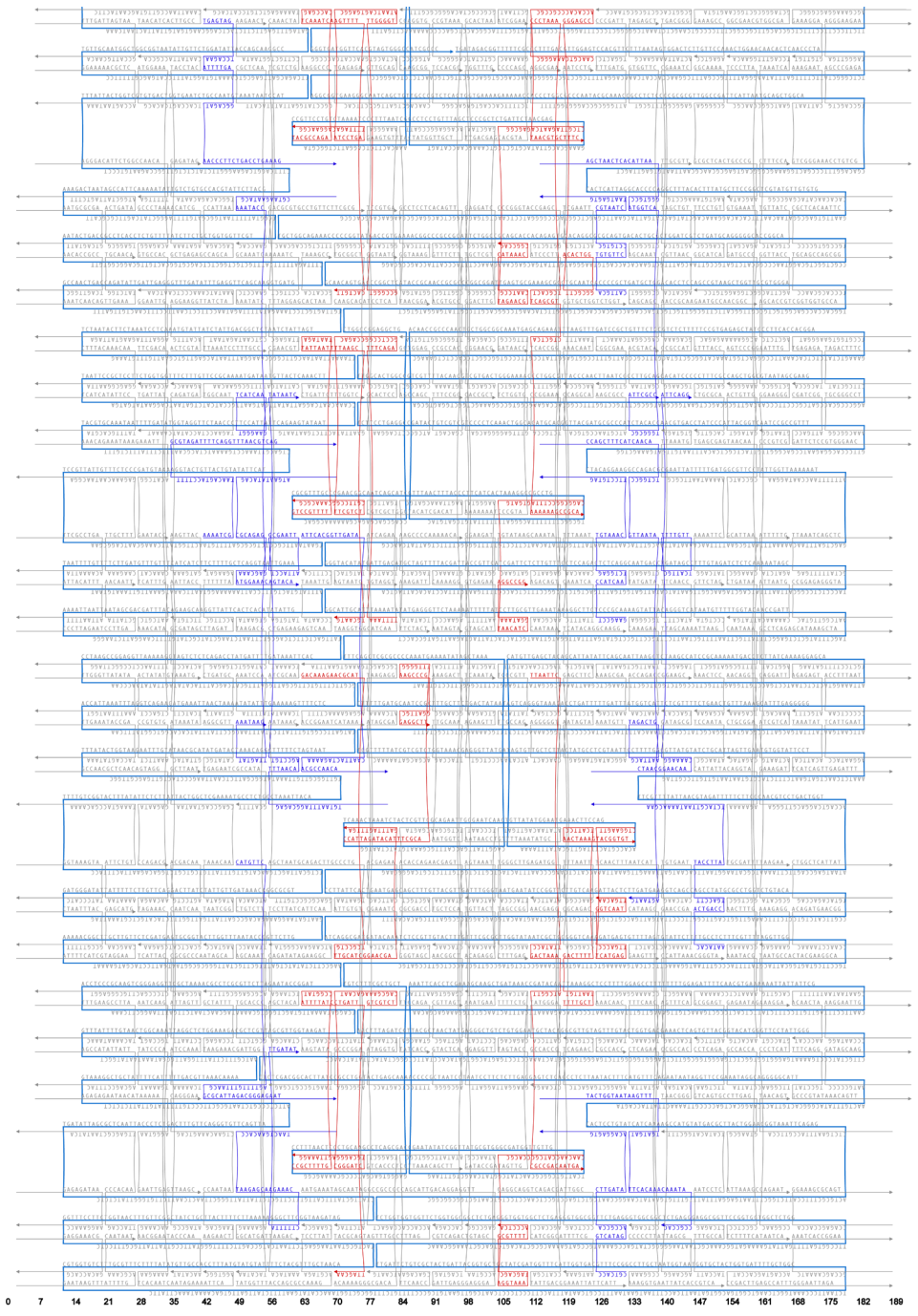

Figure 8.10: Strand diagram of brick monomer A_1 generated with caDNAno v0.2.

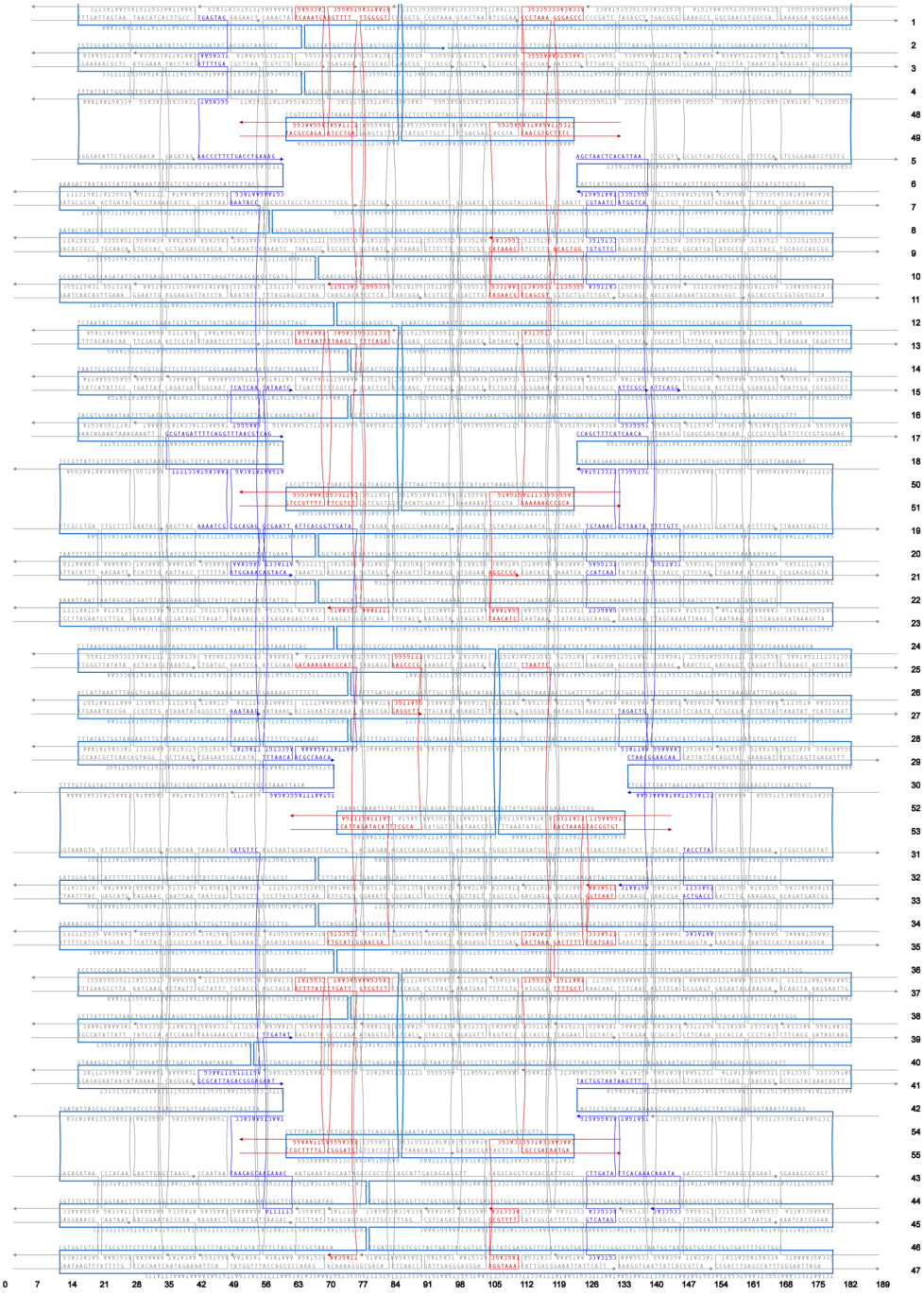

Figure 8.11: Strand diagram of brick monomer A_2 generated with caDNAno v0.2.

Part IV

Conclusion and Outlook

Chapter 9
Conclusion and Outlook

DNA and proteins are two important building blocks of cells and essential for the cellular functions. In a cell, DNA is highly compacted into a small volume and highly twisted and bent. In many cases the twist and writhe of the DNA molecule has an impact on its interaction with proteins and must be (locally) released for an effective and successful interplay. Therefore, the local and global mechanics of the DNA plays an important role in the protein-DNA interaction. Proteins also play an important role in the force response of a cell. Different proteins can withstand different forces. Furthermore, depending on their biological function, some proteins are able to not only bear a certain amount of external force, but also to refold into their native state after unfolding. Besides its biological relevance, DNA can also be used as a building block for nanotechnology. In all of the above mentioned cases, the time it takes to undergo a transition from one state to another is essential for the respective function. Magnetic Tweezers and trSAXS are two state-of-the-art techniques to investigate fast biological transitions of different samples in a time resolved manner and a wide variety of conditions.

The state-of-the-art magnetic tweezers setup built within the framework of this thesis is able to combine a large field of view with an excellent tracking accuracy. Its lens and objective combination minimizes aberration, so that a maximum resolution over the complete FOV is achieved. The overall robustness of the setup makes it stable against external influences and easy to readjust if one setup component has to be exchanged. The forces for the MyOne as well as the M270 beads were calibrated with such high precision, that the dominant error of the force is the variation between the beads. The force field was tested to be homogeneous over the whole FOV. Combined with the computational performance of the setup, it is able to track many beads in parallel with a time resolution of 58 Hz without any detectable setup-specific differences for different positions of the beads. A reduced FOV increases the time resolution up to 2500 Hz. Nevertheless, the fast developments in camera technology enable to further increase the FOV due to the higher amount of pixels. However, a larger FOV will at some point likely result in an inhomogeneous force field. A subset of recent state-of-the-art cameras allow to have multiple, small, FOVs. Hereby, the camera frequency can be increased while still many beads in parallel can be tracked. A probably necessary GPU support to handle the large amount of data is already embedded in the current software. The setup is only able to detect the position of the bead, however the sample itself, i.e. the molecule of interest, cannot

be observed directly. Recently, MT setups combined with fluorescent imaging techniques have been developed, e.g. employing total internal reflection fluorescence (TIRF) microscopy. The new generation of CMOS cameras, the so called "scientific CMOS" (sCMOS) cameras, make it possible to combine high spatiotemporal resolution with fluorescent imaging.

A software package was coded from scratch for analysis of MT traces. It consists of many different GUIs which combine different options and tasks to analyze the trajectories. It enables daily analysis and special tasks, such as a setup calibration. It was used to analyze all MT data presented in this thesis, including the setup calibration, fast hopping analysis, step analysis and deconvolution of the raw data. With its simplicity and usability, it fills a gap between the progress in setup architecture and the handling of – as a consequence – increasingly complex data. Therefore, it is already in use by different people. It is capable to analyze data recorded with a state-of-the-art MT setup including measurements that last for several days. However, improvements in the performance are still possible. The software package is coded in Matlab and uses only "simple" functions, which are optimized to handle a small and semi-large data amount, which fit into the memory of the computer. However, Matlab offers different options (connected with the "datastore function") to handle data that do not fit into memory. This will enable the software package to handle even larger amounts of data in the future. Rewriting the code in a different programming language would offer the possibility to make use of pointers for data handling, thus gaining computational speed and reducing the total amount of memory, by reducing unnecessary copies of the data. However, most likely the easily readable code will become more complex. Nevertheless, these changes have to be carefully weighted against the progress in computational speed and memory size.

When a torsionally constrained dsDNA molecule is rotated, at some point it will form loops (plectonemes). The transition from the elongated form of the DNA to the molecule shortened by one (or several) loop(s) was measured by magnetic tweezers with a high spatial and temporal resolution. Therefore, its salt and force dependency could be analyzed in detail, even for the fast dynamics of low forces and salt concentration. Therefore, the enormous differences between the dwell times of RNA and DNA at the buckling transition could be characterized. An asymmetry of the transition in the extension-, and rotational degree of freedom was discovered. The extension histogram was deconvolved with the setup response function and a 3D energy landscape, with the coordinates of the extension, linking number (here rotation of the magnets) and energy was obtained. The loop formation of DNA is important for many proteins binding to DNA. First measurements with the TATA-binding protein could already give evidence for a reduction of the energy barrier between the buckled and unbuckled state. The plectoneme formation was not clearly detectable anymore upon binding of the protein. The deconvolution process can be applied to all extension traces, independent of the system. Therefore, the unbiased, setup-independent energy landscape of different samples and experiment types can be obtained.

Some proteins can withstand external force, unfold due to external force, and refold if the force is released. However, precise measurements of the force response of proteins are difficult to achieve, especially in the low force regime. A new attachment strategy developed within this thesis combined with magnetic tweezers allows to measure the force response of proteins within a large force range, including the low force regime. With the new method, the

protein is tethered specifically between the glass surface and the bead. The attachment strategy, consisting of a covalent attachment on one side and a specific protein-ligand interaction (*streptavidin-biotin*) on the other side, was characterized by its force dependent rupture lifetime. Here, a force range well suited for typical magnetic tweezers experiments was obtained. It was shown, that the bond lifetime is described by a double-exponential decay at constant force. Between the glass surface and the protein, a linker (ELP) was introduced, in order to minimize unspecific surface interaction. The linker was characterized in its force response and a WLC-like behavior without any artifacts was obtained. Hence, a new attachment strategy for proteins tethered in MT could be established, minimizing surface interaction and providing a long lifetime of the tether before a rupture event occurs, enabling measurement durations of several days. The protein domain *ddFLN4* could be characterized in detail with special focus on its extension and rates of unfolding and refolding. In force-clamp measurements, not only full unfolding of the whole domain, but also a short-lived intermediate state could be observed. The large field-of-view made it possible to gain a lot of statistics in a short amount of time with sufficiently high temporal resolution to examine the short-lived intermediate state. Therefore, the slow as well as fast transition rates and the distance to the transition states for all transitions could be measured and analyzed. The low equilibrium rate extrapolated from faster transitions at higher forces is verified by a long measurement with a duration of more than two days at equilibrium force. In the current configuration, only one side of the attachment is covalent, while the other side can rupture, with increasing probability for higher forces. The double-exponential decay of the bond lifetime can be further investigated. The current attachment strategy relies on a tetravalent *streptavidin*, which is bound to the beads. It is an open question if a monovalent version of the *streptavidin* would result in only one single exponential decay of the tethers. Nevertheless, a fully covalent attachment strategy would allow for even longer measurement durations even when applying higher forces. However, a first attempt using an enzymatic reaction to achieve a covalent attachment on both sides of the protein failed, maybe due to the excluded volume resulting from the small distance between the glass surface and bead. An alternative approach, the so called *SpyTag-SpyCatcher* interaction [391], is another method to form covalent bonds and was already introduced to MT flow cells [394]. It does not require enzymes and thus might be able to form a second bond, when the protein is already bound to one surface, even when the bead and glass surface are close together.

DNA origamis are a promising tool to build biological functional units on the nanoscale. One important aspect is the time it takes for an origami to change its conformation. With trSAXS, the dimerization process of two shape-complementary DNA origami monomers at high magnesium chloride concentration, and a conformational change of a DNA origami switch as a function of the ionic strength, were examined. Therefor, depending on the time resolution needed, a stopped-flow device or manual mixing was used. For fast measurements, short acquisition times could be obtained at a high flux of photons. It was shown that the dimerization process of the two monomers is in the order of minutes to hours. However, the interfaces of the origami switch device, which are pre-aligned by a single, flexible, Holliday-junction, enable it to change its conformation close to the diffusion speed limit, thus in the millisecond regime. The comparable ionic conditions of the solution and same interaction mechanism of the origami monomers and switch device arms suggest that a reduction of the degree of freedom can significantly change the speed of a conformational transition. In other words, the free

orientation of the interfaces acts as an additional barrier which influences the dynamics of a DNA origami. This can be reduced by the alignment of the shape-complementary interfaces. It was shown that DNA origamis based on base-pair-stacking can be extremely fast, close to the diffusion limit. The fast conformational change of the DNA origami switch makes it a promising tool for future application, such as DNA origami boxes for drug delivery which can open at the right position and time, but also for other applications, e.g. to transmit cellular signals within the (sub-)millisecond regime. A combination of diffusion-based assembly and pre-aligned conformations has the potential to accelerate the building of large, complex, DNA origamis.

Fast tracking magnetic tweezers and trSAXS measurements enabled to study the fast kinetics of proteins, DNA, and DNA origamis. The measurements of fast kinetics within this thesis were only possible with state-of-the-art instruments. Developments in the spatiotemporal resolution in force spectroscopy will give more insights into the underlying physical-chemical mechanics. Future generations of magnetic tweezers will allow to examine even faster kinetics while measuring more molecules in parallel. Regarding its biological relevance, this will not only allow for deeper insights into the details of the DNA mechanics, it will especially help to understand the protein-DNA interactions and reduction of energy barriers as well as the stabilization of a protein-DNA complex or conformation. The conclusion drawn about the biological samples were based on the fluctuations of the bead and therefore indirect. The DNA and proteins are not visible by themselves. To some extent, fluorescent labeling in combination with a fluorescent detection method (e.g. TIRF) is able to address this drawback. However, to detect fast interactions and kinetics, imaging techniques that are label free and in solution become more important. The third generation of synchrotrons already makes trSAXS a powerful tool to detect transitions within the millisecond regime. Current and future developments in microfluidics and radiation sources, such as free electron lasers with a much higher brilliance compared to state-of-the-art synchrotrons, will enable to increase the temporal resolution up to the femtosecond regime. Besides others, this will enable to measure transitions of DNA origamis with high temporal details, but furthermore, interactions of DNA origamis with other samples can be studied in detail.
A combination of different techniques will further improve the knowledge about biological systems. For example, cryo-electron microscopy can give a high resolution image of the structure of a sample, while SAXS can give details about its structure in solution and trSAXS can detect (fast) conformational changes. DNA origamis able to apply force on another molecule have already been introduced [24]. A combination with trSAXS could in principle be used to detect conformational changes under force and could be combined with or compared to magnetic tweezers force spectroscopy data.

Part V

Appendix

Chapter 10
Appendix: Magnetic Tweezers

10.1 List of Setup Components

The setup described in chapter 4 consists of the components listed in table 10.1. In addition, several accessories (e.g. screws, adapters, linear stages) are used.

Table 10.1: List of Components of the setup described in chapter 4.

Setup Part	Supplier / Components / Comments
CPU	Core^{TM} i7-4930K
graphic board	MSI GeForce GTX X 12GB GDDR5
LED	Osram Oslon SSL, amber, 223lm (LumiTronix)
lens for illumination	Ø25 mm, f=20 mm, NA=0.543, S-LAH64, ARC: 350-700 nm (Thorlabs, USA)
x-y translation stage	00-30-101-0000, Märzhäuser Wertlar GmbH & Co, KG (Germany)
objective piezo	P-726.1CD, Physik Instrumente GmbH & Co. KG (Germany)
objective piezo controller	E-753.1CD, Physik Instrumente GmbH & Co. KG (Germany)
objective	RMS40X-PFO, 40x Olympus Plan Fluorite Oil Immersion (Olympus, Japan)
camera lens (standard)	G322311000, Achr. VIS ARB2; D=50.8; F=250, Qioptiq (France)
camera lens (optional)	G322304000, Achr. VIS ARB2; D=50; F=200, Qioptiq (France)
camera	Falcon2 12M (Teledyne DALSA, Canada)
frame grabber	1433 PCIe (National Instruments, USA)
motor stage (magnet distance)	M-126.PD2, Physik Instrumente GmbH & Co. KG (Germany)
motor controller (magnet distance)	C-863.11, Physik Instrumente GmbH & Co. KG (Germany)
motor stage (rotation)	C-150.PD, Physik Instrumente GmbH & Co. KG (Germany)
motor controller (rotation)	C-863.11, Physik Instrumente GmbH & Co. KG (Germany)
pump	ISM832C, Ismatec (Germany)
protection box	custom built
platform	custom built
magnet holder	custom built (1mm gap)
magnets	cubic (5 mm)^3 (NdFeB, N50)

10.2 Computational Performance for Different Tracker Algorithms and Tracker Settings

In section 4.3.1, only a subset of all lateral tracker algorithms and tracker settings is described. However, more tracker algorithms and tracker settings were tested for their computational effort. Hereby, only the lateral tracker algorithm is affected, while the computation of the height information with the help of a LUT stays the same. Table 10.2 gives an overview over all examined configurations. As already noted in section 4.3.1, a selection of more beads than denoted in this table will automatically reduce the frame rate and thus all positions for all beads are tracked without loss of single beads and accuracy, however, less frames are analyzed. All values were determined with a 40× oil objective. For all tracker settings, a new LUT was built with a total range of 10 μm in steps of 100 nm. The beads were tracked in the center of the LUT. For all settings, the light was constant with a mean camera response of 120.

Table 10.2: Complete list of the maximum number of beads that can be tracked in real time with 58 Hz, tested with different lateral tracker algorithms and tracker settings. "Lens" is the lens in front of the camera, "ROI" the region of interest in pixel for every bead, "Algorithm" the tracking algorithm (QI / 1D Cross-Correlation (Cross-C)) / Center-of-Mass (CoM)), "Iteration" the number of iterations for the QI tracker, "ang" and "rad" the number of pixels covered in angular and radial direction for the QI tracker (see Ref. [31] for details), CPU and GPU the number of beads that can be tracked in real time without frequency reduction on the CPU or GPU, respectively. Cross-Correlation tracker was set to: length = 30, width = 64, Iteration = 3. For pixel calibration see table 10.3.

Lens	ROI	Algorithm	Iteration	ang	rad	CPU	GPU
250	110	*QI*	3	0.7	2	60	85
250	110	*QI*	2	0.7	2	70	110
250	110	*QI*	1	0.7	2	105	180
250	110	*QI*	3	0.5	1	105	185
250	110	*QI*	2	0.5	1	120	225
250	110	*QI*	1	0.5	1	150	340
250	110	*Cross-C*	–	–	–	195	> 500
250	110	*CoM*	–	–	–	230	> 500
250	80	*QI*	3	0.7	2	140	210
250	80	*QI*	2	0.7	2	170	260
250	80	*QI*	1	0.7	2	225	400
250	80	*QI*	3	0.5	1	240	400
250	80	*QI*	2	0.5	1	260	470
250	80	*QI*	1	0.5	1	320	> 500
250	80	*Cross-C*	–	–	–	360	> 500
250	80	*CoM*	–	–	–	400	> 500
200	100	*QI*	3	0.7	2	110	170
200	100	*QI*	2	0.7	2	130	230
200	100	*QI*	1	0.7	2	165	330
200	100	*QI*	3	0.5	1	170	330
200	100	*QI*	2	0.5	1	190	410
200	100	*QI*	1	0.5	1	220	> 500
200	100	*Cross-C*	–	–	–	230	> 500
200	100	*CoM*	–	–	–	260	> 500
200	70	*QI*	3	0.7	2	160	260
200	70	*QI*	2	0.7	2	200	370
200	70	*QI*	1	0.7	2	280	> 500
200	70	*QI*	3	0.5	1	310	> 500
200	70	*QI*	2	0.5	1	350	> 500
200	70	*QI*	1	0.5	1	390	> 500
200	70	*Cross-C*	–	–	–	410	> 500
200	70	*CoM*	–	–	–	460	> 500

10.3 Setup Resolution for Different Tracker Algorithms and Tracker Settings

In section 4.3.2, only a subset of all tested lateral trackers algorithms and tracker settings is presented. Table 10.3, Fig. 10.1 and 10.2 give an overview of all examined combinations. Same configurations and settings as in section 10.2 and table 10.2 were selected. Only the lateral tracker is changed, while the algorithm to extract the height information with the LUT, and hence the z position of the bead, stays the same.

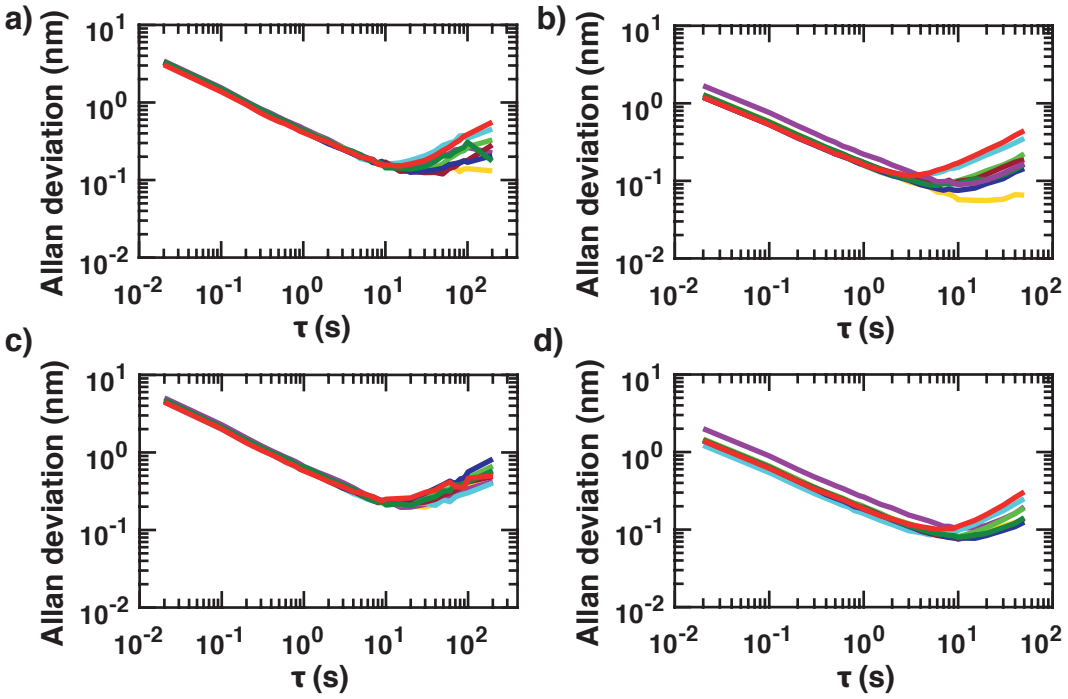

Figure 10.1: Allan deviation in z-direction for different lateral tracker algorithms and tracker settings. For the same setup configuration and same bead size, the Allan deviations of the Cross-Correlation tracker and of different QI tracker settings deviate only slightly. For all configurations, the Center-of-Mass tracker is worse. The tracking performance for 3 µm beads is consistently better compared to 1 µm beads. For the 1 µm beads the accuracy reduces slightly for the 200 mm camera lens, but stays approximately constant for the larger beads. Only the lateral computation is affected by the different tracker algorithms and tracker settings, the algorithm to extract the height with the help of a LUT is not changed. a) 1 µm beads and a 250 mm lens, b) 3 µm beads and a 250 mm lens, c) 1 µm beads and a 200 mm camera lens, d) 3 µm beads and a 200 mm lens. red: 3xQI, blue: 2xQI, green: 1xQI, dark red: 3xQI less pixels, dark blue: 2xQI less pixels, dark green: 1xQI less pixels, yellow: Cross- Correlation tracker, purple: CoM tracker. All measurements last 10 min at 58 Hz. Mean values of at least 15 beads.

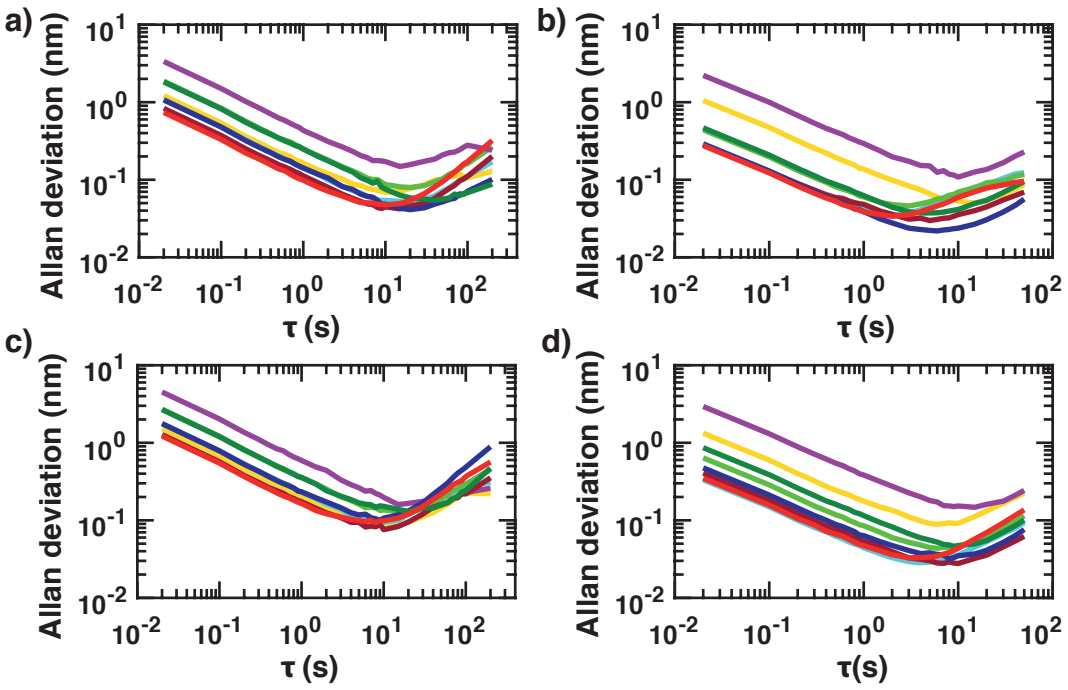

Figure 10.2: Allan deviation in x of same measurements as in figure 10.1. Different tracker algorithms and settings were tested. Throughout the setup configurations and bead sizes, the QI tracker with 2 and 3 iterations leads to the best tracking accuracy, while the number of pixels used for the QI tracker has only minor influence. The CoM tracker is significantly worse. The Allan deviation for the larger beads is smaller. For the 1 µm beads, the resolution of the QI tracker is worse as for the 200 mm lens configuration, while the tracker accuracy for the 3 µm beads stays approximately constant. a) 1 µm beads and a 250 mm lens, b) 3 µm beads and a 250 mm lens, c) 1 µm beads and a 200 mm camera lens, d) 3 µm beads and a 200 mm lens. Color code as in Fig. 10.1.

Table 10.3: Complete list of all determined standard deviations for all tracker and tracker settings examined for two different bead sizes. For an explanation of abbreviations as well as measurement conditions see table 4.2

Bead	Lens	nm/Px	ROI	Algorithm	Iteration	ang	rad	std lat.	std z
3	250	107.72	110	*QI*	3	0.7	2	0.5 ± 0.3	2.0 ± 1.2
3	250	107.72	110	*QI*	2	0.7	2	0.5 ± 0.3	1.4 ± 0.6
3	250	107.72	110	*QI*	1	0.7	2	0.8 ± 0.6	1.3 ± 0.6
3	250	107.72	110	*QI*	3	0.5	1	0.4 ± 0.2	1.3 ± 0.6
3	250	107.72	110	*QI*	2	0.5	1	0.5 ± 0.2	1.3 ± 0.6
3	250	107.72	110	*QI*	1	0.5	1	0.5 ± 0.5	1.3 ± 0.5
3	250	107.72	110	*Cross-C*	–	–	–	1.2 ± 0.5	1.3 ± 0.5
3	250	107.72	110	*CoM*	–	–	–	2.3 ± 0.9	1.8 ± 0.8
1	250	107.72	80	*QI*	3	0.7	2	1.2 ± 0.4	3.2 ± 0.3
1	250	107.72	80	*QI*	2	0.7	2	1.5 ± 0.4	3.3 ± 0.1
1	250	107.72	80	*QI*	1	0.7	2	2.2 ± 0.3	3.3 ± 0.1
1	250	107.72	80	*QI*	3	0.5	1	1.2 ± 0.3	3.3 ± 0.2
1	250	107.72	80	*QI*	2	0.5	1	1.4 ± 0.4	3.3 ± 0.1
1	250	107.72	80	*QI*	1	0.5	1	2.1 ± 0.3	3.4 ± 0.1
1	250	107.72	80	*Cross-C*	–	–	–	1.4 ± 0.1	3.3 ± 0.1
1	250	107.72	80	*CoM*	–	–	–	3.5 ± 0.8	3.5 ± 0.2
3	200	131.65	100	*QI*	3	0.7	2	0.7 ± 0.3	1.8 ± 0.3
3	200	131.65	100	*QI*	2	0.7	2	0.6 ± 0.2	1.5 ± 1.1
3	200	131.65	100	*QI*	1	0.7	2	1.0 ± 0.3	1.6 ± 0.2
3	200	131.65	100	*QI*	3	0.5	1	0.6 ± 0.2	1.5 ± 0.2
3	200	131.65	100	*QI*	2	0.5	1	0.7 ± 0.2	1.4 ± 0.1
3	200	131.65	100	*QI*	1	0.5	1	1.1 ± 0.4	1.5 ± 0.3
3	200	131.65	100	*Cross-C*	–	–	–	1.6 ± 0.2	1.5 ± 0.3
3	200	131.65	100	*CoM*	–	–	–	3.1 ± 0.3	2.1 ± 0.8
1	200	131.65	70	*QI*	3	0.7	2	1.9 ± 0.5	4.6 ± 0.4
1	200	131.65	70	*QI*	2	0.7	2	2.3 ± 0.5	4.5 ± 0.1
1	200	131.65	70	*QI*	1	0.7	2	3.1 ± 0.4	4.7 ± 0.2
1	200	131.65	70	*QI*	3	0.5	1	1.8 ± 0.5	4.7 ± 0.2
1	200	131.65	70	*QI*	2	0.5	1	2.5 ± 0.4	4.8 ± 0.2
1	200	131.65	70	*QI*	1	0.5	1	3.1 ± 0.6	4.9 ± 0.7
1	200	131.65	70	*Cross-C*	–	–	–	1.7 ± 0.1	4.7 ± 0.2
1	200	131.65	70	*CoM*	–	–	–	4.6 ± 0.1	5.1 ± 0.2

10.4 Flowcharts of MT GUI

In addition to chapter 5, flowcharts of all described GUIs are given here. Symbols are according to DIN 66001:1983-12. The flowcharts by far do not cover all functions of the software package and further do not represent all options available for all GUIs. Furthermore, it does not connect all functions within one GUI as it might be the case in the code itself. Nevertheless, they give an overview of the most relevant functions. For simplicity, some flowchart branches are not fully drawn. For example "decision" symbols have an open end. The code itself is not covered by the presented flowcharts. Many functions within one GUI only work in a consecutive order. However, these flowcharts aim to give an overview and hence these successive dependencies are mostly not presented.

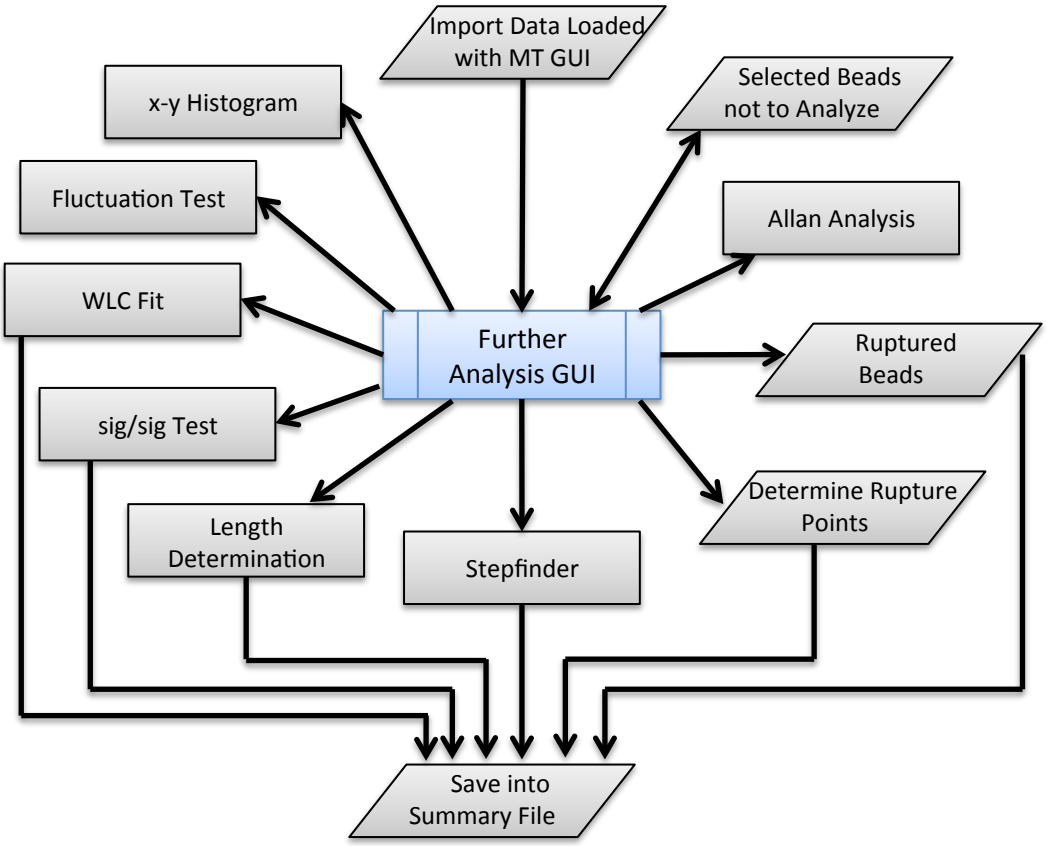

Figure 10.3: Flowchart of "Further Analysis GUI". The GUI is described in section 5.3. Its main task is to perform more detailed analysis, such as a comparison of the x and y fluctuations, WLC fits, Allan variance calculations and the application of a stepfinder algorithm. The GUI is divided into two sub panels, one of them including the ability so save the analysis into a special summary file, which can be further analyzed.

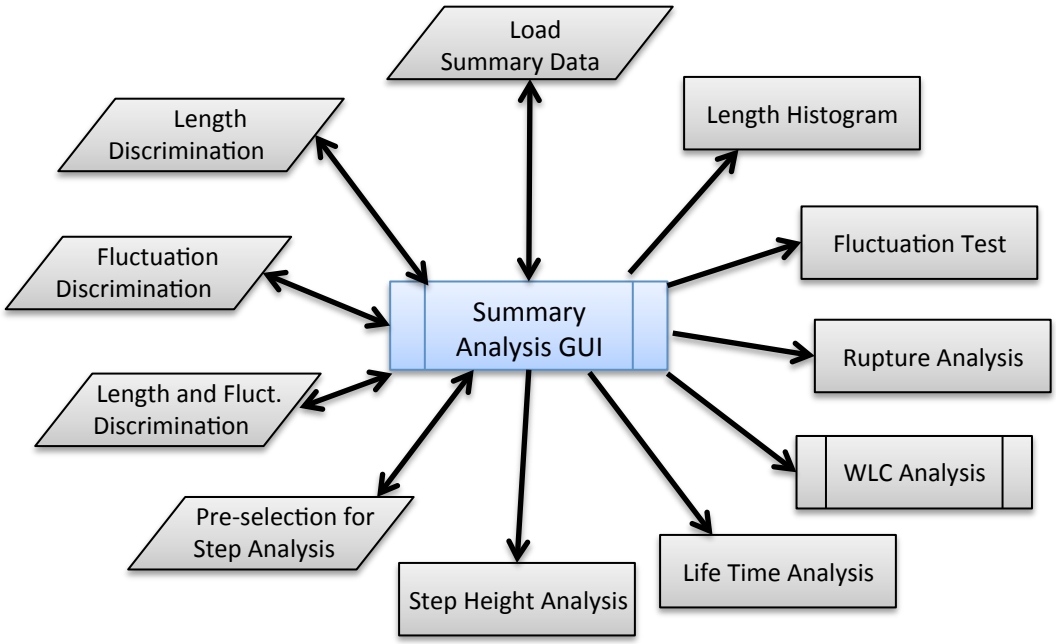

Figure 10.4: Flowchart of "Summary Analysis GUI". The GUI is described in section 5.4. Its main task and function is to analyze a summary file created with "Further Analysis GUI". Beads can be pre-selected by their length and fluctuation behaviour. Besides minor other tasks, it focuses on the analysis of step heights and lifetimes, as well as a rupture analysis of tethered beads.

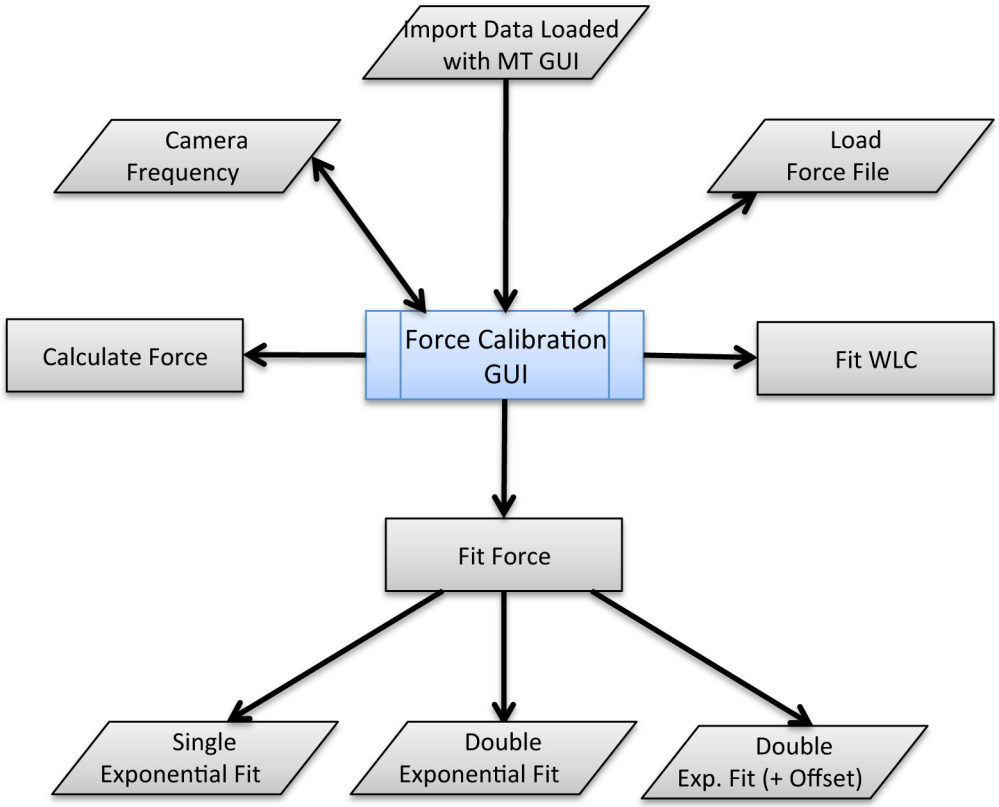

Figure 10.5: Flowchart of "Force Calibration GUI". The GUI is described in section 5.5. Its main function is to determine the force based on the fluctuation of the bead with the help of the Allan variance. Furthermore, different exponential models can be fitted to the force as a function of the distance between the magnet and the flow cell.

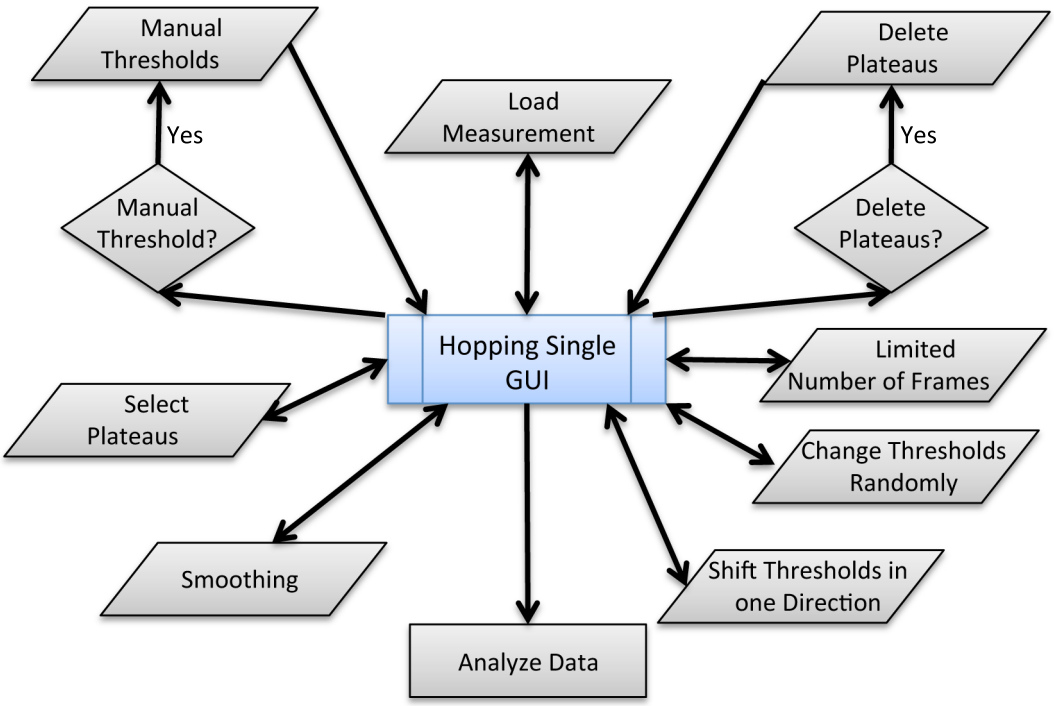

Figure 10.6: Flowchart of "Hopping Single GUI". The GUI is described in section 5.6. Its main function is to analyze a two state extension trace as function of time. It contains specific tasks to test the stability of the measurement and analysis.

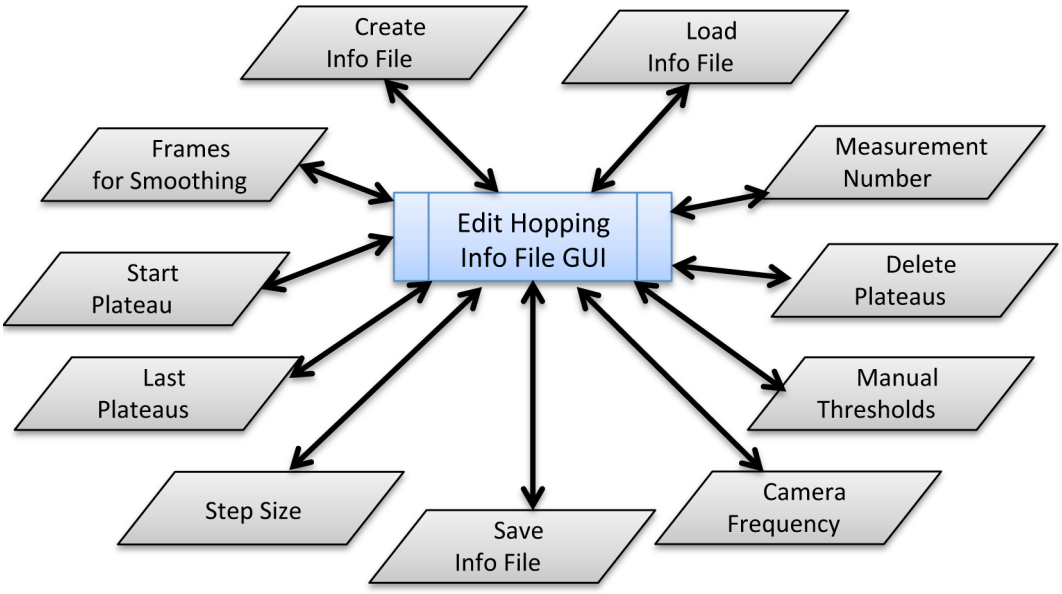

Figure 10.7: Flowchart of "Edit Hopping Info File GUI". The GUI is described in section 5.7. Its main function is to create and modify files that contain all information to quickly analyze a two state extension trace of an MT measurement. The GUI is separated into two parts, one to create a new entry to the file, and one to modify an existing entry. This flowchart only contains every function once.

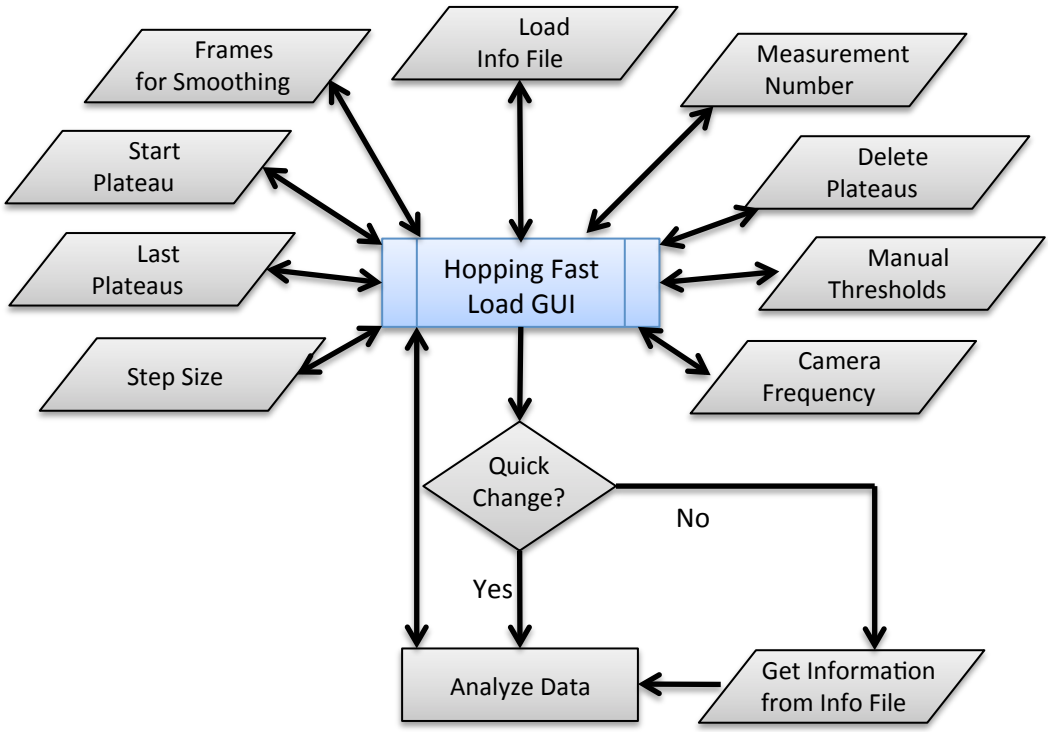

Figure 10.8: Flowchart of "Hopping Fast Load GUI". The GUI is described in section 5.7. Its main function is to analyze a two state extension trace as function of time. It is able to read all necessary information of an information file created with "Edit Hopping Info File GUI" and can additionally adjust settings with the "quick change" panel.

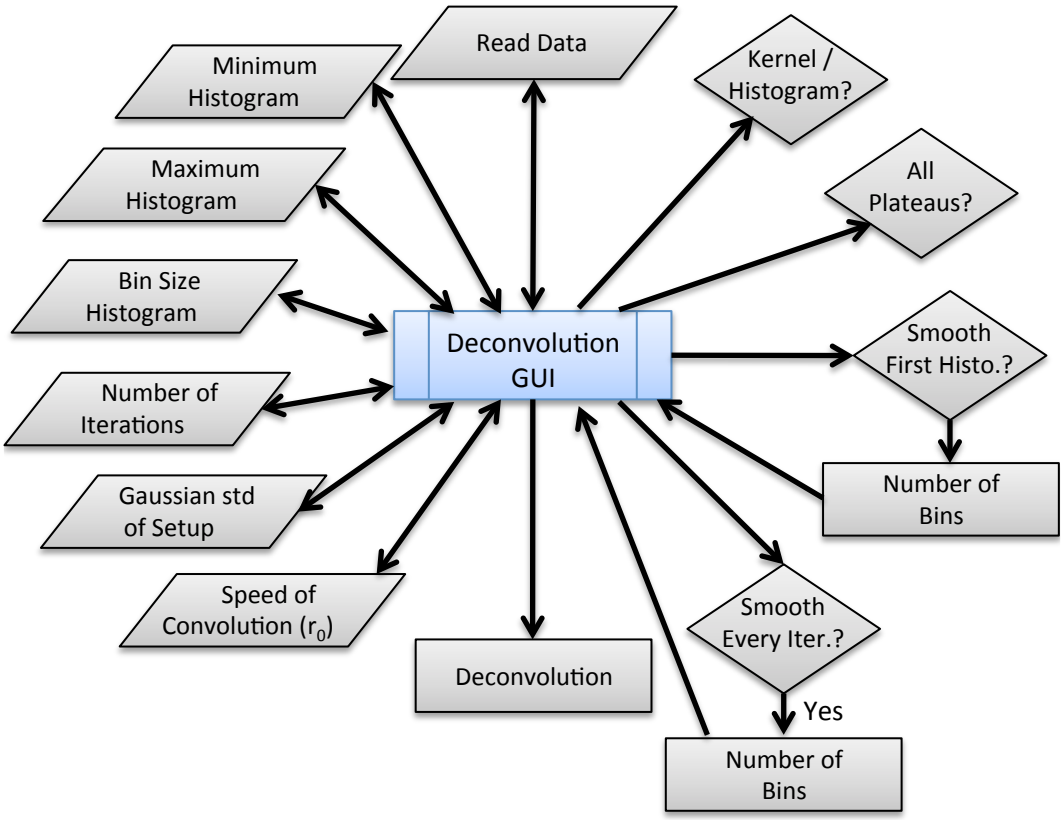

Figure 10.9: Flowchart of "Deconvolution GUI". The GUI is described in section 5.8. Its main function is to deconvolve extension histograms of MT measurements with the setup response function and to determine the energy landscape by the inverse Boltzmann approach.

Bibliography

[1] L. K. Bruetzel, P. U. Walker, T. Gerling, H. Dietz, and J. Lipfert, "Time-resolved small-angle x-ray scattering reveals millisecond transitions of a dna origami switch," *Nano Lett*, 2018.

[2] P. U. Walker, W. Vanderlinden, and J. Lipfert, "The dynamics and energy landscape of dna plectoneme nucleation," *bioRxiv*, 2018.

[3] L. K. Bruetzel, T. Gerling, S. M. Sedlak, P. U. Walker, W. Zheng, H. Dietz, and J. Lipfert, "Conformational changes and flexibility of dna devices observed by small-angle x-ray scattering," *Nano Letters*, vol. 16, no. 8, pp. 4871–9, 2016.

[4] K. Neuman, T. Lionnet, and J.-F. Allemand, "Single-molecule micromanipulation techniques," *Annual Review of Materials Research*, vol. 37, no. 1, pp. 33–67, 2007.

[5] K. C. Neuman and A. Nagy, "Single-molecule force spectroscopy: optical tweezers, magnetic tweezers and atomic force microscopy," *Nature Methods*, vol. 5, no. 6, pp. 491–505, 2008.

[6] H. Li, W. A. Linke, A. F. Oberhauser, M. Carrion-Vazquez, J. G. Kerkvliet, H. Lu, P. E. Marszalek, and J. M. Fernandez, "Reverse engineering of the giant muscle protein titin," *Nature*, vol. 418, no. 6901, pp. 998–1002, 2002.

[7] I. Schwaiger, A. Kardinal, M. Schleicher, A. A. Noegel, and M. Rief, "A mechanical unfolding intermediate in an actin-crosslinking protein," *Nat Struct Mol Biol*, vol. 11, no. 1, pp. 81–5, 2004.

[8] R. Mallik and S. P. Gross, "Molecular motors: strategies to get along," *Curr Biol*, vol. 14, no. 22, pp. R971–82, 2004.

[9] A. Ishijima and T. Yanagida, "Single molecule nanobioscience," *Trends Biochem Sci*, vol. 26, no. 7, pp. 438–44, 2001.

[10] C. Bustamante, Y. R. Chemla, N. R. Forde, and D. Izhaky, "Mechanical processes in biochemistry," *Annu Rev Biochem*, vol. 73, pp. 705–48, 2004.

[11] S. B. Smith, L. Finzi, and C. Bustamante, "Direct mechanical measurements of the elasticity of single dna molecules by using magnetic beads," *Science*, vol. 258, no. 5085, pp. 1122–6, 1992.

[12] T. R. Strick, J. F. Allemand, D. Bensimon, A. Bensimon, and V. Croquette, "The elasticity of a single supercoiled dna molecule," *Science*, vol. 271, no. 5257, pp. 1835–7, 1996.

[13] T. R. Strick, J. F. Allemand, D. Bensimon, and V. Croquette, "Behavior of supercoiled dna," *Biophys J*, vol. 74, no. 4, pp. 2016–28, 1998.

[14] F. Kriegel, N. Ermann, and J. Lipfert, "Probing the mechanical properties, conformational changes, and interactions of nucleic acids with magnetic tweezers," *Journal of Structural Biology*, vol. 197, no. 1, pp. 26–36, 2017.

[15] A. Ashkin, J. M. Dziedzic, J. E. Bjorkholm, and S. Chu, "Observation of a single-beam gradient force optical trap for dielectric particles," *Opt Lett*, vol. 11, no. 5, p. 288, 1986.

[16] D. McGloin, "Optical tweezers: 20 years on," *Philos Trans A Math Phys Eng Sci*, vol. 364, no. 1849, pp. 3521–37, 2006.

[17] F. Kilchherr, C. Wachauf, B. Pelz, M. Rief, M. Zacharias, and H. Dietz, "Single-molecule dissection of stacking forces in dna," *Science*, vol. 353, no. 6304, 2016.

[18] P. Hinterdorfer and Y. F. Dufrene, "Detection and localization of single molecular recognition events using atomic force microscopy," *Nat Methods*, vol. 3, no. 5, pp. 347–55, 2006.

[19] A. B. Churnside, R. M. Sullan, D. M. Nguyen, S. O. Case, M. S. Bull, G. M. King, and T. T. Perkins, "Routine and timely sub-piconewton force stability and precision for biological applications of atomic force microscopy," *Nano Lett*, vol. 12, no. 7, pp. 3557–61, 2012.

[20] D. T. Edwards, J. K. Faulk, M. A. LeBlanc, and T. T. Perkins, "Force spectroscopy with 9-mus resolution and sub-pn stability by tailoring afm cantilever geometry," *Biophys J*, 2017.

[21] E. Evans, K. Ritchie, and R. Merkel, "Sensitive force technique to probe molecular adhesion and structural linkages at biological interfaces," *Biophys J*, vol. 68, no. 6, pp. 2580–7, 1995.

[22] G. Sitters, D. Kamsma, G. Thalhammer, M. Ritsch-Marte, E. J. Peterman, and G. J. Wuite, "Acoustic force spectroscopy," *Nat Methods*, vol. 12, no. 1, pp. 47–50, 2015.

[23] D. Kamsma, R. Creyghton, G. Sitters, G. J. Wuite, and E. J. Peterman, "Tuning the music: Acoustic force spectroscopy (afs) 2.0," *Methods*, vol. 105, pp. 26–33, 2016.

[24] J. J. Funke, P. Ketterer, C. Lieleg, S. Schunter, P. Korber, and H. Dietz, "Uncovering the forces between nucleosomes using dna origami," *Sci Adv*, vol. 2, no. 11, p. e1600974, 2016.

[25] J. Lipfert, X. Hao, and N. H. Dekker, "Quantitative modeling and optimization of magnetic tweezers," *Biophys J*, vol. 96, no. 12, pp. 5040–9, 2009.

[26] J. Lipfert, G. M. Skinner, J. M. Keegstra, T. Hensgens, T. Jager, D. Dulin, M. Kober, Z. Yu, S. P. Donkers, F. C. Chou, R. Das, and N. H. Dekker, "Double-stranded rna under force and torque: similarities to and striking differences from double-stranded dna," *Proc Natl Acad Sci U S A*, vol. 111, no. 43, pp. 15408–13, 2014.

[27] Q. Guo, Y. He, and H. P. Lu, "Manipulating and probing enzymatic conformational fluctuations and enzyme-substrate interactions by single-molecule fret-magnetic tweezers microscopy," *Phys Chem Chem Phys*, vol. 16, no. 26, pp. 13052–8, 2014.

[28] J. Valle-Orero, J. A. Rivas-Pardo, R. Tapia-Rojo, I. Popa, D. J. Echelman, S. Haldar, and J. M. Fernandez, "Mechanical deformation accelerates protein ageing," *Angew Chem Int Ed Engl*, vol. 56, no. 33, pp. 9741–9746, 2017.

[29] I. Popa, J. A. Rivas-Pardo, E. C. Eckels, D. J. Echelman, C. L. Badilla, J. Valle-Orero, and J. M. Fernandez, "A halotag anchored ruler for week-long studies of protein dynamics," *J Am Chem Soc*, vol. 138, no. 33, pp. 10546–53, 2016.

[30] J. A. Rivas-Pardo, E. C. Eckels, I. Popa, P. Kosuri, W. A. Linke, and J. M. Fernandez, "Work done by titin protein folding assists muscle contraction," *Cell Rep*, vol. 14, no. 6, pp. 1339–1347, 2016.

[31] J. P. Cnossen, D. Dulin, and N. H. Dekker, "An optimized software framework for real-time, high-throughput tracking of spherical beads," *Rev Sci Instrum*, vol. 85, no. 10, p. 103712, 2014.

[32] J. Lipfert, M. Wiggin, J. W. Kerssemakers, F. Pedaci, and N. H. Dekker, "Freely orbiting magnetic tweezers to directly monitor changes in the twist of nucleic acids," *Nat Commun*, vol. 2, p. 439, 2011.

[33] Z. Yu, D. Dulin, J. Cnossen, M. Kober, M. M. van Oene, O. Ordu, B. A. Berghuis, T. Hensgens, J. Lipfert, and N. H. Dekker, "A force calibration standard for magnetic tweezers," *Rev Sci Instrum*, vol. 85, no. 12, p. 123114, 2014.

[34] C. Jiang, T. A. Lionberger, D. M. Wiener, and E. Meyhofer, "Electromagnetic tweezers with independent force and torque control," *Rev Sci Instrum*, vol. 87, no. 8, p. 084304, 2016.

[35] B. M. Lansdorp, S. J. Tabrizi, A. Dittmore, and O. A. Saleh, "A high-speed magnetic tweezer beyond 10,000 frames per second," *Rev Sci Instrum*, vol. 84, no. 4, p. 044301, 2013.

[36] D. Dulin, S. Barland, X. Hachair, and F. Pedaci, "Efficient illumination for microsecond tracking microscopy," *PLoS One*, vol. 9, no. 9, p. e107335, 2014.

[37] D. Dulin, T. J. Cui, J. Cnossen, M. W. Docter, J. Lipfert, and N. H. Dekker, "High spatiotemporal-resolution magnetic tweezers: Calibration and applications for dna dynamics," *Biophys J*, vol. 109, no. 10, pp. 2113–25, 2015.

[38] P. Daldrop, H. Brutzer, A. Huhle, D. J. Kauert, and R. Seidel, "Extending the range for force calibration in magnetic tweezers," *Biophysical Journal*, vol. 108, no. 10, pp. 2550–2561, 2015.

[39] M. M. van Oene, L. E. Dickinson, F. Pedaci, M. Kober, D. Dulin, J. Lipfert, and N. H. Dekker, "Biological magnetometry: torque on superparamagnetic beads in magnetic fields," *Phys Rev Lett*, vol. 114, no. 21, p. 218301, 2015.

[40] P. Lebel, A. Basu, F. C. Oberstrass, E. M. Tretter, and Z. Bryant, "Gold rotor bead tracking for high-speed measurements of dna twist, torque and extension," *Nat Methods*, vol. 11, no. 4, pp. 456–62, 2014.

[41] Z. Bryant, M. D. Stone, J. Gore, S. B. Smith, N. R. Cozzarelli, and C. Bustamante, "Structural transitions and elasticity from torque measurements on dna," *Nature*, vol. 424, no. 6946, pp. 338–41, 2003.

[42] J. Gore, Z. Bryant, M. D. Stone, M. Nollmann, N. R. Cozzarelli, and C. Bustamante, "Mechanochemical analysis of dna gyrase using rotor bead tracking," *Nature*, vol. 439, no. 7072, pp. 100–104, 2006.

[43] F. C. Oberstrass, L. E. Fernandes, and Z. Bryant, "Torque measurements reveal sequence-specific cooperative transitions in supercoiled dna," *Proc Natl Acad Sci U S A*, vol. 109, no. 16, pp. 6106–11, 2012.

[44] F. Kriegel, N. Ermann, R. Forbes, D. Dulin, N. H. Dekker, and J. Lipfert, "Probing the salt dependence of the torsional stiffness of dna by multiplexed magnetic torque tweezers," *Nucleic Acids Res*, vol. 45, no. 10, pp. 5920–5929, 2017.

[45] A. Celedon, I. M. Nodelman, B. Wildt, R. Dewan, P. Searson, D. Wirtz, G. D. Bowman, and S. X. Sun, "Magnetic tweezers measurement of single molecule torque," *Nano Lett*, vol. 9, no. 4, pp. 1720–5, 2009.

[46] J. Lipfert, J. W. Kerssemakers, T. Jager, and N. H. Dekker, "Magnetic torque tweezers: measuring torsional stiffness in dna and reca-dna filaments," *Nat Methods*, vol. 7, no. 12, pp. 977–80, 2010.

[47] D. J. Kauert, T. Kurth, T. Liedl, and R. Seidel, "Direct mechanical measurements reveal the material properties of three-dimensional dna origami," *Nano Lett*, vol. 11, no. 12, pp. 5558–63, 2011.

[48] F. Mosconi, J. F. Allemand, and V. Croquette, "Soft magnetic tweezers: a proof of principle," *Rev Sci Instrum*, vol. 82, no. 3, p. 034302, 2011.

[49] X. J. Janssen, J. Lipfert, T. Jager, R. Daudey, J. Beekman, and N. H. Dekker, "Electromagnetic torque tweezers: a versatile approach for measurement of single-molecule twist and torque," *Nano Lett*, vol. 12, no. 7, pp. 3634–9, 2012.

[50] H. Brutzer, N. Luzzietti, D. Klaue, and R. Seidel, "Energetics at the dna supercoiling transition," *Biophys J*, vol. 98, no. 7, pp. 1267–76, 2010.

[51] J. F. Allemand, D. Bensimon, R. Lavery, and V. Croquette, "Stretched and overwound dna forms a pauling-like structure with exposed bases," *Proceedings of the National Academy of Sciences*, vol. 95, no. 24, pp. 14152–14157, 1998.

[52] H. Chen, G. Yuan, R. S. Winardhi, M. Yao, I. Popa, J. M. Fernandez, and J. Yan, "Dynamics of equilibrium folding and unfolding transitions of titin immunoglobulin domain under constant forces," *J Am Chem Soc*, vol. 137, no. 10, pp. 3540–6, 2015.

[53] M. Lee, J. Lipfert, H. Sanchez, C. Wyman, and N. H. Dekker, "Structural and torsional properties of the rad51-dsdna nucleoprotein filament," *Nucleic Acids Res*, vol. 41, no. 14, pp. 7023–30, 2013.

[54] N. Chaffey, "Alberts, b., johnson, a., lewis, j., raff, m., roberts, k. and walter, p. molecular biology of the cell. 4th edn," *Annals of Botany*, vol. 91, no. 3, pp. 401–401, 2003.

[55] D. M. Crothers, "Principles of nucleic acid structure. von w. saenger. springer-verlag, berlin 1984. xx, 556 s., geb. dm 79.00. – isbn 3-540-90761-0xs," *Angewandte Chemie*, vol. 98, no. 8, pp. 762–762, 1986.

[56] H. Z. Sable, "Biochemistry: The molecular basis of cell structure and function (lehninger, albert l.)," *Journal of Chemical Education*, vol. 48, no. 4, p. A288, 1971.

[57] L. Stryer, *Biochemistry.* New York : W.H. Freeman, 1988.

[58] E. T. Burton, *Molecular Biology: Genes to Proteins.* Jones and Bartlett Learning, 2011.

[59] J. D. Watson and F. H. Crick, "Molecular structure of nucleic acids; a structure for deoxyribose nucleic acid," *Nature*, vol. 171, no. 4356, pp. 737–8, 1953.

[60] M. W. Nirenberg and J. H. Matthaei, "The dependence of cell-free protein synthesis in e. coli upon naturally occurring or synthetic polyribonucleotides," *Proc Natl Acad Sci U S A*, vol. 47, pp. 1588–602, 1961.

[61] F. H. Crick, *What Mad Pursuit: A Personal View of Scientific Discovery.* Basic Books, 1990.

[62] J. J. Shu, "A new integrated symmetrical table for genetic codes," *Biosystems*, vol. 151, pp. 21–26, 2017.

[63] R. Wing, H. Drew, T. Takano, C. Broka, S. Tanaka, K. Itakura, and R. E. Dickerson, "Crystal structure analysis of a complete turn of b-dna," *Nature*, vol. 287, no. 5784, pp. 755–8, 1980.

[64] D. Rhodes and A. Klug, "Helical periodicity of dna determined by enzyme digestion," *Nature*, vol. 286, no. 5773, pp. 573–8, 1980.

[65] C. O. Pabo and R. T. Sauer, "Protein-dna recognition," *Annu Rev Biochem*, vol. 53, pp. 293–321, 1984.

[66] P. Nelson, *Biological Physics: Energy, Information, Life.* Freeman and Co, 2004.

[67] C. Bustamante, J. F. Marko, E. D. Siggia, and S. Smith, "Entropic elasticity of lambda-phage dna," *Science*, vol. 265, no. 5178, pp. 1599–600, 1994.

[68] J. F. Marko and E. D. Siggia, "Stretching dna," *Macromolecules*, vol. 28, no. 26, pp. 8759–8770, 1995.

[69] J. A. Abels, F. Moreno-Herrero, T. van der Heijden, C. Dekker, and N. H. Dekker, "Single-molecule measurements of the persistence length of double-stranded rna," *Biophys J*, vol. 88, no. 4, pp. 2737–44, 2005.

[70] J. R. Wenner, M. C. Williams, I. Rouzina, and V. A. Bloomfield, "Salt dependence of the elasticity and overstretching transition of single dna molecules," *Biophysical Journal*, vol. 82, no. 6, pp. 3160–3169, 2002.

[71] C. G. Baumann, S. B. Smith, V. A. Bloomfield, and C. Bustamante, "Ionic effects on the elasticity of single dna molecules," *Proc Natl Acad Sci U S A*, vol. 94, no. 12, pp. 6185–90, 1997.

[72] C. Bouchiat, M. D. Wang, J. Allemand, T. Strick, S. M. Block, and V. Croquette, "Estimating the persistence length of a worm-like chain molecule from force-extension measurements," *Biophys J*, vol. 76, no. 1 Pt 1, pp. 409–13, 1999.

[73] E. Herrero-Galan, M. E. Fuentes-Perez, C. Carrasco, J. M. Valpuesta, J. L. Carrascosa, F. Moreno-Herrero, and J. R. Arias-Gonzalez, "Mechanical identities of rna and dna double helices unveiled at the single-molecule level," *J Am Chem Soc*, vol. 135, no. 1, pp. 122–31, 2013.

[74] T. Odijk, "Polyelectrolytes near the rod limit," *Journal of Polymer Science: Polymer Physics Edition*, vol. 15, no. 3, pp. 477–483, 1977.

[75] J. Skolnick and M. Fixman, "Electrostatic persistence length of a wormlike polyelectrolyte," *Macromolecules*, vol. 10, no. 5, pp. 944–948, 1977.

[76] M. Stroeck, "Dna overview (*https : //de.wikipedia.org/wiki/datei : dna_overview.png*)," *Wikimedia Foundation Inc. (GFDL License)*, 2006.

[77] T. Odijk, "Stiff chains and filaments under tension," *Macromolecules*, vol. 28, no. 20, pp. 7016–7018, 1995.

[78] S. B. Smith, Y. Cui, and C. Bustamante, "Overstretching b-dna: the elastic response of individual double-stranded and single-stranded dna molecules," *Science*, vol. 271, no. 5250, pp. 795–9, 1996.

[79] J. D. Moroz and P. Nelson, "Torsional directed walks, entropic elasticity, and dna twist stiffness," *Proc Natl Acad Sci U S A*, vol. 94, no. 26, pp. 14418–22, 1997.

[80] J. D. Moroz and P. Nelson, "Entropic elasticity of twist-storing polymers," *Macromolecules*, vol. 31, no. 18, pp. 6333–6347, 1998.

[81] T. Lepage, F. Képès, and I. Junier, "Thermodynamics of long supercoiled molecules: Insights from highly efficient monte carlo simulations," *Biophysical Journal*, vol. 109, no. 1, pp. 135–143, 2015.

[82] J. M. Schurr, "A possible cooperative structural transition of dna in the 0.25–2.0 pn range," *The Journal of Physical Chemistry B*, vol. 119, no. 21, pp. 6389–6400, 2015.

[83] R. S. Mathew-Fenn, R. Das, and P. A. B. Harbury, "Remeasuring the double helix," *Science*, vol. 322, no. 5900, pp. 446–449, 2008.

[84] R. D. Kamien, T. C. Lubensky, P. Nelson, and C. S. O. Hern, "Direct determination of dna twist-stretch coupling," *EPL (Europhysics Letters)*, vol. 38, no. 3, p. 237, 1997.

[85] J. F. Marko, "Stretching must twist dna," *EPL (Europhysics Letters)*, vol. 38, no. 3, p. 183, 1997.

[86] J. Gore, Z. Bryant, M. Nollmann, M. U. Le, N. R. Cozzarelli, and C. Bustamante, "Dna overwinds when stretched," *Nature*, vol. 442, no. 7104, pp. 836–9, 2006.

[87] T. Lionnet, S. Joubaud, R. Lavery, D. Bensimon, and V. Croquette, "Wringing out dna," *Phys Rev Lett*, vol. 96, no. 17, p. 178102, 2006.

[88] K. Olsen and J. Bohr, "The geometrical origin of the strain-twist coupling in double helices," *AIP Advances*, vol. 1, no. 1, p. 012108, 2011.

[89] F. C. Chou, J. Lipfert, and R. Das, "Blind predictions of dna and rna tweezers experiments with force and torque," *PLoS Comput Biol*, vol. 10, no. 8, p. e1003756, 2014.

[90] C. Matek, T. E. Ouldridge, J. P. Doye, and A. A. Louis, "Plectoneme tip bubbles: coupled denaturation and writhing in supercoiled dna," *Sci Rep*, vol. 5, p. 7655, 2015.

[91] C. Matek, P. Sulc, F. Randisi, J. P. Doye, and A. A. Louis, "Coarse-grained modelling of supercoiled rna," *J Chem Phys*, vol. 143, no. 24, p. 243122, 2015.

[92] K. Liebl, T. Drsata, F. Lankas, J. Lipfert, and M. Zacharias, "Explaining the striking difference in twist-stretch coupling between dna and rna: A comparative molecular dynamics analysis," *Nucleic Acids Research*, vol. 43, no. 21, pp. 10143–10156, 2015.

[93] S. K. Nomidis, F. Kriegel, W. Vanderlinden, J. Lipfert, and E. Carlon, "Twist-bend coupling and the torsional response of double-stranded dna," *Phys Rev Lett*, vol. 118, no. 21, p. 217801, 2017.

[94] P. Cluzel, A. Lebrun, C. Heller, R. Lavery, J. L. Viovy, D. Chatenay, and F. Caron, "Dna: an extensible molecule," *Science*, vol. 271, no. 5250, pp. 792–4, 1996.

[95] J. van Mameren, P. Gross, G. Farge, P. Hooijman, M. Modesti, M. Falkenberg, G. J. Wuite, and E. J. Peterman, "Unraveling the structure of dna during overstretching by using multicolor, single-molecule fluorescence imaging," *Proc Natl Acad Sci U S A*, vol. 106, no. 43, pp. 18231–6, 2009.

[96] D. H. Paik and T. T. Perkins, "Overstretching dna at 65 pn does not require peeling from free ends or nicks," *J Am Chem Soc*, vol. 133, no. 10, pp. 3219–21, 2011.

[97] M. C. Williams, J. R. Wenner, I. Rouzina, and V. A. Bloomfield, "Effect of ph on the overstretching transition of double-stranded dna: evidence of force-induced dna melting," *Biophys J*, vol. 80, no. 2, pp. 874–81, 2001.

[98] M. Rief, H. Clausen-Schaumann, and H. E. Gaub, "Sequence-dependent mechanics of single dna molecules," *Nat Struct Biol*, vol. 6, no. 4, pp. 346–9, 1999.

[99] M. C. Williams, J. R. Wenner, I. Rouzina, and V. A. Bloomfield, "Entropy and heat capacity of dna melting from temperature dependence of single molecule stretching," *Biophys J*, vol. 80, no. 4, pp. 1932–9, 2001.

[100] J. Wereszczynski and I. Andricioaei, "On structural transitions, thermodynamic equilibrium, and the phase diagram of dna and rna duplexes under torque and tension," *Proc Natl Acad Sci U S A*, vol. 103, no. 44, pp. 16200–5, 2006.

[101] J. F. Léger, G. Romano, A. Sarkar, J. Robert, L. Bourdieu, D. Chatenay, and J. F. Marko, "Structural transitions of a twisted and stretched dna molecule," *Physical Review Letters*, vol. 83, no. 5, pp. 1066–1069, 1999.

[102] A. Sarkar, J. F. Leger, D. Chatenay, and J. F. Marko, "Structural transitions in dna driven by external force and torque," *Phys Rev E Stat Nonlin Soft Matter Phys*, vol. 63, no. 5 Pt 1, p. 051903, 2001.

[103] G. A. King, P. Gross, U. Bockelmann, M. Modesti, G. J. Wuite, and E. J. Peterman, "Revealing the competition between peeled ssdna, melting bubbles, and s-dna during dna overstretching using fluorescence microscopy," *Proc Natl Acad Sci U S A*, vol. 110, no. 10, pp. 3859–64, 2013.

[104] X. Zhang, H. Chen, H. Fu, P. S. Doyle, and J. Yan, "Two distinct overstretched dna structures revealed by single-molecule thermodynamics measurements," *Proc Natl Acad Sci U S A*, vol. 109, no. 21, pp. 8103–8, 2012.

[105] N. Bosaeus, A. H. El-Sagheer, T. Brown, S. B. Smith, B. Akerman, C. Bustamante, and B. Norden, "Tension induces a base-paired overstretched dna conformation," *Proc Natl Acad Sci U S A*, vol. 109, no. 38, pp. 15179–84, 2012.

[106] R. Schopflin, H. Brutzer, O. Muller, R. Seidel, and G. Wedemann, "Probing the elasticity of dna on short length scales by modeling supercoiling under tension," *Biophys J*, vol. 103, no. 2, pp. 323–30, 2012.

[107] J. F. Marko, "Torque and dynamics of linking number relaxation in stretched supercoiled dna," *Phys Rev E Stat Nonlin Soft Matter Phys*, vol. 76, no. 2 Pt 1, p. 021926, 2007.

[108] T. Strick, J. Allemand, V. Croquette, and D. Bensimon, "Twisting and stretching single dna molecules," *Prog Biophys Mol Biol*, vol. 74, no. 1-2, pp. 115–40, 2000.

[109] E. A. Galburt, E. J. Tomko, W. T. Stump, and A. Ruiz Manzano, "Force-dependent melting of supercoiled dna at thermophilic temperatures," *Biophys Chem*, vol. 187-188, pp. 23–8, 2014.

[110] D. Salerno, A. Tempestini, I. Mai, D. Brogioli, R. Ziano, V. Cassina, and F. Mantegazza, "Single-molecule study of the dna denaturation phase transition in the force-torsion space," *Phys Rev Lett*, vol. 109, no. 11, p. 118303, 2012.

[111] A. Tempestini, V. Cassina, D. Brogioli, R. Ziano, S. Erba, R. Giovannoni, M. G. Cerrito, D. Salerno, and F. Mantegazza, "Magnetic tweezers measurements of the nanomechanical stability of dna against denaturation at various conditions of ph and ionic strength," *Nucleic Acids Res*, vol. 41, no. 3, pp. 2009–19, 2013.

[112] M. Y. Sheinin, S. Forth, J. F. Marko, and M. D. Wang, "Underwound dna under tension: structure, elasticity, and sequence-dependent behaviors," *Phys Rev Lett*, vol. 107, no. 10, p. 108102, 2011.

[113] M. Lee, S. H. Kim, and S. C. Hong, "Minute negative superhelicity is sufficient to induce the b-z transition in the presence of low tension," *Proc Natl Acad Sci U S A*, vol. 107, no. 11, pp. 4985–90, 2010.

[114] F. C. Oberstrass, L. E. Fernandes, P. Lebel, and Z. Bryant, "Torque spectroscopy of dna: base-pair stability, boundary effects, backbending, and breathing dynamics," *Phys Rev Lett*, vol. 110, no. 17, p. 178103, 2013.

[115] S. Forth, M. Y. Sheinin, J. Inman, and M. D. Wang, "Torque measurement at the single-molecule level," *Annu Rev Biophys*, vol. 42, pp. 583–604, 2013.

[116] M. Y. Sheinin and M. D. Wang, "Twist-stretch coupling and phase transition during dna supercoiling," *Phys Chem Chem Phys*, vol. 11, no. 24, pp. 4800–3, 2009.

[117] J. F. Marko and S. Neukirch, "Global force-torque phase diagram for the dna double helix: structural transitions, triple points, and collapsed plectonemes," *Phys Rev E Stat Nonlin Soft Matter Phys*, vol. 88, no. 6, p. 062722, 2013.

[118] C. Maffeo, R. Schopflin, H. Brutzer, R. Stehr, A. Aksimentiev, G. Wedemann, and R. Seidel, "Dna-dna interactions in tight supercoils are described by a small effective charge density," *Phys Rev Lett*, vol. 105, no. 15, p. 158101, 2010.

[119] J. F. Marko and S. Neukirch, "Competition between curls and plectonemes near the buckling transition of stretched supercoiled dna," *Phys Rev E Stat Nonlin Soft Matter Phys*, vol. 85, no. 1 Pt 1, p. 011908, 2012.

[120] M. T. J. van Loenhout, M. V. de Grunt, and C. Dekker, "Dynamics of dna supercoils," *Science*, vol. 338, no. 6103, pp. 94–97, 2012.

[121] J. C. Lee and R. R. Gutell, "Diversity of base-pair conformations and their occurrence in rrna structure and rna structural motifs," *J Mol Biol*, vol. 344, no. 5, pp. 1225–49, 2004.

[122] P. Taylor, F. Rixon, and U. Desselberger, "Rise per base pair in helices of double-stranded rotavirus rna determined by electron microscopy," *Virus Res*, vol. 2, no. 2, pp. 175–82, 1985.

[123] J. M. Berg, J. L. Tymoczka, and L. Stryer, *Biochemistry.* WH Freeman, 8 ed., 2015.

[124] H. Lodish, A. Berk, and P. Matsudaira, *Molecular Cell Biology.* Palgrave Macmilian, 5 ed., 2004.

[125] B. Alberts, A. Johnson, J. Lewis, M. Raff, K. Roberts, and P. Walter, *Moleular Biology of the Cell.* Garland Science, 4 ed., 2002.

[126] G. N. Ramachandran, C. Ramakrishnan, and V. Sasisekharan, "Stereochemistry of polypeptide chain configurations," *J Mol Biol*, vol. 7, pp. 95–9, 1963.

[127] J. S. Richardson, "The anatomy and taxonomy of protein structure," *Adv Protein Chem*, vol. 34, pp. 167–339, 1981.

[128] T. Shafee, "Protein structure (full).png (*https : //commons.wikimedia.org/wiki/file : protein_structure_(full).png*)," *Wikimedia Foundation Inc. (GFDL License)*, 2016.

[129] C. Levinthal, "How to fold graciously," in *Mossbauer Spectroscopy in Biological Systems: Proceedings of a meeting held at Allerton House, Monticello, Illinois* (J. T. P. Debrunnder and E. Munck, eds.), pp. 22–24, University of Illinois Press.

[130] J. Kubelka, J. Hofrichter, and W. A. Eaton, "The protein folding 'speed limit'," *Curr. Opin. Struct. Biol.*, vol. 14, no. 1, pp. 76–88, 2004.

[131] A. N. Naganathan and V. Muñoz, "Scaling of folding times with protein size," *Journal of the American Chemical Society*, vol. 127, no. 2, pp. 480–481, 2005.

[132] R. L. Baldwin and G. D. Rose, "Is protein folding hierarchic? ii. folding intermediates and transition states," *Trends Biochem Sci*, vol. 24, no. 2, pp. 77–83, 1999.

[133] S. Enoki, K. Saeki, K. Maki, and K. Kuwajima, "Acid denaturation and refolding of green fluorescent protein," *Biochemistry*, vol. 43, no. 44, pp. 14238–48, 2004.

[134] M. Mickler, R. I. Dima, H. Dietz, C. Hyeon, D. Thirumalai, and M. Rief, "Revealing the bifurcation in the unfolding pathways of gfp by using single-molecule experiments and simulations," *Proc Natl Acad Sci U S A*, vol. 104, no. 51, pp. 20268–73, 2007.

[135] F. Oesterhelt, D. Oesterhelt, M. Pfeiffer, A. Engel, H. E. Gaub, and D. J. Muller, "Unfolding pathways of individual bacteriorhodopsins," *Science*, vol. 288, no. 5463, pp. 143–6, 2000.

[136] H. Dietz and M. Rief, "Exploring the energy landscape of gfp by single-molecule mechanical experiments," *Proc Natl Acad Sci U S A*, vol. 101, no. 46, pp. 16192–7, 2004.

[137] E. Evans and K. Ritchie, "Dynamic strength of molecular adhesion bonds," *Biophysical Journal*, vol. 72, no. 4, pp. 1541–1555, 1997.

[138] G. I. Bell, "Models for the specific adhesion of cells to cells," *Science*, vol. 200, no. 4342, pp. 618–27, 1978.

[139] V. Vogel, "Mechanotransduction involving multimodular proteins: converting force into biochemical signals," *Annu Rev Biophys Biomol Struct*, vol. 35, pp. 459–88, 2006.

[140] E. M. Puchner, A. Alexandrovich, A. L. Kho, U. Hensen, L. V. Schafer, B. Brandmeier, F. Grater, H. Grubmuller, H. E. Gaub, and M. Gautel, "Mechanoenzymatics of titin kinase," *Proc Natl Acad Sci U S A*, vol. 105, no. 36, pp. 13385–90, 2008.

[141] A. del Rio, R. Perez-Jimenez, R. Liu, P. Roca-Cusachs, J. M. Fernandez, and M. P. Sheetz, "Stretching single talin rod molecules activates vinculin binding," *Science*, vol. 323, no. 5914, pp. 638–641, 2009.

[142] S. Labeit and B. Kolmerer, "Titins: giant proteins in charge of muscle ultrastructure and elasticity," *Science*, vol. 270, no. 5234, pp. 293–6, 1995.

[143] A. Minajeva, M. Kulke, J. M. Fernandez, and W. A. Linke, "Unfolding of titin domains explains the viscoelastic behavior of skeletal myofibrils," *Biophys J*, vol. 80, no. 3, pp. 1442–51, 2001.

[144] E. H. Lee, J. Hsin, E. von Castelmur, O. Mayans, and K. Schulten, "Tertiary and secondary structure elasticity of a six-ig titin chain," *Biophys J*, vol. 98, no. 6, pp. 1085–95, 2010.

[145] E. M. Puchner and H. E. Gaub, "Exploring the conformation-regulated function of titin kinase by mechanical pump and probe experiments with single molecules," *Angew Chem Int Ed Engl*, vol. 49, no. 6, pp. 1147–50, 2010.

[146] M. Rief, M. Gautel, F. Oesterhelt, J. M. Fernandez, and H. E. Gaub, "Reversible unfolding of individual titin immunoglobulin domains by afm," *Science*, vol. 276, no. 5315, pp. 1109–12, 1997.

[147] L. Tskhovrebova, J. Trinick, J. A. Sleep, and R. M. Simmons, "Elasticity and unfolding of single molecules of the giant muscle protein titin," *Nature*, vol. 387, no. 6630, pp. 308–12, 1997.

[148] T. P. Stossel, J. Condeelis, L. Cooley, J. H. Hartwig, A. Noegel, M. Schleicher, and S. S. Shapiro, "Filamins as integrators of cell mechanics and signalling," *Nat Rev Mol Cell Biol*, vol. 2, no. 2, pp. 138–45, 2001.

[149] I. Schwaiger, M. Schleicher, A. A. Noegel, and M. Rief, "The folding pathway of a fast-folding immunoglobulin domain revealed by single-molecule mechanical experiments," *EMBO Rep*, vol. 6, no. 1, pp. 46–51, 2005.

[150] P. Fucini, C. Renner, C. Herberhold, A. A. Noegel, and T. A. Holak, "The repeating segments of the f-actin cross-linking gelation factor (abp-120) have an immunoglobulin-like fold," *Nat Struct Biol*, vol. 4, no. 3, pp. 223–30, 1997.

[151] J. E. Sadler, "Biochemistry and genetics of von willebrand factor," *Annu Rev Biochem*, vol. 67, pp. 395–424, 1998.

[152] J. P. Muller, S. Mielke, A. Lof, T. Obser, C. Beer, L. K. Bruetzel, D. A. Pippig, W. Vanderlinden, J. Lipfert, R. Schneppenheim, and M. Benoit, "Force sensing by the vascular protein von willebrand factor is tuned by a strong intermonomer interaction," *Proc Natl Acad Sci U S A*, vol. 113, no. 5, pp. 1208–13, 2016.

[153] Z. M. Ruggeri, "von willebrand factor," *J Clin Invest*, vol. 99, no. 4, pp. 559–64, 1997.

[154] S. W. Schneider, S. Nuschele, A. Wixforth, C. Gorzelanny, A. Alexander-Katz, R. R. Netz, and M. F. Schneider, "Shear-induced unfolding triggers adhesion of von willebrand factor fibers," *Proceedings of the National Academy of Sciences*, vol. 104, no. 19, pp. 7899–7903, 2007.

[155] T. A. Springer, "von willebrand factor, jedi knight of the bloodstream," *Blood*, vol. 124, no. 9, pp. 1412–25, 2014.

[156] A. J. Xu and T. A. Springer, "Calcium stabilizes the von willebrand factor a2 domain by promoting refolding," *Proc Natl Acad Sci U S A*, vol. 109, no. 10, pp. 3742–7, 2012.

[157] X. Zhang, K. Halvorsen, C. Z. Zhang, W. P. Wong, and T. A. Springer, "Mechanoenzymatic cleavage of the ultralarge vascular protein von willebrand factor," *Science*, vol. 324, no. 5932, pp. 1330–4, 2009.

[158] E. Šišáková, M. Weiserová, C. Dekker, R. Seidel, and M. D. Szczelkun, "The interrelationship of helicase and nuclease domains during dna translocation by the molecular motor ecor124i," *Journal of Molecular Biology*, vol. 384, no. 5, pp. 1273–1286, 2008.

[159] M. Rutkauskas, T. Sinkunas, I. Songailiene, M. S. Tikhomirova, V. Siksnys, and R. Seidel, "Directional r-loop formation by the crispr-cas surveillance complex cascade provides efficient off-target site rejection," *Cell Reports*, vol. 10, no. 9, pp. 1534–1543, 2015.

[160] Y. Harada, O. Ohara, A. Takatsuki, H. Itoh, N. Shimamoto, and J. Kinosita, K., "Direct observation of dna rotation during transcription by escherichia coli rna polymerase," *Nature*, vol. 409, no. 6816, pp. 113–5, 2001.

[161] D. Dulin, B. A. Berghuis, M. Depken, and N. H. Dekker, "Untangling reaction pathways through modern approaches to high-throughput single-molecule force-spectroscopy experiments," *Curr Opin Struct Biol*, vol. 34, pp. 116–22, 2015.

[162] M. Manosas, A. Meglio, M. M. Spiering, F. Ding, S. J. Benkovic, F. X. Barre, O. A. Saleh, J. F. Allemand, D. Bensimon, and V. Croquette, "Magnetic tweezers for the study of dna tracking motors," *Methods Enzymol*, vol. 475, pp. 297–320, 2010.

[163] Q. Guo, Y. He, and H. P. Lu, "Interrogating the activities of conformational deformed enzyme by single-molecule fluorescence-magnetic tweezers microscopy," *Proc Natl Acad Sci U S A*, vol. 112, no. 45, pp. 13904–9, 2015.

[164] E. Drexler, *Engines of Creation: The Coming Era of Nanotechnology*. United States: Doubleday, 1986.

[165] E. Drexler, *Nanosystems: Molecular Machinery, Manufacturing, and Computation*. UK: J. Wiley and Sons, 1992.

[166] P. Rodgers, "Nanoelectronics: Single file," *Nature Nanotechnology*, 2006.

[167] S. Kralj and D. Makovec, "Magnetic assembly of superparamagnetic iron oxide nanoparticle clusters into nanochains and nanobundles," *ACS Nano*, vol. 9, no. 10, pp. 9700–9707, 2015.

[168] A. Belkin, A. Hubler, and A. Bezryadin, "Self-assembled wiggling nano-structures and the principle of maximum entropy production," *Scientific Reports*, vol. 5, p. 8323, 2015.

[169] N. C. Seeman, "Nucleic acid junctions and lattices," *Journal of Theoretical Biology*, vol. 99, no. 2, pp. 237–247, 1982.

[170] J. Chen and N. C. Seeman, "Synthesis from dna of a molecule with the connectivity of a cube," *Nature*, vol. 350, p. 631, 1991.

[171] Y. Zhang and N. C. Seeman, "Construction of a dna-truncated octahedron," *Journal of the American Chemical Society*, vol. 116, no. 5, pp. 1661–1669, 1994.

[172] P. W. Rothemund, "Folding dna to create nanoscale shapes and patterns," *Nature*, vol. 440, no. 7082, pp. 297–302, 2006.

[173] S. Kocabey, S. Kempter, J. List, Y. Xing, W. Bae, D. Schiffels, W. M. Shih, F. C. Simmel, and T. Liedl, "Membrane-assisted growth of dna origami nanostructure arrays," *ACS Nano*, vol. 9, no. 4, pp. 3530–3539, 2015.

[174] J. J. Funke and H. Dietz, "Placing molecules with bohr radius resolution using dna origami," *Nat Nanotechnol*, vol. 11, no. 1, pp. 47–52, 2016.

[175] T. Gerling, K. F. Wagenbauer, A. M. Neuner, and H. Dietz, "Dynamic dna devices and assemblies formed by shape-complementary, non-base pairing 3d components," *Science*, vol. 347, no. 6229, pp. 1446–52, 2015.

[176] K. F. Wagenbauer, C. Sigl, and H. Dietz, "Gigadalton-scale shape-programmable dna assemblies," *Nature*, vol. 552, no. 7683, pp. 78–83, 2017.

[177] Y. Tian, T. Wang, W. Liu, H. L. Xin, H. Li, Y. Ke, W. M. Shih, and O. Gang, "Prescribed nanoparticle cluster architectures and low-dimensional arrays built using octahedral dna origami frames," *Nature Nanotechnology*, vol. 10, p. 637, 2015.

[178] P. Wang, T. A. Meyer, V. Pan, P. K. Dutta, and Y. Ke, "The beauty and utility of dna origami," *Chem*, vol. 2, no. 3, pp. 359–382, 2017.

[179] R. Holliday, "A mechanism for gene conversion in fungi," *Genet Res*, vol. 89, no. 5-6, pp. 285–307, 1964.

[180] N. R. Kallenbach, R.-I. Ma, and N. C. Seeman, "An immobile nucleic acid junction constructed from oligonucleotides," *Nature*, vol. 305, p. 829, 1983.

[181] J. P. Sobczak, T. G. Martin, T. Gerling, and H. Dietz, "Rapid folding of dna into nanoscale shapes at constant temperature," *Science*, vol. 338, no. 6113, pp. 1458–61, 2012.

[182] K. F. Wagenbauer, F. A. S. Engelhardt, E. Stahl, V. K. Hechtl, P. Stommer, F. Seebacher, L. Meregalli, P. Ketterer, T. Gerling, and H. Dietz, "How we make dna origami," *Chembiochem*, vol. 18, no. 19, pp. 1873–1885, 2017.

[183] E. Stahl, T. G. Martin, F. Praetorius, and H. Dietz, "Facile and scalable preparation of pure and dense dna origami solutions," *Angew. Chem., Int. Ed. Engl.*, vol. 53, no. 47, pp. 12735–40, 2014.

[184] T. G. Martin and H. Dietz, "Magnesium-free self-assembly of multi-layer dna objects," *Nat Commun*, vol. 3, p. 1103, 2012.

[185] S. M. Douglas, H. Dietz, T. Liedl, B. Hogberg, F. Graf, and W. M. Shih, "Self-assembly of dna into nanoscale three-dimensional shapes," *Nature*, vol. 459, no. 7245, pp. 414–8, 2009.

[186] Y. Ke, L. L. Ong, W. M. Shih, and P. Yin, "Three-dimensional structures self-assembled from dna bricks," *Science*, vol. 338, no. 6111, pp. 1177–1183, 2012.

[187] P. Ketterer, E. M. Willner, and H. Dietz, "Nanoscale rotary apparatus formed from tight-fitting 3d dna components," *Science Advances*, vol. 2, no. 2, 2016.

[188] J. J. Schmied, A. Gietl, P. Holzmeister, C. Forthmann, C. Steinhauer, T. Dammeyer, and P. Tinnefeld, "Fluorescence and super-resolution standards based on dna origami," *Nat. Methods*, vol. 9, no. 12, pp. 1133–4, 2012.

[189] G. Bellot, M. A. McClintock, J. J. Chou, and W. M. Shih, "Dna nanotubes for nmr structure determination of membrane proteins," *Nature Protocols*, vol. 8, p. 755, 2013.

[190] N. A. Bell and U. F. Keyser, "Nanopores formed by dna origami: a review," *FEBS Lett*, vol. 588, no. 19, pp. 3564–70, 2014.

[191] R. Schreiber, J. Do, E.-M. Roller, T. Zhang, V. J Schüller, P. Nickels, J. Feldmann, and T. Liedl, *Hierarchical assembly of metal nanoparticles, quantum dots and organic dyes using DNA origami scaffolds*, vol. 9. 2013.

[192] A. Kuzyk, R. Schreiber, Z. Fan, G. Pardatscher, E.-M. Roller, A. Högele, F. C. Simmel, A. O. Govorov, and T. Liedl, "Dna-based self-assembly of chiral plasmonic nanostructures with tailored optical response," *Nature*, vol. 483, p. 311, 2012.

[193] N. Ponnuswamy, M. M. C. Bastings, B. Nathwani, J. H. Ryu, L. Y. T. Chou, M. Vinther, W. A. Li, F. M. Anastassacos, D. J. Mooney, and W. M. Shih, "Oligolysine-based coating protects dna nanostructures from low-salt denaturation and nuclease degradation," *Nat. Commun.*, vol. 8, p. 15654, 2017.

[194] S. D. Perrault and W. M. Shih, "Virus-inspired membrane encapsulation of dna nanostructures to achieve in vivo stability," *ACS Nano*, vol. 8, no. 5, pp. 5132–40, 2014.

[195] F. Praetorius and H. Dietz, "Self-assembly of genetically encoded dna-protein hybrid nanoscale shapes," *Science*, vol. 355, no. 6331, 2017.

[196] A. Kuzyk, K. T. Laitinen, and P. Torma, "Dna origami as a nanoscale template for protein assembly," *Nanotechnology*, vol. 20, no. 23, p. 235305, 2009.

[197] S. M. Douglas, A. H. Marblestone, S. Teerapittayanon, A. Vazquez, G. M. Church, and W. M. Shih, "Rapid prototyping of 3d dna-origami shapes with cadnano," *Nucleic Acids Res.*, vol. 37, no. 15, pp. 5001–6, 2009.

[198] R. Iinuma, Y. Ke, R. Jungmann, T. Schlichthaerle, J. B. Woehrstein, and P. Yin, "Polyhedra self-assembled from dna tripods and characterized with 3d dna-paint," *Science*, vol. 344, no. 6179, pp. 65–69, 2014.

[199] H. Dietz, S. M. Douglas, and W. M. Shih, "Folding dna into twisted and curved nanoscale shapes," *Science*, vol. 325, no. 5941, pp. 725–30, 2009.

[200] A. Udomprasert and T. Kangsamaksin, "Dna origami applications in cancer therapy," *Cancer Science*, vol. 108, no. 8, pp. 1535–1543, 2017.

[201] D. Y. Zhang and G. Seelig, "Dynamic dna nanotechnology using strand-displacement reactions," *Nat. Chem.*, vol. 3, no. 2, pp. 103–13, 2011.

[202] B. Yurke, A. J. Turberfield, J. Mills, A. P., F. C. Simmel, and J. L. Neumann, "A dna-fuelled molecular machine made of dna," *Nature*, vol. 406, no. 6796, pp. 605–8, 2000.

[203] S. M. Douglas, I. Bachelet, and G. M. Church, "A logic-gated nanorobot for targeted transport of molecular payloads," *Science*, vol. 335, no. 6070, pp. 831–4, 2012.

[204] E. S. Andersen, M. Dong, M. M. Nielsen, K. Jahn, R. Subramani, W. Mamdouh, M. M. Golas, B. Sander, H. Stark, C. L. Oliveira, J. S. Pedersen, V. Birkedal, F. Besenbacher, K. V. Gothelf, and J. Kjems, "Self-assembly of a nanoscale dna box with a controllable lid," *Nature*, vol. 459, no. 7243, pp. 73–6, 2009.

[205] K. Gehring, J. L. Leroy, and M. Gueron, "A tetrameric dna structure with protonated cytosine.cytosine base pairs," *Nature*, vol. 363, no. 6429, pp. 561–5, 1993.

[206] R. Campos, S. Zhang, J. Majikes, L. C.C. Ferraz, T. Labean, M. Dong, and E. E Ferapontova, *Electronically Addressable Nanomechanical Switching of i-Motif DNA Origami Assembled on Basal Plane HOPG*, vol. 51. 2015.

[207] A. Rajendran, M. Endo, K. Hidaka, and H. Sugiyama, "Direct and real-time observation of rotary movement of a dna nanomechanical device," *J. Am. Chem. Soc.*, vol. 135, no. 3, pp. 1117–23, 2013.

[208] Y. Kamiya and H. Asanuma, "Light-driven dna nanomachine with a photoresponsive molecular engine," *Acc Chem Res*, vol. 47, no. 6, pp. 1663–72, 2014.

[209] A. Kuzyk, Y. Yang, X. Duan, S. Stoll, A. O. Govorov, H. Sugiyama, M. Endo, and N. Liu, "A light-driven three-dimensional plasmonic nanosystem that translates molecular motion into reversible chiroptical function," *Nat. Commun.*, vol. 7, p. 10591, 2016.

[210] S. M. Reilly, D. F. Lyons, S. E. Wingate, R. T. Wright, J. J. Correia, D. M. Jameson, and R. M. Wadkins, "Folding and hydrodynamics of a dna i-motif from the c-myc promoter determined by fluorescent cytidine analogs," *Biophys J*, vol. 107, no. 7, pp. 1703–11, 2014.

[211] M. Moradi, V. Babin, C. Roland, and C. Sagui, "Reaction path ensemble of the b-z-dna transition: a comprehensive atomistic study," *Nucleic Acids Res*, vol. 41, no. 1, pp. 33–43, 2013.

[212] C. Huang and C. G. Kalodimos, "Structures of large protein complexes determined by nuclear magnetic resonance spectroscopy," *Annu Rev Biophys*, vol. 46, pp. 317–336, 2017.

[213] G. Zanotti, *Cryo-EM and X-Ray Crystallography: Complementary or Alternative Techniques?*, vol. 2. NanoWorld Journal, 2016.

[214] M. Pfreundschuh, D. Martinez-Martin, E. Mulvihill, S. Wegmann, and D. J. Muller, "Multiparametric high-resolution imaging of native proteins by force-distance curve-based afm," *Nat Protoc*, vol. 9, no. 5, pp. 1113–30, 2014.

[215] C. D. Putnam, M. Hammel, G. L. Hura, and J. A. Tainer, "X-ray solution scattering (saxs) combined with crystallography and computation: defining accurate macromolecular structures, conformations and assemblies in solution," *Q Rev Biophys*, vol. 40, no. 3, pp. 191–285, 2007.

[216] C. K. Kennaway, J. E. Taylor, C. F. Song, W. Potrzebowski, W. Nicholson, J. H. White, A. Swiderska, A. Obarska-Kosinska, P. Callow, L. P. Cooper, G. A. Roberts, J. B. Artero, J. M. Bujnicki, J. Trinick, G. G. Kneale, and D. T. F. Dryden, "Structure and operation of the dna-translocating type i dna restriction enzymes," *Genes Dev*, vol. 26, no. 1, pp. 92–104, 2012.

[217] I. Svergun, Dmitri and M. H. J. Koch, "Small-angle scattering studies of biological macromolecules in solution," *Reports on Progress in Physics*, vol. 66, no. 10, p. 1735, 2003.

[218] L. K. Bruetzel, S. Fischer, A. Salditt, S. M. Sedlak, B. Nickel, and J. Lipfert, "A mo-anode-based in-house source for small-angle x-ray scattering measurements of biological macromolecules," *Rev Sci Instrum*, vol. 87, no. 2, p. 025103, 2016.

[219] S. V. Kathuria, L. Guo, R. Graceffa, R. Barrea, R. P. Nobrega, C. R. Matthews, T. Irving, and O. Bilsel, "Structural insights into early folding events using continuous-flow time-resolved saxs," *Biopolymers*, vol. 95, no. 8, pp. 550–558, 2011.

[220] J. AlsNielsen and D. McMorrow, *Elements of Modern X-ray Physics, Second Edition.* John Wiley and Sons, Ltd, 2011.

[221] "Saxs/asaxs," *Helmholtz Zentrum Berlin (https://www.helmholtz-berlin.de)*, 2018.

[222] B. D. Cullity, *X-ray Diffraction.* ADDISON-WESLEY PUBLISHING COMPANY, 1956.

[223] M. H. Koch, P. Vachette, and D. I. Svergun, "Small-angle scattering: a view on the properties, structures and structural changes of biological macromolecules in solution," *Q Rev Biophys*, vol. 36, no. 2, pp. 147–227, 2003.

[224] D. Svergun, M. Koch, P. Timmins, and R. May, *Small Angle X-Ray and Neutron Scattering from Solutions of Biological Macromolecules.* Iucr Monographs on Crystallogr, 2013.

[225] S. Doniach, "Changes in biomolecular conformation seen by small angle x-ray scattering," *Chem Rev*, vol. 101, no. 6, pp. 1763–78, 2001.

[226] G. L. Hura, C.-L. Tsai, S. A. Claridge, M. L. Mendillo, J. M. Smith, G. J. Williams, A. J. Mastroianni, A. P. Alivisatos, C. D. Putnam, R. D. Kolodner, and J. A. Tainer, "Dna conformations in mismatch repair probed in solution by x-ray scattering from gold nanocrystals," *Proceedings of the National Academy of Sciences*, vol. 110, no. 43, pp. 17308–17313, 2013.

[227] V. M. Balcao and M. M. Vila, "Structural and functional stabilization of protein entities: state-of-the-art," *Adv Drug Deliv Rev*, vol. 93, pp. 25–41, 2015.

[228] C. M. Jeffries, M. A. Graewert, D. I. Svergun, and C. E. Blanchet, "Limiting radiation damage for high-brilliance biological solution scattering: practical experience at the embl p12 beamline petraiii," *J Synchrotron Radiat*, vol. 22, no. 2, pp. 273–9, 2015.

[229] S. Kuwamoto, S. Akiyama, and T. Fujisawa, "Radiation damage to a protein solution, detected by synchrotron x-ray small-angle scattering: dose-related considerations and suppression by cryoprotectants," *J Synchrotron Radiat*, vol. 11, no. Pt 6, pp. 462–8, 2004.

[230] J. Lipfert, D. Herschlag, and S. Doniach, "Riboswitch conformations revealed by small-angle x-ray scattering," *Methods Mol Biol*, vol. 540, pp. 141–59, 2009.

[231] J. B. Hopkins and R. E. Thorne, "Quantifying radiation damage in biomolecular small-angle x-ray scattering," *J Appl Crystallogr*, vol. 49, no. Pt 3, pp. 880–890, 2016.

[232] J. C. BrooksBartlett, R. A. Batters, C. S. Bury, E. D. Lowe, H. M. Ginn, A. Round, and E. F. Garman, "Development of tools to automate quantitative analysis of radiation damage in saxs experiments," *J Synchrotron Radiat*, vol. 24, no. Pt 1, pp. 63–72, 2017.

[233] V. Vagenende, M. G. Yap, and B. L. Trout, "Mechanisms of protein stabilization and prevention of protein aggregation by glycerol," *Biochemistry*, vol. 48, no. 46, pp. 11084–96, 2009.

[234] M. C. Alliegro, "Effects of dithiothreitol on protein activity unrelated to thiol-disulfide exchange: for consideration in the analysis of protein function with cleland's reagent," *Anal Biochem*, vol. 282, no. 1, pp. 102–6, 2000.

[235] D. Franke, C. M. Jeffries, and D. I. Svergun, "Correlation map, a goodness-of-fit test for one-dimensional x-ray scattering spectra," *Nat Methods*, vol. 12, no. 5, pp. 419–22, 2015.

[236] D. A. Jacques and J. Trewhella, "Small-angle scattering for structural biology–expanding the frontier while avoiding the pitfalls," *Protein Sci*, vol. 19, no. 4, pp. 642–57, 2010.

[237] X. Qiu, L. W. Kwok, H. Y. Park, J. S. Lamb, K. Andresen, and L. Pollack, "Measuring inter-dna potentials in solution," *Phys Rev Lett*, vol. 96, no. 13, p. 138101, 2006.

[238] A. Tardieu, A. Le Verge, M. Malfois, F. Bonneté, S. Finet, M. Riès-Kautt, and L. Belloni, "Proteins in solution:from x-ray scattering intensities to interaction potentials," *Journal of Crystal Growth*, vol. 196, no. 2, pp. 193–203, 1999.

[239] C. E. Blanchet and D. I. Svergun, "Small-angle x-ray scattering on biological macromolecules and nanocomposites in solution," *Annu Rev Phys Chem*, vol. 64, pp. 37–54, 2013.

[240] A. Guinier, *La diffraction des rayons X aux trés petits angles: application a l'étude de phénomènes ultramicroscopiques.* Paris: Annales de Physique, 1939.

[241] J. Lipfert and S. Doniach, "Small-angle x-ray scattering from rna, proteins, and protein complexes," *Annu. Rev. Biophys. Biomol. Struct.*, vol. 36, pp. 307–27, 2007.

[242] H. D. T. Mertens and D. I. Svergun, "Structural characterization of proteins and complexes using small-angle x-ray solution scattering," *Journal of Structural Biology*, vol. 172, no. 1, pp. 128–141, 2010.

[243] A. T. Tuukkanen and D. I. Svergun, "Weak protein-ligand interactions studied by small-angle x-ray scattering," *Febs j*, vol. 281, no. 8, pp. 1974–87, 2014.

[244] O. Glatter and O. Kratky, *Small Angle X-ray Scattering*. Academic Press, 1982.

[245] R. Russell, I. S. Millett, M. W. Tate, L. W. Kwok, B. Nakatani, S. M. Gruner, S. G. Mochrie, V. Pande, S. Doniach, D. Herschlag, and L. Pollack, "Rapid compaction during rna folding," *Proc Natl Acad Sci U S A*, vol. 99, no. 7, pp. 4266–71, 2002.

[246] L. K. Bruetzel, "Structure and conformational dynamics of 3d dna origami objects probed by small-angle x-ray scattering," *Ludwig-Maximilians Universitaet Muenchen*, 2017.

[247] O. Glatter, *A New Method for the Evaluation of Small-Angle Scattering Data*, vol. 10. Journal of Applied Crystallography, 1977.

[248] P. Moore, *Small-angle scattering. Information content and error analysis*, vol. 13. Journal of Applied Crystallography, 1980.

[249] D. Svergun, "Mathematical methods in small-angle scattering data analysis," *Journal of Applied Crystallography*, vol. 24, no. 5, pp. 485–492, 1991.

[250] C. M. Jeffries, M. A. Graewert, C. E. Blanchet, D. B. Langley, A. E. Whitten, and D. I. Svergun, "Preparing monodisperse macromolecular samples for successful biological small-angle x-ray and neutron-scattering experiments," *Nature Protocols*, vol. 11, p. 2122, 2016.

[251] D. I. Svergun, C. Barberato, and M. Koch, *CRYSOL– a Program to Evaluate X-ray Solution Scattering of Biological Macromolecules from Atomic Coordinates*, vol. 28. Journal of Applied Crystallography, 1995.

[252] D. I. Svergun, S. Richard, M. H. Koch, Z. Sayers, S. Kuprin, and G. Zaccai, "Protein hydration in solution: experimental observation by x-ray and neutron scattering," *Proc Natl Acad Sci U S A*, vol. 95, no. 5, pp. 2267–72, 1998.

[253] V. Makarov, B. M. Pettitt, and M. Feig, "Solvation and hydration of proteins and nucleic acids: a theoretical view of simulation and experiment," *Acc Chem Res*, vol. 35, no. 6, pp. 376–84, 2002.

[254] J. J. Virtanen, L. Makowski, T. R. Sosnick, and K. F. Freed, "Modeling the hydration layer around proteins: applications to small- and wide-angle x-ray scattering," *Biophys J*, vol. 101, no. 8, pp. 2061–9, 2011.

[255] J. Lipfert, S. Doniach, R. Das, and D. Herschlag, "Understanding nucleic acid-ion interactions," *Annu Rev Biochem*, vol. 83, pp. 813–41, 2014.

[256] R. Das, T. T. Mills, L. W. Kwok, G. S. Maskel, I. S. Millett, S. Doniach, K. D. Finkelstein, D. Herschlag, and L. Pollack, "Counterion distribution around dna probed by solution x-ray scattering," *Physical Review Letters*, vol. 90, no. 18, p. 188103, 2003.

[257] D. Schneidman-Duhovny, M. Hammel, and A. Sali, "Foxs: a web server for rapid computation and fitting of saxs profiles," *Nucleic Acids Res*, vol. 38, no. Web Server issue, pp. W540–4, 2010.

[258] K. Stovgaard, C. Andreetta, J. Ferkinghoff-Borg, and T. Hamelryck, "Calculation of accurate small angle x-ray scattering curves from coarse-grained protein models," *BMC Bioinformatics*, vol. 11, p. 429, 2010.

[259] H. Stuhrmann, *Ein neues Verfahren zur Bestimmung der Oberflächenform und der inneren Struktur von gelösten globulären Proteinen aus Röntgenkleinwinkelmessungen*, vol. 72. Zeitschrift fuer Physikalische Chemie, 1970.

[260] P. Chacon, F. Moran, J. F. Diaz, E. Pantos, and J. M. Andreu, "Low-resolution structures of proteins in solution retrieved from x-ray scattering with a genetic algorithm," *Biophys J*, vol. 74, no. 6, pp. 2760–75, 1998.

[261] D. I. Svergun, "Restoring low resolution structure of biological macromolecules from solution scattering using simulated annealing," *Biophys J*, vol. 76, no. 6, pp. 2879–86, 1999.

[262] D. Walther, F. E. Cohen, and S. Doniach, "Reconstruction of low-resolution three-dimensional density maps from one-dimensional small-angle x-ray solution scattering data for biomolecules," *Journal of Applied Crystallography*, vol. 33, no. 2, pp. 350–363, 2000.

[263] D. Franke and D. I. Svergun, "Dammif, a program for rapid ab-initio shape determination in small-angle scattering," *J Appl Crystallogr*, vol. 42, no. Pt 2, pp. 342–346, 2009.

[264] D. I. Svergun, M. V. Petoukhov, and M. H. Koch, "Determination of domain structure of proteins from x-ray solution scattering," *Biophys J*, vol. 80, no. 6, pp. 2946–53, 2001.

[265] S. S. Funari, G. Rapp, M. Perbandt, K. Dierks, M. Vallazza, C. Betzel, V. A. Erdmann, and D. I. Svergun, "Structure of free thermus flavus 5 s rrna at 1.3 nm resolution from synchrotron x-ray solution scattering," *J Biol Chem*, vol. 275, no. 40, pp. 31283–8, 2000.

[266] M. V. Petoukhov and D. I. Svergun, "Applications of small-angle x-ray scattering to biomacromolecular solutions," *Int J Biochem Cell Biol*, vol. 45, no. 2, pp. 429–37, 2013.

[267] C. Gorba and F. Tama, "Normal mode flexible fitting of high-resolution structures of biological molecules toward saxs data," *Bioinform Biol Insights*, vol. 4, pp. 43–54, 2010.

[268] W. Zheng and M. Tekpinar, "Accurate flexible fitting of high-resolution protein structures to small-angle x-ray scattering data using a coarse-grained model with implicit hydration shell," *Biophys J*, vol. 101, no. 12, pp. 2981–91, 2011.

[269] W. Wriggers, R. A. Milligan, and J. A. McCammon, "Situs: A package for docking crystal structures into low-resolution maps from electron microscopy," *J Struct Biol*, vol. 125, no. 2-3, pp. 185–95, 1999.

[270] M. Hammel, "Validation of macromolecular flexibility in solution by small-angle x-ray scattering (saxs)," *Eur Biophys J*, vol. 41, no. 10, pp. 789–99, 2012.

[271] R. P. Rambo and J. A. Tainer, "Bridging the solution divide: comprehensive structural analyses of dynamic rna, dna, and protein assemblies by small-angle x-ray scattering," *Curr Opin Struct Biol*, vol. 20, no. 1, pp. 128–37, 2010.

[272] L. Chen, K. O. Hodgson, and S. Doniach, "A lysozyme folding intermediate revealed by solution x-ray scattering," *Journal of Molecular Biology*, vol. 261, no. 5, pp. 658–671, 1996.

[273] D. J. Segel, A. L. Fink, K. O. Hodgson, and S. Doniach, "Protein denaturation: a small-angle x-ray scattering study of the ensemble of unfolded states of cytochrome c," *Biochemistry*, vol. 37, no. 36, pp. 12443–51, 1998.

[274] R. L. Owen, J. Juanhuix, and M. Fuchs, "Current advances in synchrotron radiation instrumentation for mx experiments," *Arch Biochem Biophys*, vol. 602, pp. 21–31, 2016.

[275] S. Doniach, "Fourth-generation x-ray sources: some possible applications to biology," *J Synchrotron Radiat*, vol. 7, no. Pt 3, pp. 116–20, 2000.

[276] P. Willmott, *An Introduction to Synchrotron Radiation. Techniques and Application.* Chichester UK: John Wiley and Sons, 2011.

[277] G. Margaritondo, *Characteristics and Properties of Synchrotron Radiation.* Springer, Berlin, Heidelberg, 2014.

[278] A. Balerna and S. Mobilio, *Synchrotron Radiation: Basics, Methods and Applications.* Springer Berlin Heidelberg, 2014.

[279] B. Lai, A. Khounsary, R. Savoy, E. R. Moog, and E. Gluskin, *Undulator A characteristics and specifications.* 1993.

[280] G. Aquilanti, L. Vaccari, J. R. laisier, and A. Goldoni, *Instrumentation at Synchrotron Radiation Beamlines.* Springer Berlin Heidelberg, 2015.

[281] W. H. Bragg and W. L. Bragg, "The reflection of x-rays by crystals," *Proceedings of the Royal Society of London. Series A*, vol. 88, no. 605, pp. 428–438, 1913.

[282] T. Zettl, "Enhanced structural and dynamical characterization combining gold nanocrystal labels and small-angle x-ray scattering," *Ludwig-Maximilians Universitaet Muenchen*, 2017.

[283] P. Pernot, A. Round, R. Barrett, A. De Maria Antolinos, A. Gobbo, E. Gordon, J. Huet, J. Kieffer, M. Lentini, M. Mattenet, C. Morawe, C. Mueller-Dieckmann, S. Ohlsson, W. Schmid, J. Surr, P. Theveneau, L. Zerrad, and S. McSweeney, "Upgraded esrf bm29 beamline for saxs on macromolecules in solution," *J Synchrotron Radiat*, vol. 20, no. Pt 4, pp. 660–4, 2013.

[284] P. Panine, S. Finet, T. M. Weiss, and T. Narayanan, "Probing fast kinetics in complex fluids by combined rapid mixing and small-angle x-ray scattering," *Adv. Colloid Interface Sci.*, vol. 127, no. 1, pp. 9–18, 2006.

[285] C. E. Blanchet, A. Spilotros, F. Schwemmer, M. A. Graewert, A. Kikhney, C. M. Jeffries, D. Franke, D. Mark, R. Zengerle, F. Cipriani, S. Fiedler, M. Roessle, and D. I. Svergun, "Versatile sample environments and automation for biological solution x-ray scattering experiments at the p12 beamline (petra iii, desy)," *J. Appl. Crystallogr.*, vol. 48, no. Pt 2, pp. 431–443, 2015.

[286] T. Narayanan, O. Diat, and P. Bösecke, "Saxs and usaxs on the high brilliance beamline at the esrf," *Nuclear Instruments and Methods in Physics Research Section A: Accelerators, Spectrometers, Detectors and Associated Equipment*, vol. 467-468, pp. 1005–1009, 2001.

[287] M. Sztucki and T. Narayanan, *Development of an ultra-small-angle X-ray scattering instrument for probing the microstructure and the dynamics of soft matter*, vol. 40. Journal of Applied Crystallography, 2006.

[288] K. H. Kim, S. Muniyappan, K. Y. Oang, J. G. Kim, S. Nozawa, T. Sato, S.-y. Koshihara, R. Henning, I. Kosheleva, H. Ki, Y. Kim, T. W. Kim, J. Kim, S.-i. Adachi, and H. Ihee, "Direct observation of cooperative protein structural dynamics of homodimeric hemoglobin from 100 ps to 10 ms with pump–probe x-ray solution scattering," *Journal of the American Chemical Society*, vol. 134, no. 16, pp. 7001–7008, 2012.

[289] R. Graceffa, R. P. Nobrega, R. A. Barrea, S. V. Kathuria, S. Chakravarthy, O. Bilsel, and T. C. Irving, "Sub-millisecond time-resolved saxs using a continuous-flow mixer and x-ray microbeam," *J Synchrotron Radiat*, vol. 20, no. Pt 6, pp. 820–5, 2013.

[290] L. Pollack, M. W. Tate, N. C. Darnton, J. B. Knight, S. M. Gruner, W. A. Eaton, and R. H. Austin, "Compactness of the denatured state of a fast-folding protein measured by submillisecond small-angle x-ray scattering," *Proc Natl Acad Sci U S A*, vol. 96, no. 18, pp. 10115–7, 1999.

[291] A. D. Stroock, S. K. Dertinger, A. Ajdari, I. Mezic, H. A. Stone, and G. M. Whitesides, "Chaotic mixer for microchannels," *Science*, vol. 295, no. 5555, pp. 647–51, 2002.

[292] F. Bottausci, I. Mezic, C. Meinhart, and C. Cardonne, *Mixing in the Shear Superposition Micromixer: Three-Dimensional Analysis*, vol. 362. 2004.

[293] O. Bilsel, C. Kayatekin, L. A. Wallace, and C. R. Matthews, "A microchannel solution mixer for studying microsecond protein folding reactions," *Review of Scientific Instruments*, vol. 76, no. 1, p. 014302, 2004.

[294] H. Roder, K. Maki, R. F. Latypov, H. Cheng, and M. C. R. Shastry, *Early Events in Protein Folding Explored by Rapid Mixing Methods*, pp. 491–535. Wiley-VCH Verlag GmbH, 2008.

[295] P. Regenfuss, R. M. Clegg, M. J. Fulwyler, F. J. Barrantes, and T. M. Jovin, "Mixing liquids in microseconds," *Review of Scientific Instruments*, vol. 56, no. 2, pp. 283–290, 1985.

[296] L. Pollack, "Time resolved saxs and rna folding," *Biopolymers*, vol. 95, no. 8, pp. 543–549, 2011.

[297] I. De Vlaminck and C. Dekker, "Recent advances in magnetic tweezers," *Annu Rev Biophys*, vol. 41, pp. 453–72, 2012.

[298] N. Ribeck and O. A. Saleh, "Multiplexed single-molecule measurements with magnetic tweezers," *Rev Sci Instrum*, vol. 79, no. 9, p. 094301, 2008.

[299] A. Huhle, D. Klaue, H. Brutzer, P. Daldrop, S. Joo, O. Otto, U. F. Keyser, and R. Seidel, "Camera-based three-dimensional real-time particle tracking at khz rates and angstrom accuracy," *Nat Commun*, vol. 6, p. 5885, 2015.

[300] D. A. Koster, A. Crut, S. Shuman, M. A. Bjornsti, and N. H. Dekker, "Cellular strategies for regulating dna supercoiling: a single-molecule perspective," *Cell*, vol. 142, no. 4, pp. 519–30, 2010.

[301] D. Dulin, J. Lipfert, M. C. Moolman, and N. H. Dekker, "Studying genomic processes at the single-molecule level: introducing the tools and applications," *Nat Rev Genet*, vol. 14, no. 1, pp. 9–22, 2013.

[302] J. S. Graham, R. C. Johnson, and J. F. Marko, "Concentration-dependent exchange accelerates turnover of proteins bound to double-stranded dna," *Nucleic Acids Res*, vol. 39, no. 6, pp. 2249–59, 2011.

[303] M. D. Szczelkun, M. S. Tikhomirova, T. Sinkunas, G. Gasiunas, T. Karvelis, P. Pschera, V. Siksnys, and R. Seidel, "Direct observation of r-loop formation by single rna-guided cas9 and cascade effector complexes," *Proceedings of the National Academy of Sciences*, vol. 111, no. 27, pp. 9798–9803, 2014.

[304] N. Ribeck and O. A. Saleh, "Dna unwinding by ring-shaped t4 helicase gp41 is hindered by tension on the occluded strand," *PLOS ONE*, vol. 8, no. 11, p. e79237, 2013.

[305] M. Levikova, D. Klaue, R. Seidel, and P. Cejka, "Nuclease activity of saccharomyces cerevisiae dna2 inhibits its potent dna helicase activity," *Proceedings of the National Academy of Sciences*, vol. 110, no. 22, pp. E1992–E2001, 2013.

[306] E. A. Abbondanzieri, W. J. Greenleaf, J. W. Shaevitz, R. Landick, and S. M. Block, "Direct observation of base-pair stepping by rna polymerase," *Nature*, vol. 438, no. 7067, pp. 460–5, 2005.

[307] M. Manosas, S. K. Perumal, V. Croquette, and S. J. Benkovic, "Direct observation of stalled fork restart via fork regression in the t4 replication system," *Science*, vol. 338, no. 6111, pp. 1217–1220, 2012.

[308] M. T. van Loenhout, J. W. Kerssemakers, I. De Vlaminck, and C. Dekker, "Non-bias-limited tracking of spherical particles, enabling nanometer resolution at low magnification," *Biophys J*, vol. 102, no. 10, pp. 2362–71, 2012.

[309] I. Teledyne DALSA, *Falcon2 User Manual.* 2013.

[310] B. M. Lansdorp and O. A. Saleh, "Power spectrum and allan variance methods for calibrating single-molecule video-tracking instruments," *Rev Sci Instrum*, vol. 83, no. 2, p. 025115, 2012.

[311] F. Czerwinski, A. C. Richardson, and L. B. Oddershede, "Quantifying noise in optical tweezers by allan variance," *Opt Express*, vol. 17, no. 15, pp. 13255–69, 2009.

[312] D. Allan, "Statistics of atomic frequency standards," *Proceedings of the IEEE*, vol. 54, p. 221, 1966.

[313] A. J. te Velthuis, J. W. Kerssemakers, J. Lipfert, and N. H. Dekker, "Quantitative guidelines for force calibration through spectral analysis of magnetic tweezers data," *Biophys J*, vol. 99, no. 4, pp. 1292–302, 2010.

[314] W. P. Wong and K. Halvorsen, "The effect of integration time on fluctuation measurements: calibrating an optical trap in the presence of motion blur," *Opt Express*, vol. 14, no. 25, pp. 12517–31, 2006.

[315] W. P. Wong and K. Halvorsen, "Beyond the frame rate: measuring high-frequency fluctuations with light-intensity modulation," *Optics Letters*, vol. 34, no. 3, pp. 277–279, 2009.

[316] C. Gosse and V. Croquette, "Magnetic tweezers: micromanipulation and force measurement at the molecular level," *Biophysical Journal*, vol. 82, no. 6, pp. 3314–3329, 2002.

[317] C. Bustamante, Z. Bryant, and S. B. Smith, "Ten years of tension: single-molecule dna mechanics," *Nature*, vol. 421, no. 6921, pp. 423–7, 2003.

[318] C. G. Baumann, V. A. Bloomfield, S. B. Smith, C. Bustamante, M. D. Wang, and S. M. Block, "Stretching of single collapsed dna molecules," *Biophysical Journal*, vol. 78, no. 4, pp. 1965–1978, 2000.

[319] M. D. Wang, H. Yin, R. Landick, J. Gelles, and S. M. Block, "Stretching dna with optical tweezers," *Biophys J*, vol. 72, no. 3, pp. 1335–46, 1997.

[320] T. Strick, "Mechanical supercoiling of dna and its relaxation by topoisomerases," *The University of Paris*, 1999.

[321] D. Klaue and R. Seidel, "Torsional stiffness of single superparamagnetic microspheres in an external magnetic field," *Physical Review Letters*, vol. 102, no. 2, p. 028302, 2009.

[322] G. Perry, "The absolute beginner's guide to binary, hex, bits, and bytes! how to master your computer's love language," *Inc makeright Publishing*, 2010.

[323] S. Singh, *The Code Book: The Secrets Behind Codebreaking*. Ember, 2016.

[324] T. N. LUMICKS (De Boelelaan 1085, Amsterdam *Acoustic Force Spectroscopy (AFS)*, 2017.

[325] J. W. Kerssemakers, E. L. Munteanu, L. Laan, T. L. Noetzel, M. E. Janson, and M. Dogterom, "Assembly dynamics of microtubules at molecular resolution," *Nature*, vol. 442, no. 7103, pp. 709–12, 2006.

[326] R. K. Milne, G. F. Yeo, B. W. Madsen, and R. O. Edeson, "Estimation of single channel kinetic parameters from data subject to limited time resolution," *Biophys J*, vol. 55, no. 4, pp. 673–6, 1989.

[327] A. Glycerine Producers, *Physical properties of glycerine and its solutions*. New York: Glycerine Producers' Association, 1963.

[328] M. T. Woodside, P. C. Anthony, W. M. Behnke-Parks, K. Larizadeh, D. Herschlag, and S. M. Block, "Direct measurement of the full, sequence-dependent folding landscape of a nucleic acid," *Science*, vol. 314, no. 5801, pp. 1001–4, 2006.

[329] A. P. Manuel, J. Lambert, and M. T. Woodside, "Reconstructing folding energy landscapes from splitting probability analysis of single-molecule trajectories," *Proc Natl Acad Sci U S A*, vol. 112, no. 23, pp. 7183–8, 2015.

[330] M. T. Woodside and S. M. Block, "Reconstructing folding energy landscapes by single-molecule force spectroscopy," *Annu Rev Biophys*, vol. 43, pp. 19–39, 2014.

[331] A. Jansson, Peter, *Deconvolution of images and spectra (2nd ed.)*. Academic Press, Inc., 1996.

[332] D. R. Burnham, I. De Vlaminck, T. Henighan, and C. Dekker, "Skewed brownian fluctuations in single-molecule magnetic tweezers," *PLoS One*, vol. 9, no. 9, p. e108271, 2014.

[333] K. D. L. S. D. N. M. t. f. s.-m. e. I. H. P. v. O. A. e. Vilfan I.D., Lipfert J., "Handbook of single-molecule biophysics," *Springer*, 2009.

[334] L. F. Liu and J. C. Wang, "Supercoiling of the dna template during transcription," *Proc Natl Acad Sci U S A*, vol. 84, no. 20, pp. 7024–7, 1987.

[335] N. R. Cozzarelli, G. J. Cost, M. Nollmann, T. Viard, and J. E. Stray, "Giant proteins that move dna: bullies of the genomic playground," *Nat Rev Mol Cell Biol*, vol. 7, no. 8, pp. 580–8, 2006.

[336] T. J. Stevens, D. Lando, S. Basu, L. P. Atkinson, Y. Cao, S. F. Lee, M. Leeb, K. J. Wohlfahrt, W. Boucher, A. O'Shaughnessy-Kirwan, J. Cramard, A. J. Faure, M. Ralser, E. Blanco, L. Morey, M. Sansó, M. G. S. Palayret, B. Lehner, L. Di Croce, A. Wutz, B. Hendrich, D. Klenerman, and E. D. Laue, "3d structures of individual mammalian genomes studied by single-cell hi-c," *Nature*, vol. 544, no. 7648, pp. 59–64, 2017.

[337] F. B. Fuller, "Decomposition of the linking number of a closed ribbon: A problem from molecular biology," *Proc Natl Acad Sci U S A*, vol. 75, no. 8, pp. 3557–61, 1978.

[338] J. H. White, "Self-linking and the gauss integral in higher dimensions," *American Journal of Mathematics*, vol. 91, no. 3, pp. 693–728, 1969.

[339] A. V. Vologodskii and N. R. Cozzarelli, "Conformational and thermodynamic properties of supercoiled dna," *Annu Rev Biophys Biomol Struct*, vol. 23, pp. 609–43, 1994.

[340] T. Schlick, "Modeling superhelical dna: recent analytical and dynamic approaches," *Curr Opin Struct Biol*, vol. 5, no. 2, pp. 245–62, 1995.

[341] J. Vinograd, J. Lebowitz, R. Radloff, R. Watson, and P. Laipis, "The twisted circular form of polyoma viral dna," *Proc Natl Acad Sci U S A*, vol. 53, no. 5, pp. 1104–11, 1965.

[342] J. Dekker and L. Mirny, "The 3d genome as moderator of chromosomal communication," *Cell*, vol. 164, no. 6, pp. 1110–21, 2016.

[343] A. Crut, D. A. Koster, R. Seidel, C. H. Wiggins, and N. H. Dekker, "Fast dynamics of supercoiled dna revealed by single-molecule experiments," *Proc Natl Acad Sci U S A*, vol. 104, no. 29, pp. 11957–62, 2007.

[344] S. Forth, C. Deufel, M. Y. Sheinin, B. Daniels, J. P. Sethna, and M. D. Wang, "Abrupt buckling transition observed during the plectoneme formation of individual dna molecules," *Phys Rev Lett*, vol. 100, no. 14, p. 148301, 2008.

[345] B. C. Daniels and J. P. Sethna, "Nucleation at the dna supercoiling transition," *Phys Rev E Stat Nonlin Soft Matter Phys*, vol. 83, no. 4 Pt 1, p. 041924, 2011.

[346] L. Postow, C. D. Hardy, J. Arsuaga, and N. R. Cozzarelli, "Topological domain structure of the escherichia coli chromosome," *Genes Dev*, vol. 18, no. 14, pp. 1766–79, 2004.

[347] H. Bai, J. E. Kath, F. M. Zorgiebel, M. Sun, P. Ghosh, G. F. Hatfull, N. D. Grindley, and J. F. Marko, "Remote control of dna-acting enzymes by varying the brownian dynamics of a distant dna end," *Proc Natl Acad Sci U S A*, vol. 109, no. 41, pp. 16546–51, 2012.

[348] R. Du, V. S. Pande, A. Y. Grosberg, T. Tanaka, and E. S. Shakhnovich, "On the transition coordinate for protein folding," *The Journal of Chemical Physics*, vol. 108, no. 1, pp. 334–350, 1998.

[349] J. D. Chodera and V. S. Pande, "Splitting probabilities as a test of reaction coordinate choice in single-molecule experiments," *Physical review letters*, vol. 107, no. 9, pp. 098102–098102, 2011.

[350] H. A. Kramers, "Brownian motion in a field of force and the diffusion model of chemical reactions," *Physica*, vol. 7, no. 4, pp. 284–304, 1940.

[351] P. Hänggi, P. Talkner, and M. Borkovec, "Reaction-rate theory: fifty years after kramers," *Reviews of Modern Physics*, vol. 62, no. 2, pp. 251–341, 1990.

[352] R. Berkovich, R. I. Hermans, I. Popa, G. Stirnemann, S. Garcia-Manyes, B. J. Berne, and J. M. Fernandez, "Rate limit of protein elastic response is tether dependent," *Proceedings of the National Academy of Sciences*, vol. 109, no. 36, pp. 14416–14421, 2012.

[353] H. Lannon, J. S. Haghpanah, J. K. Montclare, E. Vanden-Eijnden, and J. Brujic, "Force-clamp experiments reveal the free-energy profile and diffusion coefficient of the collapse of protein molecules," *Physical Review Letters*, vol. 110, no. 12, p. 128301, 2013.

[354] E. Stellwagen and N. C. Stellwagen, "Electrostatic coupling between dna and its counterions modulates the observed translational diffusion coefficients," *Anal Chem*, vol. 87, no. 17, pp. 9042–6, 2015.

[355] B. Sudhanshu, S. Mihardja, E. F. Koslover, S. Mehraeen, C. Bustamante, and A. J. Spakowitz, "Tension-dependent structural deformation alters single-molecule transition kinetics," *Proc Natl Acad Sci U S A*, vol. 108, no. 5, pp. 1885–90, 2011.

[356] T. A. Lionberger, D. Demurtas, G. Witz, J. Dorier, T. Lillian, E. Meyhofer, and A. Stasiak, "Cooperative kinking at distant sites in mechanically stressed dna," *Nucleic Acids Res*, vol. 39, no. 22, pp. 9820–32, 2011.

[357] R. N. Irobalieva, J. M. Fogg, J. Catanese, D. J., T. Sutthibutpong, M. Chen, A. K. Barker, S. J. Ludtke, S. A. Harris, M. F. Schmid, W. Chiu, and L. Zechiedrich, "Structural diversity of supercoiled dna," *Nat Commun*, vol. 6, p. 8440, 2015.

[358] J. S. Mitchell, C. A. Laughton, and S. A. Harris, "Atomistic simulations reveal bubbles, kinks and wrinkles in supercoiled dna," *Nucleic Acids Res*, vol. 39, no. 9, pp. 3928–38, 2011.

[359] A. Dittmore, S. Brahmachari, Y. Takagi, J. F. Marko, and K. C. Neuman, "Supercoiling dna locates mismatches," *Phys Rev Lett*, vol. 119, no. 14, p. 147801, 2017.

[360] O. K. Dudko, G. Hummer, and A. Szabo, "Theory, analysis, and interpretation of single-molecule force spectroscopy experiments," *Proc Natl Acad Sci U S A*, vol. 105, no. 41, pp. 15755–60, 2008.

[361] Y. Suzuki and O. K. Dudko, "Single-molecule rupture dynamics on multidimensional landscapes," *Phys Rev Lett*, vol. 104, no. 4, p. 048101, 2010.

[362] D. A. Koster, K. Palle, E. S. Bot, M. A. Bjornsti, and N. H. Dekker, "Antitumour drugs impede dna uncoiling by topoisomerase i," *Nature*, vol. 448, no. 7150, pp. 213–7, 2007.

[363] J. Leach, H. Mushfique, S. Keen, R. Di Leonardo, G. Ruocco, J. M. Cooper, and M. J. Padgett, "Comparison of faxen's correction for a microsphere translating or rotating near a surface," *Phys Rev E Stat Nonlin Soft Matter Phys*, vol. 79, no. 2 Pt 2, p. 026301, 2009.

[364] H. Faxén, "Der widerstand gegen die bewegung einer starren kugel in einer zähen flüssigkeit, die zwischen zwei parallelen ebenen wänden eingeschlossen ist," *Annalen der Physik*, vol. 373, no. 10, pp. 89–119, 1922.

[365] Y. M. Rhee and V. S. Pande, "One-dimensional reaction coordinate and the corresponding potential of mean force from commitment probability distribution," *The Journal of Physical Chemistry B*, vol. 109, no. 14, pp. 6780–6786, 2005.

[366] R. B. Best and G. Hummer, "Coordinate-dependent diffusion in protein folding," *Proceedings of the National Academy of Sciences*, vol. 107, no. 3, pp. 1088–1093, 2010.

[367] J. Lipfert, M. M. van Oene, M. Lee, F. Pedaci, and N. H. Dekker, "Torque spectroscopy for the study of rotary motion in biological systems," *Chem Rev*, vol. 115, no. 3, pp. 1449–74, 2015.

[368] J. C. Meiners and S. R. Quake, "Femtonewton force spectroscopy of single extended dna molecules," *Phys Rev Lett*, vol. 84, no. 21, pp. 5014–7, 2000.

[369] J. Shin, A. G. Cherstvy, and R. Metzler, "Kinetics of polymer looping with macromolecular crowding: effects of volume fraction and crowder size," *Soft Matter*, vol. 11, no. 3, pp. 472–88, 2015.

[370] K. Kiyosawa, "Volumetric properties of polyols (ethylene glycol, glycerol, meso-erythritol, xylitol and mannitol) in relation to their membrane permeability: group additivity and estimation of the maximum radius of their molecules," *Biochim Biophys Acta*, vol. 1064, no. 2, pp. 251–5, 1991.

[371] P. Del Vecchio, D. Esposito, L. Ricchi, and G. Barone, "The effects of polyols on the thermal stability of calf thymus dna," *Int J Biol Macromol*, vol. 24, no. 4, pp. 361–9, 1999.

[372] N.-S. Cheng, "Formula for the viscosity of a glycerol water mixture," *Industrial and Engineering Chemistry Research*, vol. 47, no. 9, pp. 3285–3288, 2008.

[373] S. Garcia-Manyes, J. Brujic, C. L. Badilla, and J. M. Fernandez, "Force-clamp spectroscopy of single-protein monomers reveals the individual unfolding and folding pathways of i27 and ubiquitin," *Biophys J*, vol. 93, no. 7, pp. 2436–46, 2007.

[374] J. L. Choy, S. H. Parekh, O. Chaudhuri, A. P. Liu, C. Bustamante, M. J. Footer, J. A. Theriot, and D. A. Fletcher, "Differential force microscope for long time-scale biophysical measurements," *Rev Sci Instrum*, vol. 78, no. 4, p. 043711, 2007.

[375] A. E. Wallin, H. Ojala, G. Ziedaite, and E. Haeggstrom, "Dual-trap optical tweezers with real-time force clamp control," *Rev Sci Instrum*, vol. 82, no. 8, p. 083102, 2011.

[376] C. A. Bippes, H. Janovjak, A. Kedrov, and D. J. Muller, "Digital force-feedback for protein unfolding experiments using atomic force microscopy," *Nanotechnology*, vol. 18, 2007.

[377] M. Ganji, S. H. Kim, J. van der Torre, E. Abbondanzieri, and C. Dekker, "Intercalation-based single-molecule fluorescence assay to study dna supercoil dynamics," *Nano Lett*, vol. 16, no. 7, pp. 4699–707, 2016.

[378] C. Pinto, K. Kasaciunaite, R. Seidel, and P. Cejka, "Human dna2 possesses a cryptic dna unwinding activity that functionally integrates with blm or wrn helicases," *Elife*, vol. 5, 2016.

[379] G. Kostiuk, J. Dikic, F. W. Schwarz, G. Sasnauskas, R. Seidel, and V. Siksnys, "The dynamics of the monomeric restriction endonuclease bcni during its interaction with dna," *Nucleic Acids Res*, vol. 45, no. 10, pp. 5968–5979, 2017.

[380] D. Dulin, J. J. Arnold, T. van Laar, H. S. Oh, C. Lee, A. L. Perkins, D. A. Harki, M. Depken, C. E. Cameron, and N. H. Dekker, "Signatures of nucleotide analog incorporation by an rna-dependent rna polymerase revealed using high-throughput magnetic tweezers," *Cell Rep*, vol. 21, no. 4, pp. 1063–1076, 2017.

[381] S. Haldar, R. Tapia-Rojo, E. C. Eckels, J. Valle-Orero, and J. M. Fernandez, "Trigger factor chaperone acts as a mechanical foldase," *Nat Commun*, vol. 8, no. 1, p. 668, 2017.

[382] J. Valle-Orero, R. Tapia-Rojo, E. C. Eckels, J. A. Rivas-Pardo, I. Popa, and J. M. Fernandez, "Proteins breaking bad: A free energy perspective," *J Phys Chem Lett*, vol. 8, no. 15, pp. 3642–3647, 2017.

[383] R. Janissen, B. A. Berghuis, D. Dulin, M. Wink, T. van Laar, and N. H. Dekker, "Invincible dna tethers: covalent dna anchoring for enhanced temporal and force stability in magnetic tweezers experiments," *Nucleic Acids Research*, vol. 42, no. 18, pp. e137–e137, 2014.

[384] H. Lannon, E. Vanden-Eijnden, and J. Brujic, "Force-clamp analysis techniques give highest rank to stretched exponential unfolding kinetics in ubiquitin," *Biophys J*, vol. 103, no. 10, pp. 2215–22, 2012.

[385] E. Durner, W. Ott, M. A. Nash, and H. E. Gaub, "Post-translational sortase-mediated attachment of high-strength force spectroscopy handles," *ACS Omega*, vol. 2, no. 6, pp. 3064–3069, 2017.

[386] J. Yin, P. D. Straight, S. M. McLoughlin, Z. Zhou, A. J. Lin, D. E. Golan, N. L. Kelleher, R. Kolter, and C. T. Walsh, "Genetically encoded short peptide tag for versatile protein labeling by sfp phosphopantetheinyl transferase," *Proc Natl Acad Sci U S A*, vol. 102, no. 44, pp. 15815–20, 2005.

[387] L. S. Wong, J. Thirlway, and J. Micklefield, "Direct site-selective covalent protein immobilization catalyzed by a phosphopantetheinyl transferase," *J Am Chem Soc*, vol. 130, no. 37, pp. 12456–64, 2008.

[388] L. Chan, H. F. Cross, J. K. She, G. Cavalli, H. F. Martins, and C. Neylon, "Covalent attachment of proteins to solid supports and surfaces via sortase-mediated ligation," *PLoS One*, vol. 2, no. 11, p. e1164, 2007.

[389] G. V. Los, L. P. Encell, M. G. McDougall, D. D. Hartzell, N. Karassina, C. Zimprich, M. G. Wood, R. Learish, R. F. Ohana, M. Urh, D. Simpson, J. Mendez, K. Zimmerman, P. Otto, G. Vidugiris, J. Zhu, A. Darzins, D. H. Klaubert, R. F. Bulleit, and K. V. Wood, "Halotag: A novel protein labeling technology for cell imaging and protein analysis," *ACS Chemical Biology*, vol. 3, no. 6, pp. 373–382, 2008.

[390] Y. Taniguchi and M. Kawakami, "Application of halotag protein to covalent immobilization of recombinant proteins for single molecule force spectroscopy," *Langmuir*, vol. 26, no. 13, pp. 10433–10436, 2010.

[391] B. Zakeri, J. O. Fierer, E. Celik, E. C. Chittock, U. Schwarz-Linek, V. T. Moy, and M. Howarth, "Peptide tag forming a rapid covalent bond to a protein, through engineering a bacterial adhesin," *Proc Natl Acad Sci U S A*, vol. 109, no. 12, pp. E690–7, 2012.

[392] R. Walder, M.-A. LeBlanc, W. J. Van Patten, D. T. Edwards, J. A. Greenberg, A. Adhikari, S. R. Okoniewski, R. M. A. Sullan, D. Rabuka, M. C. Sousa, and T. T. Perkins, "Rapid characterization of a mechanically labile alpha-helical protein enabled by efficient site-specific bioconjugation," *Journal of the American Chemical Society*, vol. 139, no. 29, pp. 9867–9875, 2017.

[393] W. J. Van Patten, R. Walder, A. Adhikari, S. R. Okoniewski, R. Ravichandran, C. E. Tinberg, D. Baker, and T. T. Perkins, "Improved free-energy landscape quantification illustrated with a computationally designed protein-ligand interaction," *Chemphyschem*, vol. 19, no. 1, pp. 19–23, 2018.

[394] S. Le, X. Hu, M. Yao, H. Chen, M. Yu, X. Xu, N. Nakazawa, F. M. Margadant, M. P. Sheetz, and J. Yan, "Mechanotransmission and mechanosensing of human alpha-actinin 1," *Cell Rep*, vol. 21, no. 10, pp. 2714–2723, 2017.

[395] X. Zhao, X. Zeng, C. Lu, and J. Yan, "Studying the mechanical responses of proteins using magnetic tweezers," *Nanotechnology*, vol. 28, no. 41, p. 414002, 2017.

[396] R. S. Winardhi, Q. Tang, J. Chen, M. Yao, and J. Yan, "Probing small molecule binding to unfolded polyprotein based on its elasticity and refolding," *Biophys J*, vol. 111, no. 11, pp. 2349–2357, 2016.

[397] H. Cai and S. J. Wind, "Improved glass surface passivation for single-molecule nanoarrays," *Langmuir*, vol. 32, no. 39, pp. 10034–10041, 2016.

[398] E. Celik and V. T. Moy, "Nonspecific interactions in afm force spectroscopy measurements," *J Mol Recognit*, vol. 25, no. 1, pp. 53–6, 2012.

[399] H. Johansson, M. R. Jensen, H. Gesmar, S. Meier, J. M. Vinther, C. Keeler, M. E. Hodsdon, and J. J. Led, "Specific and nonspecific interactions in ultraweak protein–protein associations revealed by solvent paramagnetic relaxation enhancements," *Journal of the American Chemical Society*, vol. 136, no. 29, pp. 10277–10286, 2014.

[400] S. D. Chandradoss, A. C. Haagsma, Y. K. Lee, J. H. Hwang, J. M. Nam, and C. Joo, "Surface passivation for single-molecule protein studies," *J Vis Exp*, no. 86, 2014.

[401] S. M. Sedlak, M. S. Bauer, C. Kluger, L. C. Schendel, L. F. Milles, D. A. Pippig, and H. E. Gaub, "Monodisperse measurement of the biotin-streptavidin interaction strength in a well-defined pulling geometry," *PLoS One*, vol. 12, no. 12, p. e0188722, 2017.

[402] F. Baumann, M. S. Bauer, M. Rees, A. Alexandrovich, M. Gautel, D. A. Pippig, and H. E. Gaub, "Increasing evidence of mechanical force as a functional regulator in smooth muscle myosin light chain kinase," *Elife*, vol. 6, 2017.

[403] T. Verdorfer, R. C. Bernardi, A. Meinhold, W. Ott, Z. Luthey-Schulten, M. A. Nash, and H. E. Gaub, "Combining in vitro and in silico single-molecule force spectroscopy to characterize and tune cellulosomal scaffoldin mechanics," *J Am Chem Soc*, vol. 139, no. 49, pp. 17841–17852, 2017.

[404] W. Ott, M. A. Jobst, M. S. Bauer, E. Durner, L. F. Milles, M. A. Nash, and H. E. Gaub, "Elastin-like polypeptide linkers for single-molecule force spectroscopy," *ACS Nano*, vol. 11, no. 6, pp. 6346–6354, 2017.

[405] R. Petrosyan, "Improved approximations for some polymer extension models," *Rheologica Acta*, vol. 56, no. 1, pp. 21–26, 2017.

[406] B. M. Dorr, H. O. Ham, C. An, E. L. Chaikof, and D. R. Liu, "Reprogramming the specificity of sortase enzymes," *Proc Natl Acad Sci U S A*, vol. 111, no. 37, pp. 13343–8, 2014.

[407] S. Roberts, M. Dzuricky, and A. Chilkoti, "Elastin-like polypeptides as models of intrinsically disordered proteins," *FEBS Lett*, vol. 589, no. 19 Pt A, pp. 2477–86, 2015.

[408] F. Berkemeier, M. Schlierf, and M. Rief, "Mechanically controlled preparation of protein intermediates in single molecule experiments," *physica status solidi (a)*, vol. 203, no. 14, pp. 3492–3495, 2006.

[409] Z. T. Yew, M. Schlierf, M. Rief, and E. Paci, "Direct evidence of the multidimensionality of the free-energy landscapes of proteins revealed by mechanical probes," *Phys Rev E Stat Nonlin Soft Matter Phys*, vol. 81, no. 3 Pt 1, p. 031923, 2010.

[410] S. Luccioli, A. Imparato, S. Mitternacht, A. Irback, and A. Torcini, "Unfolding times for proteins in a force clamp," *Phys Rev E Stat Nonlin Soft Matter Phys*, vol. 81, no. 1 Pt 1, p. 010902, 2010.

[411] M. Schlierf, F. Berkemeier, and M. Rief, "Direct observation of active protein folding using lock-in force spectroscopy," *Biophysical Journal*, vol. 93, no. 11, pp. 3989–3998, 2007.

[412] M. Schlierf and M. Rief, "Single-molecule unfolding force distributions reveal a funnel-shaped energy landscape," *Biophysical Journal*, vol. 90, no. 4, pp. L33–L35, 2006.

[413] Z. T. Yew, S. Krivov, and E. Paci, "Free-energy landscapes of proteins in the presence and absence of force," *J Phys Chem B*, vol. 112, no. 51, pp. 16902–7, 2008.

[414] P. Cossio, G. Hummer, and A. Szabo, "Kinetic ductility and force-spike resistance of proteins from single-molecule force spectroscopy," *Biophys J*, vol. 111, no. 4, pp. 832–840, 2016.

[415] B. Heymann and H. Grubmuller, "Dynamic force spectroscopy of molecular adhesion bonds," *Phys Rev Lett*, vol. 84, no. 26 Pt 1, pp. 6126–9, 2000.

[416] D. J. Brockwell, G. S. Beddard, E. Paci, D. K. West, P. D. Olmsted, D. A. Smith, and S. E. Radford, "Mechanically unfolding the small, topologically simple protein l," *Biophys J*, vol. 89, no. 1, pp. 506–19, 2005.

[417] P. M. Williams, S. B. Fowler, R. B. Best, J. L. Toca-Herrera, K. A. Scott, A. Steward, and J. Clarke, "Hidden complexity in the mechanical properties of titin," *Nature*, vol. 422, no. 6930, pp. 446–9, 2003.

[418] M. Fairhead, D. Krndija, E. D. Lowe, and M. Howarth, "Plug-and-play pairing via defined divalent streptavidins," *J Mol Biol*, vol. 426, no. 1, pp. 199–214, 2014.

[419] M. Siavashpouri, C. H. Wachauf, M. J. Zakhary, F. Praetorius, H. Dietz, and Z. Dogic, "Molecular engineering of chiral colloidal liquid crystals using dna origami," *Nat. Mater.*, vol. 16, no. 8, pp. 849–856, 2017.

[420] P. D. Halley, C. R. Lucas, E. M. McWilliams, M. J. Webber, R. A. Patton, C. Kural, D. M. Lucas, J. C. Byrd, and C. E. Castro, "Daunorubicin-loaded dna origami nanostructures circumvent drug-resistance mechanisms in a leukemia model," *Small*, vol. 12, no. 3, pp. 308–20, 2016.

[421] G. Tikhomirov, P. Petersen, and L. Qian, "Fractal assembly of micrometre-scale dna origami arrays with arbitrary patterns," *Nature*, vol. 552, p. 67, 2017.

[422] L. L. Ong, N. Hanikel, O. K. Yaghi, C. Grun, M. T. Strauss, P. Bron, J. Lai-Kee-Him, F. Schueder, B. Wang, P. Wang, J. Y. Kishi, C. Myhrvold, A. Zhu, R. Jungmann, G. Bellot, Y. Ke, and P. Yin, "Programmable self-assembly of three-dimensional nanostructures from 10,000 unique components," *Nature*, vol. 552, p. 72, 2017.

[423] A. E. Marras, L. Zhou, H. J. Su, and C. E. Castro, "Programmable motion of dna origami mechanisms," *Proc. Natl. Acad. Sci. U. S. A.*, vol. 112, no. 3, pp. 713–8, 2015.

[424] F. C. Simmel and B. Yurke, "A dna-based molecular device switchable between three distinct mechanical states," *Applied Physics Letters*, vol. 80, no. 5, pp. 883–885, 2002.

[425] J. Pan, F. Li, T. G. Cha, H. Chen, and J. H. Choi, "Recent progress on dna based walkers," *Current Opinion in Biotechnology*, vol. 34, pp. 56–64, 2015.

[426] R. Russell, X. Zhuang, H. P. Babcock, I. S. Millett, S. Doniach, S. Chu, and D. Herschlag, "Exploring the folding landscape of a structured rna," *Proc. Natl. Acad. Sci. U. S. A.*, vol. 99, no. 1, pp. 155–60, 2002.

[427] S. J. Chen and K. A. Dill, "Rna folding energy landscapes," *Proc. Natl. Acad. Sci. U. S. A.*, vol. 97, no. 2, pp. 646–51, 2000.

[428] L. Pollack and S. Doniach, *Time-resolved X-ray scattering and RNA folding*, vol. 469, book section 12, pp. 253–268. Elsevier Inc., 2009.

[429] G. L. Hura, A. L. Menon, M. Hammel, R. P. Rambo, n. Poole, F. L., S. E. Tsutakawa, J. Jenney, F. E., S. Classen, K. A. Frankel, R. C. Hopkins, S. J. Yang, J. W. Scott, B. D. Dillard, M. W. Adams, and J. A. Tainer, "Robust, high-throughput solution structural analyses by small angle x-ray scattering (saxs)," *Nature Methods*, vol. 6, no. 8, pp. 606–12, 2009.

[430] S. Fischer, C. Hartl, K. Frank, J. O. Rädler, T. Liedl, and B. Nickel, "Shape and interhelical spacing of dna origami nanostructures studied by small-angle x-ray scattering," *Nano Letters*, vol. 16, no. 7, pp. 4282–4287, 2016.

[431] J. Song, G.-N. Gomes, T. Shi, C. C. Gradinaru, and H. S. Chan, "Conformational heterogeneity and fret data interpretation for dimensions of unfolded proteins," *Biophysical Journal*, vol. 113, no. 5, pp. 1012–1024, 2017.

[432] G. Fuertes, N. Banterle, K. M. Ruff, A. Chowdhury, D. Mercadante, C. Koehler, M. Kachala, G. Estrada Girona, S. Milles, A. Mishra, P. R. Onck, F. Grater, S. Esteban-Martin, R. V. Pappu, D. I. Svergun, and E. A. Lemke, "Decoupling of size and shape fluctuations in heteropolymeric sequences reconciles discrepancies in saxs vs. fret measurements," *Proc. Natl. Acad. Sci. U. S. A.*, vol. 114, no. 31, pp. E6342–e6351, 2017.

[433] W. Kugel, A. Muschielok, and J. Michaelis, "Bayesian-inference-based fluorescence correlation spectroscopy and single-molecule burst analysis reveal the influence of dye selection on dna hairpin dynamics," *Chemphyschem*, vol. 13, no. 4, pp. 1013–22, 2012.

[434] B. Kick, F. Praetorius, H. Dietz, and D. Weuster-Botz, "Efficient production of single-stranded phage dna as scaffolds for dna origami," *Nano Lett.*, vol. 15, no. 7, pp. 4672–6, 2015.

[435] P. Atkins and J. de Paula, *Atkins' Physical Chemistry*. USA: Oxford University Press, 2002.

[436] W. Y. Yang and M. Gruebele, "Folding at the speed limit," *Nature*, vol. 423, no. 6936, pp. 193–7, 2003.

[437] D. Lehner, H. Lindner, and O. Glatter, "Determination of the translational and rotational diffusion coefficients of rodlike particles using depolarized dynamic light scattering," *Langmuir*, vol. 16, no. 4, pp. 1689–1695, 2000.

[438] M. M. Tirado, C. L. Martínez, and J. G. d. la Torre, "Comparison of theories for the translational and rotational diffusion coefficients of rod-like macromolecules. application to short dna fragments," *Journal of Chemical Physics*, vol. 81, no. 4, pp. 2047–2052, 1984.

[439] S. A. McKinney, A. C. Declais, D. M. Lilley, and T. Ha, "Structural dynamics of individual holliday junctions," *Nat. Struct. Biol.*, vol. 10, no. 2, pp. 93–7, 2003.

[440] C. Joo, S. A. McKinney, D. M. Lilley, and T. Ha, "Exploring rare conformational species and ionic effects in dna holliday junctions using single-molecule spectroscopy," *J. Mol. Biol.*, vol. 341, no. 3, pp. 739–51, 2004.

[441] F. J. Overmars and C. Altona, "Nmr study of the exchange rate between two stacked conformers of a model holliday junction," *J. Mol. Biol.*, vol. 273, no. 3, pp. 519–24, 1997.

[442] J. Yu, T. Ha, and K. Schulten, "Conformational model of the holliday junction transition deduced from molecular dynamics simulations," *Nucleic Acids Res.*, vol. 32, no. 22, pp. 6683–95, 2004.

[443] C. Hyeon and D. Thirumalai, "Chain length determines the folding rates of rna," *Biophys. J.*, vol. 102, no. 3, pp. L11–3, 2012.

List of Figures

1.1 Schematic of a Conventional Magnetic Tweezers Setup . . . 4
1.2 Height Determination with a LUT . . . 5
1.3 Variations of Magnetic Tweezers . . . 5
1.4 Angular Tracking in MTT . . . 7
1.5 Structural Model and Force-Extension Response of dsDNA . . . 8
1.6 BS-Transition and Rotation Curves of dsDNA in MT . . . 10
1.7 Protein Structure . . . 13
1.8 Structure of ddFLN4 . . . 14

2.1 Schematic of Self-Assembling DNA Origami Structure . . . 16
2.2 Examples of DNA Origamis . . . 18

3.1 Schematic of SAXS Experiments . . . 22
3.2 Elastic Rayleigh Scattering in SAXS Experiments . . . 23
3.3 Radiation Damage . . . 25
3.4 Guinier Approximation . . . 27
3.5 Different Representations of Scattering Data . . . 28
3.6 Comparison of Reciprocal and Real Space Representation . . . 29
3.7 Ab Initio 3D Shape Reconstruction . . . 30
3.8 Different Generation of Synchrotron Sources . . . 32
3.9 Illustration of the Main Components of a Synchrotron . . . 32
3.10 Magnet Configurations of a Synchrotron . . . 34
3.11 Different Emission Spectra of Bending Magnets and Undulators . . . 35
3.12 Monochromator Based on Bragg's Law . . . 36
3.13 Schematic of a Stopped-Flow Mixing Device . . . 38

4.1 Picture of the Magnetic Tweezers Setup . . . 43
4.2 Allan Deviation of Different Tracker Types and Setting . . . 48
4.3 Allan Deviation of 58 Hz and 1000 Hz . . . 49
4.4 Height Accuracy for Different Distances Between the Magnets and the Flow Cell 49
4.5 Force Calibration of MyOne Beads . . . 51
4.6 Force Calibration of M270 Beads . . . 52
4.7 Force Homogeneity Within One FOV . . . 54

5.1 Flowchart of "MT GUI" . . . 61
5.2 Main GUI of "MT GUI" . . . 62
5.3 Flowchart of the Main GUI of "MT GUI" . . . 63
5.4 "Further Analysis GUI" . . . 66
5.5 "Summary Analysis GUI" . . . 67
5.6 "WLC GUI" . . . 68

5.7 "Force Calibration GUI" . . . 69
5.8 "Hopping Single GUI" . . . 72
5.9 "Edit Hopping Info File GUI" . . . 73
5.10 "Hopping Fast Load GUI" . . . 73
5.11 "Deconvolution GUI" . . . 75

6.1 DNA Buckling Measurements in the Magnetic Tweezers . . . 84
6.2 Quantification of DNA Buckling Dynamics . . . 85
6.3 Reconstruction and Quantification of the Energy Landscape . . . 86
6.4 Energy Landscape of the DNA Buckling Transition . . . 87
6.5 Testing the Time Resolution Limits Using Brownian Dynamics Simulations of the Bead-DNA System . . . 99
6.6 Power Spectral Density of Extension Fluctuations for DNA-Tethered Beads . . . 100
6.7 Examples of Dwell Times for Pre- and Post-Buckling States . . . 100
6.8 Influence of Bead Size on DNA Buckling Transitions . . . 101
6.9 Comparison of the Sum of ΔWr_{pre} and ΔWr_{post} Compared to Directly Measured ΔWr_b . . . 101
6.10 Comparison of Different Energy Landscape Reconstruction Approaches . . . 102
6.11 Additional Analyses of the Buckling Energy Landscape . . . 102
6.12 Equilibrium Properties of the Buckling Transition for DNA . . . 103
6.13 Analysis of Energy Barrier Height and Curvature at $P_{post} = 0.5$ . . . 104
6.14 Curvature of the Reconstructed Energy Minima and Maxima . . . 105
6.15 Effect of Glycerol on Buckling Dynamics and Equilibrium Properties . . . 106
6.16 Buckling Times vs. Monovalent Salt Concentration at Different Forces . . . 107
6.17 Effect of the Correction of the Buckling Times for Finite Acquisition Time . . . 107
6.18 Magnitude of the Extension Fluctuations and Estimate of the Instrument Response Function S(z) . . . 108

7.1 Multiple Step Caused by a Nonspecific Bound Bead . . . 112
7.2 Surface Attachment Strategy with PEG . . . 113
7.3 External Specific Attachment of Beads to a Coverslip . . . 114
7.4 Specific Binding to a Functional Spot Inside a Flow Cell (PEG) . . . 115
7.5 Gray Shades after PEG Attachment . . . 116
7.6 Impact of Buffer Conditions on Nonspecific Binding . . . 117
7.7 Minimizing Nonspecific Interaction with PEG and Tween . . . 118
7.8 Surface Passivation of ELP Coated Flow Cells . . . 121
7.9 Final Attachment Strategy (ELP) . . . 122
7.10 Example Traces of ddFLN4 Unfolding and Refolding Events . . . 123
7.11 Example Traces of VWF Unfolding and Refolding . . . 125
7.12 Extension Trace of an ELP Linker as Function of Force . . . 126
7.13 Lifetime of Streptavidin-Biotin Bond Under Force . . . 127
7.14 Extension Curves as Function of Force of ddFLN4 Subdomains . . . 129
7.15 Unfolding and Refolding Rates as Function of Force for ddFLN4 . . . 130
7.16 Illustration of 1D Energy Landscape of ddFLN4 . . . 131
7.17 Rates of Complete Unfolding and Refolding of ddFLN4 as Function of Force . . . 132
7.18 Extension Trace of ddFLN4 at Equilibrium Force . . . 134

8.1 Schematic of Time-Resolved SAXS and a $MgCl_2$-dependent DNA Origami Switch Device . . . 147
8.2 TrSAXS Reveals Conformational Kinetics of a DNA Origami Switch Device . . 148
8.3 TrSAXS Measurements on Dimerization Kinetics of DNA Origami Bricks . . . 149
8.4 Scaling Relationship for Nucleic Acid Folding Rate Constants . . . 157
8.5 Time-Dependent Scattering Profiles for SwitchD16 and Two-State Fits . . . 158
8.6 Estimate of the Closing Reaction Rate Constant of SwitchD16 Particles for a Final $MgCl_2$ Concentration of 25 mM After Mixing . . . 159
8.7 Schematic Model and Length Scales of Switch D16. . . . 159
8.8 Time Evolution of Scattering Profiles from DNA Origami Dimerization Kinetics 160
8.9 Strand Diagram of the Dynamic (SwitchD16) Variant . . . 161
8.10 Strand Diagram of Brick Monomer A_1 . . . 162
8.11 Strand Diagram of Brick Monomer A_2 . . . 163

10.1 Allan Deviation in z for Different Tracker Algorithms and Tracker Settings . . 176
10.2 Allan Deviation in x for Different Tracker Algorithms and Tracker Settings . . 177
10.3 Flowchart of “Further Analysis GUI” . . . 179
10.4 Flowchart of “Summary Analysis GUI” . . . 180
10.5 Flowchart of “Force Calibration GUI” . . . 181
10.6 Flowchart of “Hopping Single GUI” . . . 182
10.7 Flowchart of “Edit Hopping Info File GUI” . . . 182
10.8 Flowchart of “Hopping Fast Load GUI” . . . 183
10.9 Flowchart of “Deconvolution GUI” . . . 184

List of Tables

3.1 Properties of Selected Beamlines at Two Synchrotron Facilities 37

4.1 Maximum Number of Beads Trackable in Real Time 45
4.2 Standard Deviation of Different Tracker Settings and Bead Sizes 47

10.1 List of Components of the Magnetic Tweezers Setup 173
10.2 Complete List of Maximum Number of Beads Trackable in Real Time for all Tracker and Tracker Settings Examined 175
10.3 Complete List of Standard Deviations for all Tracker and Tracker Settings Examined for Two Bead Sizes 178

Acknowledgments

Auf dem Weg zu und während meiner Promotion haben mich viele Menschen unterstützt, bei all denen ich mich bedanken möchte. Ganz besonders möchte ich mich bedanken bei:

Jan Lipfert für die Unterstützung während meiner Promotion, sowie die großen Freiheiten die ich genießen konnte. Dies beinhaltet vor allem mein Umschwenken von Magnetic Tweezers zu SAXS ohne auf Widerstand gestoßen zu sein, sowie das Dulden von mehr oder weniger sinnvollen deep-neural-networks Berechnungen.

Hermann Gaub für die Finanzhilfen für meine Stelle, das Setup, sowie dem Kicker.

Linda Brützel für die große moralische Unterstützung auf dem Weg zum Sinn der Promotion. Danke für dein geduldiges Erklären der SAXS-Grundlagen und dass du mit unserem gemeinsamen SAXS-Origami-Projekt es mir ermöglicht hast zum Ende meiner Promotion ein spannendes Projekt durchzuführen. Es hat viel Spaß gemacht im Büro zusammen zu diskutieren, aber auch an den Beamlines mit konstruktiven Besprechungen unseren Messplan immer schnell und unter Zeitdruck an aktuelle Gegebenheiten (erfolgreich) anzupassen.

Achim Löf für die humorvolle und dennoch sehr konstruktive Zusammenarbeit bei den Proteinen in den Tweezers, sowie den Ginabenden im Innenhof und für das immer positiv bleiben, wenn die Problemliste eines Projektes schneller wächst als sie abgearbeitet wird (falls sie abgearbeitet wird). Natürlich auch Danke für das Korrekturlesen der Dissertation!

Willem Vanderlinden für die tolle Zusammenarbeit beim "hopping" paper, insbesondere für den bio-chemischen Input. Natürlich auch für das mir schmackhaft machen von "fish-and-chips"!

Franziska Kriegel für die vielen hilfreichen Diskussionen rund um die Arbeit, aber auch für die gute Stimmung im Büro.

Thomas Zettl für die IT Unterstützung bei der Workstation und natürlich die hilfreichen Diskussionen während des BWL Kurses!

Thomas Gerling für die DNA-Origami Massenproduktion.

Philipp Walker für die vielen Selbstgespräche und kompetenten Meinungen.

Sebastian Konrad für das Anfixen mit machine learning und deep-neural-netwoks, und die gute Stimmung im Büro.

Markust Jobst für die Unterstützung bei der wahren Hürde zum Doktor: eine Prüfungskommission zusammenzustellen.

Sylvia Kreuzer für die organisatorische Unterstützung und die vielen vielen Gummibärchen …

Thomas Nicolaus … stellt euch nur mal ein Labor ohne Toms Coverslips vor …

Constantin Schöler für den gemeinsam geschriebenen, erfolgreichen, Antrag für den Lehrstuhl-Kicker, so wie die viele Kickerspiele und aufheiternde Gespräche.

viele mehr, dies beinhaltet vor allem den **LS Gaub** und die **AG Lipfert**, für die gute Atmosphäre und Zusammenarbeit.

Natürlich habe ich auch während meines Studiums und meiner Promotion viel private Unterstützung bekommen, dafür möchte ich mich insbesondere bei **Andrea** und **meiner Familie** bedanken!